

Development of Predictive Models of Flow Induced and Localized Corrosion

Kevin L. Heppner

A Thesis submitted to the

College of Graduate Studies and Research

as partial fulfillment of the requirements for the degree of

Doctor of Philosophy

in Chemical Engineering

University of Saskatchewan

© Copyright Kevin L. Heppner, May 2006. All rights reserved.

Permission to Use

In presenting this thesis in partial fulfillment of the requirements for a doctorate of philosophy degree from the University of Saskatchewan, I agree that the Libraries of this University may make it freely available for inspection. I further agree that permission for copying of this thesis in any manner, in whole or in part, for scholarly purposes may be granted by Dr. Richard Evitts who supervised my thesis work or, in his absence, by the Head of the Chemical Engineering Department or the Dean of the College of Engineering. It is understood that any copying, publication, or use of this thesis or parts thereof for financial gain shall not be allowed without my written permission. It is also understood that due recognition shall be given to me and to the University of Saskatchewan in any scholarly use which may be made of any material in my thesis.

Requests for permission to copy or to make other use of material in this thesis in whole or part should be addressed to:

Head of the Department of Chemical Engineering

University of Saskatchewan

Saskatoon, Saskatchewan

Canada

S7N 5C5

Abstract

Corrosion is a serious industrial concern. According to a cost of corrosion study released in 2002, the direct cost of corrosion is approximately \$276 billion dollars in the United States – approximately 3.1% of their Gross Domestic Product*. Key influences on the severity of corrosion include: metal and electrolyte composition, temperature, turbulent flow, and location of attack. In this work, mechanistic models of localized and flow influenced corrosion were constructed and these influences on corrosion were simulated.

A rigorous description of mass transport is paramount for accurate corrosion modelling. A new moderately dilute mass transport model was developed. A customized hybrid differencing scheme was used to discretize the model. The scheme calculated an appropriate upwind parameter based upon the Peclet number. Charge density effects were modelled using an algebraic charge density correction. Activity coefficients were calculated using Pitzer's equations. This transport model was computationally efficient and yielded accurate simulation results relative to experimental data. Use of the hybrid differencing scheme with the mass transport equation resulted in simulation results which were up to 87% more accurate (relative to experimental data) than other conventional differencing schemes. In addition, when the charge density correction was used during the solution of the electromigration-diffusion equation, rather than solving the charge density term separately, a sixfold increase in the simulation time to real time was seen (for equal time steps in both simulation strategies). Furthermore, the charge density correction is algebraic, and thus, can be

* Reference: <http://www.nace.org/nace/content/publicaffairs/cocorrindex.asp>

applied at larger time steps that would cause the solution of the charge density term to not converge.

The validated mass transport model was then applied to simulate crevice corrosion initiation of passive alloys. The cathodic reactions assumed to occur were crevice-external oxygen reduction and crevice-internal hydrogen ion reduction. Dissolution of each metal in the alloy occurred at anodic sites. The predicted transient and spatial pH profile for type 304 stainless steel was in good agreement with the independent experimental data of others. Furthermore, the pH predictions of the new model for 304 stainless steel more closely matched experimental results than previous models.

The mass transport model was also applied to model flow influenced CO_2 corrosion. The CO_2 corrosion model accounted for iron dissolution, H^+ , H_2CO_3 , and water reduction, and FeCO_3 film formation. The model accurately predicted experimental transient corrosion rate data.

Finally, a comprehensive model of crevice corrosion under the influence of flow was developed. The mass transport model was modified to account for convection. Electrode potential and current density in solution was calculated using a rigorous electrode-coupling algorithm. It was predicted that as the crevice gap to depth ratio increased, the extent of fluid penetration also increased, thereby causing crevice washout. However, for crevices with small crevice gaps, external flow increased the cathodic limiting current while fluid penetration did not occur, thereby increasing the propensity for crevice corrosion.

Acknowledgements

Firstly, I wish to thank my wonderful wife, Erin. She was my greatest supporter throughout my Ph.D. and her love continues to encourage me. Erin, you are my love and my life. Thank you so much.

I am so grateful to my parents, Alfred Heppner and Edna Heppner, for inspiring me through their life example to work hard to reach my goals. I am also grateful to my mother and father-in-law, Ken and Ardyss Johnston, for their love and support, and for treating me as one of their own as I studied away from my home.

I would like to acknowledge my supervisor and friend, Dr. Richard Evitts. The guidance and opportunities that he provided to me were invaluable in my training. He graciously sent me to numerous conferences and encouraged me to publish my work. For the effort he put into my training, I am very grateful.

I wish to acknowledge my co-supervisor, Dr. John Postlethwaite. His breadth of experience from many years as a corrosion specialist and educator was a tremendously valuable resource. I also acknowledge my Ph.D. committee members – Drs. Aaron Phoenix, Mehdi Nemati, Rob Sumner, and Don Bergstrom.

I acknowledge the work of Glyn Kennell, a talented young researcher who worked as a summer student under my supervision. I also thank my co-workers and friends for many great memories throughout my Ph.D. – Lin Lu, Curtis Rempel, Greg Del Frari, Michael Wormsbecker, Jason Wiens, Greg Sample, and Troy Koepke.

Scholarship support for my Ph.D. was provided by the Natural Sciences and Engineering Research Council (NSERC) and by the University of Saskatchewan Department of Chemical Engineering.

This thesis is dedicated to my family

Erin and Jacob

Alfred Heppner and Edna Heppner

Ken and Ardys Johnston

Tamara Dutchak

Lori and Remmus Reichert

Table of Contents

PERMISSION TO USE	I
ABSTRACT	II
ACKNOWLEDGEMENTS	IV
NOMENCLATURE	XI
LIST OF TABLES	XVI
LIST OF FIGURES	XVII
CHAPTER 1. INTRODUCTION	1
1.1 General Summary	1
1.2 Significance of Contributions	3
1.3 Research Objective	5
CHAPTER 2. INTRODUCTION TO CREVICE CORROSION MODELLING	7
2.1 The Stages of Crevice Corrosion	7
2.1.1 Crevice deoxygenation	7
2.1.2 Crevice acidification	8
2.1.3 Development of a critical crevice solution	10
2.1.4 Active crevice corrosion	11
2.2 Numerical Modelling of Crevice Corrosion	11
2.2.1 Modelling of electromigration and diffusion mass transport	14
2.2.2 Modelling of charge density effects on mass transport	15
2.2.3 Modelling of electrode kinetics	15
2.2.4 Modelling of chemical equilibrium	15
2.2.5 Solution methodology	17
2.3 References	20
CHAPTER 3. MASS TRANSPORT MODELLING	21
3.1 Introduction	21
3.2 The Charge Density Correction Scheme	21

3.2.1 Model development	23
3.2.1.1 Mass transport	23
3.2.1.2 Charge density correction	25
3.2.2 Model validation	29
3.2.3 Numerical experiment	30
3.2.3.1 Effect of concentration	33
3.2.3.2 Effect of current density	38
3.2.3.3 Effect of spatial step size	44
3.2.3.4 Effect of time step size	46
3.2.3.5 Computational efficiency	51
3.2.4 Conclusions	54
3.2.5 References	58
3.3 The Hybrid Differencing Scheme	60
3.3.1 Development of the electrolyte mass transport hybrid differencing scheme	62
3.3.1.1 Background	62
3.3.1.2 Model derivation	64
3.3.1.3 Stability of the electrolyte mass transport hybrid differencing scheme	70
3.3.2 Discrete transport model development	74
3.3.3 Modelling of the Fu and Chan moving boundary experiment	79
3.3.3.1 Effect of charge density	84
3.3.3.2 Effect of spatial step size	85
3.3.3.3 Computational efficiency	89
3.3.4 Conclusions	91
3.3.5 References	95
CHAPTER 4. CREVICE CORROSION INITIATION OF PASSIVE METALS	98
4.1 Effect of the Crevice Gap on Crevice Corrosion Initiation	100
4.1.1 Mathematical model	101
4.1.1.1 Mass transport	101
4.1.1.2 Electrochemical reactions	102
4.1.2 Model implementation	104
4.1.3 Results	105
4.1.3.1 Simulation of Alavi and Cottis experiment	105
4.1.3.2 Effect of the crevice gap on the incubation period of titanium	111
4.1.3.3 Effect of the crevice gap on the steady state iR drop and charge density in a titanium crevice solution	125
4.1.4 Conclusions	133
4.1.5 References	136
4.2 Effect of Solution Composition on Crevice Corrosion Initiation	141
4.2.1 Mathematical model of crevice corrosion	142
4.2.1.1 Mass transport	142
4.2.1.2 Chemical equilibrium	144
4.2.1.3 Electrochemical reactions	145
4.2.2 Ionic interaction model	147

4.2.3 Results and discussion	152
4.2.3.1 Type 304 stainless steel crevice	154
4.2.3.2 Titanium crevice	161
4.2.4 Conclusions	165
4.2.5 References	171
4.3 Effect of Hydrogen Ion Reduction on Crevice Corrosion Initiation	174
4.3.1 Introduction	175
4.3.2 The mathematical model	176
4.3.3 Numerical solution of the model	178
4.3.4 Results and discussion	179
4.3.5 Conclusions	185
4.3.6 References	187
4.4 Application of the Crevice Corrosion Initiation Model to Alloy Ranking	188
4.4.1 Introduction	189
4.4.2 Crevice corrosion mechanism	190
4.4.3 Mathematical model	192
4.4.3.1 Mass transport	192
4.4.3.2 Electrode reactions	193
4.4.3.3 Chemical equilibrium	194
4.4.3.4 The numerical model	194
4.4.4 Simulation of crevice corrosion initiation	197
4.4.5 Results and discussion	198
4.4.5.1 Simulation of Grade 2 titanium crevice corrosion initiation	198
4.4.5.2 Relationship between critical crevice pH and the PREN	201
4.4.5.3 Type 308 stainless steel	205
4.4.5.4 Type 314 stainless steel	205
4.4.5.5 Type 304 stainless steel	207
4.4.5.6 Type 405 stainless steel	209
4.4.5.7 Ranking of the alloys	211
4.4.6 Conclusions	211
4.4.7 References	214
CHAPTER 5. CARBON DIOXIDE CORROSION	217
5.1 Background on Carbon Dioxide Corrosion	217
5.2 Literature on Carbon Dioxide Corrosion	219
5.2.1 Experimental work	220
5.2.1.1 De Waard and Milliams (1975)	220
5.2.1.2 Schmitt and Rothmann (1977)	220
5.2.1.3 Gray et al. (1989)	221
5.2.1.4 Nestic et al. (1995)	221
5.2.1.5 Schmitt and Rothmann (1978)	221
5.2.2 Modelling work	222
5.2.2.1 DeWaard and Milliams (1975)	222

5.2.2.2 Gray et al. (1989, 1990)	222
5.2.2.3 Nestic et al. (1995)	222
5.2.2.4 Turgoose et al. (1990)	223
5.2.2.5 Wang (1997)	223
5.2.2.6 Nordsveen et al., Nestic et al., Nestic and Lee (2003)	223
5.3 Numerical Model of Carbon Dioxide Corrosion	224
5.3.1 Effect of flow	228
5.4 References	232
CHAPTER 6. FLOW INFLUENCED CREVICE CORROSION	235
6.1 Computational Fluid Dynamics Model	237
6.1.1 Flow boundary conditions	238
6.1.1.1 Boundary conditions at laminar sublayer thickness	240
6.1.2 Relationship between sublayer thickness and Reynolds number	242
6.2 Simulation of Crevice Washout	243
6.3 Conclusions	252
6.4 References	253
CHAPTER 7. SUMMARY AND CONCLUSIONS	254
7.1 Summary	254
7.2 Conclusions	255
7.2.1 Modelling of electrolyte mass transport	255
7.2.2 Simulation of crevice corrosion initiation of passive metals	256
7.2.3 Simulation of flow influenced CO ₂ corrosion	259
7.2.4 Simulation of flow influenced crevice corrosion	259
7.3 Overall Conclusions	261
CHAPTER 8. RECOMMENDATIONS	263
APPENDIX A. SENSITIVITY OF PREDICTED ACTIVITY COEFFICIENTS ON PARAMETERS FOR PITZER'S EQUATIONS	265
A.1 Pitzer's Equations	265
A.2 Parameter Sensitivity Analysis	266
A.3 Summary	270

APPENDIX B. ELECTROCHEMICAL MASS TRANSPORT MODEL IN A TWO-DIMENSIONAL CREVICE	273
B.1 Mass Transport	273
B.2 Calculation of the Potential Field in Solution	278
B.3 Electrode Reactions	282
B.3.1 Coupling of anode-cathode pairs	284
B.4 Overall Algorithm	290
B.5 References	292
APPENDIX C. LIST OF PUBLICATIONS	293

Nomenclature

Symbol	Units	Definition
a	mol/L	Activity
a		Discrete equation coefficient
A_{cs}	m^2	Crevice cross sectional area
A_m	m^2	Metal surface area
A_ϕ	$(kg/mol)^{1/2}$	Debye-Hückel parameter
b		Tafel Slope
b_ϕ	$(kg/mol)^{1/2}$	Universal parameter in Pitzer's equations
B		Modified second virial coefficient in Pitzer's equations
B'		Modified second virial coefficient in Pitzer's equations
B^ϕ		Modified second virial coefficient in Pitzer's equations
C		Modified third virial coefficient in Pitzer's equations
C'		Modified third virial coefficient in Pitzer's equations
C^ϕ		Modified third virial coefficient in Pitzer's equations
C_i	mol/m^3	Molar concentration of i^{th} species

D	m^2/s	Mass diffusion coefficient
D	m	Pipe diameter
E	V	Electrical potential of metal
${}^E\theta$		Term accounting for electrostatic unsymmetrical mixing effect
E_a	J/mol	Activation energy of passive corrosion current
f		Fanning friction factor
f^γ		Debye-Hückel term
F	C/mol	Faraday's constant (96487)
F^γ		Debye-Hückel summation term
g		Function used in Pitzer's equations
g'		Function used in Pitzer's equations
K		Chemical Equilibrium Constant
i	A/m^2	Current density
\mathbf{i}	A/m^2	Current density vector
i_o	A/m^2	Exchange Current density
I	mol/kg	Ionic strength
L	m	Crevice depth
m_i	mol/kg	Molality of species i in solution
m_s	mol/kg	Molality of solvent in solution
M	g/mol	Molecular weight

n		Number of electrons transferred during electrode reaction
N_i	mol/m ² s	Mass flux of i^{th} species
P		Peclet number
P'		Modified Peclet number
R	J/(mol K)	Universal Gas Constant (8.3145)
R_i		Chemical reaction source term for i^{th} species
Re		Reynolds number
t	s	Time
T	K	Temperature
u_i	m ² mol/J s	Mobility of i^{th} species
u^+		Dimensionless velocity in universal velocity profile
u_τ	m/s	Friction velocity
\mathbf{v}	m/s	Velocity
v_x	m/s	x-direction component of velocity vector
v_y	m/s	y-direction component of velocity vector
V_b	m/s	Bulk velocity
x	m	Spatial Coordinate
y	m	Spatial Coordinate
y^+		Dimensionless distance in universal velocity profile

z		Charge number of ion
Z	mol/kg	Sum of ionic charge molality product
Greek Letters		
α		Electromigration upwinding parameter
α		Parameter in Pitzer's equations
β		Convection upwinding parameter
β		Parameter in Pitzer's equations
ϕ		Osmotic coefficient
Φ	V	Electrical potential in solution
ε	Farad / m	Dielectric constant of water
λ		Original second virial coefficient
λ	m	Viscous sublayer thickness
ν	m ² /s	Kinematic viscosity
ν		Stoichiometric coefficient
μ	Pa s	Solution viscosity
μ		Original third virial coefficient
γ		Activity Coefficient
ρ	kg/m ³	Density
δ	C/m ³	Charge density in solution
κ	S/m	Solution conductivity
ψ		Proportionality constant in charge density correction

Ψ Fraction of cathodic charge supplied by hydrogen ion reduction

τ_w Pa Wall shear stress

Subscripts and Superscripts

a Anode

c Cathode

cdp Convection diffusion potential

e East interface

E East

i Index

j Index

k Index

lim Limiting

O Old

P Point

rev Reversible

rxn Of the reaction

species Of the species

t Turbulence

w West interface

W West

x In the x direction

y In the y direction

List of Tables

Table 3.2.1. Comparison of the ratio of simulation time to real time when using the algebraic charge density correction and the operator splitting method for a variety of grid spacings for simulating the Fu and Chan experiment. Simulations were performed using a 3.06 GHz Intel Pentium 4 computer with 1 GB of RAM.....	53
Table 4.1.1. Chemical reactions occurring in a type 304 stainless steel crevice solution	108
Table 4.1.2. Chemical reactions occurring in a titanium crevice solution.....	114
Table 4.2.1. Parameters and their representation used in the activity model of Pitzer.	149
Table 4.2.2. Binary cation-anion interaction parameters for the type 304 stainless steel crevice solution	152
Table 4.2.3. Binary anion-anion or cation-cation interaction parameters for the type 304 stainless steel crevice solution	152
Table 4.2.4. Ternary anion-anion-cation or cation-cation-anion interaction parameters for the type 304 stainless steel crevice solution.....	153
Table 4.2.5. Default values of Pitzer model parameters used when no experimentally determined values are available	153
Table 4.4.1. Assumed composition of alloys used in this study [16]. Iron comprises balance. Impurities are neglected.....	198
Table 4.4.2. Critical crevice pH values used in this study.....	203
Table A.1. Sensitivity of the cationic activity coefficient to the fundamental parameters of Pitzer's equations.....	270
Table A.2. Sensitivity of the anionic activity coefficient to the fundamental parameters of Pitzer's equations.....	270

List of Figures

Figure 2.1. Processes occurring during crevice corrosion initiation. Grey double-sided arrows indicate transport mechanisms while dark arrows indicate electrochemical and chemical reactions.	9
Figure 2.2. Typical kinetic corrosion diagram of crevice corrosion: (a) crevice in passivated state; (b) crevice in active state.	12
Figure 2.3. (a) Computational grid which is used to discretize the crevice solution; (b) Computational node which is labelled to illustrate the point (P), east (E), and west (W) indices. Boundaries are spaced halfway between nodes and represent control volume interfaces.	16
Figure 2.4. Flowsheet of solution algorithm used to solve passive crevice corrosion problem.	18
Figure 3.2.1. Diagram of the experimental apparatus used by Fu and Chan in the moving boundary experiment.	31
Figure 3.2.2. Comparison of the predicted transient position of the Ag^+/K^+ moving boundary with the experimental observations of Fu and Chan.	32
Figure 3.2.3. Comparison of the spatial and transient Ag^+ and K^+ concentration profiles predicted by the operator splitting scheme and the algebraic charge density correction for a 0.1 M KNO_3 solution ($318 \mu\text{A}/\text{cm}^2$ current density, $\Delta x = 0.05 \text{ cm}$, $\Delta t = 0.1 \text{ s}$): a) moving boundary region after 40 minutes simulation time; b) spatial profile of error between predictions of operator splitting scheme and algebraic charge density correction after 40 minutes simulation time; c) transient profile of space-averaged error between predictions of operator splitting scheme and algebraic charge density correction.	35
Figure 3.2.4. Comparison of the spatial and transient Ag^+ and K^+ concentration profiles predicted by the operator splitting scheme and the algebraic charge density correction for a 1 M KNO_3 solution ($318 \mu\text{A}/\text{cm}^2$ current density, $\Delta x = 0.05 \text{ cm}$, $\Delta t = 0.1 \text{ s}$): a) moving boundary region after 40 minutes simulation time; b) spatial profile of error between predictions of operator splitting scheme and algebraic charge density correction after 40 minutes simulation time; c) transient profile of space-averaged error between predictions of operator splitting scheme and algebraic charge density correction.	36
Figure 3.2.5. Comparison of the spatial and transient Ag^+ and K^+ concentration profiles predicted by the operator splitting scheme and the algebraic charge density correction for a current density of $10 \mu\text{A}/\text{cm}^2$ (0.1 M KNO_3 solution, $\Delta x = 0.05 \text{ cm}$, $\Delta t = 0.1 \text{ s}$): a) moving boundary region after 40 minutes simulation time; b) spatial profile of error between predictions of operator splitting scheme and algebraic charge density correction after 40 minutes simulation time; c) transient profile of space-averaged error between predictions of operator splitting scheme and algebraic charge density correction.	39
Figure 3.2.6. Comparison of the spatial and transient Ag^+ and K^+ concentration profiles predicted by the operator splitting scheme and the algebraic charge density correction for a current density of $100 \mu\text{A}/\text{cm}^2$ (0.1 M KNO_3 solution, $\Delta x = 0.05 \text{ cm}$, $\Delta t = 0.1 \text{ s}$): a) moving boundary region after 40 minutes simulation	

time; b) spatial profile of error between predictions of operator splitting scheme and algebraic charge density correction after 40 minutes simulation time; c) transient profile of space-averaged error between predictions of operator splitting scheme and algebraic charge density correction.....	42
Figure 3.2.7. Comparison of the spatial and transient Ag^+ and K^+ concentration profiles predicted by the operator splitting scheme and the algebraic charge density correction for a current density of $500 \mu\text{A}/\text{cm}^2$ (0.1 M KNO_3 solution, $\Delta x = 0.05 \text{ cm}$, $\Delta t = 0.1 \text{ s}$): a) moving boundary region after 20 minutes simulation time; b) spatial profile of error between predictions of operator splitting scheme and algebraic charge density correction after 20 minutes simulation time; c) transient profile of space-averaged error between predictions of operator splitting scheme and algebraic charge density correction.....	43
Figure 3.2.8. Relationship between the velocity of the moving boundary and the applied current density (0.1 M KNO_3 solution, $\Delta x = 0.05 \text{ cm}$, $\Delta t = 0.1 \text{ s}$). Discrete data points were obtained from numerical simulation results presented in Figs. 5 – 7. A least squares linear fit is shown ($R^2 = 1$).....	45
Figure 3.2.9. Moving boundary profile after 40 minutes predicted using the operator splitting and algebraic correction charge density calculation methods for differing spatial step sizes (0.1 M KNO_3 solution, $318 \mu\text{A}/\text{cm}^2$ current density, $\Delta t = 0.1 \text{ s}$): (a) $\Delta x = 0.5 \text{ cm}$ (10 nodes); (b) $\Delta x = 0.05 \text{ cm}$ (100 nodes); (c) $\Delta x = 0.005 \text{ cm}$ (1000 nodes).	47
Figure 3.2.10. Difference between moving boundary profiles after 40 minutes predicted using the operator splitting and algebraic correction charge density calculation methods for differing spatial step sizes (0.1 M KNO_3 solution, $318 \mu\text{A}/\text{cm}^2$ current density, $\Delta t = 0.1 \text{ s}$): (a) $\Delta x = 0.5 \text{ cm}$ (10 nodes); (b) $\Delta x = 0.05 \text{ cm}$ (100 nodes); (c) $\Delta x = 0.005 \text{ cm}$ (1000 nodes)	48
Figure 3.2.11. Moving boundary profile after 40 minutes predicted using the operator splitting and algebraic correction charge density calculation methods for differing time step sizes (0.1 M KNO_3 solution, $318 \mu\text{A}/\text{cm}^2$ current density, $\Delta x = 0.05 \text{ cm}$): (a) $\Delta t = 0.01 \text{ s}$; (b) $\Delta t = 0.1 \text{ s}$; (c) $\Delta t = 1 \text{ s}$; (d) $\Delta t = 10 \text{ s}$	50
Figure 3.2.12. Difference between moving boundary profiles after 40 minutes predicted using the operator splitting and algebraic correction charge density calculation methods for differing time step sizes (0.1 M KNO_3 solution, $318 \mu\text{A}/\text{cm}^2$ current density, $\Delta x = 0.05 \text{ cm}$): (a) $\Delta t = 0.01 \text{ s}$; (b) $\Delta t = 0.1 \text{ s}$; (c) $\Delta t = 1 \text{ s}$; (d) $\Delta t = 10 \text{ s}$.	52
Figure 3.3.1. The spatial upwind parameter profile across a computational control volume over a range of Peclet numbers.....	69
Figure 3.3.2. Solution of the electromigration-diffusion balance equation across a computational control volume as solution charge density increases. Critical damping occurs when $\delta \approx 7.7 \times 10^{-9} \text{ C}/\text{m}^3$	72
Figure 3.3.3. Solution of the electromigration-diffusion balance equation across a computational control volume as the concentration profile is shifted upwards: a) $\delta = 0 \text{ C}/\text{m}^3$; b) $\delta = 5 \times 10^{-9}$; c) $\delta = 1 \times 10^{-8} \text{ C}/\text{m}^3$; c) $\delta = 1 \times 10^{-7} \text{ C}/\text{m}^3$. Critical damping occurs when $\delta \approx 7.7 \times 10^{-9} \text{ C}/\text{m}^3$	75
Figure 3.3.4. The variation of $a_E \Delta x / D_i$ with the Peclet number.....	80
Figure 3.3.5. The mass transport model solution algorithm presented as a flow sheet.	82

Figure 3.3.6. The calculated moving boundary region of the Fu and Chan experimental apparatus: a) after 5 minutes; b) after 20 minutes; c) after 30 minutes; d) after 40 minutes. In each sub-figure, the vertical line represents the experimentally observed position of the boundary (boundary position was linearly interpolated from raw data).....	83
Figure 3.3.7. The effect of charge density on the predicted moving boundary region of the Fu and Chan experiment.....	86
Figure 3.3.8. The calculated unit charge upwind parameter as a function of space step size, Δx , for the model of the Fu and Chan experiment.....	87
Figure 3.3.9. The effect of step size on the predicted boundary region of the Fu and Chan experiment after 10 minutes.....	88
Figure 3.3.10. The percentage increase in simulation time required when using the hybrid differencing scheme rather than the upwind differencing scheme as a function of the number of nodes used in the numerical solution.....	90
Figure 4.1.1. Flowsheet of solution algorithm used to solve passive crevice corrosion problem.....	106
Figure 4.1.2. Finite volume grid used to obtain solution to crevice corrosion problem.....	107
Figure 4.1.3. Comparison of predicted and experimental pH profile in a type 304 stainless steel crevice of 90 μm gap, 2.5 cm width, and 8 cm depth (0.6 M NaCl aqueous solution at 25°C): a) 1 cm deep; b) 2 cm deep; c) 4 cm deep; d) 7.5 cm deep.....	110
Figure 4.1.4. Comparison of predicted spatial pH profile of present model with that of previous models. Type 304 stainless steel crevice of 90 μm gap, 2.5 cm width, and 8 cm depth (0.6 M NaCl aqueous solution at 25°C). Reference passive current density is 0.1 $\mu\text{A}/\text{cm}^2$	112
Figure 4.1.5. Comparison of predicted spatial pH profile of present model with that of previous models. Type 304 stainless steel crevice of 90 μm gap, 2.5 cm width, and 8 cm depth (0.6 M NaCl aqueous solution at 25°C). Reference passive current density is 1 $\mu\text{A}/\text{cm}^2$	113
Figure 4.1.6. Transient iR drop profile referenced to tip in a titanium crevice of 0.1 μm gap, 1 cm width, and 1 cm depth (0.5 M NaCl aqueous solution at 25°C).....	115
Figure 4.1.7. Transient conductivity profile in a titanium crevice of 0.1 μm gap, 1 cm width, and 1 cm depth (0.5 M NaCl aqueous solution at 25°C).....	116
Figure 4.1.8. Transient pH profile in a titanium crevice of 0.1 μm gap, 1 cm width, and 1 cm depth (0.5 M NaCl aqueous solution at 25°C).....	118
Figure 4.1.9. Transient passive current profile in a titanium crevice of 0.1 μm gap, 1 cm width, and 1 cm depth (0.5 M NaCl aqueous solution at 25°C).....	119
Figure 4.1.10. Transient iR drop profile referenced to tip in a titanium crevice of 1 μm gap, 1 cm width, and 1 cm depth (0.5 M NaCl aqueous solution at 25°C).....	120
Figure 4.1.11. Transient conductivity profile in a titanium crevice of 1 μm gap, 1 cm width, and 1 cm depth (0.5 M NaCl aqueous solution at 25°C).....	122
Figure 4.1.12. Transient pH profile in a titanium crevice of 1 μm gap, 1 cm width, and 1 cm depth (0.5 M NaCl aqueous solution at 25°C).....	123

Figure 4.1.13. Transient passive current profile at tip, center, and mouth of a titanium crevice of 1 μm gap, 1 cm width, and 1 cm depth (0.5 M NaCl aqueous solution at 25°C).....	124
Figure 4.1.14. Spatial iR drop and E_{corr} deviation profile in a titanium crevice of 0.1 μm gap, 1 cm width, and 1 cm depth (0.5 M NaCl aqueous solution at 25°C)	126
Figure 4.1.15. Spatial iR drop and E_{corr} deviation profile in a titanium crevice of 1 μm gap, 1 cm width, and 1 cm depth (0.5 M NaCl aqueous solution at 25°C)	127
Figure 4.1.16. Spatial iR drop and E_{corr} deviation profile in a titanium crevice of 10 μm gap, 1 cm width, and 1 cm depth (0.5 M NaCl aqueous solution at 25°C)	128
Figure 4.1.17. Spatial electroneutrality deviation profile in a titanium crevice of 0.1 μm gap, 1 cm width, and 1 cm depth (0.5 M NaCl aqueous solution at 25°C)	130
Figure 4.1.18. Spatial electroneutrality deviation profile in a titanium crevice of 1 μm gap, 1 cm width, and 1 cm depth (0.5 M NaCl aqueous solution at 25°C)	132
Figure 4.1.19. Spatial electroneutrality deviation profile in a titanium crevice of 10 μm gap, 1 cm width, and 1 cm depth (0.5 M NaCl aqueous solution at 25°C)	134
Figure 4.2.1. Comparison of Predicted Transient pH Profile to Experimentally Determined Profile in a Type 304 Stainless Steel Crevice (25°C, 0.6 Molar NaCl Bulk Solution, Dimensions 90 μm x 2.5 cm x 8.0 cm): a) 1 cm from mouth; b) 2 cm from mouth; c) 4 cm from mouth; d) 7.5 cm from mouth	157
Figure 4.2.2. Comparison of Predicted pH Profile Against Predictions of Previously Published Models and the Experimental Observations of Alavi and Cottis in a Type 304 Stainless Steel Crevice (25°C, 0.6 Molar NaCl Bulk Solution, Dimensions 90 μm x 2.5 cm x 8.0 cm).....	158
Figure 4.2.3. Predicted Transient Activity Coefficient Profile of Several Important Ions 7.5 cm From the Mouth of a Type 304 Stainless Steel Crevice (25°C, 0.6 Molar NaCl Bulk Solution, Dimensions 90 μm x 2.5 cm x 8.0 cm).....	159
Figure 4.2.4. Predicted Transient Ionic Strength and Transient Passive Corrosion Current Profiles 7.5 cm From the Mouth of a Type 304 Stainless Steel Crevice (25°C, 0.6 Molar NaCl Bulk Solution, Dimensions 90 μm x 2.5 cm x 8.0 cm)....	162
Figure 4.2.5. Predicted Activity of Several Important Ions in a Type 304 Stainless Steel Crevice (25°C, 0.6 Molar NaCl Bulk Solution, Dimensions 90 μm x 2.5 cm x 8.0 cm): a) 1 cm from Mouth; b) 2 cm from Mouth; c) 4 cm from Mouth; d) 7.5 cm from Mouth	163
Figure 4.2.6. Predicted Activity Coefficients of Several Important Ions in a Titanium Crevice (25°C, 0.5 Molar NaCl Bulk Solution, Dimensions 1 μm x 1.0 cm x 1.0 cm)	166
Figure 4.2.7. Predicted Transient pH Profile at the Tip, Center, and Mouth of a Titanium Crevice (25°C, 0.5 Molar NaCl Bulk Solution, Dimensions 1 μm x 1.0 cm x 1.0 cm)	167
Figure 4.2.8. Predicted Transient Chloride Ion Activity Profile at the Tip, Center, and Mouth of a Titanium Crevice (25°C, 0.5 Molar NaCl Bulk Solution, Dimensions 1 μm x 1.0 cm x 1.0 cm).....	168
Figure 4.3.1. Predicted transient iR drop along the crevice length, pH at the tip, and conductivity at the tip in a titanium crevice measuring 1 μm across the gap, 1 cm deep, and 1 cm wide and immersed in a 0.5 M NaCl solution at 70°C: (a) 0%	

hydrogen evolution; (b) 20% hydrogen evolution; (c) 40% hydrogen evolution; (d) 60% hydrogen evolution; (e) 80% hydrogen evolution.....	183
Figure 4.3.2. Variation of steady state solution properties with ψ : (a) pH at the crevice tip; (b) iR drop along the crevice length; (c) conductivity at the crevice tip.....	184
Figure 4.4.1. (a) Computational grid which is used to discretize the crevice solution; (b) Computational node which is labelled to illustrate the point (P), east (E), and west (W) indices.....	196
Figure 4.4.2. Transient pH profile in a Grade 2 titanium crevice measuring 90 μm across the gap, 2.5 cm wide, and 8 cm deep. Crevice is immersed in a Saskatchewan potash brine (3.39 M NaCl, 3.62 M KCl, 25°C, pH = 7).....	202
Figure 4.4.3. Relationship between the critical crevice pH (CCP) and the pitting resistance equivalent number (PREN).....	204
Figure 4.4.4. Transient pH profile in a type 308 SS crevice measuring 90 μm across the gap, 2.5 cm wide, and 8 cm deep. Crevice is immersed in a Saskatchewan potash brine (3.39 M NaCl, 3.62 M KCl, 25°C, pH = 7).....	206
Figure 4.4.5. Transient pH profile in a type 314 SS crevice measuring 90 μm across the gap, 2.5 cm wide, and 8 cm deep. Crevice is immersed in a Saskatchewan potash brine (3.39 M NaCl, 3.62 M KCl, 25°C, pH = 7).....	208
Figure 4.4.6. Transient pH profile in a type 304 SS crevice measuring 90 μm across the gap, 2.5 cm wide, and 8 cm deep. Crevice is immersed in a Saskatchewan potash brine (3.39 M NaCl, 3.62 M KCl, 25°C, pH = 7).....	210
Figure 4.4.7. Transient pH profile in a type 405 SS crevice measuring 90 μm across the gap, 2.5 cm wide, and 8 cm deep. Crevice is immersed in a Saskatchewan potash brine (3.39 M NaCl, 3.62 M KCl, 25°C, pH = 7).....	212
Figure 5.1. Corrosion rate in a mild steel pipe with carbonic acid solution flowing through it. ($T = 80\text{ }^\circ\text{C}$, $\text{pH} = 6.26$, $P_{\text{CO}_2} = 0.54\text{ bar}$, $[\text{Fe}^{2+}] = 250\text{ ppm}$, and $V_b = 1\text{ m/s}$).....	230
Figure 5.2. Effect of flowrate on steady state CO_2 corrosion rate of mild steel. ($T = 25\text{ }^\circ\text{C}$, $\text{pH} = 6.26$, $P_{\text{CO}_2} = 0.54\text{ bar}$, $[\text{Fe}^{2+}] = 250\text{ ppm}$).....	231
Figure 6.1. The coupled flow influenced and localized corrosion system. The size of the crevice on the duct wall is exaggerated for clarity.	239
Figure 6.2. Predicted velocity field in the flow influenced crevice system. Crevice is 50 μm deep and 10 μm across the gap. Flow is modelled within 20 μm of the pipe wall. The bulk Reynolds number is 5.4×10^5 . The velocity is in units of m/s. ...	244
Figure 6.3. Predicted velocity field in the flow influenced crevice system. Crevice is 50 μm deep and 20 μm across the gap. Flow is modelled within 20 μm of the pipe wall. The bulk Reynolds number is 5.4×10^5 . The velocity is in units of m/s. ...	245
Figure 6.4. Predicted velocity field in the flow influenced crevice system. Crevice is 50 μm deep and 50 μm across the gap. Flow is modelled within 20 μm of the pipe wall. The bulk Reynolds number is 5.4×10^5 . The velocity is in units of m/s. ...	246
Figure 6.5. Predicted velocity field in the flow influenced crevice system. Crevice is 50 μm deep and 100 μm across the gap. Flow is modelled within 20 μm of the pipe wall. The bulk Reynolds number is 5.4×10^5 . The velocity is in units of m/s. ...	247

Figure 6.6. Predicted velocity field in the flow influenced crevice system. Crevice is 50 μm deep and 200 μm across the gap. Flow is modelled within 20 μm of the pipe wall. The bulk Reynolds number is 5.4×10^5 . The velocity is in units of m/s. ...	248
Figure 6.7. Velocity magnitude along crevice centreline for varying gap sizes. The magnitude of the velocity is determined from the vector velocity data presented in Figures 6.2 – 6.6.	249
Figure 7.1. Comparison of Predicted pH Profile Against Predictions of Previously Published Models and the Experimental Observations of Alavi and Cottis in a Type 304 Stainless Steel Crevice (25°C, 0.6 Molar NaCl Bulk Solution, Dimensions 90 μm x 2.5 cm x 8.0 cm).....	258
Figure A.1. Plot of $g(x)$ and $g'(x)$, functions utilized in Pitzer's equations.	272
Figure B.1. Control volume stencil used in 2-D discretization. Dotted lines represent the control volume interfaces. Large black dots represent nodes where property values are calculated. Arrows represent flux through the control volume interface.	279
Figure B.2. Graphical representation of the electrode coupling algorithm: (a) Electrode which will become cathodic relative to the other; (b) Electrode which will become anodic relative to the other; (c) Coupling of the two electrodes to determine the excess current flowing between the two.	288

Chapter 1. Introduction

1.1 General Summary

Estimated to cost the United States economy nearly \$276 Billion (approximately 3.1% of their GNP), metallic corrosion is a serious concern. Of particular importance is localized corrosion, due to its ability to dramatically reduce service life of infrastructure and equipment. A key danger of localized corrosion is that a microscopic crevice or pit may corrode to the extent of catastrophic failure without being detected. To mitigate localized corrosion, a fundamental understanding of the processes that lead to material failure is required. In this work, new mathematical models of crevice corrosion have been developed to aid in the characterization of alloys for their use in corrosive environments.

In addition to studying localized corrosion, this project also includes research into flow influenced corrosion. While general corrosion is relatively well understood and engineers can incorporate corrosion allowances into designs, turbulent flow can dramatically increase the rate of general corrosion. One particularly important case of flow accelerated corrosion is CO₂ corrosion of pipeline and downhole oil well infrastructure. This form of corrosion is frequently encountered in the oil and gas industry and is also often associated with H₂S (acid gas) corrosion and microbially induced corrosion. Dissolved CO₂ in water forms carbonic acid which corrodes the steel.

This type of corrosion is very devastating near obstructions to flow where turbulence intensity is greatest (i.e. near flanges, threadings, etc.).

A third thrust of this research project is the development of a model of crevice corrosion that accounts for the effect of external flow. The effect of external flow on crevice corrosion may be beneficial or detrimental depending upon the aspect ratio of the crevice. For a deep crevice with a sufficiently small gap, bulk solution fluid will not significantly penetrate the crevice. However, turbulent flow will increase the rate of transport of cathodic reagents to the surface, giving the bold surface cathode increased throwing power, thus accelerating the rate of crevice corrosion. For a shallow crevice with a larger gap, bulk fluid will penetrate the crevice causing crevice washout. In this case, the replacement of the acid-chloride solution that develops in a crevice with the more neutral bulk solution will slow down the rate of crevice corrosion. However, this may cause mesa corrosion which is a natural extension of the present work. Flow influenced crevice corrosion is prevalent, and an example of this is when pitting occurs in processing equipment. During a shutdown, stagnant fluid may cause pitting. Upon restart of the process, turbulent flow now influences the crevices formed on the surface due to pitting. There are many other situations where this phenomenon would occur.

This thesis is arranged in the following order:

1. A description of mass transport modelling is given and two new methods for solving the electromigration-diffusion equation accurately and efficiently are shown. This is the first part of the thesis because mass transport modelling is fundamental to the prediction of all forms of corrosion.

2. The mass transport model is applied to crevice corrosion initiation of passive metals. The transport model is applied to predict crevice corrosion initiation at varying temperature, solution composition, and size of crevice gap. After thorough validation of the crevice corrosion initiation models, it is used to rank passive alloys for their propensity for crevice corrosion in potash brine.
3. The mass transport model is then applied to predict carbon dioxide corrosion in a pipeline. The Navier-Stokes equations, along with an eddy viscosity turbulence model, are used to calculate the turbulent velocity profile in a pipeline. The eddy viscosity is then incorporated into the mass transport equation to predict the effects of turbulent mixing on the rate of carbon dioxide corrosion. The CO₂ corrosion model incorporates the effect of FeCO₃ film formation.
4. The studies in both crevice corrosion and flow influenced corrosion are brought together with a study of flow influenced crevice corrosion. In this model, the passivation state of the crevice metal is not assumed. Thus, the model is applicable to either passive or non-passive metals. A turbulent flowfield is simulated. However, due to the scale of a crevice, only the viscous sublayer is modelled to keep the scale of the problem computationally feasible.

1.2 Significance of Contributions

This work breaks new ground in several areas. The crevice corrosion initiation model, discussed in Chapter 4, presents a new crevice corrosion model utilizing a sophisticated representation of non-ideal solution effects due to electrolyte interactions. The use of Pitzer's model has not been incorporated into a crevice corrosion initiation

model previously, and this study shows that its use dramatically improves the model's accuracy relative to experimental data (see Sections 4.2 and 4.3).

In addition, the carbon dioxide corrosion model is unique because it uses a novel method to determine the limiting current. Rather than relying upon correlations based upon experimental observations, this method to determine the current allows the model to be applicable to situations where the correlations do not apply. The limiting current is determined using the mass transport equation itself. When a cathodic reaction is controlled by charge transfer processes, a corrosion flux boundary condition is used. The rate of the cathodic reaction is determined using the Butler-Volmer equation. However, once a reagent involved in the cathodic reaction becomes limiting, the boundary condition for that reagent becomes a zero concentration boundary condition, and the cathodic current is calculated using the diffusion limited current. The use of this algorithm to dynamically change the species boundary condition allows the diffusion limiting current to be calculated without the use of correlations.

The flow influenced localized corrosion brought the localized corrosion and flow influenced corrosion models together. This model is capable of predicting crevice washout. The flow model is coupled with an electrolyte mass transport model and an electrode kinetics model. Electrode potential and current density is calculated using a novel electrode coupling algorithm. Based upon the net potential difference between cells (i.e. the difference in electrode potential less the ohmic potential drop between the electrodes), coupling between electrode sites is rigorously determined. This electrode coupling algorithm supplies the boundary conditions for mass transport and is capable of modelling both passive and active crevice corrosion.

Throughout the development of corrosion models, studies into theoretical mass transport were also conducted. From this work, a new method for incorporating charge density into the calculation of mass transport rates was developed. This method improves upon previously available charge density correction schemes because it is algebraic in nature, rather than other methods that require the solution of a stiff ordinary differential equation. Thus, this method dramatically increases the computational efficiency and stability of solving equations for electrolyte mass transport, while incorporating the important effect of charge density. In addition, a new differencing scheme customized for the electromigration-diffusion equation was developed. When using this scheme, rather than using a pure upwind differencing scheme, predicted mass transport rates are up to 87% closer to experimentally determined transport rates.

1.3 Research Objective

The objective of this research is to improve upon previous localized corrosion models through the development of more sophisticated mass transport models and algorithms. The applicability of the mass transport models to other problems will be shown through use in flow influenced CO₂ corrosion simulations. The goals of this research will be accomplished through the following tasks:

1. Development of a rigorous description of mass transport which improves upon previous models in both accuracy and computational efficiency. The model should incorporate charge density effects in a mechanistic fashion. Effects of diffusion on electromigration should be accounted for through diffusion potential.
2. Development and validation of a crevice corrosion initiation model for passive metals. A key difference between this model and previous models will be the

rigorous treatment of the charge density term. Even slight charge density invokes a large parabolic contortion of the electrical field, which then alters the current density field to neutralize the charge. It has been thought that because charge density is small, its net effect upon mass transport in a crevice is small. However, it will be shown that charge density is a key driving force for the mass transport process in a crevice.

3. Development of a flow influenced CO₂ corrosion model. The mass transport model described above will be applied to model CO₂ corrosion influenced by turbulent flow. The effect of iron carbonate film formation on the CO₂ corrosion process will be demonstrated.
4. Development of a comprehensive model of crevice corrosion under the influence of turbulent flow. A two-dimensional computational fluid dynamics model will be developed to simulate flow patterns in and around a crevice. The flowfield will be incorporated into the mass transport model. This model will be able to predict crevice washout for crevices with large gap to depth ratios and accelerated crevice corrosion due to increased mass transport at the external cathode for crevices with large gap to depth ratios.

Chapter 2. Introduction to Crevice Corrosion Modelling

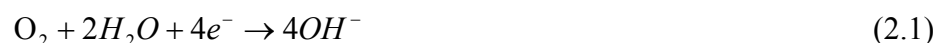
Crevice corrosion occurs in passive metals, which form a protective tenacious oxide film. This film is of the order of angstroms to nanometers thick and has a very low electronic and/or ionic conductivity. Therefore, the film acts as an electrical resistance, rather than a diffusion barrier. The low conductivity of this film acts to limit the corrosion current to a small leakage current, of the order of $0.1 - 10 \mu\text{A}/\text{cm}^2$. However, in sufficiently strong acid-chloride solutions, this film may be destroyed. The pH of this critical crevice solution is dependent upon the metal or alloy.

Strong acid-chloride solutions may develop inside a crevice undergoing crevice corrosion initiation. There are four stages of crevice corrosion – Crevice deoxygenation, crevice acidification, development of an critical crevice solution, and active crevice corrosion. The first three stages are considered the initiation period. Figure 2.1 illustrates the processes occurring during crevice corrosion initiation.

2.1 The Stages of Crevice Corrosion

2.1.1 Crevice deoxygenation

Initially, oxygen reduction both occurs inside and outside of the crevice. The crevice is filled with a solution that has identical composition to the bulk or external solution. Oxygen reduction occurs according to the following reaction:



This cathodic reaction is balanced by an anodic reaction. The anodic reaction is the dissolution of metal:



Metal cations in solution undergo hydrolysis to produce H^{+} :



Prior to deoxygenation, the passive current essentially maintains the structure of the passive film on both the crevice-interior surface and on the surface surrounding the crevice, which is called the bold surface. If the crevice gap is small enough such that the solution is stagnant, then oxygen can be transported into the crevice only by diffusion. If the rate of diffusion of oxygen is less than that of oxygen reduction in the crevice, the crevice will deoxygenate. This will have two important consequences:

- Anode and cathode will be physically separated. Anodic dissolution will occur inside the crevice and oxygen reduction will occur on the bold surface. This will cause a potential gradient between the crevice interior and the bold surface.

Hydrolysis of metal cations produced by metal dissolution will cause acidification of the crevice. This will cause the rate of dissolution to increase, which will then increase the potential gradient. Thus, the process is autocatalytic.

2.1.2 Crevice acidification

Before the crevice was deoxygenated, both oxygen reduction (which produces OH^{-} , see equation (2.1)) and metal dissolution (which produces H^{+} via hydrolysis, see equation (2.3)) occurred in the crevice. Now that the crevice is deoxygenated, OH^{-} is no longer produced at the same rate as H^{+} and, consequently, the pH drops.

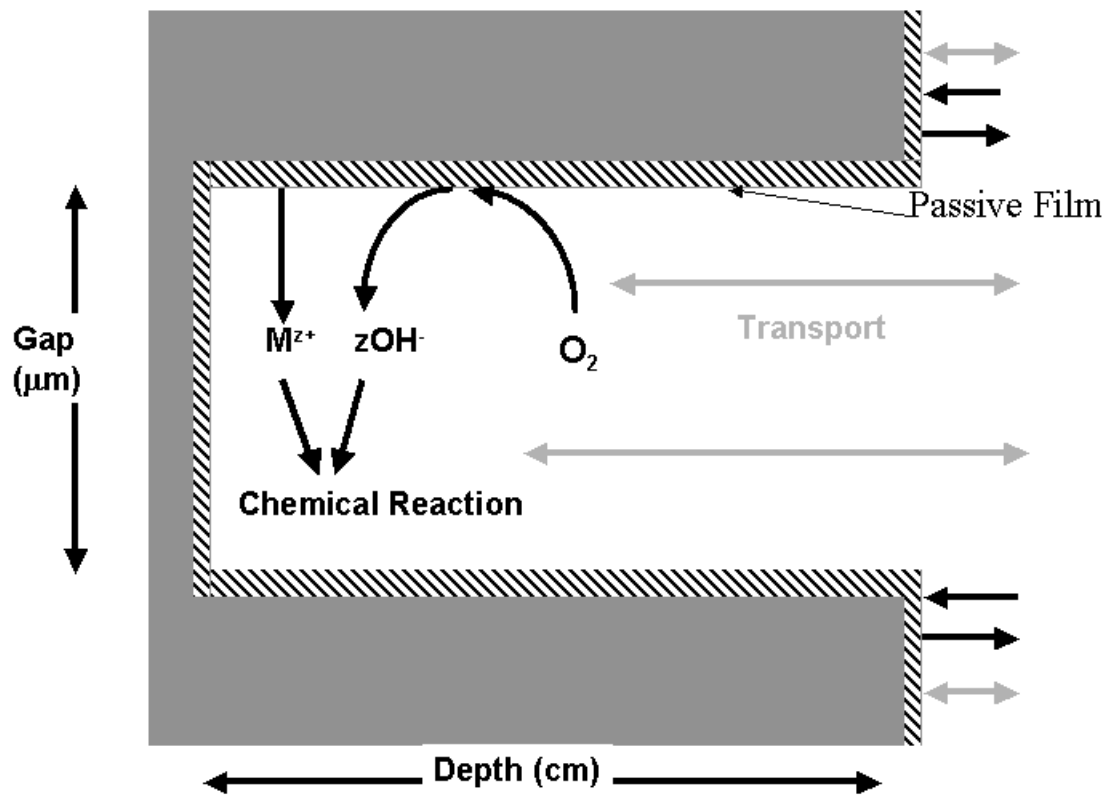


Figure 2.1. Processes occurring during crevice corrosion initiation. Grey double-sided arrows indicate transport mechanisms while dark arrows indicate electrochemical and chemical reactions.

The pH affects the rate of anodic dissolution. As the pH drops, the dissolution rate will increase according to the following relationship [1]:

$$\frac{\partial \log i_p}{\partial pH} = -n \quad (2.4)$$

Here, n increases with increasing charge number of the metal cation [1]. From equation (2.4), as the pH drops, the passive current increases. The rate of anodic dissolution is proportional to the passive current as described by Faraday's Law [1]. As the rate of anodic dissolution increases, so does the rate of hydrolysis, which causes the pH to drop more rapidly. The drop in pH, in turn, then causes the passive current to increase. Thus, an autocatalytic coupling is formed. Because of the autocatalytic nature of the crevice corrosion initiation process, the crevice solution can have a very low pH. In addition, because anodic reactions occur only inside the crevice while cathodic reactions occur only at the bold surface, there is an electrical potential difference between the inside and outside of the crevice. The bold surface supplies cathodic charge to the anodic processes inside the crevice. This potential gradient, which is proportional to the size of the passive current, causes electromigration of anions, such as chloride, into the crevice while cations electromigrate out of the crevice. The autocatalytic coupling between passive current and pH causes an increase in the potential gradient which increases the rate of chloride transport into the crevice. Therefore, crevice solutions can have much lower pH and much higher chloride concentrations than the bulk solution.

2.1.3 Development of a critical crevice solution

If the pH drops below the critical pH, the passive film will be destroyed and crevice corrosion will ensue. The critical pH is an experimentally determined parameter that is metal specific. There are critical pH values available in the literature for

commonly used passive metals [2, and references therein]. Two methods used to calculate the critical pH are described in the literature [3, 4].

Figure 2.2 shows the kinetic corrosion diagram of a metal crevice in the passive state and in the active state. In the passive state, the cathodic line intersects only the vertical part of the anodic line. When the crevice becomes active, the cathodic line intersects the “nose” of the anodic line, causing a large increase in the current. This intersection is usually due to the movement of the anodic line to the right because of increased temperature and decreased pH.

2.1.4 Active crevice corrosion

Crevice corrosion now occurs inside the crevice. The rate of dissolution is balanced by the rate of oxygen reduction at the cathode. Electromigration causes anions, such as chloride ions, to move into the crevice while cations move out of the crevice. Because the anode and cathode are physically separated, there is a potential gradient along the crevice length which is opposed by the iR drop in solution. The iR drop is inversely proportional to the solution conductivity. The conductivity of the crevice solution is significantly higher than the conductivity of the bulk solution due to metal ion hydrolysis, which produces hydrogen ions, and transport of chloride ions into the crevice.

2.2 Numerical Modelling of Crevice Corrosion

The rate of crevice acidification is largely controlled by the rate of metal dissolution. The rate at which the pH inside the crevice builds is influenced by the rate of mass transport of hydrogen ions out of the crevice. In addition, the chloride ion concentration in the crevice is a direct function of the rate of mass transport.

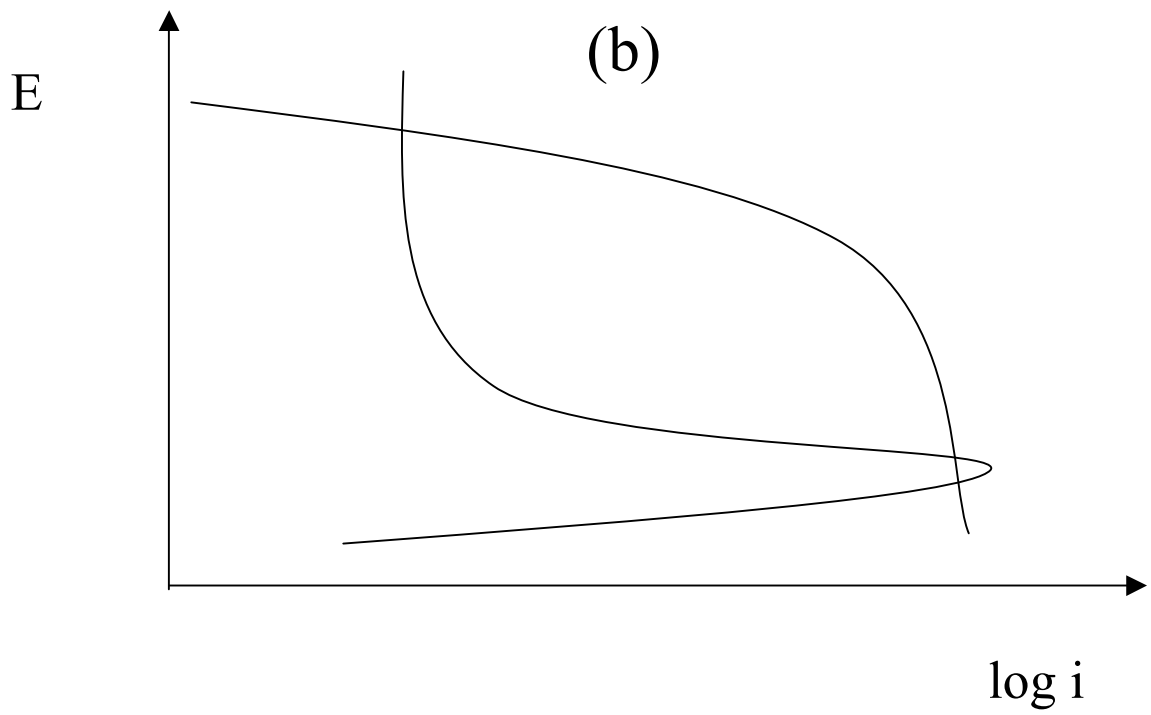
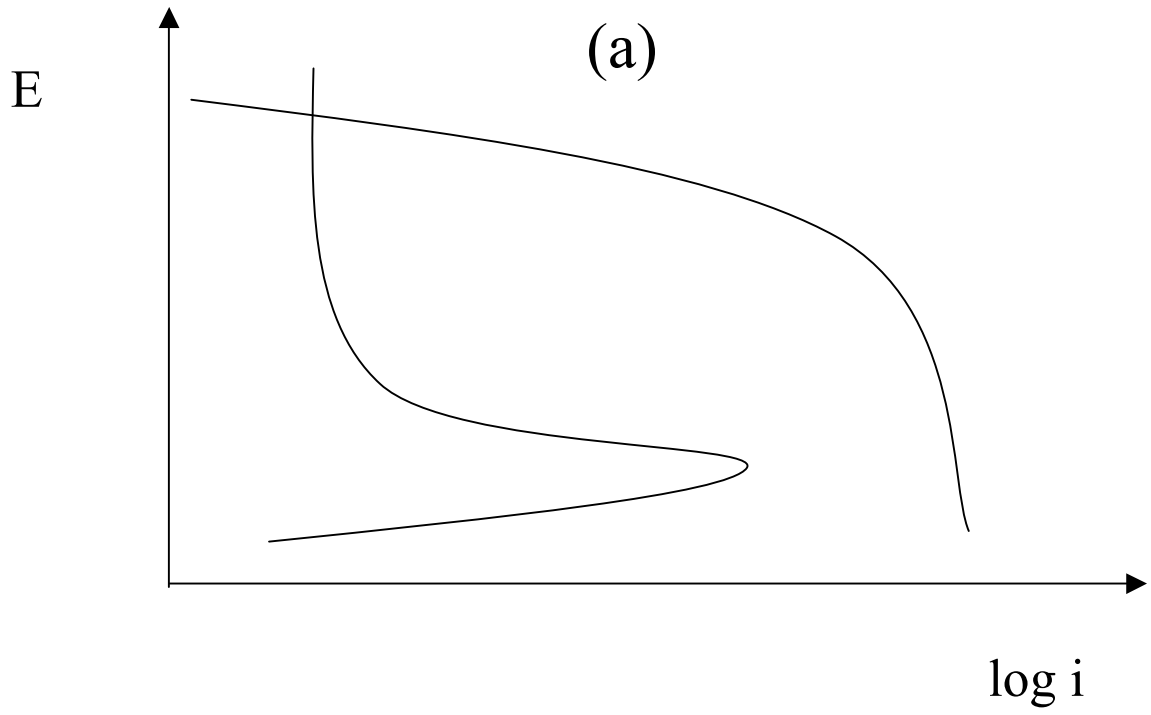


Figure 2.2. Typical kinetic corrosion diagram of crevice corrosion: (a) crevice in passivated state; (b) crevice in active state.

Thus, modeling electrolyte mass transport is a key part of modeling crevice corrosion. A crevice corrosion model is comprised of the following models:

- An electrolyte mass transport model.
- An electrode kinetics model
- A chemical equilibrium model

When the solution in the crevice is stagnant throughout, transport occurs via electromigration of charge species and diffusion of charged and neutral species. The electrode kinetics model calculates the boundary conditions necessary for the mass transport model. The crevice solution chemistry predicted by the mass transport model is also affected by chemical equilibrium. A chemical equilibrium model is a set of non-linear algebraic equations which is solved via a non-linear equation solver, e.g., the Newton-Raphson solver.

Mass transport in electrochemical systems is described by an incredibly stiff partial differential equation. Compared to electromigration and diffusion, the effect of charge density on mass transport is nearly instantaneous. The result of this physical phenomenon is that electromigration and diffusion transport occurs on time scales that are many orders of magnitude larger than time scales associated with charge density mass transport. To deal with this difficulty, the mass transport model is further subdivided into two models which are solved sequentially:

- Electromigration and diffusion terms
- Charge density correction

The development and implementation of the charge density correction, as well as charge density models of previous authors, is described in Chapter 3.

2.2.1 Modelling of electromigration and diffusion mass transport

Electromigration and diffusion occur at similar time scales, and thus, they can be solved simultaneously in a finite volume numerical integration scheme. Discrete transport coefficients for the mass transport equation are:

$$a_E = \frac{D_i}{\Delta x} \left[1 + \frac{P'_P}{2} + \left| \frac{P'_P \alpha}{2} \right| \right] \quad (2.5)$$

$$a_W = \frac{D_i}{\Delta x} \left[1 - \frac{P'_P}{2} + \left| \frac{P'_P \alpha}{2} \right| \right] \quad (2.6)$$

$$a_P^0 = \frac{\Delta x}{\Delta t} \quad (2.7)$$

$$a_P = a_E + a_W + a_P^0 + z_i u_i F \frac{\delta_P}{\mathcal{E}} \Delta x - D_i \frac{\ln \gamma_{iE} + \ln \gamma_{iW} - 2 \ln \gamma_{iP}}{\Delta x} \quad (2.8)$$

where a_E , a_W , a_P^0 , and a_P are the transport coefficients of the east, west, old, and point node respectively, as illustrated in Figure 2.3(b). These coefficients appear in the discrete transport equation:

$$a_P C_{iP} = a_E C_{iE} + a_W C_{iW} + a_P^0 C_{iP}^0 \quad (2.9)$$

Equation (2.9) is written for each computational node in the system. The resulting equation set is solved iteratively as it is nonlinear. Figure 2.3(a) shows a diagram of the computational grid over which these discrete equations are solved. All variables used in the above equations are defined in the nomenclature and will not be described in detail here. However, it is important to note that α , the upwind parameter, is a function of the Peclet number, P' . The model for the upwind parameter is described in Chapter 3. Furthermore, the activity coefficient, γ_i , is calculated using Pitzer's equations. The

implementation of Pitzer's equations in the crevice corrosion model is described in Chapter 4.

2.2.2 Modelling of charge density effects on mass transport

Charge density effects are modeling using the solution of Poisson's equation for charge density. This is solved separately from electromigration and diffusion because it operates on a much smaller time scale than electromigration and diffusion. The Poisson term appearing in the mass transport equation is:

$$\frac{dC_i}{dt} = -z_i u_i F C_i \frac{\delta}{\varepsilon} \quad (2.10)$$

This equation is solved using an Euler numerical integration scheme with an optimized time step that enables the solution to be found in a single time step. The derivation of this method is discussed in detail in Chapter 3.

2.2.3 Modelling of electrode kinetics

Boundary conditions for the mass transport model are the rate of consumption or generation of chemical species due to electrode reactions at a reactive wall. The rate of reaction is proportional to the passive current:

$$-D_i \frac{dC_i}{dx} = \frac{i_p}{z_i F} \quad (2.11)$$

Equation (2.11) is a mass balance at a reactive wall. The rate of metal dissolution is equal to the rate of diffusion of metal ions away from the wall.

2.2.4 Modelling of chemical equilibrium

Chemical equilibrium is described mathematically by the following equation:

$$\prod_j C_j^{\nu_j} = K \quad (2.12)$$

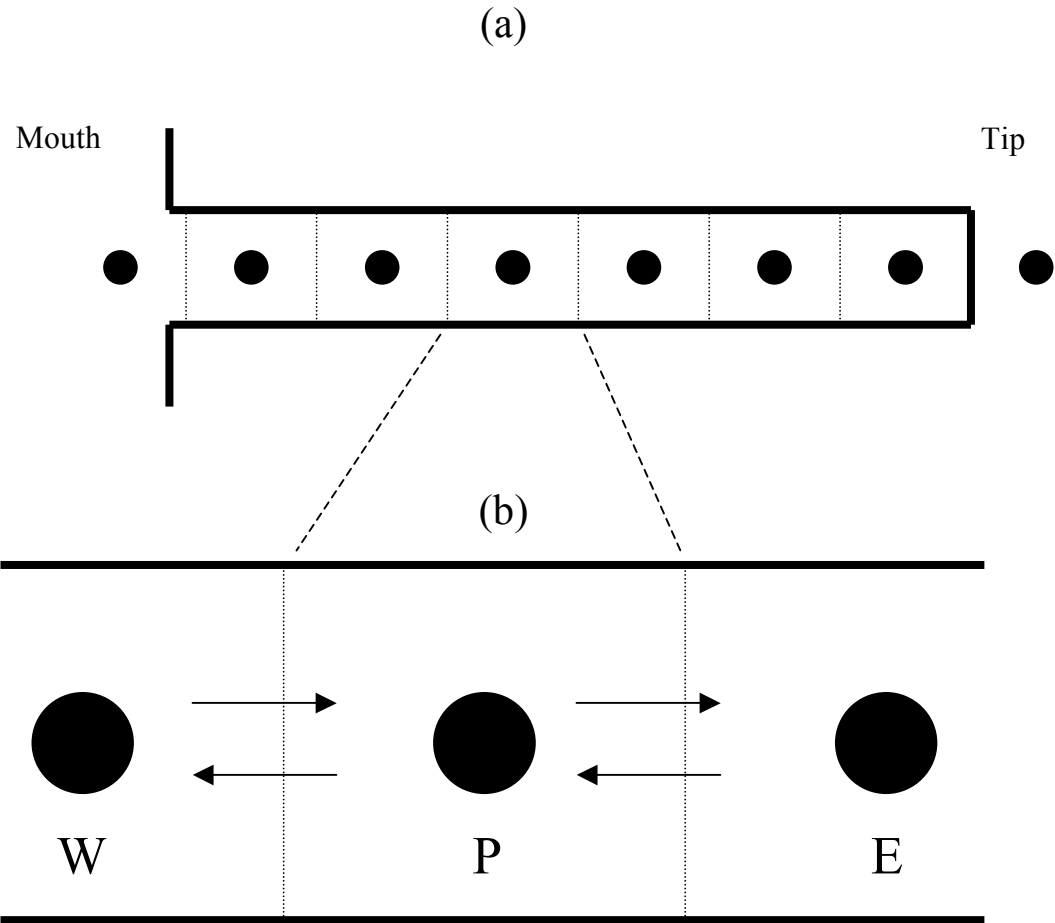


Figure 2.3. (a) Computational grid which is used to discretize the crevice solution; (b) Computational node which is labelled to illustrate the point (P), east (E), and west (W) indices. Boundaries are spaced halfway between nodes and represent control volume interfaces.

Here, K is an equilibrium constant and ν_j is the stoichiometric coefficient. This equation is written for each reaction occurring in solution and the resulting set of equations is solved using the Newton-Raphson method.

2.2.5 Solution methodology

Modelling crevice corrosion requires calculating mass transfer rates due to electromigration and diffusion. An electrode kinetics model that calculates the passive current supplies the boundary conditions for the mass transport model. The predictions of the mass transport model are then adjusted so that the solution is electrically neutral and chemical equilibrium constraints are met. The flowsheet of the crevice corrosion initiation model is shown in Figure 2.4.

The model requires the following types of data:

- Mass diffusivities of each species in solution.
- Chemical equilibrium data for each reaction occurring. For each reaction, the required data consists of the stoichiometric coefficient of each species involved in the chemical reaction and its equilibrium constant. If the crevice solution temperature is different from the temperature at which the equilibrium constant is reported, the heat of reaction is also required.
- A reference passive current and the conditions at which it is measured (i.e. temperature and pH). The activation energy is also required to adjust the passive current for temperature. This parameter is experimentally determined and depends upon the electronic/ionic conductivity and structure of the passive film.
- Pitzer interaction parameters for calculation of activity coefficients via Pitzer's equations [5].

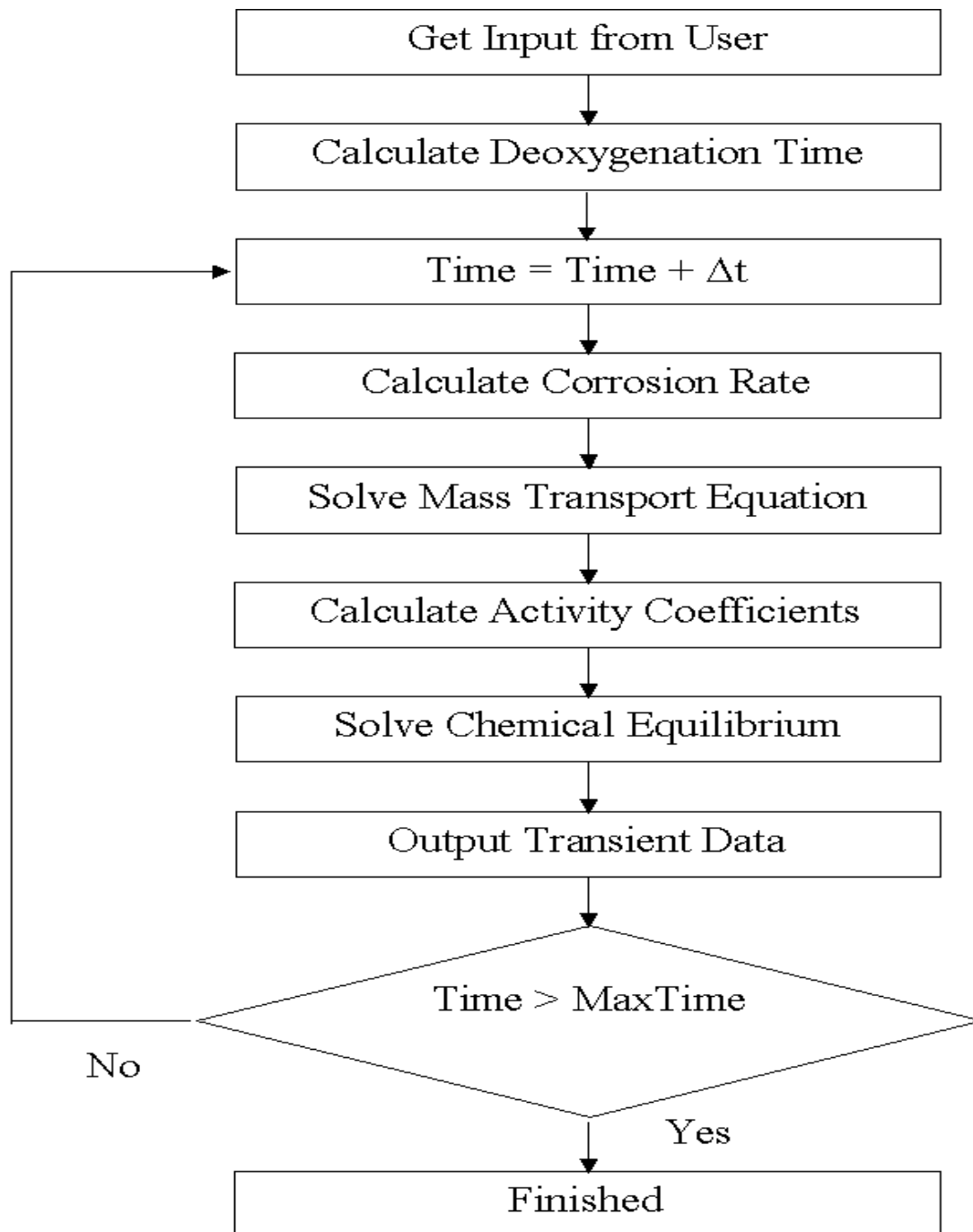


Figure 2.4. Flowsheet of solution algorithm used to solve passive crevice corrosion problem

- Geometric properties (crevice depth and gap)
- Bulk solution composition and temperature
- The composition of the alloy from which the crevice is formed
- The space and time step size, Δx and Δt .

The computer program gathers the required data through reading text files and through user input. Then, the time required to deoxygenate the crevice is calculated. This is done using a simple mass balance. Once the deoxygenation time is calculated, the mass transport calculations proceed. Starting with an initial passive current that is calculated from the reference passive current, the current density in solution is calculated. The mass transport equation is then solved using the calculated current density as input and determining the concentration field of each species in solution as output. The concentration field is then adjusted by solving Poisson's equation until the solution is electrically neutral. With knowledge of the concentration field, activity coefficients are calculated using Pitzer's equations. The activity coefficients are used in the chemical equilibrium model and in the next iteration when the mass transport equation is solved once again. This process is repeated for a set number of time steps until the maximum time is reached.

2.3 References

1. L. L. Shrier, R. A. Jarman, G. T. Burstein, Corrosion, 3rd Ed. (Oxford, UK: Butterworth-Heinemann Ltd, 1994). p. 2:20.
2. M.K. Watson, “Numerical Simulation of Crevice Corrosion”, Ph.D. Dissertation, University of Saskatchewan, Saskatoon SK (1989).
3. Crolet, J.L., J. M. Defranoux, L. Seraphin, and R. Tricot, Memoires Scientifique Revue Metallurgique **71**, 797 – 805 (1974).
4. Oldfield, J. W., and W. H. Sutton, British Corrosion Journal **13**, 13-22 (1978).
5. K. S. Pitzer, Activity Coefficients in Electrolyte Solutions, 2nd Ed. (Boca Raton, FL: CRC Press, 1991). pp. 88 – 90.

Chapter 3. Mass Transport Modelling

3.1 Introduction

Mass transport in electrochemical systems is widely applicable to many industrial problems. It is used in the fundamental modelling of macroscopic and microscopic corrosion processes, fuel cells, ion exchange technology, and industrial electrochemical processes. In an electrochemical system, mass transport is driven by gradients of electrochemical potential and fluid velocity. This chapter is focused upon mass transport in stagnant electrochemical systems. Two computational methods are herein described that were derived to more accurately and efficiently solve the electromigration-diffusion equation.

3.2 The Charge Density Correction Scheme*

In the development of rigorous models for electrochemical systems, such as localized corrosion cells, an accurate description of mass transport is of paramount importance. In a stagnant system, the effect of charge density upon mass transport may be significant [1, 2]. Because localized corrosion often occurs in stagnant zones, modelling mass transport in stagnant electrochemical systems is very important for predicting localized corrosion damage.

* Reference: K.L. Heppner and R.W. Evitts (2005), A New Method for Calculating Charge Density in Electrochemical Systems, Corrosion Engineering, Science, and Technology, In Press.

It has been shown previously that charge density significantly influences mass transport processes in a localized corrosion cell [1, 2]. Charge density provides a very strong coupling effect between mass transport of different ions. Thus, accurately modelling the effect of charge density on mass transport is one of the keys to characterizing the whole mass transport process.

However, charge density appears in a very stiff term of the electromigration-diffusion equation. While a significant body of research in electrolyte mass transport modelling has come from crevice corrosion studies, few works incorporated the charge density term of the mass transport equation. Previous authors working in crevice corrosion modelling have developed strategies for calculating the effect of charge density on mass transport. One approach was to “absorb” the solution charge onto a reference ion thereby forcing electroneutrality [3 – 9]. However, this method allowed for multiple solutions to the mass transport equation (i.e., a different solution resulted from each reference ion selection). Later, Evitts [10] and Watson [11] both independently proposed an operator splitting method whereby the charge density term was solved separately from the remainder of the mass transport equation. Heppner et al. subsequently used this method for their crevice corrosion models [1, 2, 12, 13]. In the current work, a new technique is presented that improves upon the accuracy of the operator splitting technique. In addition, use of this new model increases the computational efficiency by 4 – 6 times over the operator splitting method.

In this new charge density correction algorithm, the electromigration and diffusion terms of the mass transport equation are solved while neglecting the charge density term. Then, the charge density effect is simulated using a simple algebraic correction to the

concentration field. The correction is designed such that the charge density is immediately neutralized. The derivation and application of this algebraic correction is the focus of this paper.

3.2.1 Model development

3.2.1.1 Mass transport

The mass flux through an electrolytic medium under the influence of an electrical field is [3]:

$$\mathbf{N}_i = -z_i u_i F C_i \nabla \Phi - D_i \nabla C_i \quad (3.2.1)$$

The use of equation (3.2.1) implies that infinitely dilute solution theory is assumed to adequately model the solution chemistry of the system. A mass conservation statement may be written:

$$\frac{\partial C_i}{\partial t} = -\nabla \cdot \mathbf{N}_i \quad (3.2.2)$$

Substitution of (3.2.1) into (3.2.2) yields:

$$\frac{\partial C_i}{\partial t} = z_i u_i F \nabla C_i \nabla \Phi + z_i u_i F C_i \nabla^2 \Phi + D_i \nabla^2 C_i \quad (3.2.3)$$

Poisson's equation for charge density relates the second order gradient of the electrical field to the charge density:

$$\nabla^2 \Phi = -\frac{\delta}{\varepsilon} \quad (3.2.4)$$

where ε is the dielectric constant of the electrolyte solution and δ is the charge density which is calculated via the following equation:

$$\delta = F \sum_j z_j C_j \quad (3.2.5)$$

Furthermore, the potential gradient may be expressed as a function of regular and diffusion-potential current density via Ohm's Law for a non-uniform concentration field:

$$\nabla\Phi = -\frac{\mathbf{i} + \mathbf{i}_{\text{dp}}}{\kappa} \quad (3.2.6)$$

where \mathbf{i}_{dp} is the diffusion-potential current density:

$$\mathbf{i}_{\text{dp}} = F \sum_j z_j D_j \nabla C_j \quad (3.2.7)$$

and κ is the conductivity of the solution:

$$\kappa = F^2 \sum_j z_j^2 u_j C_j \quad (3.2.8)$$

The diffusion-potential current density represents an additional current that opposes the current induced by multicomponent diffusion. As an ion diffuses through an electrolytic solution, it drags along with it ions of opposite charge to maintain electroneutrality. The diffusion-potential current density is representative of this effect. It can be easily shown that the diffusion-potential current density is equal and opposite to the current induced by multicomponent diffusion, i.e.:

$$\mathbf{i}_{\text{diffusion}} = F \sum_j z_j N_j = -F \sum_j z_j D_j \nabla C_j = -\mathbf{i}_{\text{dp}} \quad (3.2.9)$$

Substitution of (3.2.4) and (3.2.6) into (3.2.3) gives the final form of the mass transport equation:

$$\frac{\partial C_i}{\partial t} = -z_i u_i F \nabla C_i \frac{\mathbf{i} + \mathbf{i}_{\text{dp}}}{\kappa} - z_i u_i F C_i \frac{\delta}{\varepsilon} + D_i \nabla^2 C_i \quad (3.2.10)$$

Obtaining a numerical solution to equation (3.2.10) is very costly from a computational standpoint. The second term on the right hand side of equation (3.2.10) is the charge density term. This term is incredibly stiff, and thus, extremely small time steps (of the

order of 10^{-12} seconds) are required to solve it directly when implementing a finite volume solution. Physically, this means that the time constant associated with charge density is much smaller than those of electromigration or diffusion. This feature of electrolyte mass transport makes obtaining a solution for equation (3.2.10), from a practical standpoint, impossible. The algebraic charge density correction method is a remedy for this problem.

3.2.1.2 Charge density correction

This scheme is based upon a segregated solution strategy. The electromigration and diffusion terms of the mass transport equation are solved separately from the charge density term. To clearly explain this scheme, terms in equation (3.2.10) due to electromigration, diffusion, and charge density are written as follows:

$$\frac{\partial C_i}{\partial t} = \left(\frac{\partial C_i}{\partial t} \right)_{\text{electromigration}} + \left(\frac{\partial C_i}{\partial t} \right)_{\text{diffusion}} + \left(\frac{\partial C_i}{\partial t} \right)_{\text{poisson}} \quad (3.2.11)$$

At very small time scales, the combined effect of electromigration and diffusion is small compared to charge density. At larger time scales, the effect of charge density is small compared to electromigration and diffusion and, thus, equation (3.2.10) can be solved without the charge density term for large finite volume time steps. Thus, equation (3.2.10) can be solved as two equations. Each equation is solved sequentially rather than simultaneously such that the Poisson term provides a charge density correction to the solution of the electromigration and diffusion terms. The two equations are:

$$\frac{\partial C_i}{\partial t} = \left(\frac{\partial C_i}{\partial t} \right)_{\text{electromigration}} + \left(\frac{\partial C_i}{\partial t} \right)_{\text{diffusion}} = -z_i u_i F \nabla C_i \frac{\mathbf{i} + \mathbf{i}_{dp}}{\kappa} + D_i \nabla^2 C_i \quad (3.2.12a)$$

$$\frac{dC_i}{dt} = \left(\frac{\partial C_i}{\partial t} \right)_{\text{poisson}} = -z_i u_i F C_i \frac{\delta}{\varepsilon} \quad (3.2.12b)$$

The operator splitting method of Evitts [10] and Watson [11] used a finite volume solution of equation (3.2.12a) to determine the charge density correction required to neutralize the charge of the electrolyte solution. The algebraic correction to be developed is based upon the form of equation (3.2.12b), the charge density ODE used in the operator splitting algorithm described above. This new charge density correction method has the distinct advantage that the numerical solution of equation (3.2.12b) is not required. Thus, the new method avoids the solution of a series of coupled, non-linear, stiff ordinary differential equations. Its use improves on the performance and accuracy of a mass transport model compared to the use of the operator splitting scheme and its derivation follows.

Discretization of equation (3.2.12b) using Euler's method yields the following equation:

$$C_i = C_i^{old} - z_i u_i F C_i \frac{\delta}{\varepsilon} \Delta t \quad (3.2.13)$$

Thus, the change in concentration over a time step is:

$$\Delta C_i = -z_i u_i C_i \frac{F \delta}{\varepsilon} \Delta t \quad (3.2.14)$$

In equation (3.2.14), the quotient, F/ε , has a magnitude of the order of 10^{16} V m / mol. Thus, the concentration change predicted using (3.2.14) would be extremely large over even a very small time step. It would therefore be advantageous to determine a value of ΔC_i for each species in solution that would force electroneutrality on the system. If the value of charge density does not change significantly as any particular ionic concentration changes (i.e. ΔC_i is very small), charge density can be assumed constant in equation (3.2.14). This assumption reduces equation (3.2.12b) to a linear ODE. Furthermore, with

this assumption in place, it can be seen from equation (3.2.14) that the change in concentration is proportional to the product of the charge number, mobility, and concentration of the species of interest. All variables in equation (3.2.14) that are not species specific (F , δ , ε , and Δt) can be combined into one proportionality constant. Equation (3.2.14) can then be written as:

$$\Delta C_i = \psi z_i u_i C_i \quad (3.2.15)$$

By this formulation, ψ is a function of Δt , which is yet unknown. Thus, ψ itself is also an unknown quantity. Thus, a value of ψ can be selected such that the change in concentration neutralizes the charge density. To determine this value, equation (3.2.15) is substituted into the definition of electroneutrality:

$$F \sum_j z_j (C_j + \Delta C_j) = F \sum_j z_j (C_j + \psi z_j u_j C_j) = 0 \quad (3.2.16)$$

Isolation of the proportionality constant ψ in equation (3.2.16) followed by appropriate substitutions yields the value of ψ which satisfies the electroneutrality condition:

$$\psi = -\frac{F\delta}{\kappa} \quad (3.2.17)$$

Substitution of (3.2.17) into (3.2.15) yields the final form of the charge density correction:

$$C_i = C_i^{old} - z_i u_i C_i \frac{F\delta}{\kappa} \quad (3.2.18)$$

Equation (3.2.18) may be used to modify the last obtained solution of equation (3.2.10), thereby producing a concentration field that is free of net electrical charge.

Examination of equation (3.2.17), the proportionality constant formula, will confirm the physical significance of this correction method. For a dilute solution (κ is small), charge density has a large effect on the concentration of ionic species in solution.

However, for a more concentrated solution (κ is large), the effect of charge density on the concentration of any individual species is relatively small. Thus, the effect of charge density upon species concentration profiles is damped in concentrated solutions (i.e. there are more ions available to dissipate the electrical charge). This is a physically realistic phenomenon which is emulated in this model.

By comparison of equation (3.2.18) with equation (3.2.12b), the time required to eradicate charge density can be determined:

$$\Delta t_{Poisson} = \frac{\varepsilon}{\kappa} \quad (3.2.19)$$

Equation (3.2.19) is the time step that, when applied to equation (3.2.12b), will neutralize the electrolyte solution in a single time step. This time step is extremely small. For example, in a 0.1 M KNO₃ solution, ε has a magnitude of the order of 10^{-12} C/(V m) while κ has a magnitude of the order of 10^{-4} C/(V m s). In this typical situation, the time required to annihilate the solution charge density is approximately $\Delta t_{Poisson} = 10^{-8}$ seconds. In a physical sense, this time is the quotient of the net solution charge to the rate at which the charge can be neutralized. This can be shown mathematically through a combination of Ohm's Law with Poisson's equation for charge density. Ohm's Law reads:

$$\nabla\Phi = -\frac{\mathbf{i}}{\kappa} \quad (3.2.20)$$

To simplify the mathematics, it will be assumed that concentration, and thus conductivity, is constant. Taking the gradient of equation (3.2.20) yields:

$$\nabla^2\Phi = -\frac{1}{\kappa} \nabla \cdot \mathbf{i} \quad (3.2.21)$$

Substitution of Poisson's equation for charge density (equation (3.2.4)) into equation (3.2.21) yields:

$$\frac{\delta}{\varepsilon} = \frac{1}{\kappa} \nabla \cdot \mathbf{i} \quad (3.2.22)$$

Rearrangement yields the following expression for ε/κ :

$$\frac{\varepsilon}{\kappa} = \frac{\delta}{\nabla \cdot \mathbf{i}} \quad (3.2.23)$$

For a uniform concentration field, the charge continuity equation reads:

$$\frac{\partial \delta}{\partial t} = -\nabla \cdot \mathbf{i} \quad (3.2.24)$$

Substitution of equation (3.2.24) into (3.2.23) yields the following relationship:

$$\frac{\varepsilon}{\kappa} = \Delta t_{Poisson} = -\frac{\delta}{\frac{\partial \delta}{\partial t}} \quad (3.2.25)$$

Thus, the quantity ε/κ is the ratio of the total charge density in solution to its rate of change. The quotient ε/κ will always be a positive quantity because the sign of δ and its rate of change will always be opposite. This is because when a net charge density exists, the electrical field will spontaneously contort to reduce the Gibb's Free Energy and, thus reduce the net charge density of the system [2].

3.2.2 Model validation

To show the utility of the charge density correction method, the moving boundary experiment of Fu and Chan [14] was simulated. The moving boundary experiment was chosen because of its simplicity and because of the availability of experimental results. Fu and Chan's experimental apparatus consisted of a long glass tube that opened to a large glass beaker. The end of the glass tube was plugged with a silver anode while a

silver cathode was immersed in the beaker. The entire apparatus was filled with a 0.1 M KNO_3 solution at 25°C . A DC power source was connected in series between the anode and cathode with silver wires. When the power source was switched on, a current density of approximately 318 A/m^2 was conducted through the KNO_3 electrolyte solution in the glass tube. The applied current caused silver dissolution at the anode. Figure 3.2.1 shows a diagram of the Fu and Chan apparatus.

Throughout the experiment, Ag^+ ions entered the solution from the anode. The applied current in solution drove the Ag^+ and K^+ cations away from the anode while inducing the movement of NO_3^- anions towards the anode. The point of intersection of the Ag^+ and K^+ profiles was made visible by introducing a small amount of ascorbic acid into the solution. This visible intersection was referred to as the moving boundary and its rate of movement was indicative of mass flux. Thus, Fu and Chan tracked and recorded the moving boundary position as a function of time. An implicit finite volume method coupled with the algebraic charge density model was used to solve the system of equations. Figure 3.2.2 compares the position of the moving boundary predicted using the present model with the experimental observations of Fu and Chan. The similarity between the predicted and experimental moving boundary position shown in Figure 3.2.2 validates this model and the charge density correction method.

3.2.3 Numerical experiment

With the present model validated, its limits of applicability were then tested. It had been shown previously that the operator splitting method proposed by Evitts and Watson worked well for modelling the Fu and Chan experiment [14].

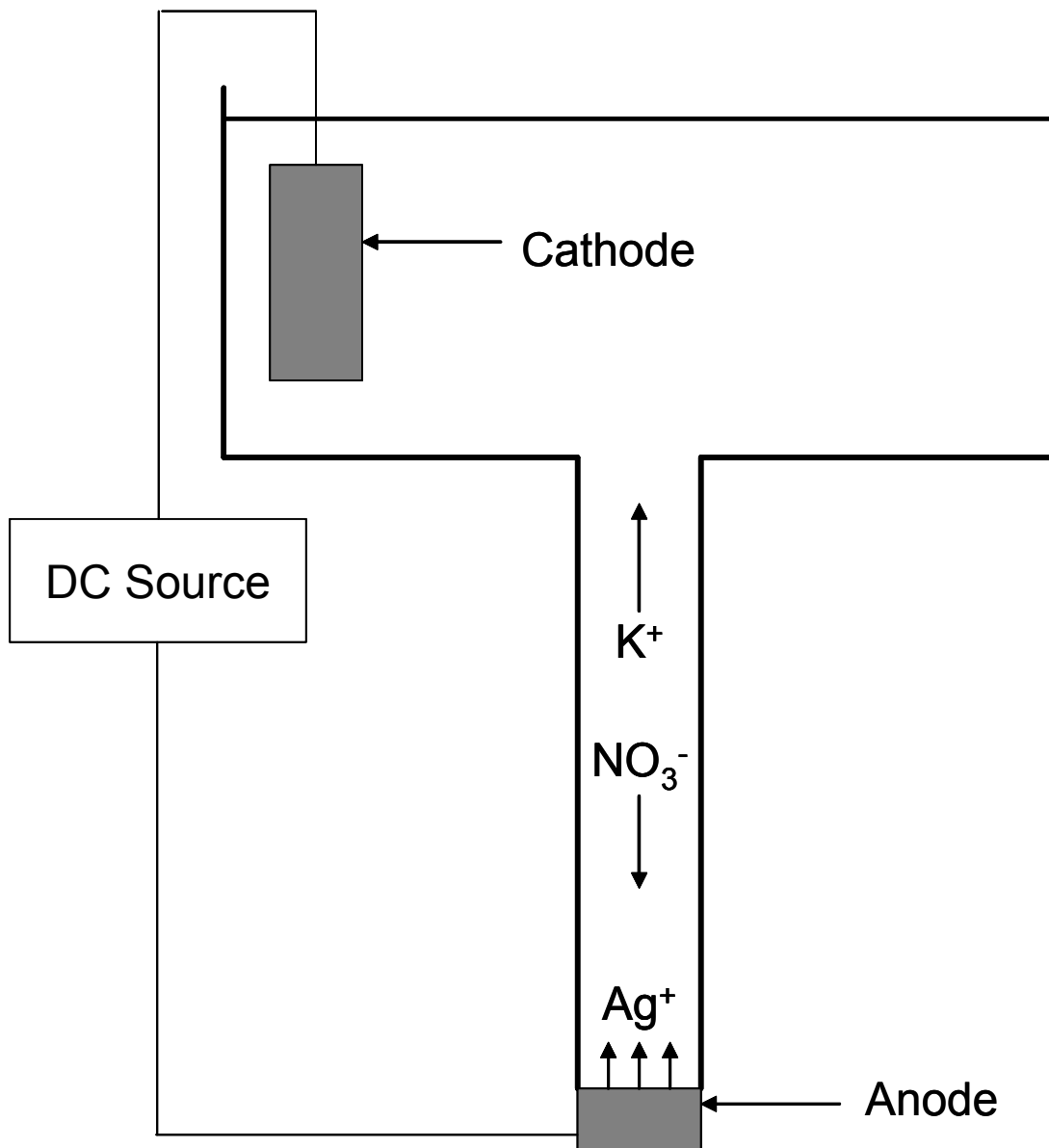


Figure 3.2.1. Diagram of the experimental apparatus used by Fu and Chan in the moving boundary experiment

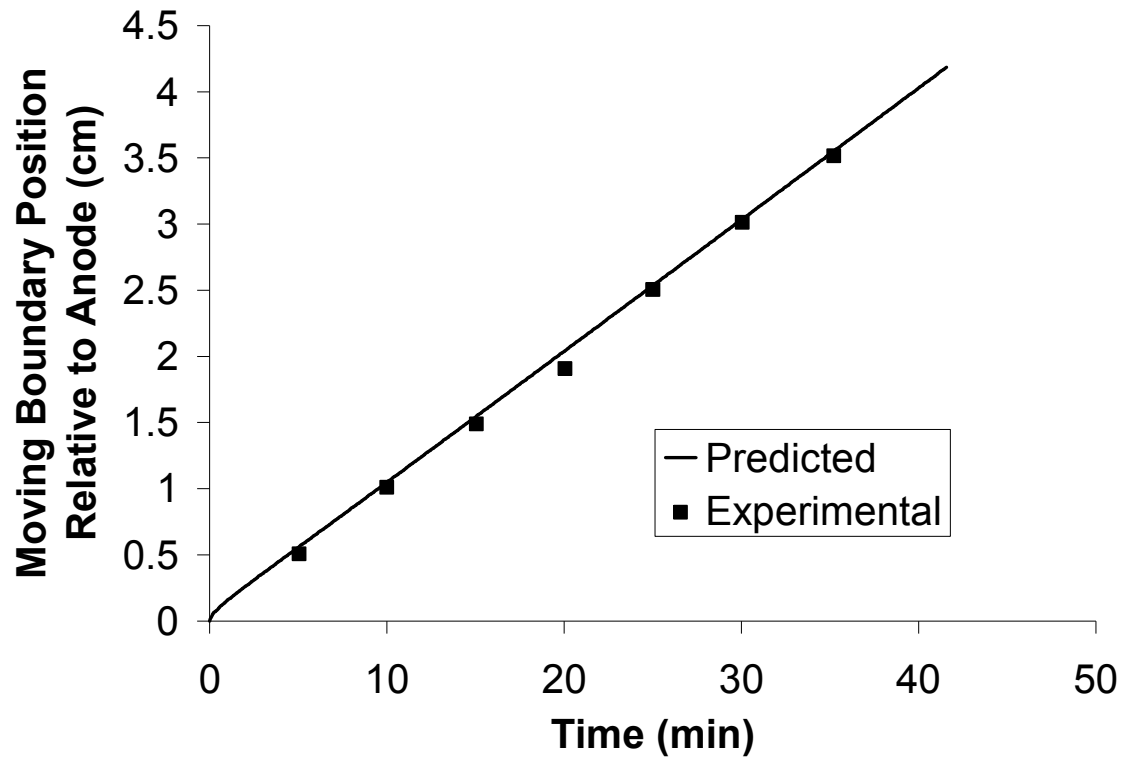


Figure 3.2.2. Comparison of the predicted transient position of the Ag^+/K^+ moving boundary with the experimental observations of Fu and Chan.

Thus, the utility of the algebraic charge density correction method was determined based upon its ability to match and/or outperform the operator splitting method for a variety of conditions. For each of the forthcoming simulations, the basic elements of the Fu and Chan system were retained. However, the performance of the new charge density model was tested as simulation conditions changed. Thus, the KNO_3 solution concentration, the magnitude of the applied current density, the space step, and the time step were each varied individually. It can be shown that using this new charge density model improves the accuracy of the simulation and significantly reduces computation time as compared to the operator splitting method.

In each of the simulations, only the Ag^+ and K^+ concentration profiles are reported. This has been done to more clearly illustrate the important features of the moving boundary region. However, the NO_3^- concentration profile can be determined by the sum of the Ag^+ and K^+ concentration profiles (due to charge conservation).

3.2.3.1 Effect of concentration

As ionic concentration increases, the effect of charge density is dampened. This is because there are more ions available to absorb a net charge. As a result, the change in concentration of any individual species due to charge density is reduced as concentration increases. Figures 3.2.3 and 3.2.4 display the predicted Ag^+/K^+ concentration profiles after 40 minutes of simulation time using both the operator splitting algorithm and the algebraic charge density correction. These results are displayed alongside the differences between the predicted profiles when using the two charge density calculation methods. The difference is presented as both a spatial profile after 40 minutes of simulation time and as a space-averaged transient profile.

Comparison of Figures 3.2.3 and 3.2.4 illustrate the effect of increasing concentration upon the performance of the charge density correction. As concentration increases, the conductivity of the solution also increases. When the current density is held constant (as is the case here) and the conductivity increases, the potential gradient along the glass tube drop will decrease. Because potential difference is the driving force for ionic electromigration, the rate of mass transport drops as concentration increases. This is evidenced by the reduction of the rate of movement of the Ag^+/K^+ boundary in Figure 3.2.4 (a) compared to Figure 3.2.3 (a).

Increased conductivity also reduces the effect of charge density upon mass transport. This is shown mathematically by the previously derived charge density correction formula (see equation (3.2.18)). The amount that the concentration of each ion in solution is corrected to restore electroneutrality is inversely proportional to conductivity. Thus, for a highly conductive solution, the amount of charge counteracted by any particular ion is reduced. In other words, the effect of charge density is dampened in more concentrated solutions. This effect can be seen by comparing Figures 3.2.3 and 3.2.4. As the concentration increases, there is greater similarity between profiles predicted using both the operator splitting method and the charge density correction method. The predictions of both methods converge as the effect of charge density decreases.

For the spatial and transient difference profiles shown in Figures 3.2.3 and 3.2.4, there is greater deviation between the K^+ concentration profiles predicted using both charge density calculation methods than the Ag^+ concentration profiles.

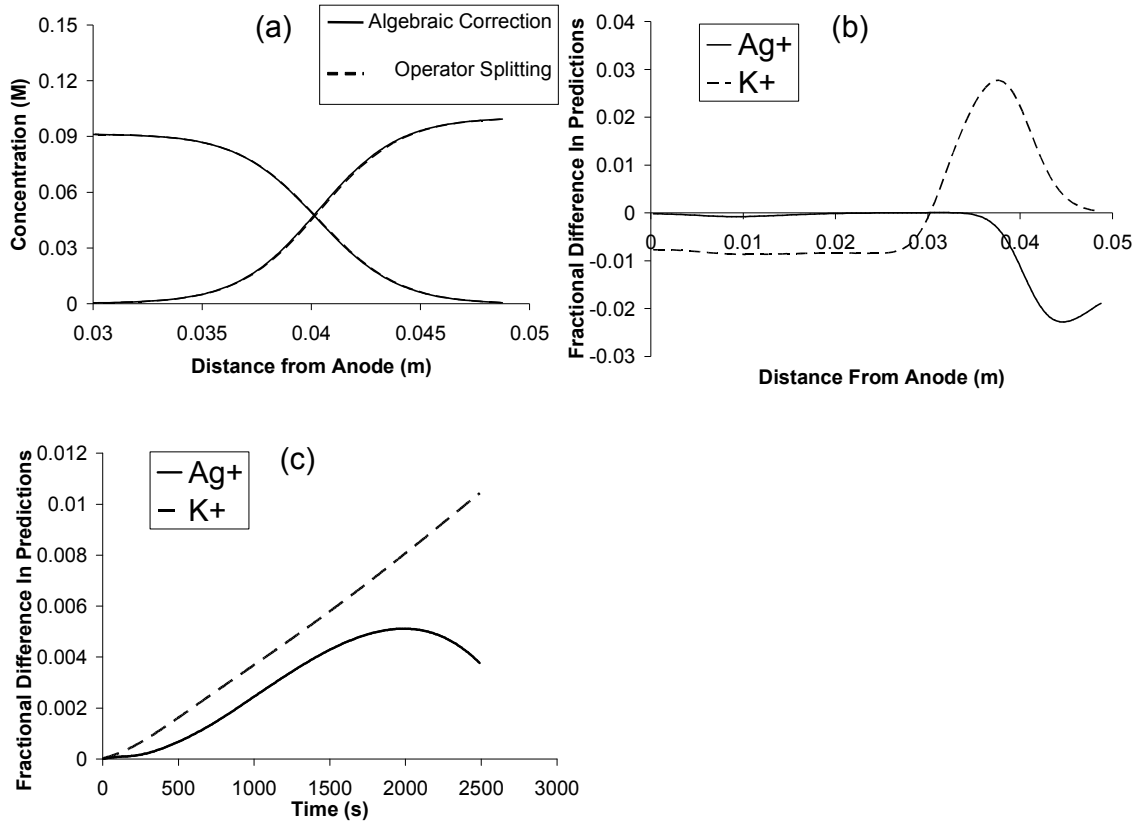


Figure 3.2.3. Comparison of the spatial and transient Ag^+ and K^+ concentration profiles predicted by the operator splitting scheme and the algebraic charge density correction for a 0.1 M KNO_3 solution ($318 \mu\text{A}/\text{cm}^2$ current density, $\Delta x = 0.05 \text{ cm}$, $\Delta t = 0.1 \text{ s}$): a) moving boundary region after 40 minutes simulation time; b) spatial profile of error between predictions of operator splitting scheme and algebraic charge density correction after 40 minutes simulation time; c) transient profile of space-averaged error between predictions of operator splitting scheme and algebraic charge density correction

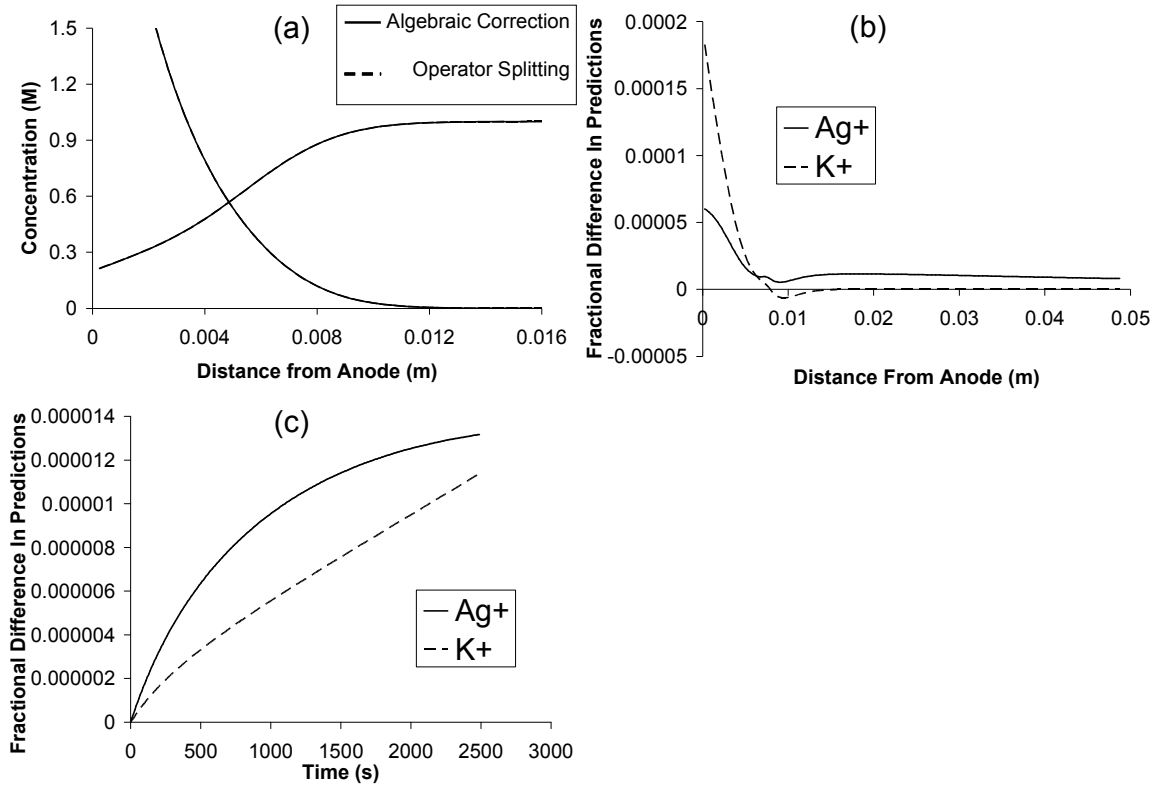


Figure 3.2.4. Comparison of the spatial and transient Ag^+ and K^+ concentration profiles predicted by the operator splitting scheme and the algebraic charge density correction for a 1 M KNO_3 solution ($318 \mu\text{A}/\text{cm}^2$ current density, $\Delta x = 0.05 \text{ cm}$, $\Delta t = 0.1 \text{ s}$): a) moving boundary region after 40 minutes simulation time; b) spatial profile of error between predictions of operator splitting scheme and algebraic charge density correction after 40 minutes simulation time; c) transient profile of space-averaged error between predictions of operator splitting scheme and algebraic charge density correction.

The cause of this phenomenon can be explained through inspection of the governing mass transport equation:

$$\frac{\partial C_i}{\partial t} = \underbrace{-z_i u_i F \nabla C_i \frac{\mathbf{i} + \mathbf{i}_{dp}}{\kappa} + D_i \nabla^2 C_i}_{1} - \underbrace{z_i u_i F C_i \frac{\delta}{\varepsilon}}_{2} \quad (3.2.26)$$

For clarity, the two terms to be examined have been numbered. Term 1 in equation (3.2.26) will not contribute to mass transport unless a concentration gradient exists. Term 2 in equation (3.2.26) does not depend on a gradient but rather induces a concentration gradient. The accuracy of this mass transport model depends upon how accurately Term 2 (the charge density term) can be modelled. Recall from earlier in the paper that Term 2 cannot be directly solved with Term 1 because of the resulting stiffness of the transport equation. In the Fu and Chan experiment, a silver anode is being dissolved at one end of the tube. This introduces a Robin type boundary condition for Ag^+ :

$$z_i u_i F C_i \frac{i + i_{dp}}{\kappa} - D_i \nabla C_i = \frac{i}{z_i F} \quad (3.2.27)$$

This boundary condition induces an Ag^+ concentration gradient at the anode-solution interface that propagates throughout the entire solution domain. No such boundary condition exists for K^+ . Thus, the sole gradient inducer for the K^+ concentration profile is the charge density term (Term 2 in equation (3.2.26)). Therefore, the K^+ concentration profile is more dependent upon charge density effects than Ag^+ and, thus, the K^+ concentration profile is more sensitive to the choice of the charge neutralization algorithm. Thus, for any electrochemical process model, charge density will have the greatest effect upon chemical species that are not produced or consumed in electrode reactions.

3.2.3.2 Effect of current density

Current density is the driving force for electromigration of Ag^+ , K^+ , and NO_3^- in solution. It is also proportional to the rate at which silver is dissolved at the anode. It therefore controls the rate at which the whole process operates and dramatically influences the velocity of the Ag^+/K^+ moving boundary.

In this set of numerical experiments, the current density flowing through the 0.1 M KNO_3 solution that filled the glass tube was increased from $10 \mu\text{A}/\text{cm}^2$ to $100 \mu\text{A}/\text{cm}^2$ and then to $500 \mu\text{A}/\text{cm}^2$. At each current density level, the concentration profiles of Ag^+ , K^+ , and NO_3^- were numerically simulated using both the operator splitting scheme and the new charge density correction algorithm.

Figure 3.2.5 shows simulation results when the current density is $10 \mu\text{A}/\text{cm}^2$. Figure 3.2.5 (a) shows the Ag^+/K^+ moving boundary after 40 minutes of simulation time. Figure 3.2.5 (b) and 3.2.5 (c) shows the difference in predicted concentration profiles as a function of space and time respectively when either operator splitting or algebraic charge density correction methods are used. Figure 3.2.5 (a) shows that the moving boundary has a very low velocity at this low current density. Because the driving force for mass transport is reduced, the effect of charge density is also reduced. This is seen in Figures 3.2.5 (b) and 3.2.5 (c) – the difference in predictions of the two charge density calculation methods being compared is small. In fact, the concentration profiles shown in Figure 3.2.5 (a) predicted using both charge density calculation methods are indistinguishable.

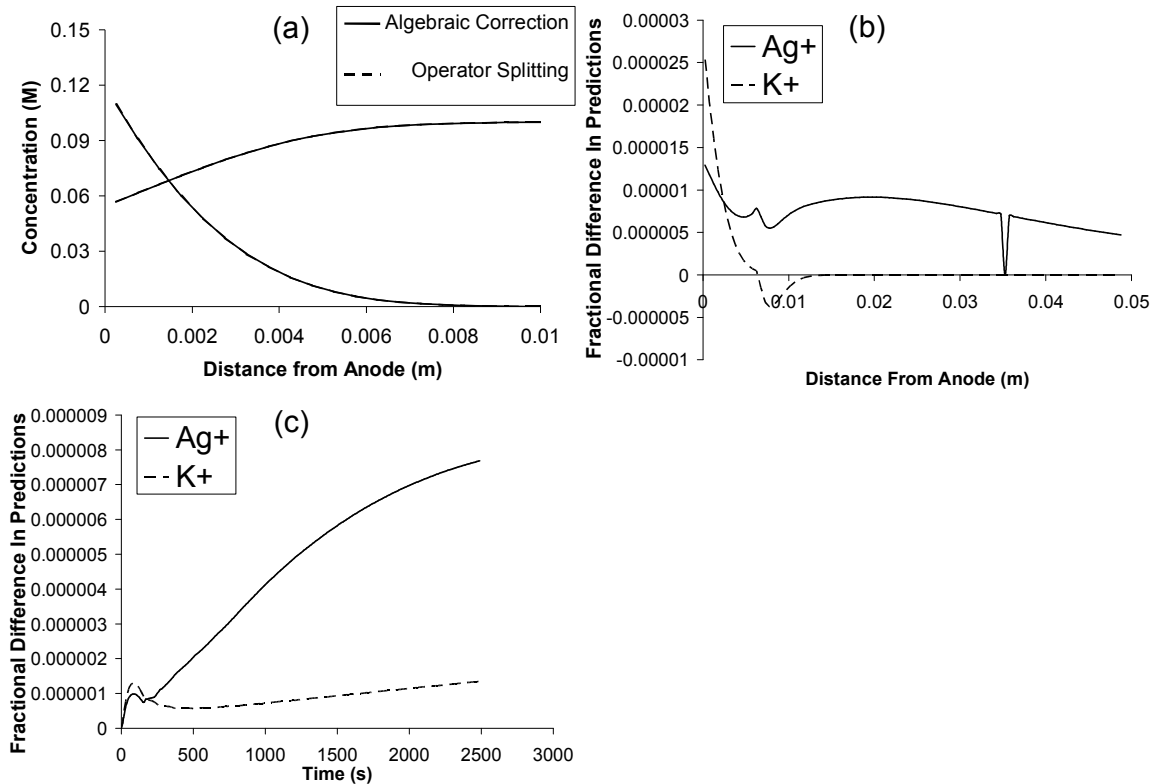


Figure 3.2.5. Comparison of the spatial and transient Ag^+ and K^+ concentration profiles predicted by the operator splitting scheme and the algebraic charge density correction for a current density of $10 \mu\text{A}/\text{cm}^2$ (0.1 M KNO_3 solution, $\Delta x = 0.05 \text{ cm}$, $\Delta t = 0.1 \text{ s}$): a) moving boundary region after 40 minutes simulation time; b) spatial profile of error between predictions of operator splitting scheme and algebraic charge density correction after 40 minutes simulation time; c) transient profile of space-averaged error between predictions of operator splitting scheme and algebraic charge density correction

Figure 3.2.6 displays similar simulation results to Figure 3.2.5 when the current density is increased by an order of magnitude from the previous simulation to $100 \mu\text{A}/\text{cm}^2$. Again in Figure 3.2.6 (a), the concentration profiles predicted using both charge density calculation methods for both Ag^+ and K^+ are very similar. Furthermore, by comparing Figure 3.2.6 (a) with Figure 3.2.5 (a), it can be seen that increasing the current density has a direct and significant effect upon the velocity of the moving boundary. The velocity of the moving boundary has increased from approximately $3.75 \times 10^{-5} \text{ m/min}$ (at current density of $10 \mu\text{A}/\text{cm}^2$) to approximately $3.25 \times 10^{-4} \text{ m/min}$ (at current density of $100 \mu\text{A}/\text{cm}^2$), an increase in velocity of nearly one order of magnitude.

Figure 3.2.6 (b) and 3.2.6 (c) show the difference in predictions between the operator splitting method and the charge density correction method for the case where current density is $100 \mu\text{A}/\text{cm}^2$. By comparing these Figures with Figures 3.2.5 (b) and 3.2.5 (c), it is seen that increasing the current density from $10 \mu\text{A}/\text{cm}^2$ to $100 \mu\text{A}/\text{cm}^2$ increases the difference between predictions of the two charge density calculation schemes. This indicates that the effect of charge density upon the mass transport process has increased. This result was expected as increased electromigration and Ag^+ dissolution rates caused steeper concentration gradients, and thus, diffusion rates increased. The steepness of the concentration gradient is indicative of the amount of coupling between electromigration and diffusion. Electromigration and diffusion are coupled because, as electromigration becomes stronger, concentration gradients increase, thus increasing the strength of diffusion. Increased diffusion rates cause an increased diffusion-potential current, which is additive to the primary electromigration current. Thus, electromigration and diffusion are coupled. This coupling has been shown to promote charge density in

solution. Therefore, when modelling problems with strongly coupled electromigration and diffusion, the simulation results will be more affected by the choice of the charge neutralization algorithm.

Figure 3.2.7 again displays similar simulation results to Figures 3.2.5 and 3.2.6 when the current density is increased to $500 \mu\text{A}/\text{cm}^2$. In this figure, the spatial Ag^+/K^+ concentration profiles after 20 minutes are reported. The charge density algorithm is beginning to play a more important role in the mass transport model predictions. In Figure 3.2.7 (a), slight differences are distinguishable between the profiles predicted using the operator splitting scheme and the new charge density correction algorithm. Figure 3.2.7 (b) shows the difference in spatial profile predictions for both Ag^+ and K^+ when either the operator splitting method or the charge density correction is used. By comparison of Figure 3.2.7 (a) and 3.2.7 (b), it can be seen that the greatest difference in prediction is seen near the point of intersection of the Ag^+ and K^+ concentration profiles. It is at this point that concentration gradients are the most steep and, thus, diffusion offers the most resistance to electromigration. Thus, here the electromigration-diffusion coupling is the strongest and, as a result, the effect of charge density is greatest. This same phenomenon is also clearly observable in Figures 3.2.3 and 3.2.6.

From Figure 3.2.7 (a), it can be calculated that the velocity of the moving boundary has increased from $3.25 \times 10^{-4} \text{ m}/\text{min}$ (at current density of $100 \mu\text{A}/\text{cm}^2$) to $1.6 \times 10^{-3} \text{ m}/\text{min}$ (at current density of $500 \mu\text{A}/\text{cm}^2$). In Figure 3.2.8, the moving boundary velocity was plotted against current density and a linear relationship was found. The rate of mass transport is, in theory, not directly proportional to current density.

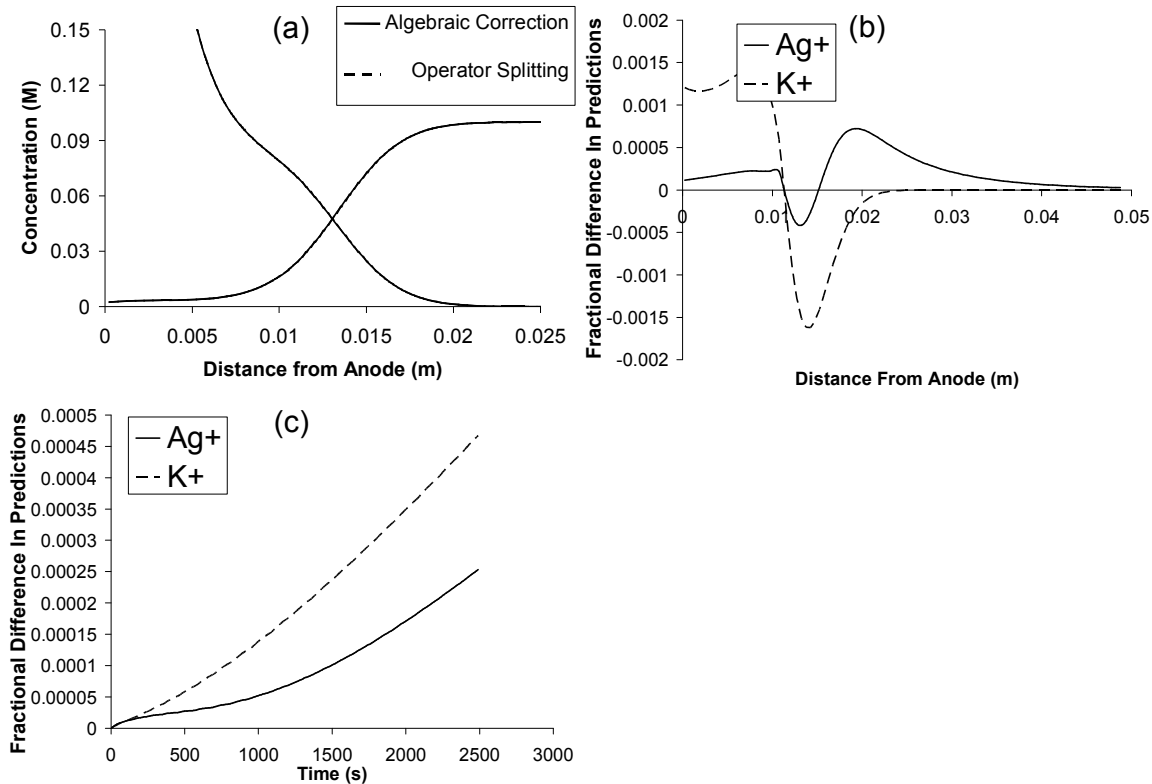


Figure 3.2.6. Comparison of the spatial and transient Ag^+ and K^+ concentration profiles predicted by the operator splitting scheme and the algebraic charge density correction for a current density of $100 \mu\text{A}/\text{cm}^2$ (0.1 M KNO_3 solution, $\Delta x = 0.05 \text{ cm}$, $\Delta t = 0.1 \text{ s}$): a) moving boundary region after 40 minutes simulation time; b) spatial profile of error between predictions of operator splitting scheme and algebraic charge density correction after 40 minutes simulation time; c) transient profile of space-averaged error between predictions of operator splitting scheme and algebraic charge density correction

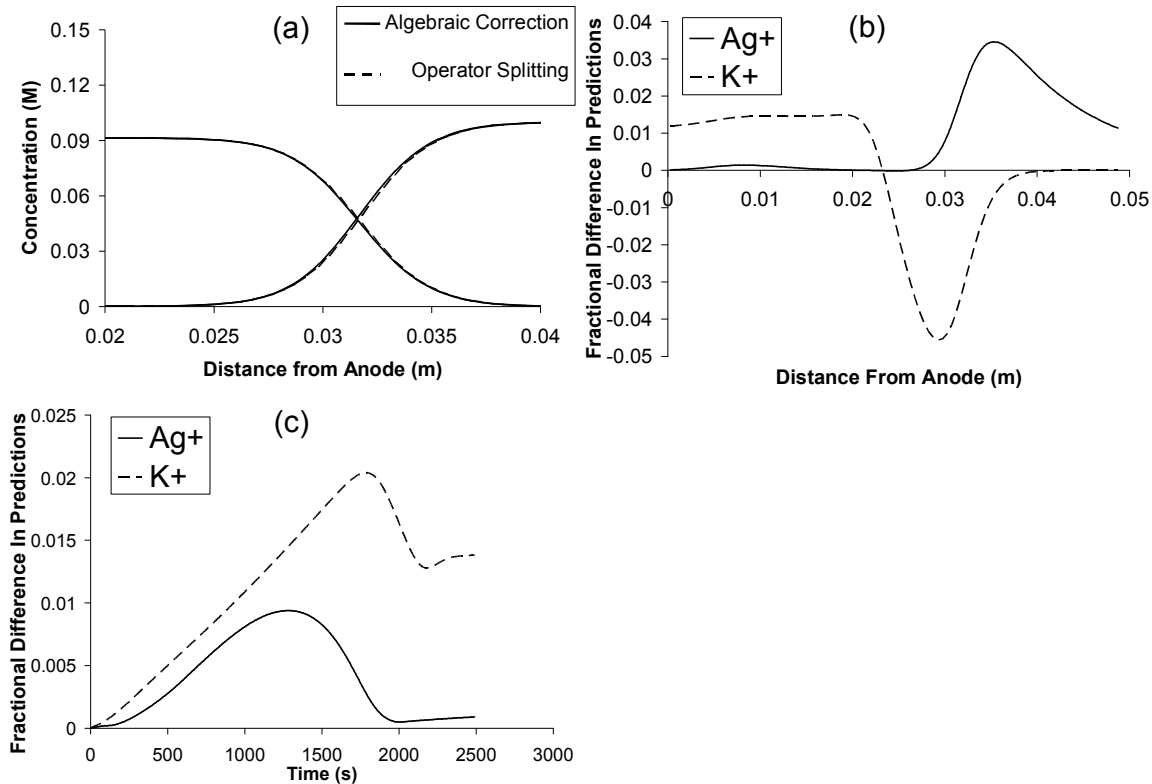


Figure 3.2.7. Comparison of the spatial and transient Ag^+ and K^+ concentration profiles predicted by the operator splitting scheme and the algebraic charge density correction for a current density of $500 \mu\text{A}/\text{cm}^2$ (0.1 M KNO_3 solution, $\Delta x = 0.05 \text{ cm}$, $\Delta t = 0.1 \text{ s}$): a) moving boundary region after 20 minutes simulation time; b) spatial profile of error between predictions of operator splitting scheme and algebraic charge density correction after 20 minutes simulation time; c) transient profile of space-averaged error between predictions of operator splitting scheme and algebraic charge density correction

Rather, it is proportional to the potential gradient, which is a function of both current density and conductivity. Therefore, because Figure 3.2.8 shows that current density and the rate of mass transport are proportional, it can be inferred that conductivity is not a strong function of the current density flowing through solution when the current density is less than $500 \mu\text{A}/\text{cm}^2$. It would be logical for the conductivity to be a stronger function of current density as current density increases but this is not seen in the range of current densities covered in the scope of this work.

3.2.3.3 Effect of spatial step size

The choice of step size influences the performance of the finite volume mass transport solver and this will impact the performance of each of the charge density calculation schemes. Figures 3.2.9 and 3.2.10 show the Ag^+ and K^+ concentration profiles and the difference between predicted Ag^+ and K^+ profiles when using the operator splitting scheme versus the charge density correction.

Examination of Figures 3.2.9 and 3.2.10 shows that the predictions of the two methods deviate from one another as the size of the spatial step decreases (i.e., more nodes are used in the solution of the mass transport equation). This can be theoretically justified by examining the effect of the spatial step size upon the diagonal dominance of the transport coefficient matrix.

As the diagonal dominance of the mass transport coefficient matrix increases, the change in concentration predicted by the mass transport equation over the time step will decrease. The diagonal dominance for the Fu and Chan simulation has been derived previously and is [2]:

$$\frac{|a_p|}{|a_E| + |a_W|} = 1 + \frac{\Delta x^2}{D_i \Delta t (2 + |P_p|)} \quad (3.2.28)$$

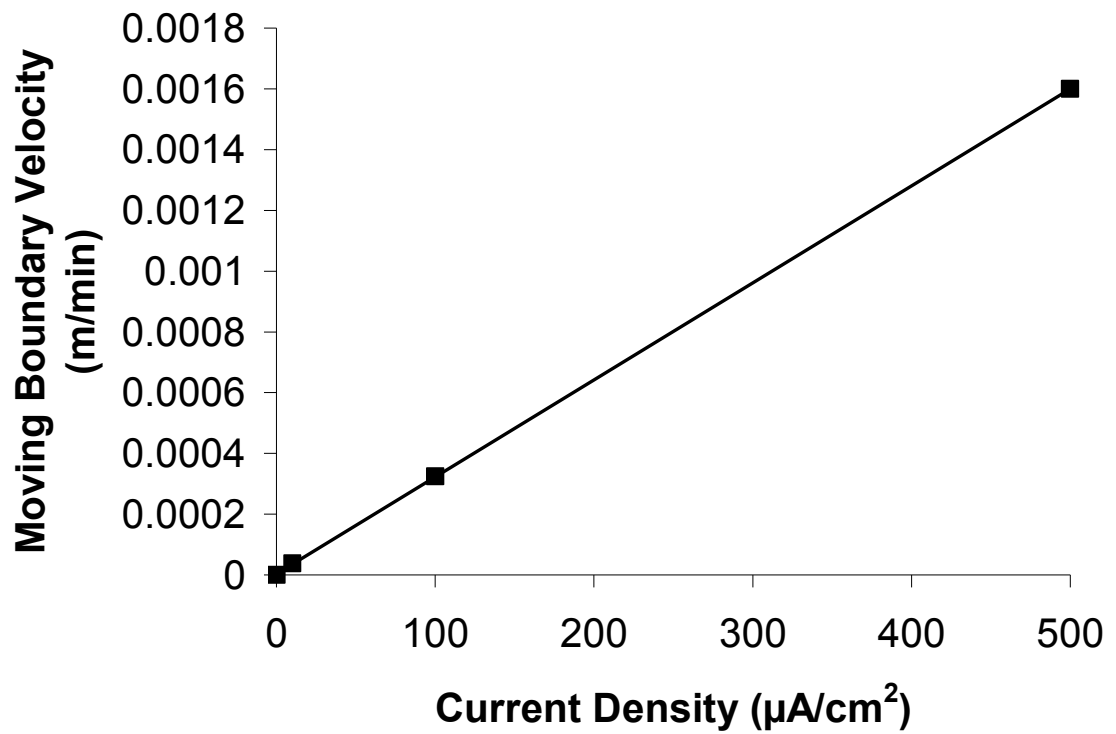


Figure 3.2.8. Relationship between the velocity of the moving boundary and the applied current density (0.1 M KNO_3 solution, $\Delta x = 0.05$ cm, $\Delta t = 0.1$ s). Discrete data points were obtained from numerical simulation results presented in Figs. 5 – 7. A least squares linear fit is shown ($R^2 = 1$).

Here, a_p , a_E , and a_W are discrete transport coefficients used in the finite volume solution of the mass transport equation. The diagonal dominance is the ratio of the point coefficient to the sum of its neighbours. In equation (3.2.28), the Peclet number is defined as:

$$P_p = \frac{F\Delta x}{\kappa_p RT} z_i (i_p + i_{dpP}) \quad (3.2.29)$$

If the time step, Δt , is held constant, the functionality of the diagonal dominance upon Δx is of the form:

$$\frac{|a_p|}{|a_E| + |a_W|} = f(\Delta x) \quad (3.2.30)$$

Thus, as the value of Δx in equation (3.2.28) increases, the diagonal dominance increases. This is evidenced in the simulation results presented in Figures 3.2.9 and 3.2.10. As Δx increases, the deviations in the concentration profiles resulting from using different charge density calculation schemes decreases. The concentration change predicted by the mass transport equation decreases for increasing Δx . Thus, the effect of the charge density model on species concentrations is more pronounced when a refined grid is employed.

3.2.3.4 Effect of time step size

As the time step size in the finite volume method increases, the change in concentration between time steps increases. Thus, as the time step increases, the deviation from charge neutrality that occurred during the last solution of the mass transport equation increases, as does the influence of the choice of charge density calculation scheme. This intuitive assertion is validated by the results of the present simulation.

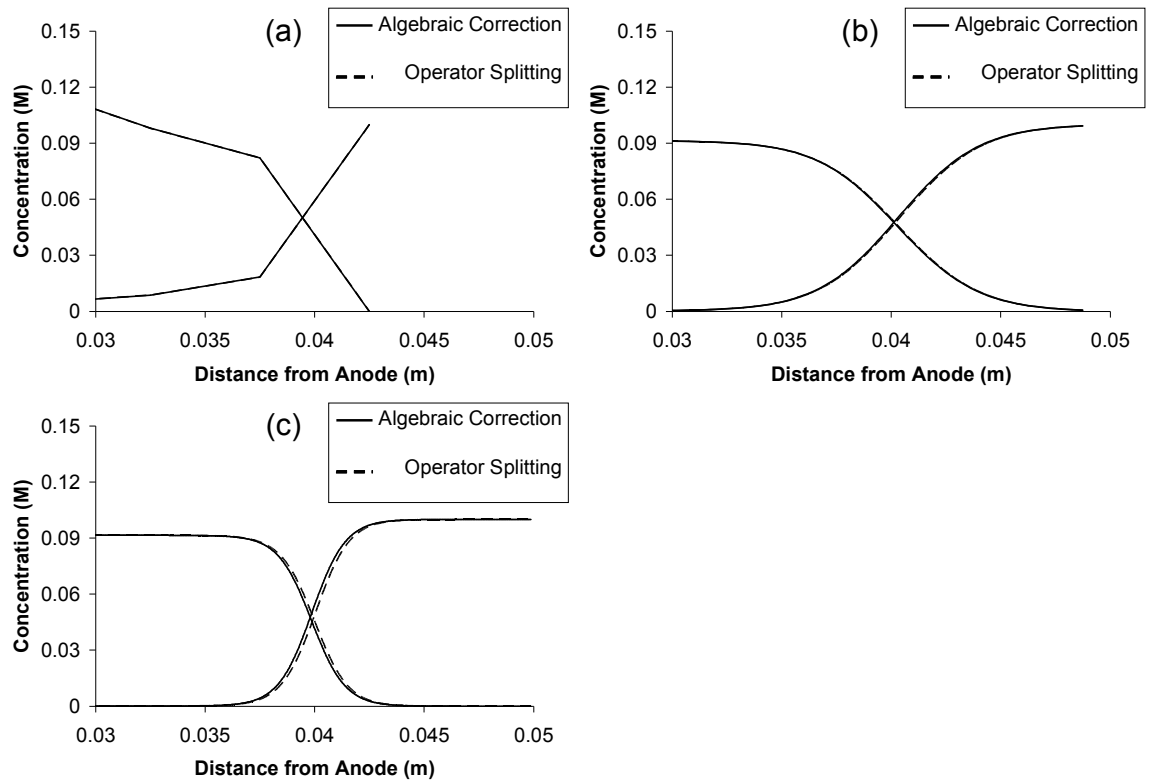


Figure 3.2.9. Moving boundary profile after 40 minutes predicted using the operator splitting and algebraic correction charge density calculation methods for differing spatial step sizes (0.1 M KNO_3 solution, $318 \mu\text{A}/\text{cm}^2$ current density, $\Delta t = 0.1$ s): (a) $\Delta x = 0.5$ cm (10 nodes); (b) $\Delta x = 0.05$ cm (100 nodes); (c) $\Delta x = 0.005$ cm (1000 nodes).

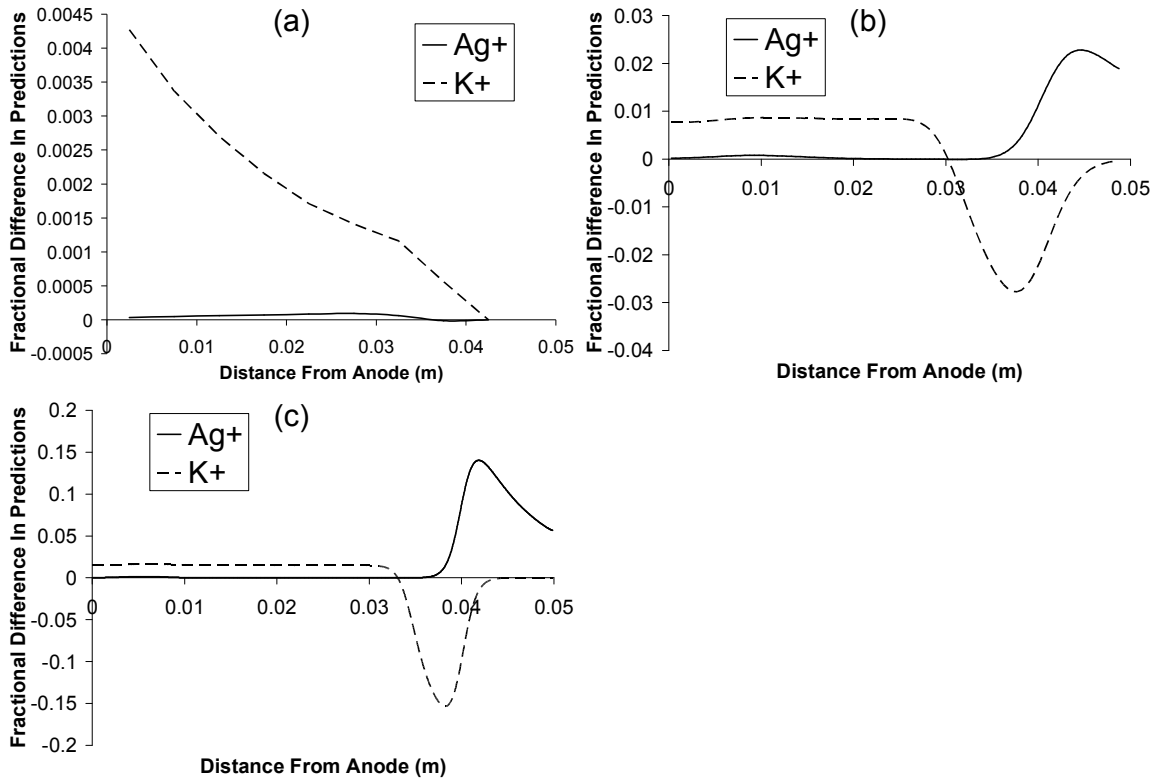


Figure 3.2.10. Difference between moving boundary profiles after 40 minutes predicted using the operator splitting and algebraic correction charge density calculation methods for differing spatial step sizes (0.1 M KNO_3 solution, $318 \mu\text{A}/\text{cm}^2$ current density, $\Delta t = 0.1$ s): (a) $\Delta x = 0.5$ cm (10 nodes); (b) $\Delta x = 0.05$ cm (100 nodes); (c) $\Delta x = 0.005$ cm (1000 nodes)

Figure 3.2.11 shows the moving boundary region profile predicted using both the algebraic correction and the operator splitting scheme. In this figure, the increased accuracy of simulation obtained using the new algebraic correction is apparent. As the time step increases, the amount of numerical charge density that accumulates from integrating the mass transport equation over the time step increases. For $\Delta t > 1\text{sec}$, the magnitude of the numerical charge density accumulated causes the operator splitting scheme to fail to accurately predict the effect of charge density. This is manifested as the significant change in the moving boundary structure as the time step increases that is predicted using the operator splitting scheme (Figure 3.2.11). This numerical error is not seen in the results obtained using the algebraic charge density correction scheme. This implies that the solution of the ODE, equation (3.2.12b), fails as the time step increases while the algebraic correction continues to provide an accurate calculation for the charge density effect. From this observation, it is proven that the new algebraic correction gives a more accurate model of the effect of charge density on mass transport than the direct solution of the charge density term of the mass transport equation. Thus, each difference profile presented up to now is actually an error profile, where the error arises from using the operator splitting scheme rather than the charge density correction scheme.

Figure 3.2.12 shows the error of the predicted Ag^+ and K^+ concentration profiles obtained when using the operator splitting scheme compared to using the algebraic charge density correction. Figure 3.2.12 shows that the error increases as the time step increases. This can be predicted theoretically by again examining the diagonal dominance of the transport coefficient matrix as a function of time step.

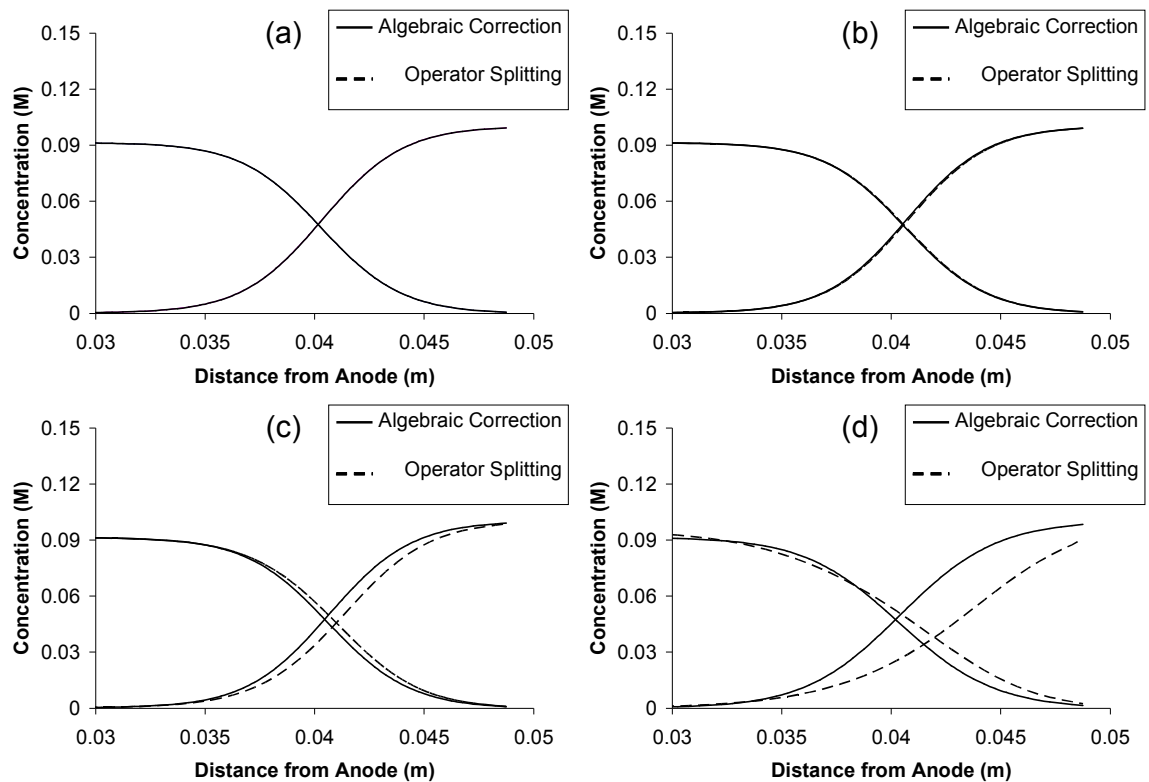


Figure 3.2.11. Moving boundary profile after 40 minutes predicted using the operator splitting and algebraic correction charge density calculation methods for differing time step sizes (0.1 M KNO_3 solution, $318 \mu\text{A}/\text{cm}^2$ current density, $\Delta x = 0.05 \text{ cm}$): (a) $\Delta t = 0.01 \text{ s}$; (b) $\Delta t = 0.1 \text{ s}$; (c) $\Delta t = 1 \text{ s}$; (d) $\Delta t = 10 \text{ s}$

If the spatial step size is held constant, equation (3.2.28) implies the following functionality of the diagonal dominance upon Δt :

$$\frac{|a_P|}{|a_E| + |a_W|} = f\left(\frac{1}{\Delta t}\right) \quad (3.2.31)$$

From equation (3.2.31), the diagonal dominance of the transport coefficient matrix will decrease as the time step increases. As the diagonal dominance of the transport coefficient matrix decreases, the change in concentration predicted by the solution of the mass transport equation over the time step will increase. A greater concentration change will, in turn, increase the numerical charge density that accumulated over the time step. Thus, the charge density algorithm will have to neutralize a greater net charge in solution after each time step as the size of the time step increases. When the time step reached one second and beyond, the numerical charge density accumulated over the time step overwhelmed the operator splitting scheme and the scheme failed.

3.2.3.5 Computational efficiency

The computational efficiency of the algebraic charge density correction method was determined by running a series of identical simulations while varying the space step size. The computer used to run the simulations was a 3.06 GHz Pentium[®] 4 computer with 1 GB of RAM. Table 3.2.1 shows the results of these simulations.

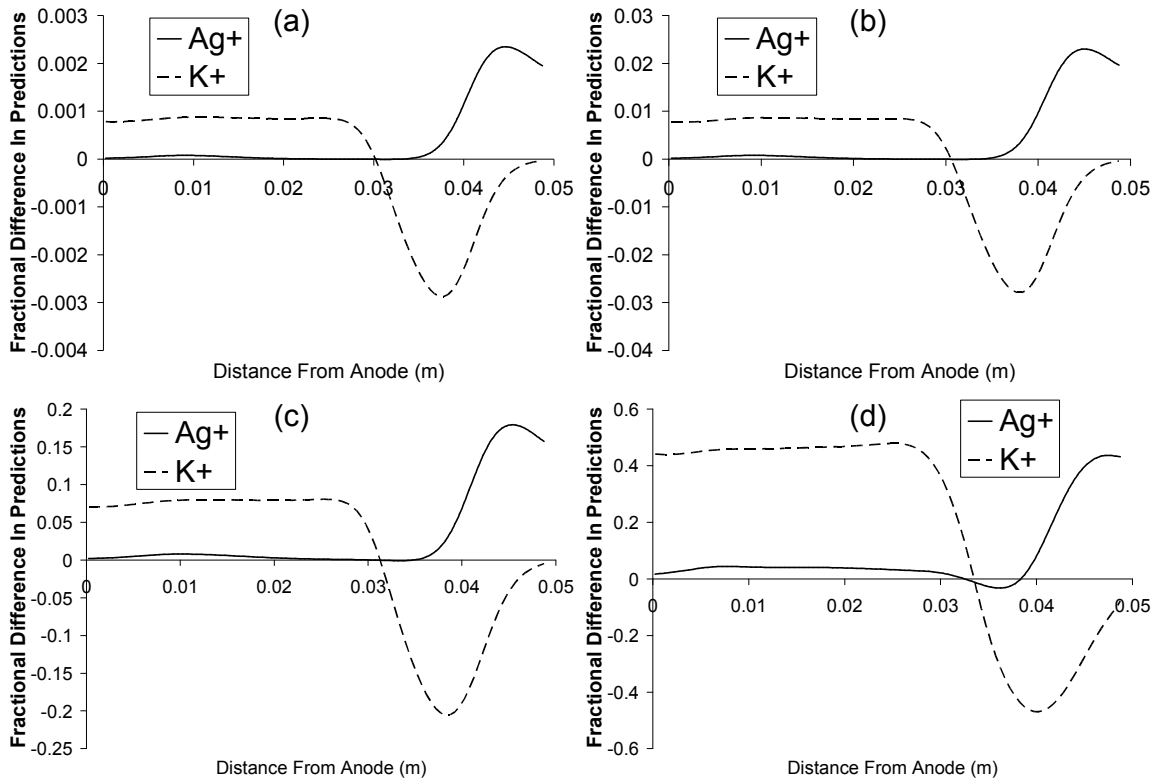


Figure 3.2.12. Difference between moving boundary profiles after 40 minutes predicted using the operator splitting and algebraic correction charge density calculation methods for differing time step sizes (0.1 M KNO_3 solution, $318 \mu\text{A}/\text{cm}^2$ current density, $\Delta x = 0.05 \text{ cm}$): (a) $\Delta t = 0.01 \text{ s}$; (b) $\Delta t = 0.1 \text{ s}$; (c) $\Delta t = 1 \text{ s}$; (d) $\Delta t = 10 \text{ s}$.

Number of Nodes	Simulation Time : Real Time	
	Algebraic Correction	Operator Splitting
10	156:1	33:1
100	34:1	7.0:1
1000	6.4:1	1.0:1
5000	1.1:1	0.17:1

Table 3.2.1. Comparison of the ratio of simulation time to real time when using the algebraic charge density correction and the operator splitting method for a variety of grid spacings for simulating the Fu and Chan experiment. Simulations were performed using a 3.06 GHz Intel Pentium 4 computer with 1 GB of RAM.

In each of the simulations above, the Fu and Chan system was modelled with a $318 \mu\text{A}/\text{cm}^2$ current density, a 0.1 M KNO_3 solution filling the beaker, and a time step of 0.1 seconds. From the results above, it can be seen that the use of the algebraic charge density correction dramatically reduces the computational time. This improvement in performance increases as the number of nodes increases. This is expected because, as the number of nodes increase (Δx decreases), the diagonal dominance of the transport coefficient matrix decreases. This results in increased numerical charge density after each time step. This was shown previously by examination of the diagonal dominance as a function of Δx . From the results presented in Table 3.2.1, it can be calculated that for 10 nodes, the algebraic correction was 4.7 times faster than the operator splitting scheme while for 1000 nodes, the algebraic correction was 6.2 times faster.

3.2.4 Conclusions

Throughout this section, it has been shown that the new charge density model provides a stable and accurate method for calculating charge density effects. It also significantly improves the computational efficiency of an electrolyte mass transport model. From the results presented in this section, the following conclusions can be made:

1. A new algebraic charge density correction method has been derived. It provides a more accurate and efficient method for computation of the charge density term of the mass transport equation than the operator splitting method of Evitts [10] and Watson [11].
2. The theoretical time required to neutralize an electrolyte solution has been theoretically derived. It is calculated to be the ratio of the electrical permittivity to the conductivity of the solution, i.e.,

$$\Delta t_{Poisson} = \frac{\epsilon}{\kappa}$$

Physically, this time is the ratio of the net charge of the solution to the rate at which the charge may be dissipated. Based on Ohm's Law and Poisson's equation, it can also be shown that:

$$\Delta t_{Poisson} = - \frac{\delta}{\frac{\partial \delta}{\partial t}}$$

3. For accurate calculation of the concentration profile of species not involved in electrode reactions, using an accurate model of charge density is of paramount importance. In the simulations presented, the concentration profile of K^+ was

more sensitive to the choice of the charge density calculation method than the concentration profile of Ag^+ . This is because, while an Ag^+ concentration gradient is formed primarily due to dissolution at the anode-solution interface, the K^+ concentration gradient is formed solely by its coupling to Ag^+ and NO_3^- through the charge density term. Thus, predicted concentrations of ionic species not involved in electrode reactions are more dependent upon the charge density model.

4. Increased concentration damps the effect of charge density upon mass transport. This was shown in the simulations presented herein: the predicted Ag^+ and K^+ profiles using the two different charge density correction methods became more similar as solution concentration, and thus solution conductivity, increased. This observation is physically realistic because, as the conductivity increases, more ions are available to counteract a net charge. Thus, each ionic species undergoes a smaller concentration change to neutralize charge in a more concentrated solution.
5. As the potential gradient in solution increases, the effect of charge density upon ionic concentration also increases. This conclusion is evidenced in the present work by the following observation: the predicted Ag^+ and K^+ profiles using the two different charge density correction methods deviated further from one another as the applied current density was increased. This is because the coupling between electromigration and diffusion became stronger as the current density increased. This interaction caused an increase in charge density. Thus, as the

potential gradient became increasingly steep, the effect of charge density on ionic concentration profiles increased.

6. The conductivity in solution is a weak function of the applied current density. It was shown that the velocity of the moving boundary, which should theoretically be proportional to the potential gradient (the ratio of current density to conductivity), was in fact directly proportional to the current density.
7. The effect of the charge density model is greater for a more refined spatial grid. For example, in the present work, the predicted Ag^+ and K^+ profiles using the two different charge density correction methods deviated further from one another as the spatial step size decreased. This occurred because the diagonal dominance of the transport coefficient matrix reduces with decreasing Δx . As the diagonal dominance decreases, a greater change in concentration is predicted through the solution of the mass transport equation. Increased concentration changes caused greater numerical charge density to accumulate over a time step. Thus, ionic concentration profiles become more sensitive to the choice of charge density model as the spatial grid is refined.
8. As the time step increased, the calculated profiles became more sensitive to the choice of charge density calculation method. In fact, for $\Delta t \geq 1\text{ s}$, the operator splitting method failed to accurately characterize the effect of charge density while

the algebraic charge density correction method continued to provide a realistic prediction of charge density effects.

9. Using the algebraic charge density correction method rather than the operator splitting method results in between 4.75 and 6.2 times more simulation time for a given amount of real time for the same time step. In addition, the algebraic method can be applied when larger time steps are used in the solution of the mass transport equation, thus further increasing the simulation time. This dramatic increase in computational efficiency makes the new correction a valuable tool for mass transport modelling.

3.2.5 References

1. K.L. Heppner, R.W. Evitts, J. Postlethwaite, *Corrosion* **60** (2005) 718.
2. K.L. Heppner, R.W. Evitts, *Dynamics of Continuous, Discrete, and Impulsive Systems – Series B* **11** (2004) 29.
3. Newman, J., “Infinitely Dilute Solutions” in “Electrochemical Systems”, Prentice Hall, Toronto, ON (1973), pp. 233 – 234.
4. S. M. Sharland, P.W. Tasker, *Corrosion Science* **28**, (1988) 603.
5. S.M. Gravano, J.R. Galvele, *Corrosion Science* **24** (1984) 517.
6. J. W. Oldfield, W. H. Sutton, *British Corrosion Journal* **13**, (1978): p. 13.
7. Bernhardsson, S., L. Eriksson, J. Ooppelstrup, I. Puigdomenech, T. Wallin, “Crevice Corrosion of Stainless Steels, Calculations of Concentrations and pH Changes” in “Proc. 8th International Congress on Metallic Corrosion” **1**, Mainz, Federal Republic of Germany, September 6-11, pp. 193 – 198 (1981).
8. K. Hebert, R. Alkire, *Journal of the Electrochemical Society* **130**, (1983) 1007.
9. S. M. Sharland, *Corrosion Science* **33**, (1992) 183.
10. R. W. Evitts, “Modeling of Crevice Corrosion”, Ph.D. thesis, University of Saskatchewan, Saskatoon, Saskatchewan, Canada (1997).
11. M.K. Watson, “Numerical Simulation of Crevice Corrosion”, Ph.D. Dissertation, University of Saskatchewan, Saskatoon SK (1989).
12. K. L. Heppner, R. W. Evitts, and J. Postlethwaite, *Canadian Journal of Chemical Engineering* **80**, (2002) 849.
13. K. L. Heppner, R. W. Evitts, and J. Postlethwaite, *Canadian Journal of Chemical Engineering* **80**, (2002) 857.

14. J. W. Fu, S. Chan, Corrosion **40**, (1984) 540.

3.3 The Hybrid Differencing Scheme*

The previous section outlined a method by which to dramatically improve the computational efficiency of solving the electromigration-diffusion equation. In this section, another numerical scheme is developed which provides a more accurate method to numerically simulate electrolyte mass transport using a finite volume method.

Considerable research effort has been focused upon technological areas in which the understanding of electrochemical kinetics coupled with electrolytic mass transport is of paramount importance. Such areas include corrosion control, energy generation via fuel cells, electrochemical separation techniques including ion exchange and electrophoresis, and electrochemical reactors. This particular research is focused upon the accurate modeling of electrolyte mass transport under the influence of an encompassing electrical field. A new differencing scheme for mass transport was developed and then validated against the moving boundary experiment [1].

Several differencing schemes have been developed for solving the convection-diffusion equation. The idea of an upwind differencing scheme (UDS) was first introduced by Courant et al. [2] and subsequent work by Barakat and Clark [3], Gentry et al. [4], and Runchal and Wolfshtein [5] followed. UDS replaces first order derivative expressions with forward finite difference analogs. This scheme is appropriate for highly convective problems; only the upwind node influences the control volume. The central differencing scheme (CDS), appropriate for diffusive problems, employs central finite difference discretization thus equally dispersing influence to all physical control volume

* Reference: K.L. Heppner and R.W. Evitts (2005), A Hybrid Differencing Scheme for Mass Transport in Electrochemical Systems, *International Journal of Numerical Methods for Heat and Fluid Flow* **15**, pp. 842 – 862.

boundaries. Other schemes have since been developed which are appropriate where neither convection nor diffusion dominate. These schemes compromise between UDS and CDS based upon local physics [6, 7, 8].

The electrolyte mass transport equation is unique from the convection-diffusion equation because an additional condition is added. Around each ion is a cloud of ions of opposing charge which, at equilibrium, exactly balance the space-averaged charge. However, when an electrolyte is a transport medium between two electrodes of differing electrical potential, a small portion of the Gibb's Free Energy gradient that drives the coupled electrode charge transfer, mass transport, and chemical equilibrium process is stored in the electrolytic solution as charge density. Although small, the charge density has a large impact on the second order gradient of the electrical potential field; this feature induces significant instability in mass transport calculations. Therefore, ensuring a very small charge density in the solution is of paramount importance when simulating electrolytic mass transfer. In this work, mass transport is assumed to occur in a solution of moderate dilution [9]. The mass transport equation for such a solution is written as:

$$\frac{\partial C_i}{\partial t} = -z_i u_i F \left[\frac{\nabla C_i \cdot (\mathbf{i} + \mathbf{i}_{dp})}{\kappa} + C_i \frac{\delta}{\varepsilon} \right] + D_i (\nabla^2 C_i + \nabla C_i \nabla \ln \gamma_i + C_i \nabla^2 \ln \gamma_i) + G_i \quad (3.3.1)$$

Equation (3.3.1) is the electromigration-diffusion transport equation and its solution is the focus of this work.

Accurately modeling electrolytic mass transport is essential when developing predictive models for localized corrosion. Previous authors have prescribed upwind parameters based upon the local Peclet number or have simply assumed electromigrative domination. Walton et al. [10] modeled the crevice corrosion of type 304 stainless steel

using UDS when the absolute value of the Peclet number was greater than two and CDS otherwise. Evitts [11], Watson [12], Watson and Postlethwaite [13 – 15], and Heppner et al. [16, 17] modelled the initiation of crevice corrosion in passive metals using UDS. To this point, no differencing scheme has been developed which uses an electromigration-diffusion balance equation to prescribe appropriate upwind parameters for mass transport under the influence of a potential gradient. For this reason, a HDS has been developed which varies the upwind parameter according to the solution of the pseudo steady state electromigration-diffusion equation. This new differencing scheme enables more accurate prescription of the upwind parameter where neither electromigration nor diffusion dominates the mass transport process.

3.3.1 Development of the electrolyte mass transport hybrid differencing scheme

3.3.1.1 Background

The electrochemical potential gradient, which is composed of activity gradient and potential gradient contributions, is the sole driving force for mass transport of ions in a stagnant electrochemical system. In a moderately dilute solution, the transport of ions can be decomposed into two inter-coupled mechanisms:

- Electromigration – the transport of ionic species via an electrical potential gradient. Its mathematical form is similar to convection.
- Diffusion – the transport of ionic and neutral species along an activity gradient.

The upwind and downwind positions, referred to frequently in the forthcoming discussion, represent the origin and destination respectively of ions driven by electromigration. Consider electromigration and diffusion balancing a chemical reaction source term at steady state in an infinitely dilute medium:

$$\left(z_i u_i F \frac{d\Phi}{dx} \right) \frac{dC_i}{dx} + D_i \frac{d^2 C_i}{dx^2} = G_i \quad (3.3.2)$$

As the potential gradient, $d\Phi/dx$, increases, the strength of electromigration relative to diffusion increases and the contribution of diffusion becomes insignificant:

$$\left(z_i u_i F \frac{d\Phi}{dx} \right) \frac{dC_i}{dx} = G_i \quad (3.3.3)$$

The solution of this first order differential equation requires knowledge of only the upwind boundary. Thus, in regions of strong electromigration, the space-averaged concentration of ionic species in the control volume is highly dependent upon the concentration at the upwind boundary. In the absence of electromigration, both control volume boundaries have equal influence on the control volume. When the potential gradient is negligible, no electromigration occurs and (3.3.2) becomes:

$$D_i \frac{d^2 C_i}{dx^2} = G_i \quad (3.3.4)$$

Equation (3.3.4) is a form of the diffusion equation and conditions at both surrounding boundaries are required for its solution.

This phenomenon can be explained through a physical analogy. Consider that you are standing halfway between a pig barn (to the east) and a chocolate factory (to the west). If the wind is coming from the east, you'll smell the pig barn. However, if the wind is coming from the west, you'll smell the chocolate factory. If the air is calm, you'll smell a mix of both. In the same way, if electromigration is moving the ionic species from the east node towards the west node, the interfacial concentration will be more influenced by C_E ($\alpha < 0$). However, if the ionic species is electromigrating from the west to the east, the interfacial concentration will be more influenced by C_W ($\alpha > 0$). If no potential gradient

exists, and thus electromigration is not occurring, the interfacial concentration will be influenced equally by both surrounding nodes ($\alpha = 0$).

Mathematically accounting for the dynamic boundary influence encountered in electrolytic mass transport problems requires the calculation of an upwind factor, a weighting parameter that adjusts the relative influence of the upwind node proportionate to the relative strength of electromigration versus diffusion. The upwind factor, α , modifies the interpolated value at an interface between two control volumes:

$$C_{i+1/2} = \frac{1+\alpha}{2} C_i + \frac{1-\alpha}{2} C_{i+1} \quad (3.3.5)$$

Here, i is a spatial node index. The mathematical description of α is based upon the solution of an electromigration-diffusion balance and its derivation follows.

3.3.1.2 Model derivation

The velocity of an ion migrating through an electrical field is [9]:

$$v_i = -z_i u_i F \frac{d\Phi}{dx} \quad (3.3.6)$$

The velocity of an ion under the influence of pure diffusion is:

$$v_i = -\frac{D_i}{\Delta x} \quad (3.3.7)$$

The ratio of the two velocities gives a Peclet number for the electrolyte mass transport problem:

$$P = \frac{z_i u_i F \Delta x}{D_i} \frac{d\Phi}{dx} \quad (3.3.8)$$

The net mass flux across an arbitrary interface driven by an electrochemical potential gradient is described as:

$$\mathbf{N}_i = -\frac{D_i}{RT} C_i \nabla \tilde{\mu}_i \quad (3.3.9)$$

Assuming that moderately dilute solution theory is applicable, the electrochemical potential gradient can be segregated into an activity gradient (diffusion) and potential gradient (electromigration) contribution:

$$\mathbf{N}_i = -D_i \nabla C_i - D_i C_i \nabla \ln \gamma_i - z_i u_i F C_i \nabla \Phi \quad (3.3.10)$$

A pseudo-steady state mass balance on an infinitesimal one-dimensional control volume may be written:

$$\nabla \cdot \mathbf{N}_i = 0 \quad (3.3.11)$$

The pseudo-steady state assumption is valid provided that relatively small time steps are used. Equation (3.3.11) also assumes that chemical reactions occur much faster than mass transport, and thus, are at equilibrium. Substitution of (3.3.10) into (3.3.11) and subsequent application of the chain rule and rearrangement yields the following equation (in one dimension):

$$\frac{d^2 C_i}{dx^2} + \left(\frac{z_i u_i F}{D_i} \frac{d\Phi}{dx} + \frac{d \ln \gamma_i}{dx} \right) \frac{dC_i}{dx} + \left(\frac{z_i u_i F}{D_i} \frac{d^2 \Phi}{dx^2} + \frac{d^2 \ln \gamma_i}{dx^2} \right) C_i = 0 \quad (3.3.12)$$

Poisson's equation for charge density describes the electrical potential distribution for a given electroneutrality condition:

$$\frac{d^2 \Phi}{dx^2} = -\frac{\delta}{\epsilon} \quad (3.3.13a)$$

where δ is the charge density:

$$\delta = F \sum_j z_j C_j \quad (3.3.13b)$$

Equation (3.3.13a) can be substituted into equation (3.3.12) to yield:

$$\frac{d^2 C_i}{dx^2} + \left(\frac{z_i u_i F}{D_i} \frac{d\Phi}{dx} + \frac{d \ln \gamma_i}{dx} \right) \frac{dC_i}{dx} + \left(-\frac{z_i u_i F}{D_i \varepsilon} \delta + \frac{d^2 \ln \gamma_i}{dx^2} \right) C_i = 0 \quad (3.3.14)$$

By substitution of equation (3.3.8) into (3.3.14), this second order homogenous ordinary differential equation can be written in terms of the Peclet number:

$$\frac{d^2 C_i}{dx^2} + \left(\frac{P}{\Delta x} + \frac{d \ln \gamma_i}{dx} \right) \frac{dC_i}{dx} + \left(-\frac{z_i u_i F}{D_i \varepsilon} \delta + \frac{d^2 \ln \gamma_i}{dx^2} \right) C_i = 0 \quad (3.3.15)$$

Equation (3.3.15) can then be expressed as:

$$\xi \frac{d^2 C_i}{dx^2} + \psi \frac{dC_i}{dx} + \zeta C_i = 0 \quad (3.3.16)$$

Where:

$$\begin{aligned} \xi &= 1 \\ \psi &= \frac{P}{\Delta x} + \frac{d \ln \gamma_i}{dx} \\ \zeta &= -\frac{z_i u_i F}{D_i \varepsilon} \delta + \frac{d^2 \ln \gamma_i}{dx^2} \end{aligned}$$

The gradient of the logarithm of the activity coefficient is a weak function of the concentration and is therefore assumed constant. Also, the charge density is very small and its variation with concentration is also neglected. With these two assumptions, equation (3.3.16) is a linear ordinary differential equation. The over-damped solution of equation (3.3.16) is the desired physically realistic non-oscillatory solution. This occurs when $\psi^2 > 4\xi\zeta$. To ensure that the problem is always over-damped, two additional assumptions are made to eradicate the coefficient, ζ :

1. Any charge separation in an electrolytic solution invokes powerful forces that quickly reinstate electroneutrality. Outside of the electrical double layer region

which is located very near an electrochemically reactive wall (such as a corroding metal surface), it is reasonable to assume an electrically neutral system ($\delta = 0$).

2. Where activity coefficient gradients do not vary significantly, it can be assumed that the second order derivative of the activity coefficient is zero ($d^2 \ln \gamma_i / dx^2 = 0$).

With these two assumptions, the coefficient, ζ , can be neglected:

$$\zeta = -\frac{z_i u_i F}{D_i \varepsilon} \delta + \frac{d^2 \ln \gamma_i}{dx^2} = 0 \quad (3.3.17)$$

A non-oscillatory solution is then guaranteed across each computational node.

Now consider one computational control volume across which the particular solution to the ordinary differential equation can be obtained. At the western interface ($x=0$), the concentration is equal to C_{iw} while at the eastern interface ($x=\Delta x$), the concentration is C_{ie} . Through application of these boundary conditions, the particular solution of the second order problem is obtained:

$$C_i(x) = C_{iw} + (C_{ie} - C_{iw}) \frac{e^{-\frac{\psi}{\xi} x} - 1}{e^{-\frac{\psi}{\xi} \Delta x} - 1} \quad (3.3.18)$$

Substituting the definition of ξ and ψ gives the final form of the solution:

$$C_i(x) = C_{iw} + (C_{ie} - C_{iw}) \frac{e^{-P' \frac{x}{\Delta x}} - 1}{e^{-P'} - 1} \quad (3.3.19a)$$

where:

$$P' = P + \frac{d \ln \gamma_i}{dx} \Delta x \quad (3.3.19b)$$

Equation (3.3.19b) shows that the magnitude of the activity coefficient gradient has a direct effect on the dominance of electromigration in electrolyte mass transport problems. The activity coefficient gradient accounts for the influence of other ions in solution on the i^{th} ion. It is the force that propels the ion towards regions of lower ionic strength. From equation (3.3.19a), the concentration at the center of the control volume is then:

$$C_{iP} = C_{iw} + (C_{ie} - C_{iw}) \frac{e^{\frac{P'}{2}} - 1}{e^{-P'} - 1} \quad (3.3.20)$$

By assuming an upwinding function of the form:

$$C_{iP} = \left(\frac{1 + \alpha}{2} \right) C_{iw} + \left(\frac{1 - \alpha}{2} \right) C_{ie} \quad (3.3.21)$$

Equations (3.3.20) and (3.3.21) can be solved simultaneously to yield a formula for α :

$$\alpha = 1 - 2 \left(\frac{e^{\frac{P'}{2}} - 1}{e^{-P'} - 1} \right) \quad (3.3.22)$$

When the charge density and second order derivative of the activity coefficient is assumed negligible, the resulting upwind parameter formula is similar to the exponential differencing scheme [7, 8]. However, unlike convective problems where the Reynolds number is dependent upon the velocity and viscosity of the fluid, the electrolyte mass transport Peclet number is dependent upon the electrical field, the diffusivity, and the magnitude of the activity coefficient gradient. This is a one-dimensional scheme which can be applied to multidimensional problems. However, application of a 1-D scheme to 2-D and 3-D problems will introduce artificial viscosity effects [18]. This phenomenon may be controlled through grid refinement. The spatial upwind parameter profile is shown for a range of Peclet numbers in Figure 3.3.1.

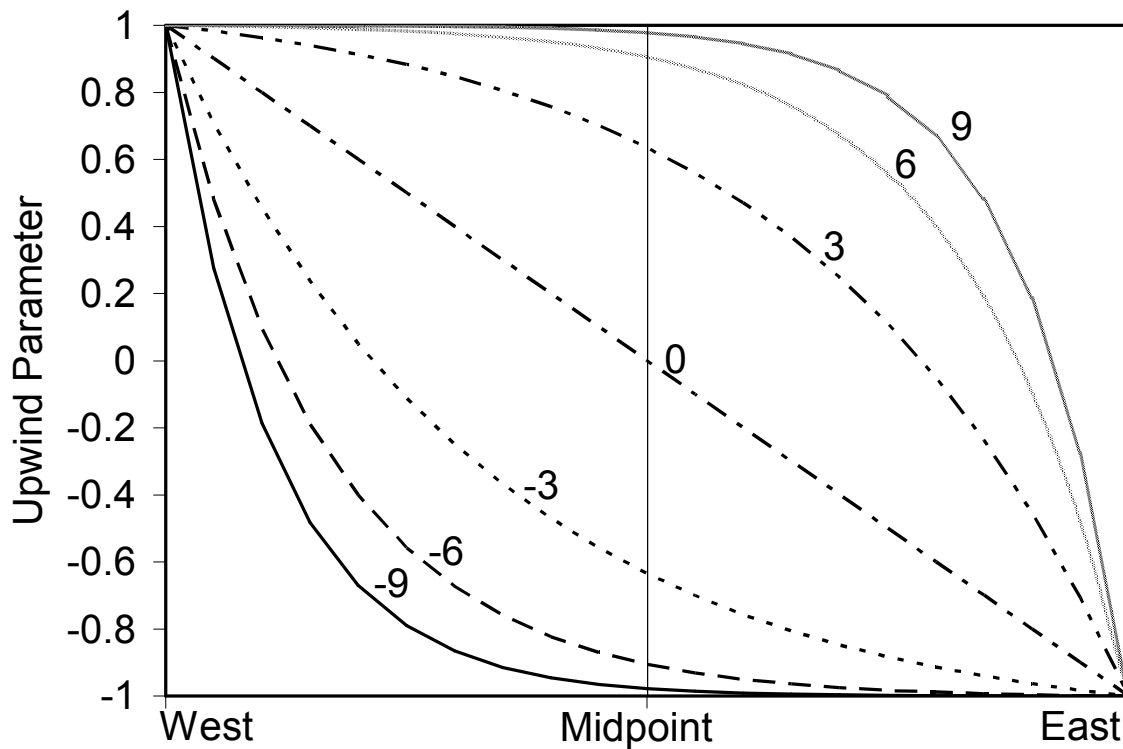


Figure 3.3.1. The spatial upwind parameter profile across a computational control volume over a range of Peclet numbers.

There are cases where the assumptions used to obtain equation (3.3.22) are not valid. Two examples are the modelling of transport in regions of strong coupled electromigration and diffusion, where charge density cannot be neglected, and in electromigration-dominated problems where the activity coefficient gradient may vary significantly in space. In these cases, equation (3.3.22) should not be used. Instead, the value of $(\psi^2 - 4\xi\zeta)$ should be determined and, based upon its sign, the appropriate solution to the ordinary differential equation (under-damped, over-damped, or critically damped) should be selected. Then, C_{iP} , C_{ie} , and C_{iw} may be calculated. The appropriate value for α can be obtained through rearrangement of equation (3.3.21):

$$\alpha = \frac{C_{iw} + C_{ie} - 2C_{iP}}{C_{ie} - C_{iw}} \quad (3.3.23)$$

Depending upon the size of the second order derivative of the activity coefficient, and in particular, the charge density, the predicted upwind parameter may not be physically realistic (the solution may be under-damped). The following section demonstrates the effect of charge density on the stability of the mass transport problem.

3.3.1.3 Stability of the electrolyte mass transport hybrid differencing scheme

Unlike the convection-diffusion equation, the electromigration-diffusion mass transport problem is influenced by an electrical field. The mass transport problem is therefore governed by the following condition: unless a very large amount of work is done on the system, the solution must possess negligible charge density. To obtain the exponential formula for the upwinding parameter previously presented, the solution charge density was assumed to be negligible. For this assumption to be valid, care must be taken to ensure that the numerical solution algorithm respects the electroneutrality

condition inherent to the mass transport mechanism. If the charge density tolerance during the numerical solution of the mass transport equation is too high, the steady state balance between electromigration and diffusion will become under-damped. The particular solution of the under-damped electromigration-diffusion balance equation ($\psi^2 < 4\xi\zeta$) is:

$$C_i(x) = e^{\tau x} \left\{ C_{iw} \cos(\beta x) + [C_{ie} e^{-\tau \Delta x} - C_{iw} \cos(\beta \Delta x)] \frac{\sin(\beta x)}{\sin(\beta \Delta x)} \right\} \quad (3.3.24a)$$

where the real and imaginary components, respectively, of the complex conjugate roots of the characteristic equation are:

$$\tau = -\frac{\psi}{2\xi} \quad (3.3.24b)$$

$$\beta = \frac{\sqrt{(4\xi\zeta - \psi^2)}}{2\xi} \quad (3.3.24c)$$

This solution predicts a sinusoidal concentration profile across the computational control volume and is clearly physically unrealistic. Figure 3.3.2 displays the predicted control volume concentration profile for a range of very small charge densities. As the charge density increases, the solution becomes under-damped; the increasingly sinusoidal concentration profile causes physically unrealistic predictions of the upwind parameter.

When numerically based or artificial charge density is present, equation (3.3.14) shows that the concentration profile is now dependent upon not only the gradient of the concentration field but also on the value of the concentration. This introduces new instability problems – as the concentration profile rises or falls, the profile will mutate to an extent proportionate to the level of charge density in solution. Figure 3.3.3 demonstrates this effect.

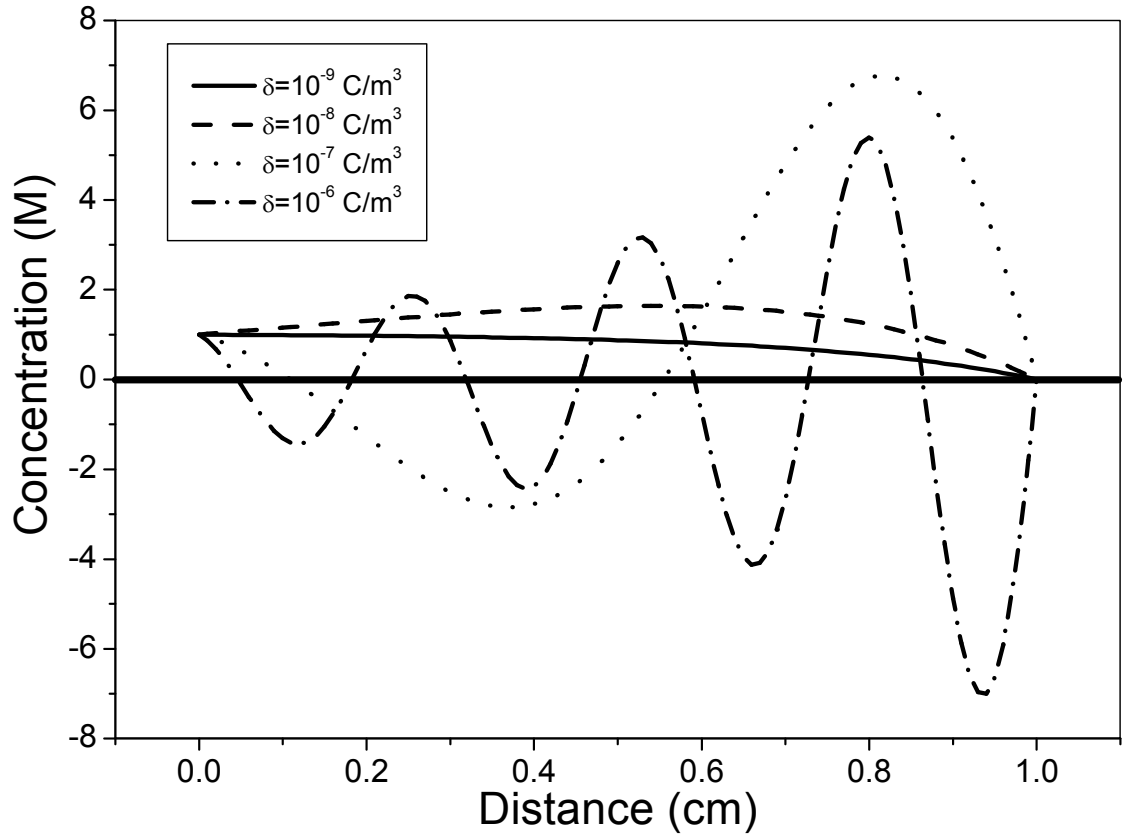


Figure 3.3.2. Solution of the electromigration-diffusion balance equation across a computational control volume as solution charge density increases. Critical damping occurs when $\delta \approx 7.7 \times 10^{-9} \text{ C/m}^3$.

Figure 3.3.3 (a) shows that the shape of the concentration profile is invariant with the value of concentration for an electrically neutral system. However, even before the critical damping charge density (approximately $7.7 \times 10^{-9} \text{ C/m}^3$ for this example) is surpassed, the concentration profile begins to bulge beyond the electrically neutral profile, a feature that is exaggerated as the concentration profile boundary conditions are increased. Where the concentration profile extends beyond the range $[C(x=0), C(x=\Delta x)]$, the predicted upwind parameter will lie outside of $[-1, 1]$. An acceptable value of the upwind parameter lies in the range $[-1, 1]$. Figure 3.3.3 (c) is a slightly under-damped system. Examination of equation (3.3.24a) shows that the real component of the complex conjugate roots of the characteristic equation, τ , determines the amplitude while β , the imaginary component of the roots, controls the frequency. Because β is small relative to τ , the period of the oscillation is greater than Δx and the sinusoidal influence is not observable. As the value of the boundary conditions are increased, the concentration profile extends well beyond $[C(x=0), C(x=\Delta x)]$ and unrealistic values of the upwind parameter will be predicted. In Figure 3.3.3 (d), the frequency of the oscillations has increased due to the increased imaginary component of the complex conjugate roots. The sinusoidal component of the mass balance equation solution dominates and an unrealistic sinusoidal concentration profile is observed. The amplitude of the oscillations increases as the concentration profile is raised.

Results presented in the preceding discussion show that even slight charge density arising in the numerical solution algorithm is detrimental to the fidelity of the predicted upwind parameter. This feature makes electrolyte mass transport unique from other forms of transport and adds an additional concern when developing codes for its

prediction. A method has been developed by Heppner et al. [16, 17] to eradicate charge density in an electrolyte solution.

3.3.2 Discrete transport model development

Transport of ions and neutral species in a moderately dilute electrolyte solution under the influence of an electrochemical potential gradient can be described by:

$$\begin{aligned} \frac{\partial C_i}{\partial t} = & -z_i u_i F \left[\frac{\nabla C_i \cdot (\mathbf{i} + \mathbf{i}_{dp})}{\kappa} + C_i \frac{\delta}{\varepsilon} \right] + \\ & D_i (\nabla^2 C_i + \nabla C_i \nabla \ln \gamma_i + C_i \nabla^2 \ln \gamma_i) + G_i \end{aligned} \quad (3.3.25)$$

Where the current density induced by diffusion potential is:

$$\mathbf{i}_{dp} = F \sum_{j=1}^k z_j D_j (\nabla C_j + C_j \nabla \ln \gamma_j) \quad (3.3.26)$$

and the local net charge of the solution is given by equation (3.3.13b). Discretization using central finite difference approximations to first and second order derivatives respectively transforms (3.3.25) and (3.3.26) to a second order accurate analog form:

$$\begin{aligned} \frac{C_{iP} - C_{iP}^0}{\Delta t} = & -z_i u_i F \left[\frac{C_{ie} - C_{iw}}{\Delta x} \frac{i_P + i_{dpP}}{\kappa_P} + C_{iP} \frac{\delta_P}{\varepsilon} \right] + \\ & D_i \left(\frac{C_{iE} + C_{iW} - 2C_{iP}}{\Delta x^2} + \frac{(C_{ie} - C_{iw})(\ln \gamma_{iE} - \ln \gamma_{iW})}{2\Delta x^2} \right. \\ & \left. + C_{iP} \frac{\ln \gamma_{iE} + \ln \gamma_{iW} - 2\ln \gamma_{iP}}{\Delta x^2} \right) + G_{iP} \end{aligned} \quad (3.3.27)$$

where the diffusion potential current density at the point node is:

$$i_{dpP} = F \sum_{j=1}^k z_j D_j \left(\frac{C_{je} - C_{jw}}{\Delta x} + C_{jP} \frac{\ln \gamma_{je} - \ln \gamma_{jw}}{\Delta x} \right) \quad (3.3.28)$$

The P , E , and W nodes in this fully implicit discrete transport equation are the point, east and west nodes respectively. Subscripts e and w denote the east and west control volume interfaces, respectively, located halfway between the surrounding nodes for a uniform grid.

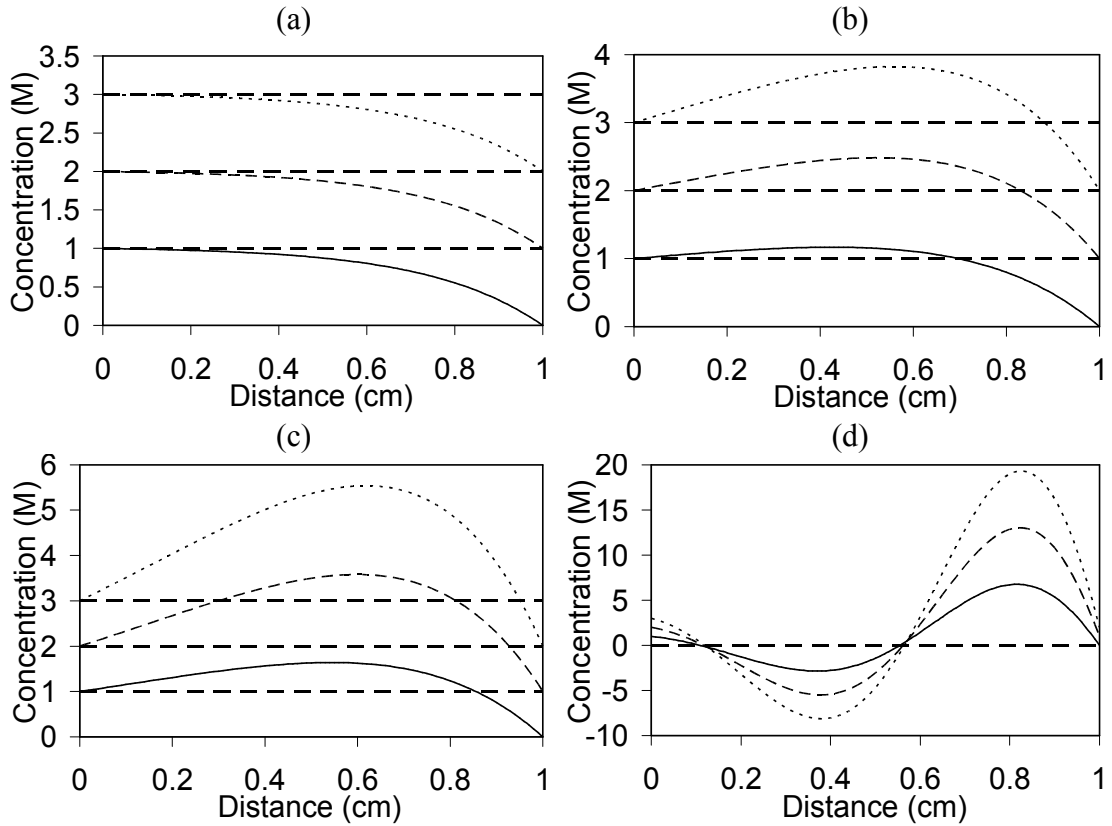


Figure 3.3.3. Solution of the electromigration-diffusion balance equation across a computational control volume as the concentration profile is shifted upwards: a) $\delta = 0$ C/m^3 ; b) $\delta = 5 \times 10^{-9}$; c) $\delta = 1 \times 10^{-8}$ C/m^3 ; d) $\delta = 1 \times 10^{-7}$ C/m^3 . Critical damping occurs when $\delta \approx 7.7 \times 10^{-9}$ C/m^3 .

The expression of interfacial properties - C_{ie} , C_{iw} , $\ln \gamma_{ie}$, and $\ln \gamma_{iw}$ - as functions of nodal values is accomplished using the upwind parameter formulation, i.e.:

$$C_{ie} = \frac{1+\alpha}{2} C_{iP} + \frac{1-\alpha}{2} C_{iE} \quad (3.3.29)$$

Substitutions analogous to equation (3.3.29) are made for each interfacial property appearing in equation (3.3.27) to yield the following discrete mass transport equation:

$$\frac{C_{iP} - C_{iP}^0}{\Delta t} = -z_i u_i F \left[\frac{\frac{1+\alpha}{2} C_{iP} + \frac{1-\alpha}{2} C_{iE} - \frac{1+\alpha}{2} C_{iW} - \frac{1-\alpha}{2} C_{iP}}{\Delta x} \frac{i_P + i_{dPP}}{\kappa_P} \right] + C_{iP} \frac{\delta_P}{\varepsilon} \quad (3.3.30)$$

$$D_i \left(\frac{C_{iE} + C_{iW} - 2C_{iP}}{\Delta x^2} + \frac{(C_{ie} - C_{iw})(\ln \gamma_{iE} - \ln \gamma_{iW})}{2\Delta x^2} \right) + G_{iP}$$

$$+ C_{iP} \frac{\ln \gamma_{iE} + \ln \gamma_{iW} - 2\ln \gamma_{iP}}{\Delta x^2}$$

By sequestering time-step lagged non-linear terms into transport coefficients, equation (3.3.30) can be rearranged into a linear algebraic discrete transport equation which is solved iteratively:

$$a_P C_{iP} = a_E C_{iE} + a_W C_{iW} + a_P^0 C_{iP}^0 + G_i \Delta x \quad (3.3.31)$$

Using the proposed hybrid differencing scheme to express the interfacial concentrations,

C_{ie} and C_{iw} , as nodal values, the discrete transport coefficients are:

$$a_E = \frac{D_i}{\Delta x} \left[1 + \frac{P_P'}{2} + \left| \frac{P_P' \alpha}{2} \right| \right] \quad (3.3.32)$$

$$a_W = \frac{D_i}{\Delta x} \left[1 - \frac{P_P'}{2} + \left| \frac{P_P' \alpha}{2} \right| \right] \quad (3.3.33)$$

$$a_P^0 = \frac{\Delta x}{\Delta t} \quad (3.3.34)$$

$$a_p = a_E + a_W + a_p^0 + z_i u_i F \frac{\delta_p}{\varepsilon} \Delta x - D_i \frac{\ln \gamma_{iE} + \ln \gamma_{iW} - 2 \ln \gamma_{iP}}{\Delta x} \quad (3.3.35)$$

Where the local Peclet number, P_p' , is defined in equation (3.3.19b). The diffusion potential current density, equation (3.3.28), is also recast in terms of nodal values using the upwind formulation. After rearrangement, the following expression results:

$$i_{dp} = F \sum_{j=1}^k z_j D_j \left(\begin{array}{l} \frac{2\alpha C_{jP} + C_{jE} - C_{jW} - \alpha(C_{jE} + C_{jW})}{2\Delta x} \\ + C_{jP} \frac{2\alpha \ln \gamma_{jP} + \ln \gamma_{jE} - \ln \gamma_{jW} - \alpha(\ln \gamma_{jE} + \ln \gamma_{jW})}{2\Delta x} \end{array} \right) \quad (3.3.36)$$

Patankar [19] stated that to ensure a physically realistic solution, the point coefficient should be the sum of the east, west, and previous iteration point coefficient and each coefficient should be positive. This mass transport model follows Patankar's suggestion but also contains non-linear influence from a net solution charge imbalance, δ_p , and the second order derivative of the activity coefficient. The point coefficient is extremely sensitive to this charge imbalance which can possess a positive or negative value. A negative δ_p will reduce the diagonal dominance of the solution matrix. Furthermore, it is shown in Figure 3.3.2 that a charge imbalance will cause the hybrid differencing scheme to give unrealistic upwind parameters. The second order activity coefficient gradient will also have an effect on the convergence of the mass transport problem. If the second order gradient of the activity coefficient is positive in sign, it will increase the diagonal dominance and the speed of convergence of the system. Conversely, a positive second order gradient of the activity coefficient will decrease the diagonal dominance. A diagonally dominant linear system satisfies the Scarborough Criterion and is guaranteed to converge by the Gauss – Seidel method. The Scarborough Criterion is [20]:

$$\frac{|a_E| + |a_W|}{|a_P|} \begin{cases} \leq 1 & \text{(for all grid points)} \\ < 1 & \text{(for one grid point)} \end{cases} \quad (3.3.37)$$

The diagonal dominance of the coefficient matrix is largely controlled by a_p^0 - decreasing the time step increases a_p^0 and the point coefficient, a_p . However, if the charge density and/or the second order activity gradient are significant, extremely small time steps may be required to negate these influences and ensure satisfaction of (3.3.37) [16, 17]. The charge density term in the a_p coefficient formulation is extremely sensitive to charge density. Therefore, to ensure the diagonal dominance of the matrix, Heppner et al. recommended the removal of the electroneutrality deviation term from the a_p coefficient through an operator splitting strategy [16, 17]. After removal of the charge density term, the Scarborough Criterion for the variable upwind differencing scheme can be shown to be:

$$\frac{|a_E| + |a_W|}{|a_P|} = \frac{1}{1 + \frac{1}{2 + P_p' \alpha} \left(\frac{\Delta x^2}{D_i \Delta t} - \ln \gamma_{iE} - \ln \gamma_{iW} + 2 \ln \gamma_{iP} \right)} \quad (3.3.38)$$

Equation (3.3.38) is bounded between 0 and 1 when:

$$0 \leq \frac{1}{2 + P_p' \alpha} \left(\frac{\Delta x^2}{D_i \Delta t} - \ln \gamma_{iE} - \ln \gamma_{iW} + 2 \ln \gamma_{iP} \right) \leq \infty \quad (3.3.39a)$$

or when:

$$-\infty \leq \frac{1}{2 + P_p' \alpha} \left(\frac{\Delta x^2}{D_i \Delta t} - \ln \gamma_{iE} - \ln \gamma_{iW} + 2 \ln \gamma_{iP} \right) \leq -2 \quad (3.3.39b)$$

Therefore, the Scarborough criterion is not bounded between 0 and 1 when:

$$-2 < \frac{1}{2 + P_p' \alpha} \left(\frac{\Delta x^2}{D_i \Delta t} - \ln \gamma_{iE} - \ln \gamma_{iW} + 2 \ln \gamma_{iP} \right) < 0 \quad (3.3.39c)$$

Condition (3.3.39a) would be guaranteed if $(x_E, \ln \gamma_{iE})$, $(x_W, \ln \gamma_{iW})$, and $(x_P, \ln \gamma_{iP})$ were points on a linear function. However, if $\ln \gamma_i$ possesses a non-zero second order gradient over the range $[x_W, x_E]$, condition (3.3.39a) may not be satisfied. The second order gradient of the activity coefficient is capable of inducing instability through reduction of diagonal dominance in the mass transport calculation procedure. To ensure that the Scarborough Criterion is satisfied, the time step should be lowered where the second order gradient of the activity coefficient is significant and positive in sign. If condition (3.3.39a) or (3.3.39b) is met, and if Dirichlet conditions exist at any physical domain boundary, the discrete mass transport problem satisfies the Scarborough Criterion. Figure 3.3.4 plots the east transport coefficient divided by $D_i/\Delta x$ against the Peclet number. The west coefficient is the mirror image of the east coefficient reflected across the y-axis. By Figure 3.3.4, it is shown that the east and west transport coefficients will never acquire a negative value.

3.3.3 Modelling of the Fu and Chan moving boundary experiment

Fu and Chan placed a silver anode plug at one end of a long glass tube. The tube opened into a large beaker in which a silver cathode was immersed. Initially, the entire apparatus was filled with a 0.1 M KNO_3 solution. A current density of $318 \mu\text{A}/\text{cm}^2$ was applied across the tube length inducing silver dissolution at the anode plug and silver plating at the cathode. The electrical current forced Ag^+ and K^+ ions out of the tube towards the cathode while NO_3^- ions were driven towards the silver anode plug. A visible moving boundary was formed where the aqueous solution transitioned from being predominantly KNO_3 to being predominantly AgNO_3 . The rate of movement of this boundary indicated the rate of mass transport in the tube.

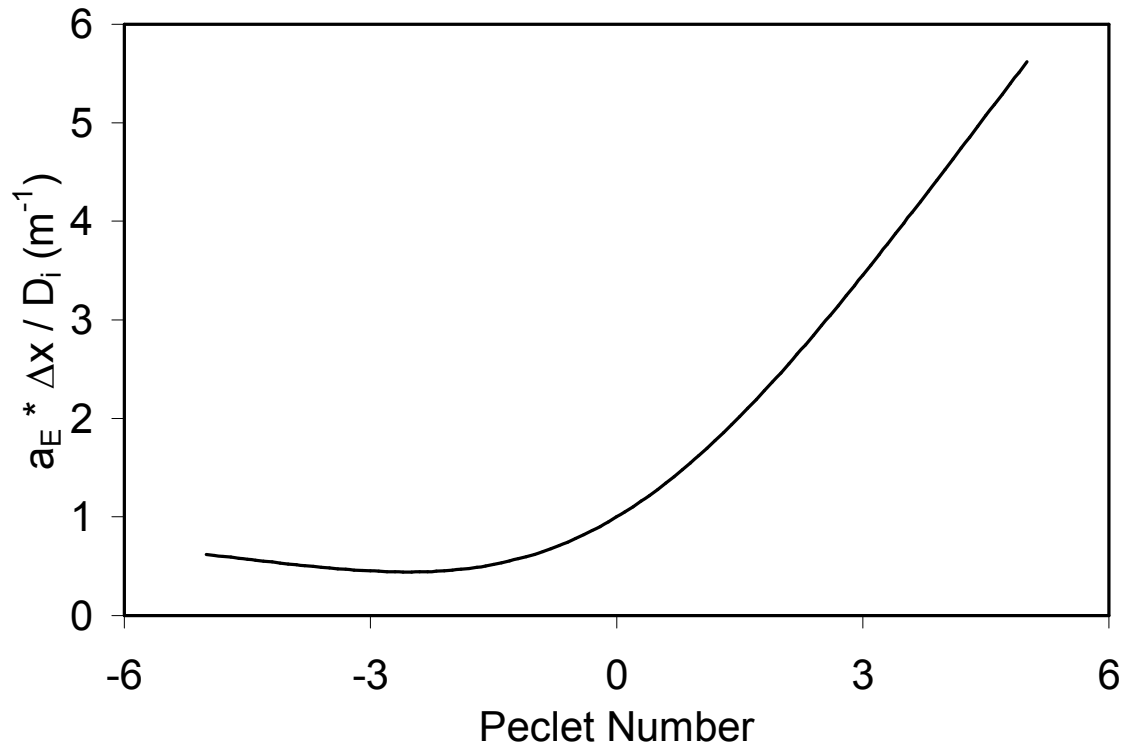


Figure 3.3.4. The variation of $a_E \Delta x / D_i$ with the Peclet number.

Fu and Chan accurately recorded the position of the moving boundary. Using data obtained from the moving boundary experiment performed by Fu and Chan [1], the ability of this hybrid differencing scheme to improve the physical realism of solutions of the electrolyte mass transport equation is showcased.

Using the present transport model, the boundary region predicted using UDS and HDS is compared. For both differencing schemes, the solution domain was discretized into 1000 nodes ($\Delta x = 5 \times 10^{-3} \text{ cm}$) and a time step of 0.1 seconds was used. The solution algorithm is illustrated as a flow chart in Figure 3.3.5.

Figure 3.3.6 displays the predicted moving boundary region after 5, 20, 30, and 40 minutes using both UDS and HDS. The vertical line in each figure represents the position of the boundary at the respective time (interpolated from raw data) observed experimentally by Fu and Chan. At each time, discretizing the mass transport model using HDS, rather than UDS, results in the formation of steeper concentration gradients, and thus faster mass transport rates, throughout the moving boundary region. The fact that using HDS predicts increased mass transfer rates is evidenced by both the faster movement of the predicted Ag^+/K^+ concentration profile intersection, and by a lower AgNO_3 concentration at the anode-solution interface (not seen in figure). Comparison of Figures 3.3.6 (a) and 3.3.6 (b) shows that sometime between 5 and 20 minutes after the start of the simulation, the moving boundary predicted using HDS passes the moving boundary predicted using UDS. In each case, the mass transport model discretized using HDS either matches or improves on the accuracy of the same transport model discretized using UDS. The average error between the predicted boundary position and that measured experimentally has decreased by 61% by using HDS rather than UDS.

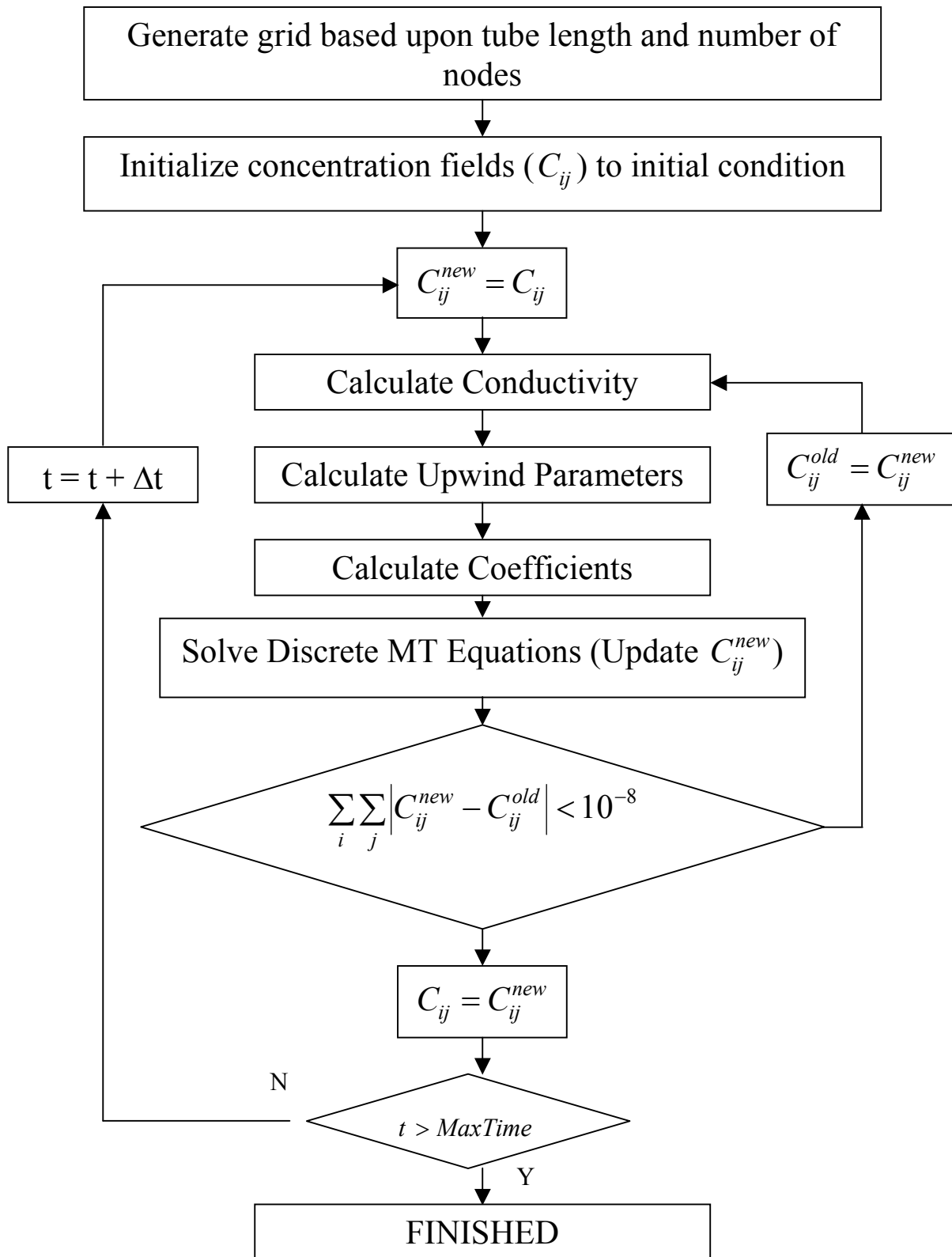


Figure 3.3.5. The mass transport model solution algorithm presented as a flow sheet.

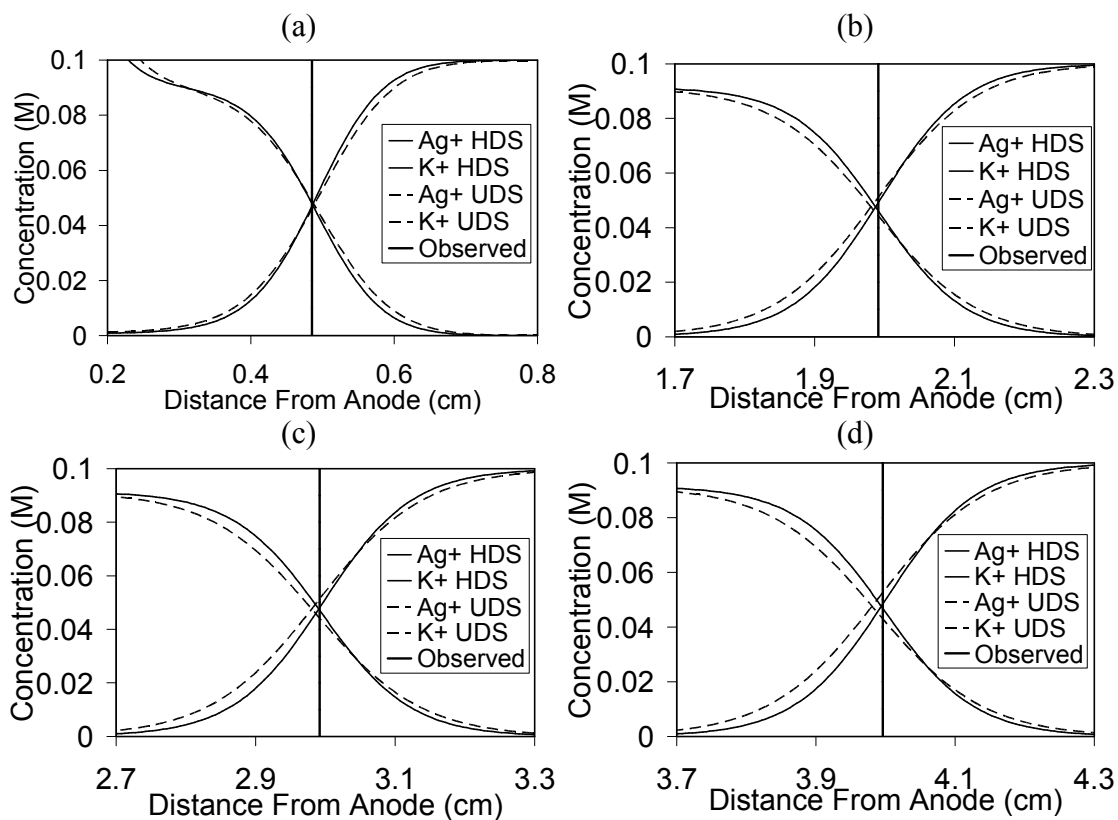


Figure 3.3.6. The calculated moving boundary region of the Fu and Chan experimental apparatus: a) after 5 minutes; b) after 20 minutes; c) after 30 minutes; d) after 40 minutes. In each sub-figure, the vertical line represents the experimentally observed position of the boundary (boundary position was linearly interpolated from raw data).

The greatest increase in accuracy is seen in Figure 3.3.6(d) where the error decreased by 87%. Using the new differencing scheme enables the discrete mass transport model to more accurately predict the experimental observations of Fu and Chan.

3.3.3.1 Effect of charge density

The previous section showed the ability of the discrete mass transport model coupled with the HDS upwind parameter solver to accurately predict mass transport in an electrolytic system. Inherent to HDS is the assumption of electroneutrality throughout the system. Although a physical system will not possess an appreciable charge density unless a substantial amount of work is done on the system, numerical charge density arising through solution of the constitutive mass conservation equations can cause oscillations in the solution of the electromigration-diffusion balance equation. Obviously, predicted concentration profiles that are sinusoidal and feature negative values are not physically realistic. Therefore, one cannot expect to obtain a physically meaningful value of the upwind parameter from such a profile. The sensitivity of the numerical solution to accumulated charge density in the solution is now tested. Figure 3.3.7 shows the predicted moving boundary region as the amount of charge density in the solution is increased. Increased charge density had a large effect on the stability of the numerical algorithm. As the charge density was increased, the mass transport equation became more difficult to solve. When the charge density was set to 10^{-9} C/m³ or greater, the solution to the migration-diffusion equation became under-damped and the simulation ultimately failed to converge. When the charge density reached a value such that it caused under-damping of the predicted concentration profile, the simulation immediately

failed. However, until the profile became critically damped, the simulation was able to proceed but provided results with significant amounts of error.

3.3.3.2 Effect of spatial step size

As the spatial step size is decreased, the predicted concentration profiles approach the exact solution to the constitutive equations. However, decreasing the step size also affects the predicted Peclet number and, thus, the upwind parameter. Figure 3.3.8 illustrates the effect of increasing the spatial step size. As Δx was increased, the predicted upwind profile approached unity (UDS) while at very small values of Δx , the upwind parameter approached zero (CDS). As Δx decreases, the profile in the control volume approaches the linear profile predicted by differential calculus (the tangent line) and a central differencing scheme becomes appropriate. Figure 3.3.8 was generated using the mathematical model describing Fu and Chan's moving boundary experiment.

Besides having a direct impact on the value of the upwind parameter, the step size showed significant influence on the predicted concentration profile in the moving boundary region. Figure 3.3.9 illustrates the variation of the predicted moving boundary Ag^+/K^+ concentration profile after 10 minutes as the number of computational nodes used in the numerical solution is increased. The predicted concentration gradients of both K^+ and Ag^+ were predicted steeper as the number of computational nodes increased. However, the velocity of the moving boundary also decreased with increasing computational nodes. Where an inadequate number of nodes were used, a less steep concentration gradient and an increased rate of mass transport was predicted – a phenomenon that defies physical transport laws.

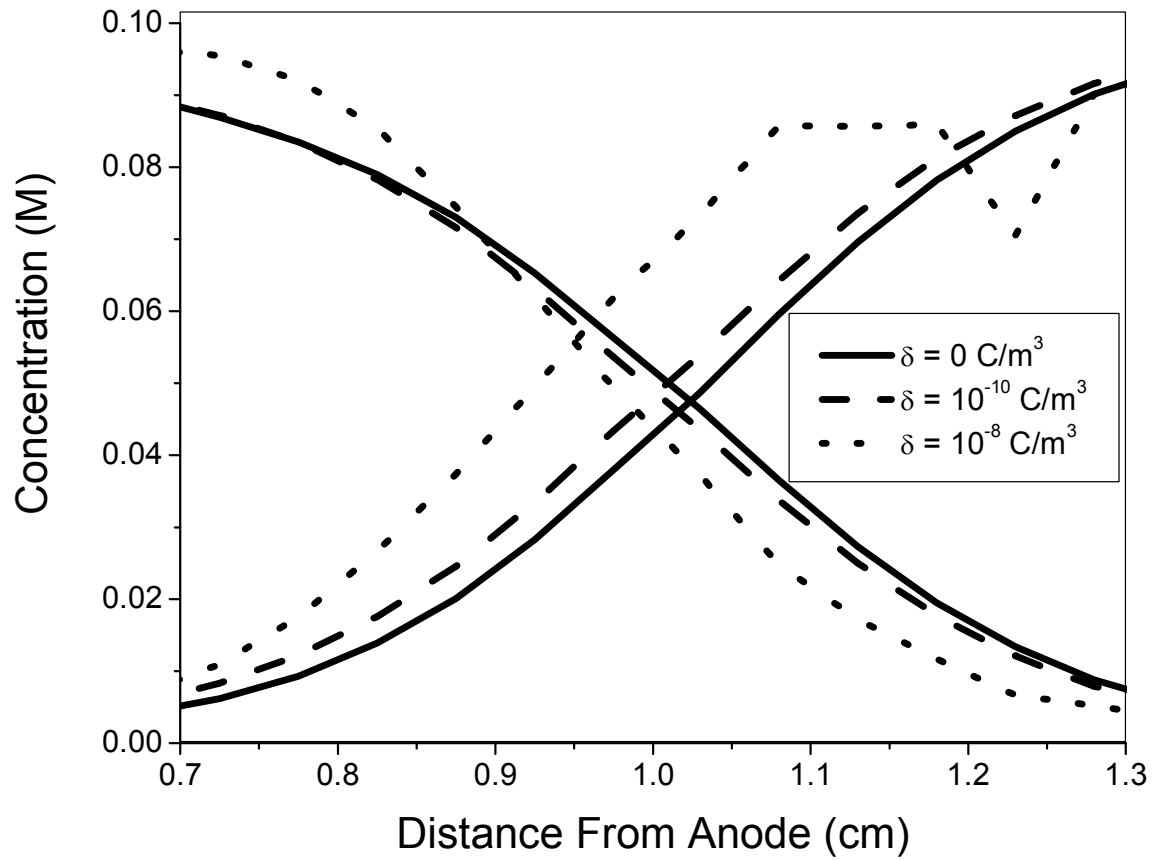


Figure 3.3.7. The effect of charge density on the predicted moving boundary region of the Fu and Chan experiment.

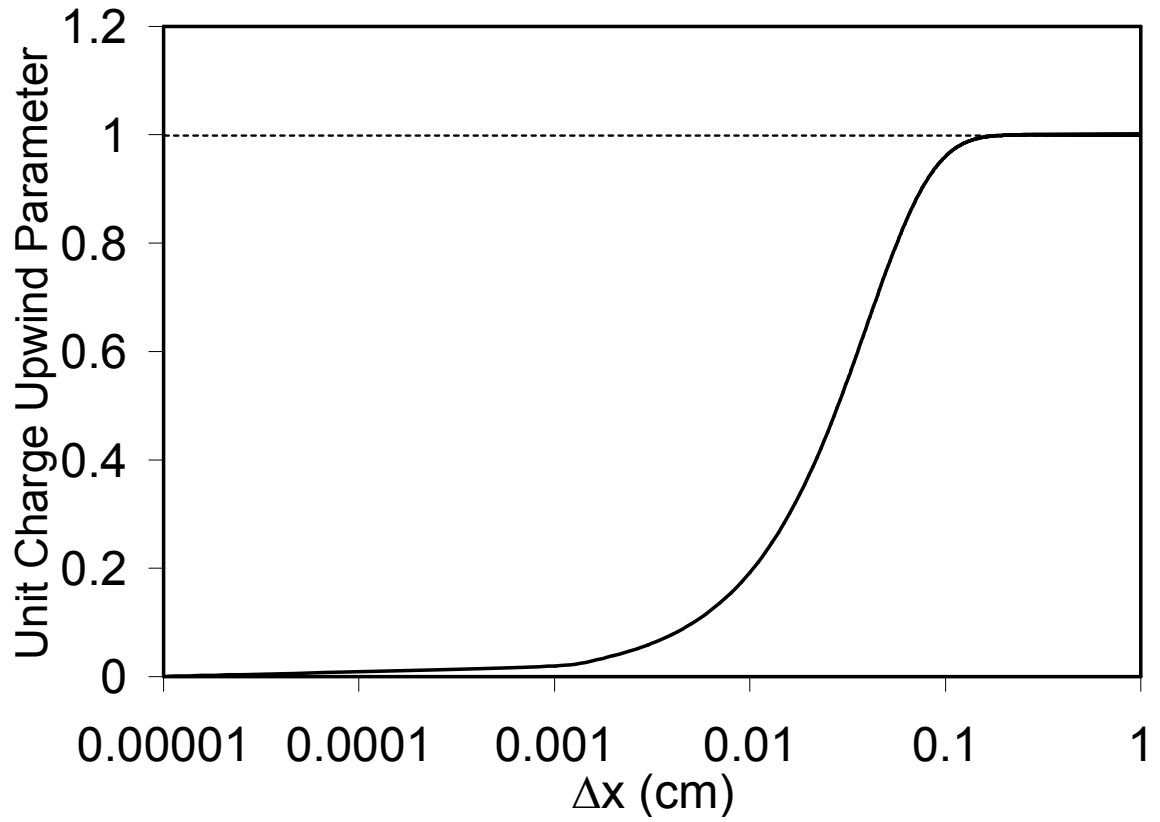


Figure 3.3.8. The calculated unit charge upwind parameter as a function of space step size, Δx , for the model of the Fu and Chan experiment.

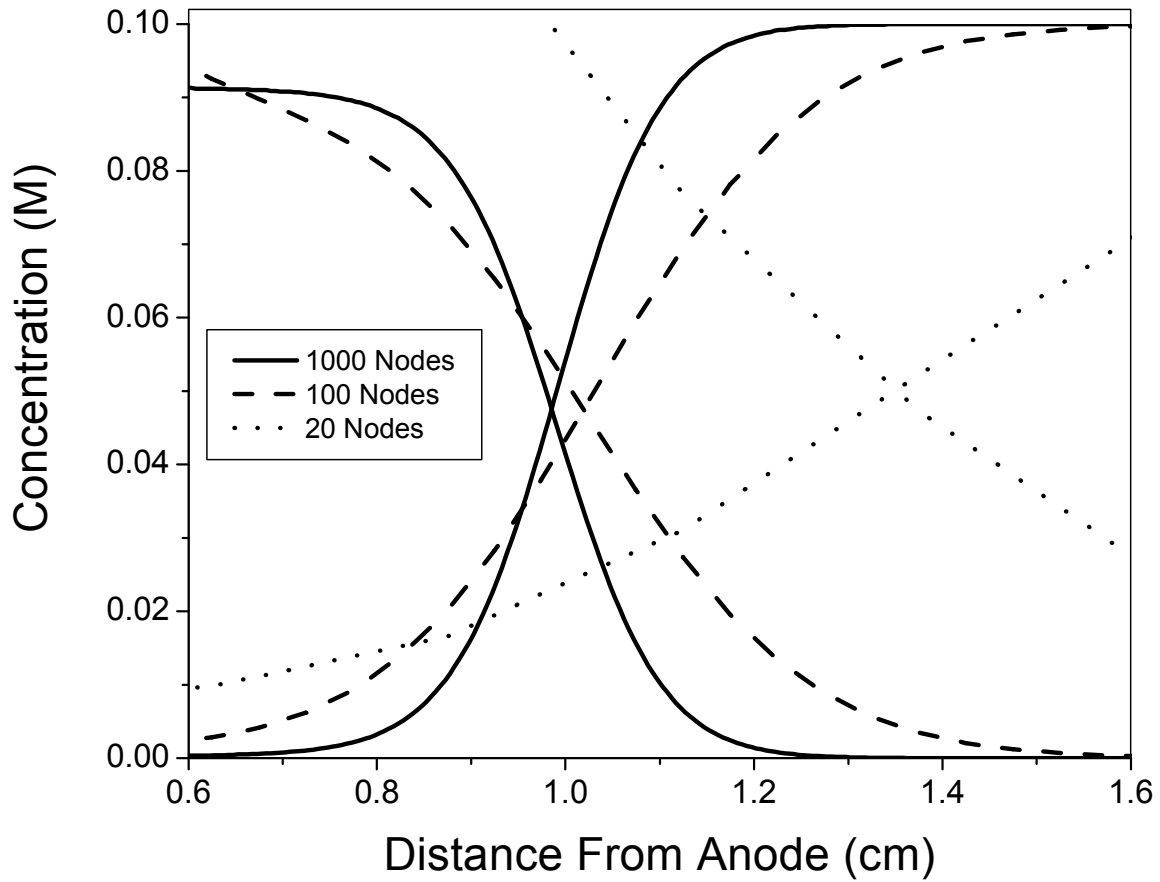


Figure 3.3.9. The effect of step size on the predicted boundary region of the Fu and Chan experiment after 10 minutes.

By inspection of the electromigration term of equation (3.3.25), the rate of mass transport due to electromigration is proportional to the concentration gradient. Therefore, the predicted profile becomes physically unrealistic as the number of nodes decrease. Furthermore, the predicted boundary position moves further away from the experimentally observed boundary position (1 cm after 10 minutes) [1].

3.3.3.3 Computational efficiency

The additional computational effort or simulation time required when using HDS rather than UDS was investigated. At each iteration, the use of HDS requires the computation of the Peclet number and the evaluation of the upwind parameter. The upwind parameter calculation is particularly expensive as it requires the computation of numerous exponential functions, each of which are computed as truncated Maclaurin series expansions. Because the additional time required to obtain a converged solution when using HDS is dependent upon both the specific mass transport problem being solved and the specifications of the computer, the computational efficiency of using HDS was investigated using the percentage increase in time, rather than the actual increase in time. The following results are therefore specific to modelling the Fu and Chan experiment but are independent of the processor speed of the computer being used. The ratio of the total number of operations that the computer is required to perform when solving the transient mass transport problem using HDS, rather than UDS, can be calculated from the following expression:

$$\text{Operations Ratio} = \frac{(\text{HDS Operations per iteration})(\text{HDS Iterations})}{(\text{UDS Operations per iteration})(\text{UDS Iterations})} \quad (3.3.40)$$

The operations ratio is a measure of the increased computational effort required to use HDS rather than UDS.

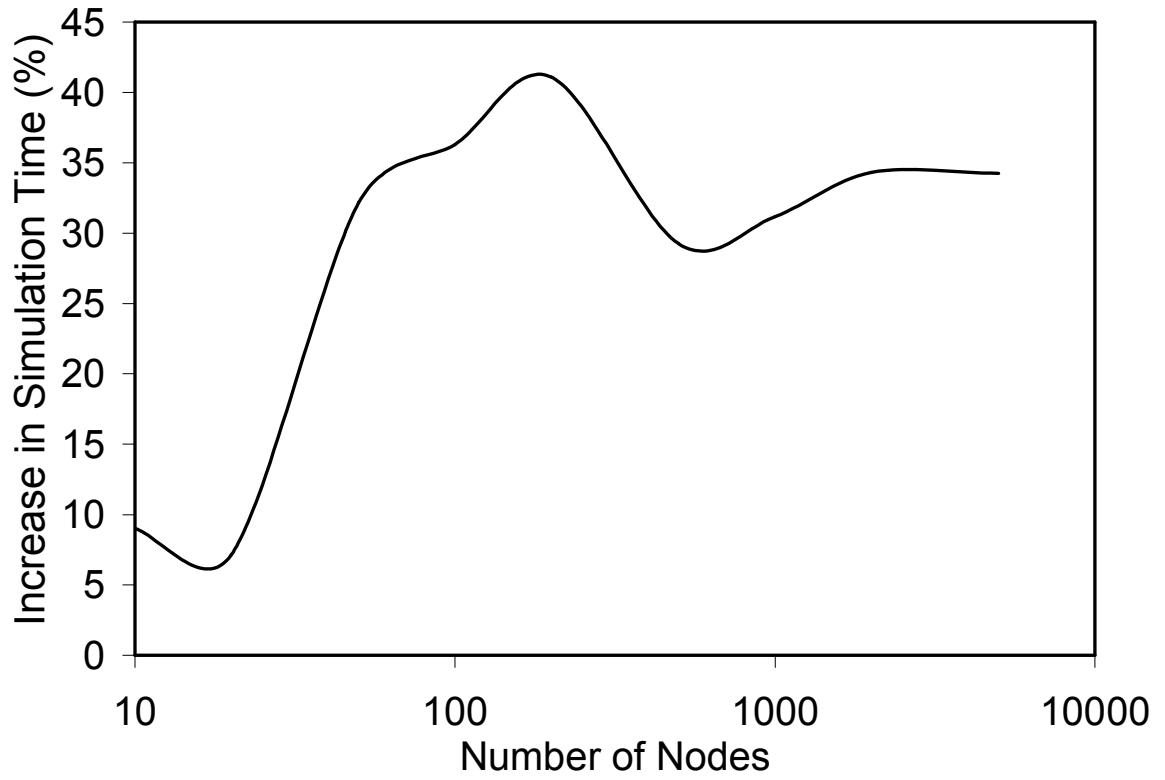


Figure 3.3.10. The percentage increase in simulation time required when using the hybrid differencing scheme rather than the upwind differencing scheme as a function of the number of nodes used in the numerical solution.

Because the operations required per iteration are fixed for a particular grid, variation in the value of the operations ratio is due solely to changes in the ratio of the number of iterations required to use HDS to the number of iterations required to use UDS. Figure 3.3.10 shows the percentage change in simulation time resulting when HDS, rather than UDS, is used in the mass transport solver as the number of nodes is increased.

The ease of convergence of the model can be estimated by the diagonal dominance of the transport coefficient matrix. Examining the relevant terms from equation (3.3.38), the following relationship may be written:

$$\frac{|a_p|}{|a_E| + |a_W|} \propto \frac{\Delta x^2}{P_p' \alpha} \quad (3.3.41)$$

Equation (3.3.41) seems to imply that the diagonal dominance will increase for a coarser solution grid (Δx becomes larger). However, both α and P_p' are proportional to Δx creating a competing effect of Δx upon the diagonal dominance. This competition is manifested as the peculiar functionality of the computational efficiency upon the number of nodes seen in Figure 3.3.10. In general, the results of Figure 3.3.10 demonstrate that, as the number of nodes increase, the transport coefficient matrix becomes less diagonally dominant and the additional effort required using HDS rather than UDS increases (i.e. the computational efficiency of the model decreases).

3.3.4 Conclusions

Based upon a pseudo-steady state balance between electromigration and diffusion, a novel method to interpolate interfacial properties from nodal values for electrolyte mass transport under the influence of an electrical potential field has been developed. Simulation of the moving boundary experiment of Fu and Chan [1] provided a means of

quantifying the influence of the upwind parameter on the predictions of the electrolyte mass transport model. The following conclusions can be made from this research:

1. Use of HDS rather than UDS results in predictions that more closely match the experimental observations of Fu and Chan. The error between model predictions and experimental data is reduced by an average of 61% when HDS rather than UDS is used. Therefore, using the one-dimensional solution of the electromigration-diffusion balance equation as a means to prescribe appropriate weighting for approximation of interfacial properties is valid for electrolyte mass transport modelling.
2. Adjustment of the time step in regions where the second order gradient of the activity coefficient is significant and positive in sign will ensure that the mass transport problem coupled with HDS satisfies the Scarborough criterion, a condition that checks diagonal dominance. Thus, convergence of the matrix of transport coefficients, assembled at each iteration, by the Gauss-Seidel method is guaranteed. Transport coefficients are guaranteed to be positive thus ensuring a physically realistic solution [19].
3. The presence of electrical charge density has a detrimental effect on the stability of the mass transport solution algorithm. As charge density increases, the solution to the steady state electromigration-diffusion equation approaches critical damping. Physically unrealistic oscillations develop in the predicted concentration profile thus altering the predicted upwind parameter. Charge density may also reduce the diagonal dominance of the coefficient matrix during the solution of the mass transport model and reduce the speed of convergence.

Thus, charge density must be annihilated through direct solution of the Poisson equation for charge density or through the method proposed by Heppner et al. [16, 17].

4. When the charge density and the second order gradient of the activity coefficient is negligible, the hybrid differencing scheme for electrolyte mass transport possesses the form similar to the exponential differencing formula used in computational fluid dynamics [7, 8]. Therefore, electromigration in a stagnant, electrically neutral, infinitely dilute electrolyte under the influence of a potential gradient is analogous to convection under the influence of a pressure gradient and the use of a Peclet number based method to estimate interfacial properties is appropriate for electrolyte mass transport.
5. The Peclet number for mass transport in a non-ideal solution is affected not only by the potential gradient but also by the activity coefficient gradient. The effect of the activity coefficient gradient is a manifestation of the force exerted upon an ion to move towards regions of decreasing ionic strength. The additional term in the Peclet number formulation accounts for interactions between the ion of interest and other ions in solution.
6. The computational efficiency of the mass transport model coupled with HDS is highly dependent upon the spatial step size. Thus, the percentage increase in simulation time varied between 6% and 43% (based on step size). However, the error between the simulation results and the observations of the Fu and Chan experiment increased by as much as 87% by using HDS rather than UDS.

7. This differencing scheme represents the first scheme developed specifically for the solution of the electromigration-diffusion equation. Previous schemes, such as the exponential scheme, power law scheme, and other schemes, have been developed for the convection-diffusion equation (refer to Patankar [19] for a concise summary of these differencing schemes). The electromigration-diffusion equation is unique and different from the convection-diffusion equation in that its solution, if physically realistic, must satisfy the condition of charge neutrality (or very low charge density). Thus, mass transport of each ion in solution is mathematically very strongly inter-coupled with mass transport of all other ions. This unique feature is represented in the differencing scheme by the activity coefficient term in the modified Peclet number formula (equation 19b) and by the effect of charge density upon the upwind parameter.

3.3.5 References

1. Fu, J.W., Chan, S. (1984), Corrosion, vol. 40, pp. 540 - 544.
2. Courant, R., Isaacson, E., Rees, M. (1952), Comm. Pure Appl. Math., vol. 5, p. 243.
3. Barakat, H.Z., Clark, J.A. (1966), "Analytical and Experimental Study of Transient Laminar Natural Convection Flows in Partially Filled Containers", *Proceedings of 3rd Int. Heat Transfer Conference II*, Chicago IL, paper 57 p. 152.
4. Gentry, R.A., Martin, R.E., Daly, B.J. (1966), J. Comp. Phys., vol. 1, p. 87.
5. Runchal A.K., Wolfshtein, M. (1969), J. Mech. Eng. Sci., vol. 11, p. 445.
6. Patankar, S.V., Spalding, D.B. (1970), "Heat and Mass Transfer in Boundary Layers", 2nd Ed., Intertext, London.
7. Spalding, D.B. (1972), Int. J. Num. Methods Eng., vol. 4, p. 551.
8. Raithby, G.D., Torrence, K.E. (1974), Comput. Fluids, vol. 2, p. 191.
9. Newman, J. (1973), "Electrochemical Systems", Prentice Hall, Toronto, ON.

10. Walton, J.C., Cragnolino, G., Kalandros, S. K. (1996), *Corrosion Science*, vol. 38, pp. 1 – 18.
11. R. W. Evitts, “Modeling of Crevice Corrosion”, Ph.D. thesis, University of Saskatchewan, Saskatoon, Saskatchewan, Canada (1997).
12. M.K. Watson, “Numerical Simulation of Crevice Corrosion”, Ph.D. Dissertation, University of Saskatchewan, Saskatoon SK (1989).
13. Watson, M. K. , Postlethwaite, J. (1990a), *Corrosion*, vol. 46, pp. 522 – 530.
14. Watson, M. K., Postlethwaite, J. (1990b), “Numerical Simulation of Crevice Corrosion”, *Proceedings of Corrosion/90*, Las Vegas, NV, April 23-27, 1990, NACE International, Houston, TX, pp. 156:1 – 156:19.
15. Watson, M. K., Postlethwaite, J. (1991), *Corrosion Science*, vol. 32, pp. 1253 – 1262.
16. Heppner, K.L., Evitts, R.W., Postlethwaite, J. (2002), *Canadian Journal of Chemical Engineering*, vol. 80, pp. 849 – 856.
17. Heppner, K.L., Evitts, R.W. (2004), *Dynamics of Continuous, Discrete, and Impulsive Systems – B*, vol. 11, no. 1-2, p. 29 – 46.

18. Raithby, G.D., Schneider, G.E. (1980), Journal of Heat Transfer, vol. 102, p. 138 – 45.
19. Patankar, S.V. (1980), “Numerical Heat Transfer and Fluid Flow”, Hemisphere.
20. Scarborough, J.B. (1958), “Numerical Mathematical Analysis”, 4th Ed., Johns Hopkins Press, Baltimore MD.

Chapter 4. Crevice Corrosion Initiation of Passive Metals

The previous chapter discussed two methods designed to improve the accuracy and computational efficiency of the numerical integration of the electromigration-diffusion equation. An accurate and computationally efficient model of electrolytic mass transport is important in the simulation of crevice corrosion initiation of passive metals. In this section, the numerical methodologies previously discussed are applied to a prevalent and destructive form of corrosion – crevice corrosion.

Crevice corrosion is a localized acid-chloride attack. It occurs in occluded regions of the metal surface such as under deposits, at the meeting of metal surfaces, in imperfect welds, beneath gaskets and washers, and in corrosion and/or stress induced pits and cracks. This feature of crevice corrosion makes it particularly dangerous as it can go undetected until failure. This form of corrosion affects passive metals, which are generally corrosion resistant and form a thin tenacious oxide film of low electrical or ionic conductivity. This film is referred to as the passive film. Due to the low conductivity, only a small leakage current, which is called the passive current, can pass through the film. Thus, when the film is present, the metal dissolves at an extremely slow rate. However, in a sufficiently strong acid-chloride solution, which is often called a critical crevice solution, this protective film may be damaged. Due to differential

aeration, such acid-chloride solutions may develop autocatalytically inside a crevice, which may then initiate active crevice corrosion.

In this work, moderately dilute and infinitely dilute mass transport models were applied to electrolyte solution at temperatures of 25°C and 70°C inside a passive metal crevice. The model was used to predict how the crevice gap, solution composition, and internal hydrogen ion reduction affected conditions inside the crevice. Finally, the moderately dilute model was applied to rank alloys for corrosive duty. Each of these studies will now be explained in detail.

4.1 Effect of the Crevice Gap on Crevice Corrosion Initiation*

Crevice corrosion occurs when the protective, tenacious oxide film known as the passive film is destroyed by acid chloride attack. As the crevice gap decreases in size, a smaller cross sectional area causes increased current density flowing in the crevice solution; the rate of transport via electromigration of anions, such as the chloride ion, into the anodic crevice increases. The length of the incubation period, the time required to develop a critical crevice solution, is strongly dependent upon the crevice gap.

This work focuses upon modeling crevice corrosion initiation of two different metals, type 304 stainless steel (UNS S30400) and pure titanium, immersed in aqueous NaCl solution. The effect of the crevice gap on the solution conductivity, iR drop, and charge density in the titanium crevice solution is investigated in detail. Models of similar purpose have been constructed by several authors – Oldfield and Sutton [1], Bernhardsson et al. [2, 3], Fu and Chan [4], Alkire and Siitari [5], Hebert and Alkire [6], Turnbull and Ferris [7], Sharland [8, 9], Watson [10], Watson and Postlethwaite [11, 12], Evitts et al. [13 – 16], Evitts [17], Postlethwaite et al. [18], Walton et al. [19], Oldfield et al. [20], Heppner et al. [21, 22], and others. The present work uses the mass transport model of Watson and Postlethwaite [11, 12] but improves the solution through adjustment of chemical equilibrium for non-ideality and through incorporating the effect of solution charge density on ionic migration. This work assumes that two cathodic reactions, oxygen reduction outside the crevice and hydrogen reduction inside the crevice, support

* Reference: K.L. Heppner, R.W. Evitts, and J. Postlethwaite (2004) The Effect of the Crevice Gap on the Initiation of Crevice Corrosion in Passive Metals. *Corrosion* **80**. pp. 718 – 728.

anodic metal dissolution. It is known that titanium dissolution is substantially supported by hydrogen evolution while type 304 stainless steel dissolution is largely supported by external oxygen reduction [23 – 25]. An empirically based fraction, based upon the work of He et al. [25], distributes the total cathodic load between the two electrode reactions for the titanium crevice model.

4.1.1 Mathematical model

4.1.1.1 Mass transport

Electrolyte transport in a geometrically restrictive, non-convective crevice solution is represented by the following conservation statement proposed by Watson and Postlethwaite [11, 12]:

$$\begin{aligned} \frac{\partial C_i}{\partial t} = & -\frac{z_i u_i F^2 C_i}{\varepsilon} \sum_j z_j C_j \\ & - \frac{z_i u_i}{F \sum_j z_j^2 u_j C_j} \frac{\partial C_i}{\partial x} \left[i + F \sum_j \left(z_j D_j \frac{\partial C_j}{\partial x} \right) \right] + D_i \frac{\partial^2 C_i}{\partial x^2} + R_i \end{aligned} \quad (4.1.1)$$

While all charged and neutral species are transported by diffusion, cations are transported towards the external cathode as anions move towards the anode by an electrical potential gradient formed by anode-cathode separation. Poisson's equation for charge density represents the effect of charge distribution on electrolyte transport and appears as the first term on the right hand side of equation (4.1.1). A chemical reaction mass source or sink, represented as R_i , is obtained through solution of a set of chemical equilibrium relations at each time step:

$$\prod_j (C_j \gamma_j)^{\nu_j} - K_i = 0 \quad (4.1.2)$$

C_j and γ_j are the concentration and activity coefficient respectively of the j^{th} species at equilibrium. The activity coefficient represents deviation from non-ideal solution theory due to short and long range inter-ionic forces, the net effect of which is quantified by the model of Pitzer [26]. The activity coefficient of each cation is:

$$\begin{aligned} \ln(\gamma_M) = & z_M^2 F^\gamma + \sum_a m_a (2B_{Ma} + ZC_{Ma}) \\ & + \sum_c \left[m_c \left(2\Omega_{Mc} + \sum_a m_a \psi_{Mca} \right) \right] + \sum_a \sum_{a'} m_a m_{a'} \psi_{Maa'} \\ & + z_M \sum_c \sum_a m_c m_a C_{ca} + 2 \sum_n m_n \lambda_{nM} + \dots \end{aligned} \quad (4.1.3)$$

The activity coefficient of each anion is:

$$\begin{aligned} \ln(\gamma_X) = & z_X^2 F^\gamma + \sum_c m_c (2B_{cX} + ZC_{cX}) \\ & + \sum_a \left[m_a \left(2\Omega_{Xa} + \sum_c m_c \psi_{cXa} \right) \right] + \sum_c \sum_{c'} m_c m_{c'} \psi_{Xcc'} \\ & + |z_X| \sum_c \sum_a m_c m_a C_{ca} + 2 \sum_n m_n \lambda_{nX} + \dots \end{aligned} \quad (4.1.4)$$

The activity coefficient of each neutral species is:

$$\ln(\gamma_N) = 2 \left(\sum_c m_c \lambda_{Nc} + \sum_a m_a \lambda_{Na} + \sum_n m_n \lambda_{Nn} \right) + \dots \quad (4.1.5)$$

These equations are based upon a virial expansion of excess Gibbs energy and are derived by Pitzer [27].

4.1.1.2 Electrochemical reactions

Faraday's Law governs the rate of anodic metal dissolution reactions occurring on the interior crevice surface:

$$R_i = \frac{A_m}{z_i F} i_p \quad (4.1.6)$$

Mixed potential theory demands the rates of the anodic and cathodic reaction to be equal. For alloys, the rate of dissolution of each metal species is assumed proportional to its mole fraction in the alloy [1, 3]. An Arrhenius expression adjusts the passive current for thermal effects [28]:

$$i_p = i_{p,T_0} \exp \left[- \left(\frac{E_a}{RT} \left(\frac{1}{T} - \frac{1}{T_0} \right) \right) \right] \quad (4.1.7)$$

The activation energy for dissolution has been experimentally determined for several industrially relevant metals immersed in sodium chloride solutions by Griess [24], Shrier [28], and others. A reference passive current density is specified based upon the ionic conductivity of the passive oxide film. A typical value used for titanium and type 304 stainless steel is of the order of $0.1 \mu\text{A}/\text{cm}^2$. This value has been determined based upon interpolation from experimental work of Griess [24]. Adjustment of the passive current for pH is given by a Freundlich isotherm [28]:

$$\log(i_p) = \log(k) - n \cdot pH \quad (4.1.8)$$

The value of k is determined by the pH and passive current at the start of the simulation and n is a function of the dissolved metal ion valence state [28]. This work assumes that the cathodic charge required to support metal dissolution is jointly carried by internal hydrogen ion reduction and external oxygen reduction. While hydrogen reduction is not observed on stainless steel crevices [23], it is evident in titanium crevices and amounts to 60 – 75% of the cathodic current [24, 25]. The portion of the anodic current density provided by hydrogen ion reduction is then:

$$i_{H^+_{redox}} = \Psi i_p \quad (4.1.9)$$

where $i_{H^+_{redox}}$ is the cathodic current density driving hydrogen ion reduction and Ψ is an empirically determined fraction defining the portion of the anodic current supplied by hydrogen evolution. During the initiation period, the effect of hydrogen bubbles on the crevice system is assumed negligible, an assumption used by other authors [5]. The net current density leaving the crevice wall, which is the passive current density less the hydrogen ion reduction current density, when integrated along the length of the crevice starting at the tip, gives the electrical current responsible for primary electromigration at an arbitrary distance ξ from the crevice tip:

$$i|_{x=\xi} = \frac{\int_0^{\xi} i_p (1 - \Psi) P dx}{A_{cs}|_{x=\xi}} \quad (4.1.10)$$

where P is a function defining the perimeter of the crevice at any position in the crevice.

4.1.2 Model implementation

Prediction of the transient crevice solution composition requires the following calculations at each discrete time step:

1. Calculation of the passive current and corrosion rate: The passive current is adjusted for temperature and changes in pH according to equations (4.1.7) and (4.1.8). The metal dissolution rate is determined by equation (4.1.6). The increase in activity of each metal species in each discrete control volume for the current time step is calculated.
2. Solution of the mass transport equation: Solution of the partial differential equation (4.1.1) is accomplished using a fully upwinded Crank-Nicolson

discretization technique. Boundary conditions are provided by the bulk solution composition at the mouth and a zero-flux requirement at the tip. Non-linearities inherent in the mass transport problem are iterated to convergence.

3. Correction for chemical equilibrium: Equilibrium relationships are written for each reaction occurring in the solution; mass balances for each species involved in the reaction are written supplementary to the equilibrium set. A Newton-Raphson method is employed to rapidly solve the non-linear equation set to a prescribed tolerance.

This sequence of calculations continues until a specified simulation time has been reached. Figure 4.1.1 displays the flowsheet describing the solution algorithm. Figure 4.1.2 illustrates the discrete finite volume grid over which the solution is obtained. The crevice is modeled as a three-dimensional rectangular box. Metal is dissolved into the crevice solution from the sides, top, and bottom of the crevice interior. The model is uni-dimensional as gradients are assumed to exist only along the crevice length. Time steps must be kept small to ensure that the segregated solution scheme presented will produce accurate transient crevice solution behavior.

4.1.3 Results

4.1.3.1 Simulation of Alavi and Cottis experiment

Alavi and Cottis [23] used an engineered type 304 stainless steel crevice formed from the space between a plate of steel and an acrylic electrode holder.

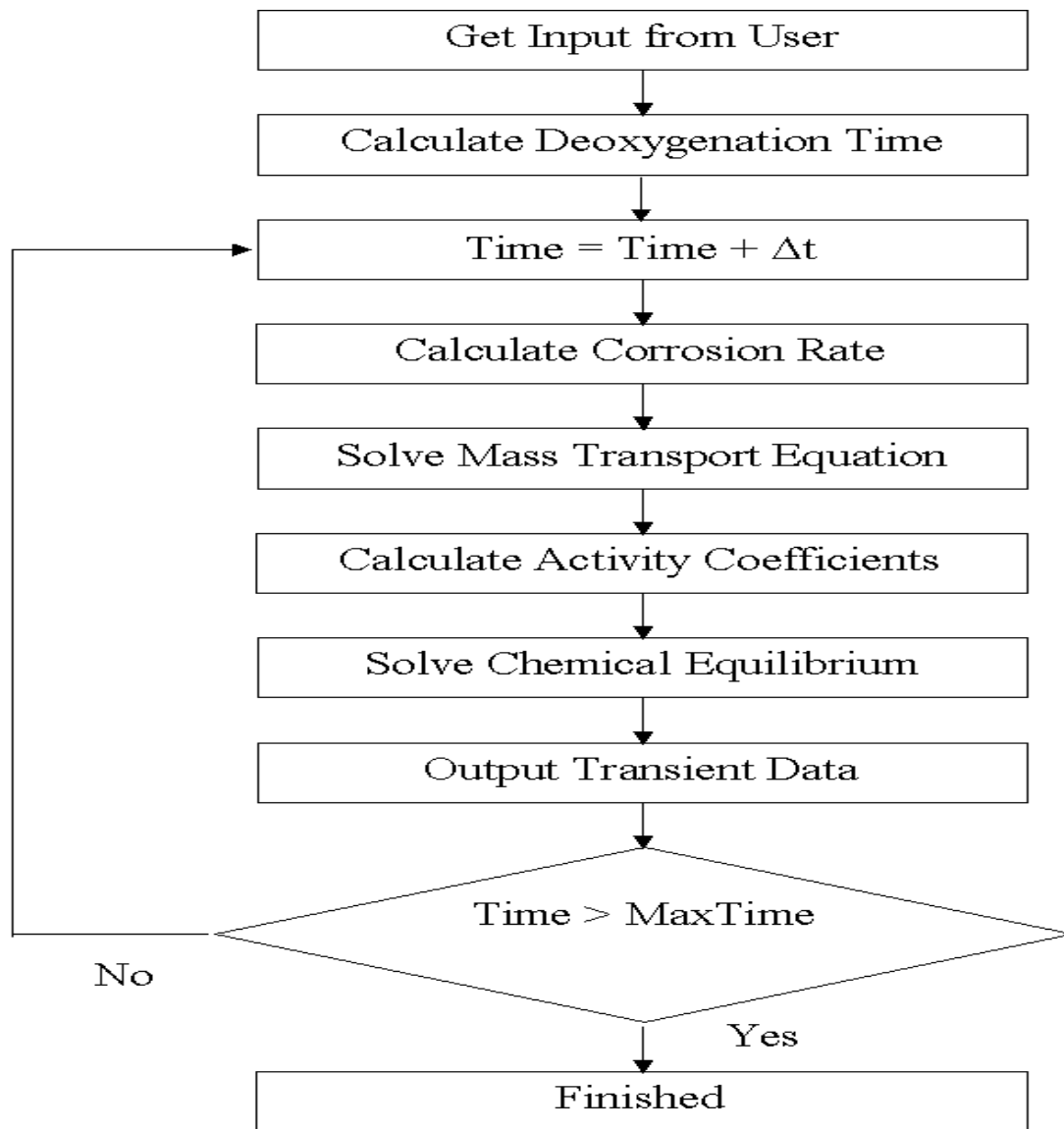


Figure 4.1.1. Flowsheet of solution algorithm used to solve passive crevice corrosion problem

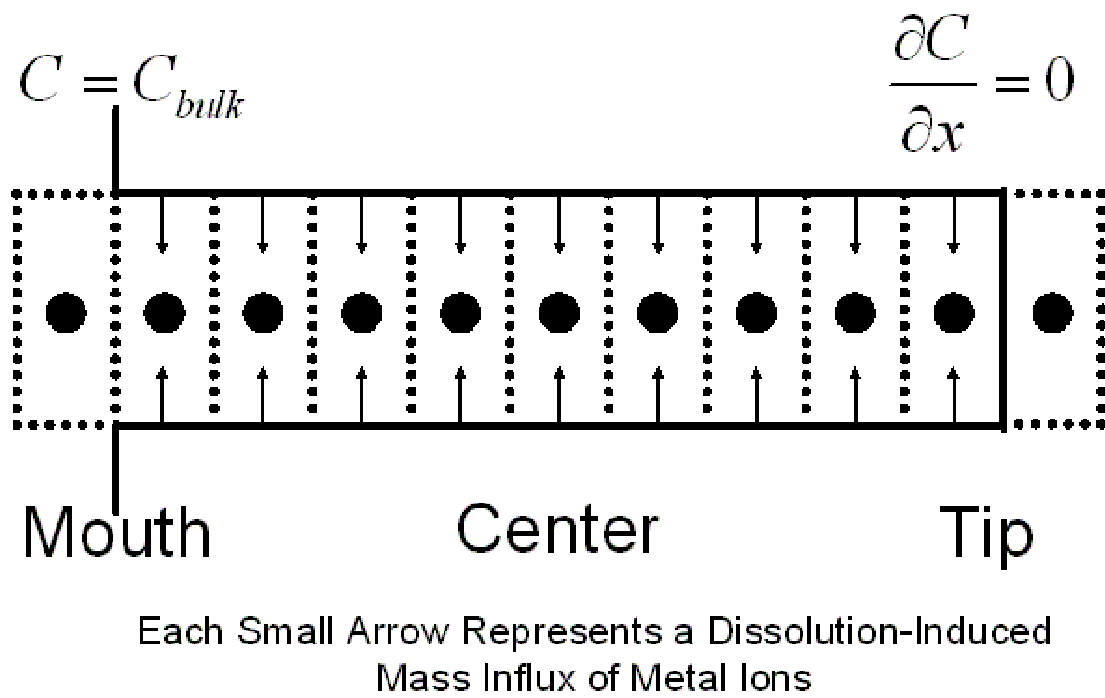


Figure 4.1.2. Finite volume grid used to obtain solution to crevice corrosion problem

The rectangular crevice with a 90 μm gap, measuring 2.5 cm wide and 8.0 cm deep was immersed in a 0.6 M aqueous NaCl solution at 25°C. The current model is validated against experimental results obtained from this crevice apparatus assuming chemical reactions given in Table 4.1.1 occur in the crevice solution [1, 19, 29].

Chemical Reaction	$\log_{10}(K_{\text{eq}})$
$\text{Cr}^{3+} + \text{H}_2\text{O} \rightleftharpoons \text{Cr}(\text{OH})^{2+} + \text{H}^+$	-3.8
$\text{Cr}(\text{OH})^{2+} + \text{H}_2\text{O} \rightleftharpoons \text{Cr}(\text{OH})_2^+ + \text{H}^+$	-6.2
$\text{Cr}(\text{OH})_2^+ + \text{H}_2\text{O} \rightleftharpoons \text{Cr}(\text{OH})_3 + \text{H}^+$	-6.2
$\text{Cr}^{3+} + \text{Cl}^- \rightleftharpoons \text{CrCl}^{2+}$	-0.149
$\text{Cr}^{3+} + 2\text{Cl}^- \rightleftharpoons \text{CrCl}_2^+$	0.158
$\text{Fe}^{2+} + \text{H}_2\text{O} \rightleftharpoons \text{Fe}(\text{OH})^+ + \text{H}^+$	-8.3
$\text{Fe}(\text{OH})^+ + \text{H}_2\text{O} \rightleftharpoons \text{Fe}(\text{OH})_2 + \text{H}^+$	-11.1
$\text{Fe}^{2+} + \text{Cl}^- \rightleftharpoons \text{FeCl}^+$	-0.161
$\text{Fe}^{2+} + 2\text{Cl}^- \rightleftharpoons \text{FeCl}_2$	-2.45
$\text{Fe}^{2+} + 4\text{Cl}^- \rightleftharpoons \text{FeCl}_4^{2-}$	-1.90
$\text{Ni}^{2+} + \text{H}_2\text{O} \rightleftharpoons \text{Ni}(\text{OH})^+ + \text{H}^+$	-9.5
$\text{Ni}(\text{OH})^+ + \text{H}_2\text{O} \rightleftharpoons \text{Ni}(\text{OH})_2 + \text{H}^+$	-9.1
$\text{Ni}^{2+} + \text{Cl}^- \rightleftharpoons \text{NiCl}^+$	-0.996

Table 4.1.1. Chemical reactions occurring in a type 304 stainless steel crevice solution

Figure 4.1.3, a comparison between predicted and measured transient pH at various distances down the type 304 stainless steel crevice from the mouth, shows agreement

within experimental uncertainty. However, Alavi and Cottis measured highest and lowest acidity near the mouth and tip respectively of the artificial crevice. This contradicts predictions of all prevalent crevice corrosion models and proposed mechanisms [9, 19]. The most obvious explanation would be that hydrogen evolution carried a portion of the cathodic load. However, Alavi and Cottis made no mention of hydrogen evolution occurring inside the 304 stainless steel crevice [23]. They argued that the observed minimum pH, located 2 cm from the mouth, resulted from migration overpowering diffusion – while migration moves the hydrogen ion out of the crevice towards the mouth region, diffusion moves hydrogen ions out of the mouth region into the bulk solution via an activity gradient. These abnormalities in the spatial pH profile could also be the result of slightly misaligned electrodes in the experimental apparatus. Watson and Postlethwaite showed the importance of placing electrodes exactly flush with the wall [12]. Even a slight misalignment, in the order of microns, can cause localized spatial acidity profile abnormalities. Regardless of the cause of localized acidity change, the model predicts the correct trends observed by Alavi and Cottis at all depths and shows reasonable agreement with their observations.

After validation of the model against the experimental work of Alavi and Cottis, the model was compared with the simulation work of others. Figures 4.1.4 and 4.1.5 compare the spatial pH profile in a type 304 stainless steel crevice solution predicted by the present model with the spatial pH profile predictions of the models of Evitts [17], Sharland [8], Walton et al. [19], and the experimental work of Alavi and Cottis [23]. In Figure 4.1.4, a reference passive current density of $0.1 \mu\text{A}/\text{cm}^2$ was initially applied while in Figure 4.1.5, a reference passive current density of $1 \mu\text{A}/\text{cm}^2$ was used.

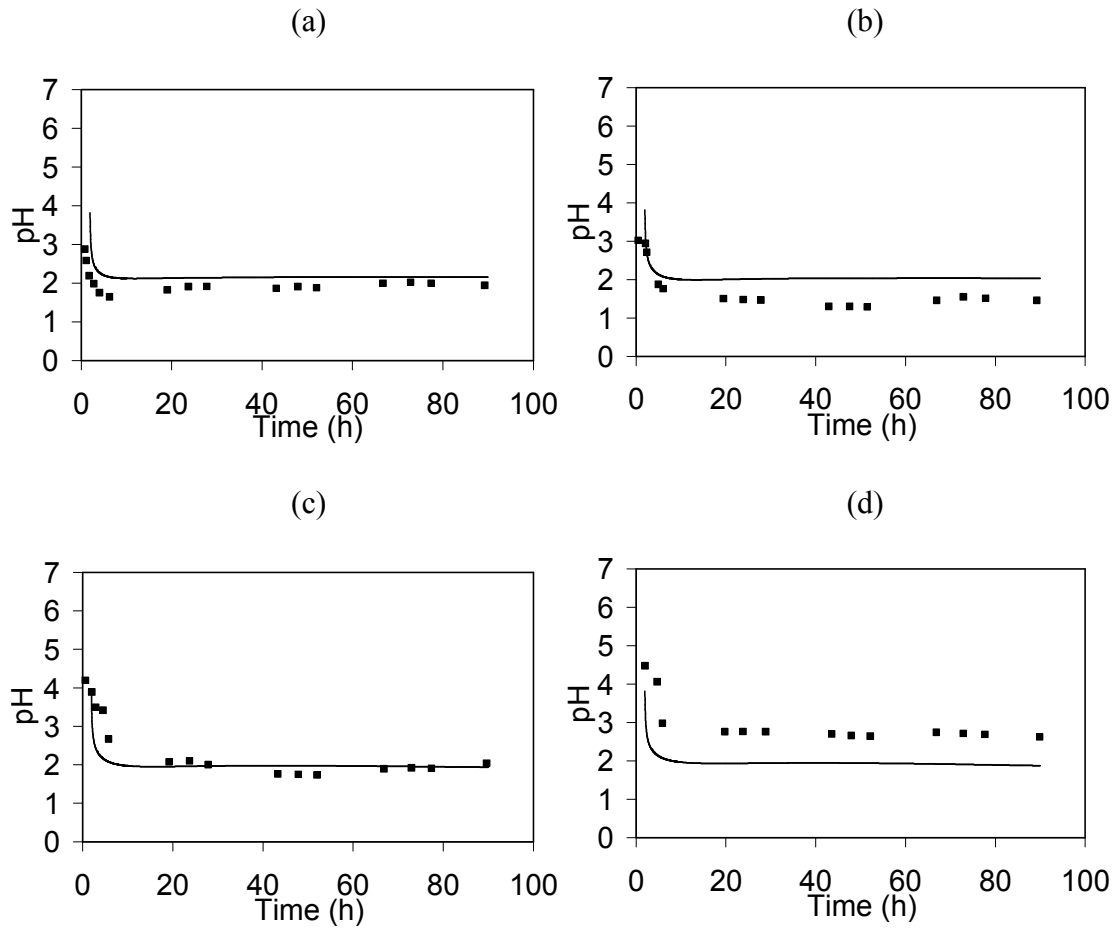


Figure 4.1.3. Comparison of predicted and experimental pH profile in a type 304 stainless steel crevice of 90 μm gap, 2.5 cm width, and 8 cm depth (0.6 M NaCl aqueous solution at 25°C): a) 1 cm deep; b) 2 cm deep; c) 4 cm deep; d) 7.5 cm deep.

The present model predicts the work of Alavi and Cottis with the greatest accuracy for both passive current densities. The lower pH predicted by the present model is likely the result of using a more sophisticated activity coefficient model to determine activity coefficients in the electrolyte solution. Because Pitzer's activity model accounts for the effect of short range interactions of ions of like and unlike charge, these short range interactions reduce the efficiency of transport of the hydrogen ion out of the crevice and the pH becomes lower.

4.1.3.2 Effect of the crevice gap on the incubation period of titanium

The previous section demonstrated the validity of the mass transport model through simulation of the experimental crevice of Alavi and Cottis [23]. Because the influence of mass transport and chemical equilibrium on both a type 304 stainless steel crevice and a titanium crevice are similar, the same model is applicable to titanium crevice corrosion after incorporation of internal hydrogen evolution as a cathodic reaction. The hydrogen ion reduction model uses an empirically determined fraction, based upon the work of He et al., which divides the total cathodic charge between internal hydrogen evolution and external oxygen reduction.

Simulations were performed on a rectangular titanium crevice immersed in 0.5 M aqueous NaCl solution at 25°C measuring 1 cm wide and 1 cm deep with varying gap. Table 4.1.2 displays the chemical reactions assumed to occur in the titanium crevice solution [30]. Comprehensive simulation results are graphically displayed in Figures 4.1.6 – 4.1.19.

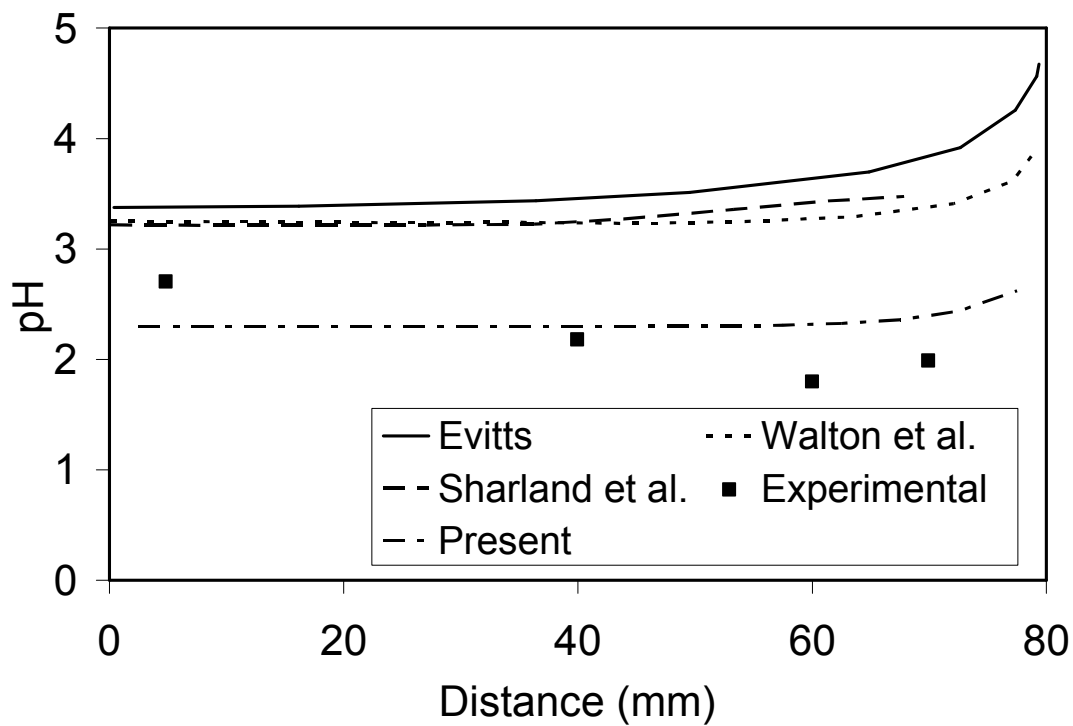


Figure 4.1.4. Comparison of predicted spatial pH profile of present model with that of previous models. Type 304 stainless steel crevice of 90 μm gap, 2.5 cm width, and 8 cm depth (0.6 M NaCl aqueous solution at 25°C). Reference passive current density is 0.1 $\mu\text{A}/\text{cm}^2$.

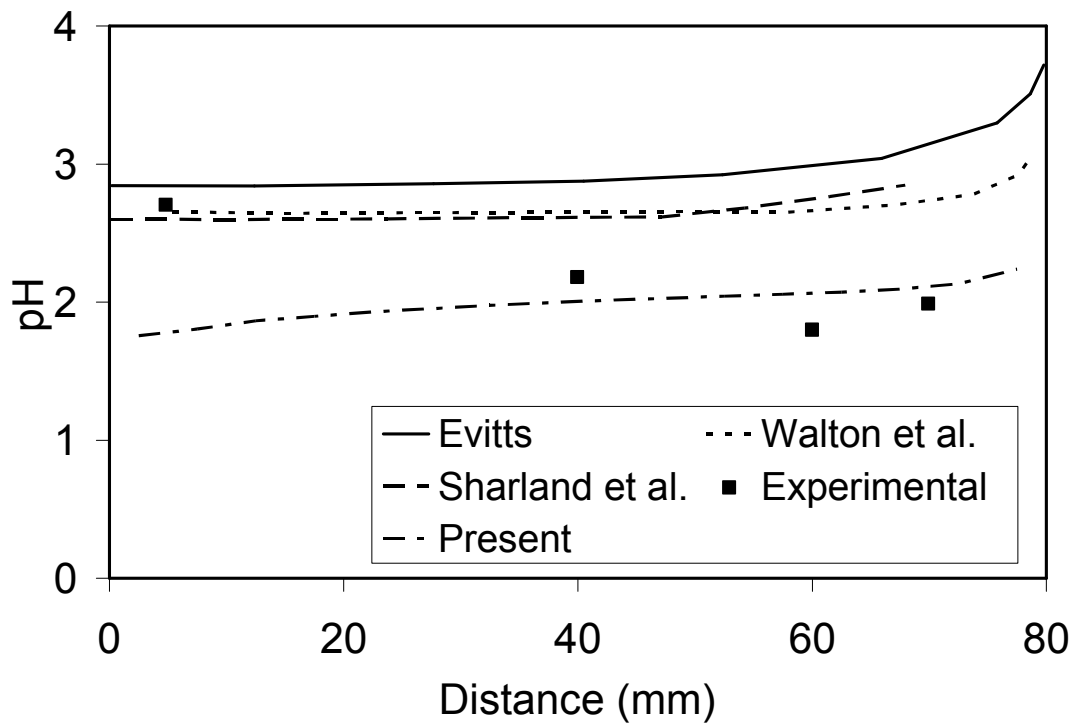


Figure 4.1.5. Comparison of predicted spatial pH profile of present model with that of previous models. Type 304 stainless steel crevice of 90 μm gap, 2.5 cm width, and 8 cm depth (0.6 M NaCl aqueous solution at 25°C). Reference passive current density is 1 $\mu\text{A}/\text{cm}^2$.

Chemical Reaction	$\log_{10}(K_{eq})$
$Ti^{4+} + H_2O \rightleftharpoons Ti(OH)^{3+} + H^+$	-2.0
$Ti(OH)^{3+} + H_2O \rightleftharpoons Ti(OH)_2^{2+} + H^+$	-1.8
$Ti(OH)_2^{2+} + H_2O \rightleftharpoons Ti(OH)_3^+ + H^+$	-2.4
$Ti(OH)_3^+ + H_2O \rightleftharpoons Ti(OH)_4 + H^+$	-4.0

Table 4.1.2. Chemical reactions occurring in a titanium crevice solution

Oxygen diffusing into the crevice is quickly consumed by cathodic reactions initially occurring inside a crevice with a 0.1 μm gap; deoxygenation is predicted in 7.7 seconds. Once oxygen is depleted, a differential aeration cell is formed forcing separation of the half-cells. Figure 4.1.6, the transient profile of iR drop referenced to the tip, displays the electrical potential field that induces electromigration of charged species. An initially high iR drop is seen in the early stages of the simulation when the crevice solution conductivity is low. As anions immigrate into the crevice and cations are produced via dissolution, the conductivity of the crevice solution increases and the iR drop along the crevice length decreases. Diffusion, working to minimize activity gradients throughout the crevice, is overpowered by electromigration forcing anions into the anodic crevice. Transient electrical conductivity at the tip, center, and mouth of the 0.1 μm gap crevice is displayed in Figure 4.1.7.

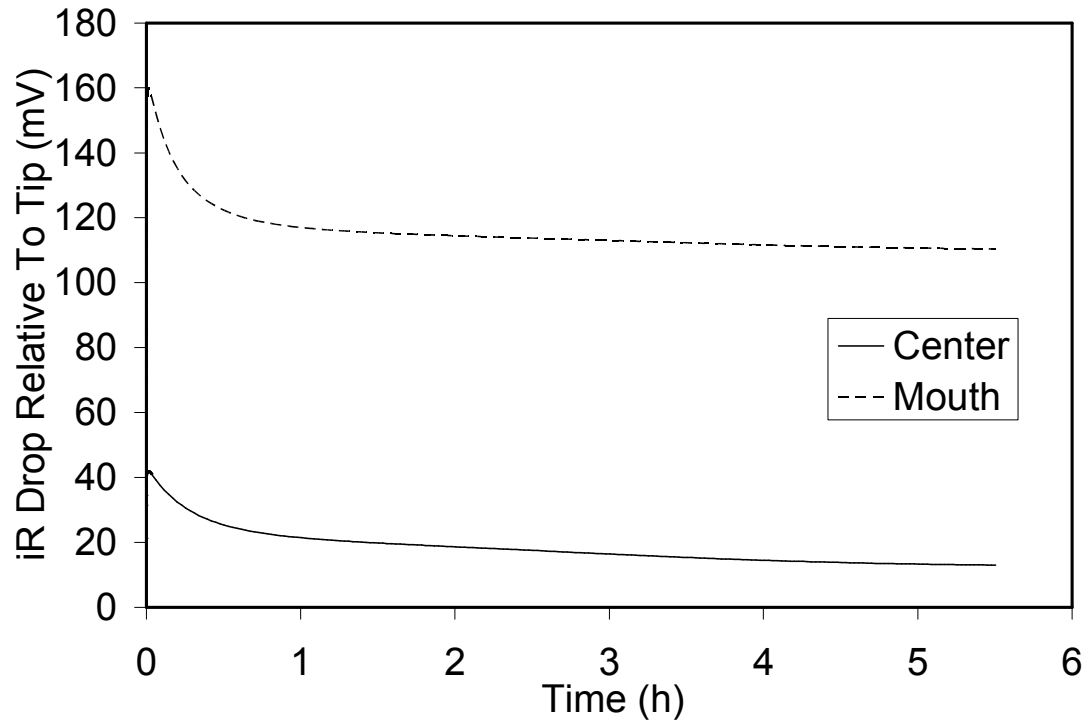


Figure 4.1.6. Transient iR drop profile referenced to tip in a titanium crevice of 0.1 μm gap, 1 cm width, and 1 cm depth (0.5 M NaCl aqueous solution at 25°C)

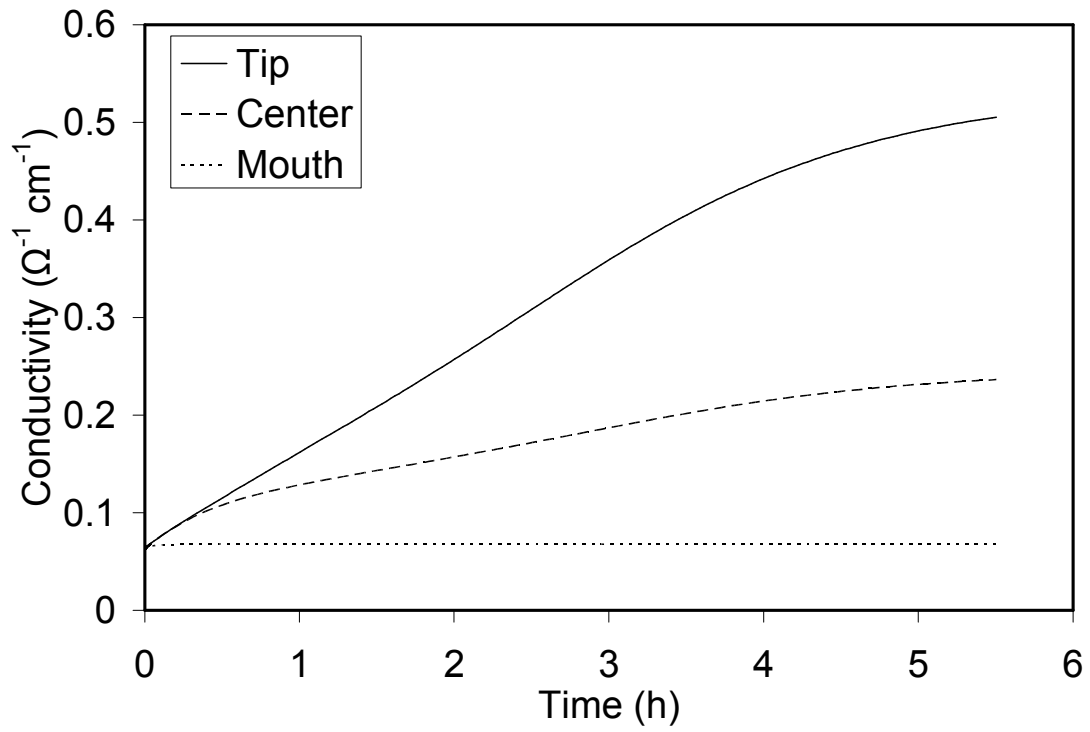


Figure 4.1.7. Transient conductivity profile in a titanium crevice of 0.1 μm gap, 1 cm width, and 1 cm depth (0.5 M NaCl aqueous solution at 25°C)

Electrical conductivity, increasing as ionic strength increases in the crevice, decreases the potential gradient required to transport ions thereby increasing the rate of electromigration; increased electromigration increases ionic activity forming an autocatalytic coupling.

Crevice solution pH is autocatalytically coupled to the passive current; a Freundlich isotherm increases the rate of heterogeneous electrochemical dissolution reactions as pH drops causing increased production of hydrogen ions through chemical reaction of metal cations. The passive current, i_p , and the pH are indicative of the state of the crevice. Transient pH and passive current profiles in the 0.1 μm gap titanium crevice solution are displayed in Figures 4.1.8 and 4.1.9 respectively. The critical crevice pH of titanium is approximately 1.0 in 0.5 M NaCl aqueous solution [31], and thus, the crevice will remain passivated as the pH does not drop below this level. Conductivity, proportional to the ionic strength, is a good indicator of steady state onset of the system and from Figure 4.1.7, the onset of steady state in the 0.1 μm crevice is predicted after approximately 5.5 hours.

Figure 4.1.10, the transient profile of iR drop referenced to the tip for a 1 μm gap, when compared to Figure 4.1.6, the transient iR drop profile for a 0.1 μm gap, shows that the increased crevice gap has caused the tip to mouth iR drop at steady state to decrease from 110 mV to 18 mV. Therefore, the domination of electromigration transport decreases as the crevice gap becomes larger. Resultant decrease in mass transport is manifested as lower ionic activity and solution conductivity.

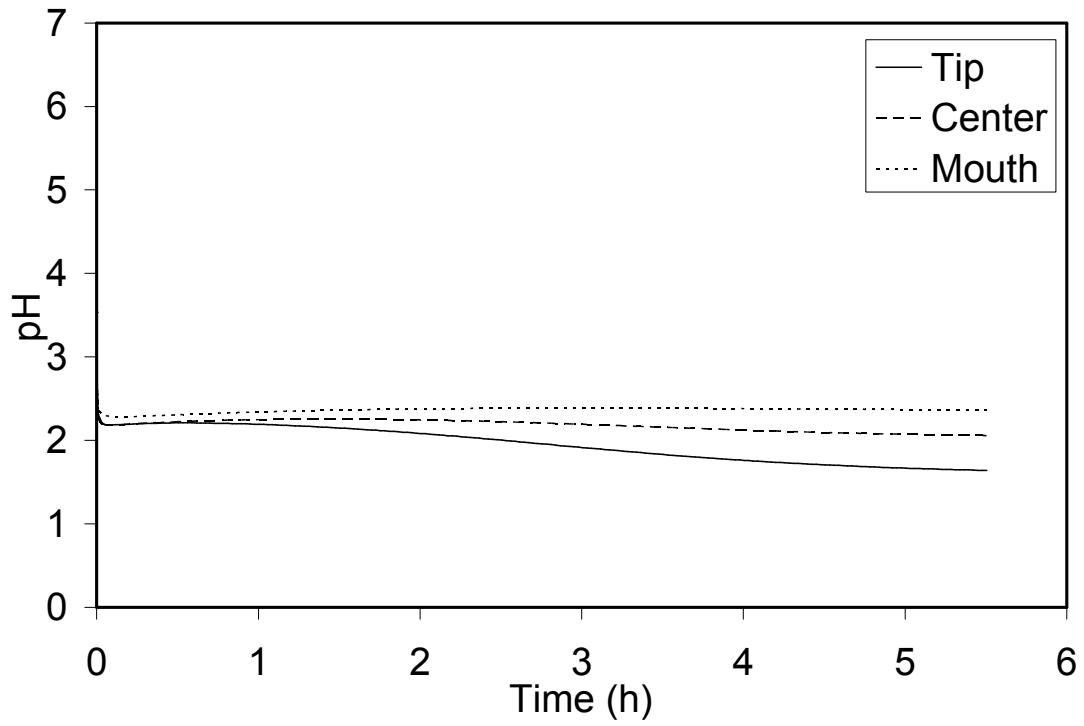


Figure 4.1.8. Transient pH profile in a titanium crevice of 0.1 μm gap, 1 cm width, and 1 cm depth (0.5 M NaCl aqueous solution at 25°C)

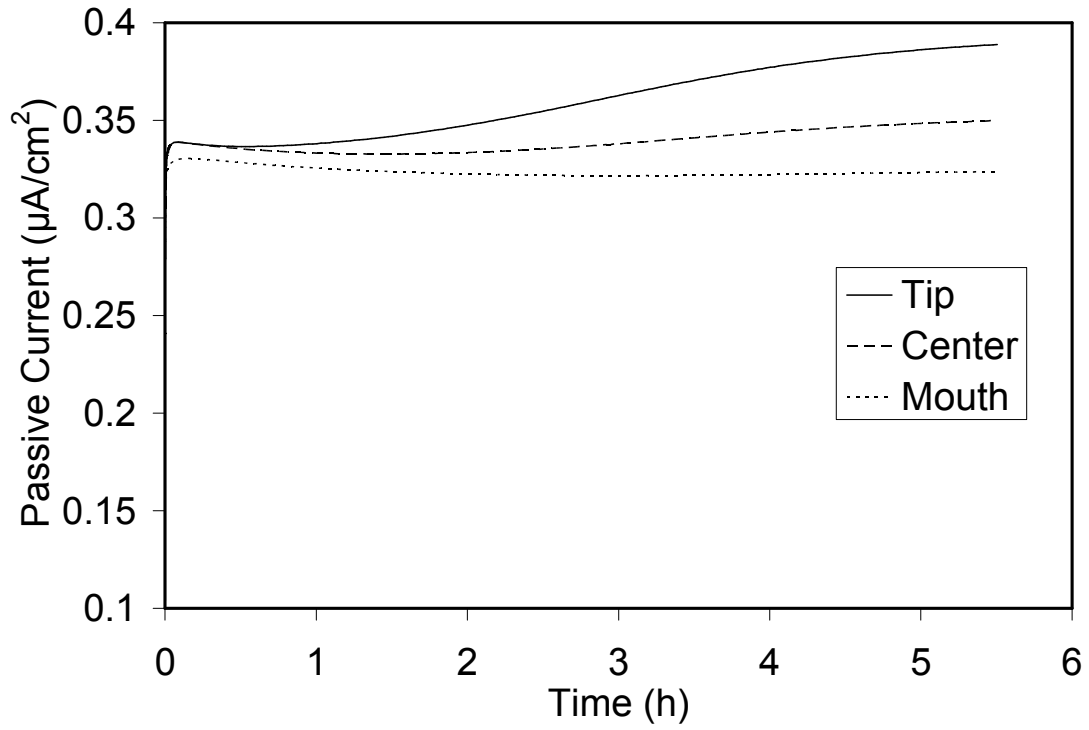


Figure 4.1.9. Transient passive current profile in a titanium crevice of 0.1 μm gap, 1 cm width, and 1 cm depth (0.5 M NaCl aqueous solution at 25°C)

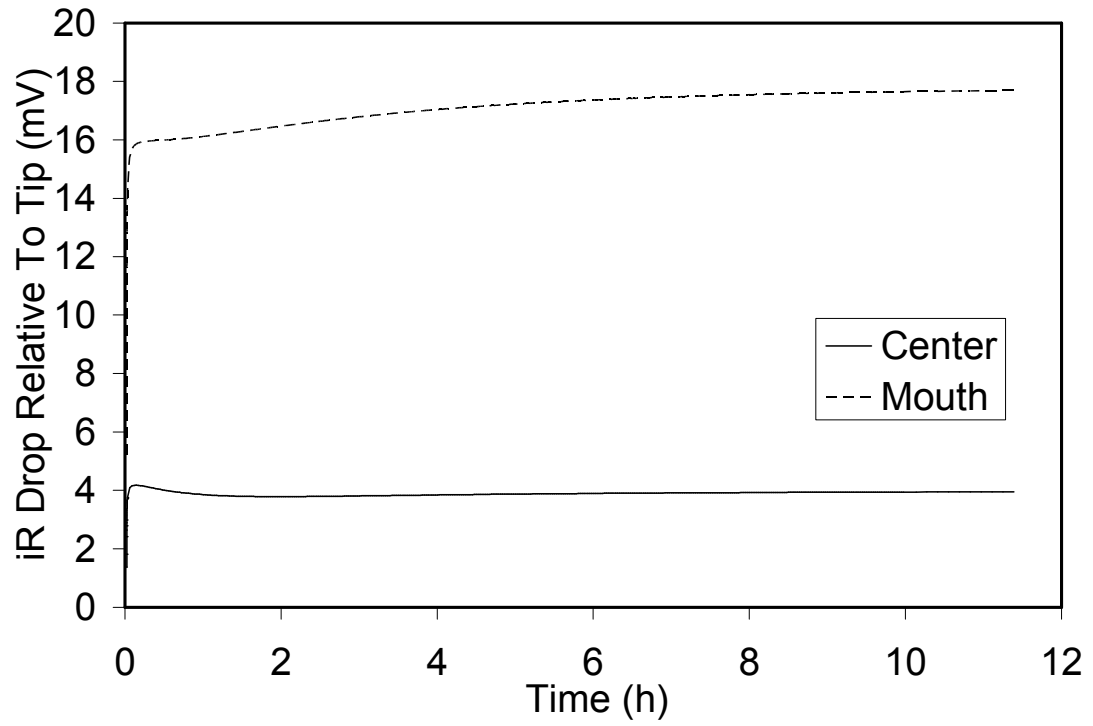


Figure 4.1.10. Transient iR drop profile referenced to tip in a titanium crevice of 1 μm gap, 1 cm width, and 1 cm depth (0.5 M NaCl aqueous solution at 25°C)

Comparison of Figure 4.1.11, the transient electrical conductivity at the tip, center, and mouth of the 1 μm gap crevice, with Figure 4.1.7, the transient electrical conductivity for the 0.1 μm gap crevice, shows that the conductivity at the crevice tip has dropped from 0.5 S/cm to 0.11 S/cm as a result of the increasing gap size. Lower solution conductivity requires a greater iR drop along the corrosion cell to maintain a specific solution current density. However, the current density flowing through solution, by definition, will decrease by the same proportion that cross sectional area increases. Because the cross-sectional area increases by an order of magnitude, the current density is reduced by one order of magnitude and a lower iR drop across the crevice length results. This shows that the sensitivity of the current density is greater than the sensitivity of the conductivity to a change in the crevice gap size and, therefore, the iR drop is lower for a larger crevice gap.

Figures 4.1.12 and 4.1.13, the transient pH and passive current respectively in a 1 μm gap crevice, show a lower passive current and higher pH than the 0.1 μm gap crevice (Figures 4.1.8 and 4.1.9), indicative of a crevice further away from critical conditions. As the size of the crevice gap increases, the crevice solution composition is predicted to be more moderate with higher pH, resultant lower passive current density, and reduced chloride concentration. Compared to the smaller crevice, the time to steady state has increased; a larger crevice will more slowly approach a steady state condition. Mathematically, a larger crevice gap damps the response of the crevice solution to dissolution-induced metal ion influx – the problem becomes less stiff and a steady state condition takes longer to achieve. Figure 4.1.11, the transient conductivity profile for the 1 μm crevice gap, shows that approximately 10 hours is required to reach steady state.

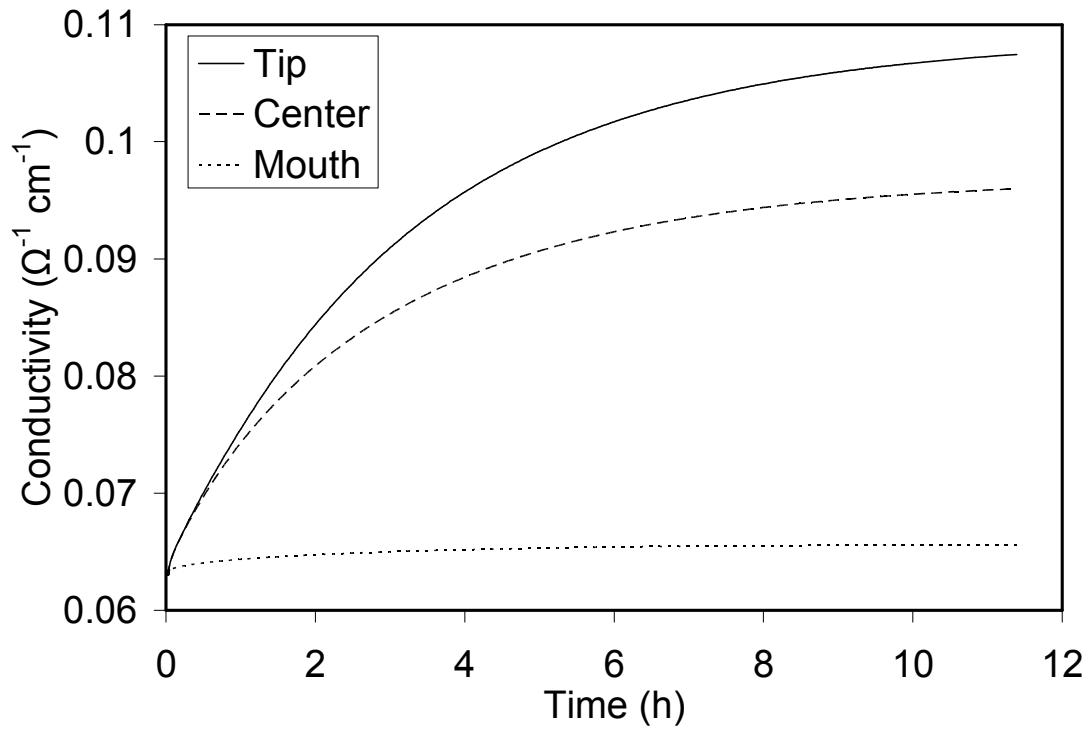


Figure 4.1.11. Transient conductivity profile in a titanium crevice of 1 μm gap, 1 cm width, and 1 cm depth (0.5 M NaCl aqueous solution at 25°C)

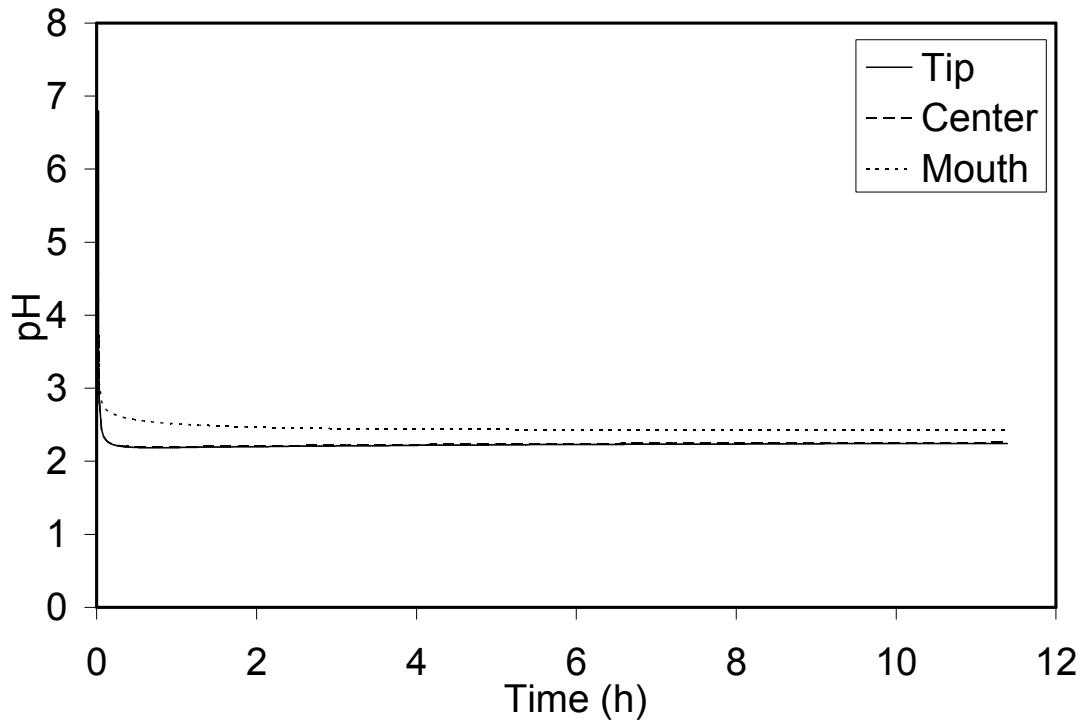


Figure 4.1.12. Transient pH profile in a titanium crevice of 1 μm gap, 1 cm width, and 1 cm depth (0.5 M NaCl aqueous solution at 25°C)

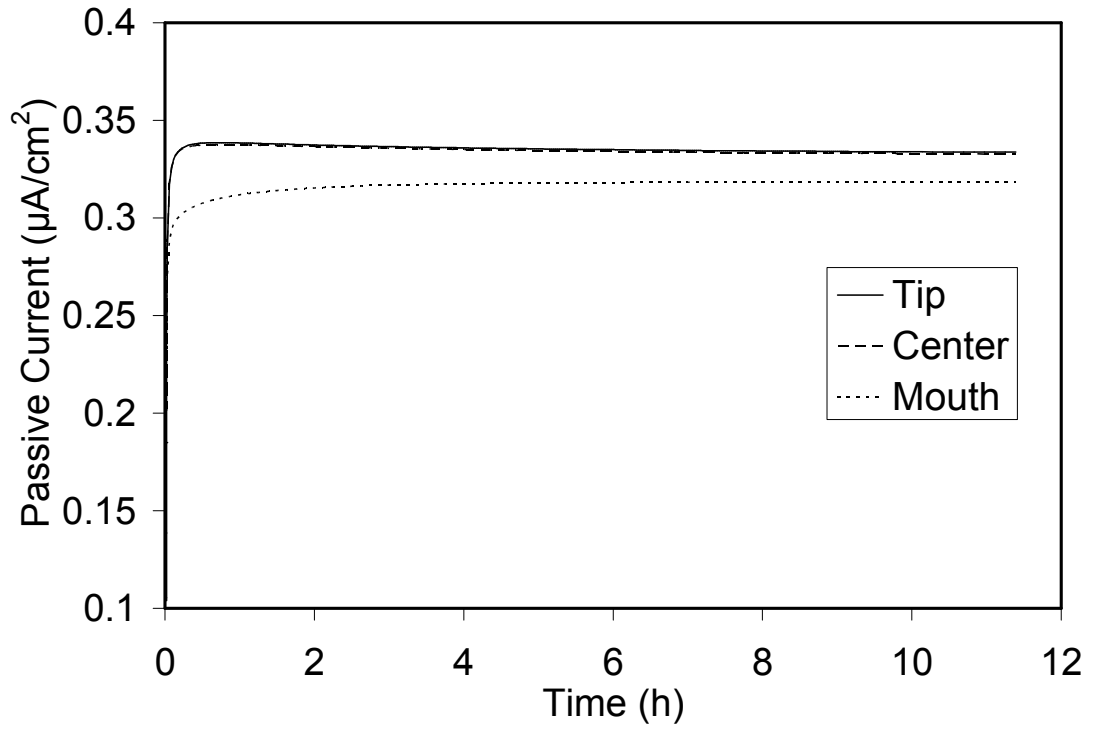


Figure 4.1.13. Transient passive current profile at tip, center, and mouth of a titanium crevice of 1 μm gap, 1 cm width, and 1 cm depth (0.5 M NaCl aqueous solution at 25°C)

Similar trends discussed in the previous section are again observed for a titanium crevice with a 10 μm gap. The predicted tip to mouth iR drop decreases further as the crevice gap is increased. The predicted crevice solution is less acidic and less electrically conductive while the passive current density decreases as the crevice gap increases in size.

4.1.3.3 Effect of the crevice gap on the steady state iR drop and charge density in a titanium crevice solution

iR drop causes the electrical potential of anodic sites to deviate from E_{corr} along the crevice interior inducing electromigration. Figures 4.1.14 – 4.1.16 illustrate steady state iR drop and E_{corr} deviation profiles along the crevice length for 0.1, 1, and 10 μm crevice gaps respectively. Figure 4.1.14 shows that as the crevice mouth is approached, the iR drop and its gradient increases. Just as tributaries add to a river, current leaving the metal-solution interface adds to the current density flowing through solution towards the mouth. Thus, the magnitude of the current density increases as the mouth is approached. The iR drop is proportional to the current density and, therefore, the electrical potential gradient and iR drop in the solution will increase towards the mouth. Similar profiles are shown in Figures 4.1.15 and 4.1.16. The mathematical expression of the potential gradient is [17]:

$$\nabla\Phi = -\frac{i}{\kappa} - \frac{F}{\kappa} \sum_j z_j D_j \nabla C_j \quad (4.1.11)$$

The second order gradient of electrical potential is Poisson's equation for charge density:

$$\nabla^2\Phi = -\frac{\delta}{\varepsilon} \quad (4.1.12)$$

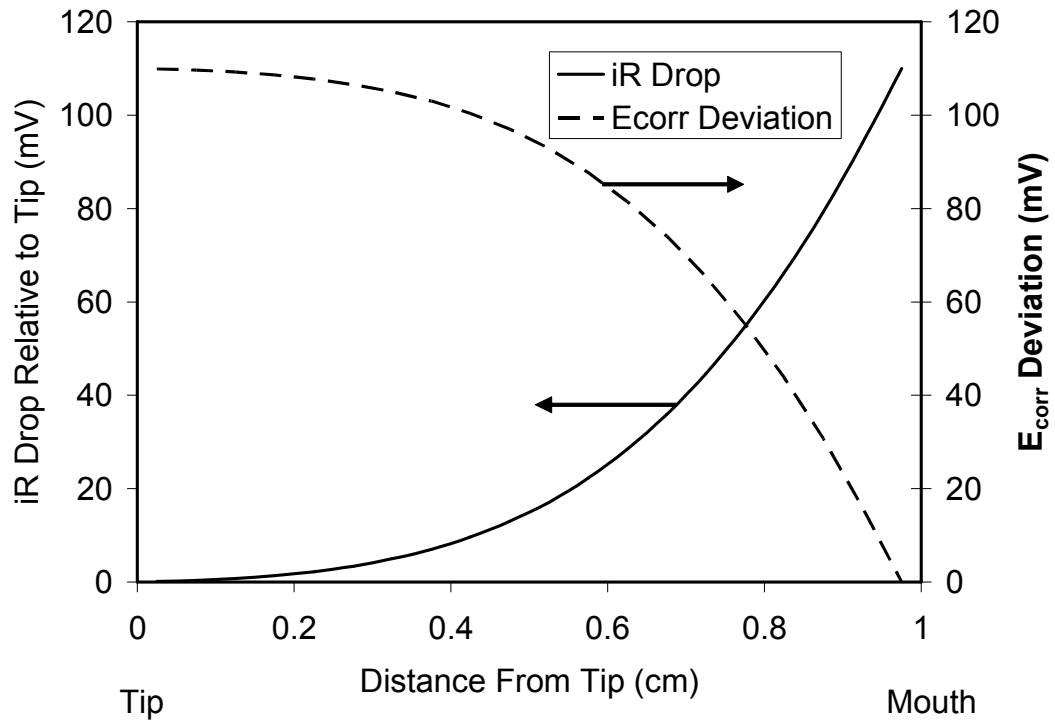


Figure 4.1.14. Spatial iR drop and E_{corr} deviation profile in a titanium crevice of $0.1 \mu\text{m}$ gap, 1 cm width, and 1 cm depth (0.5 M NaCl aqueous solution at 25°C)

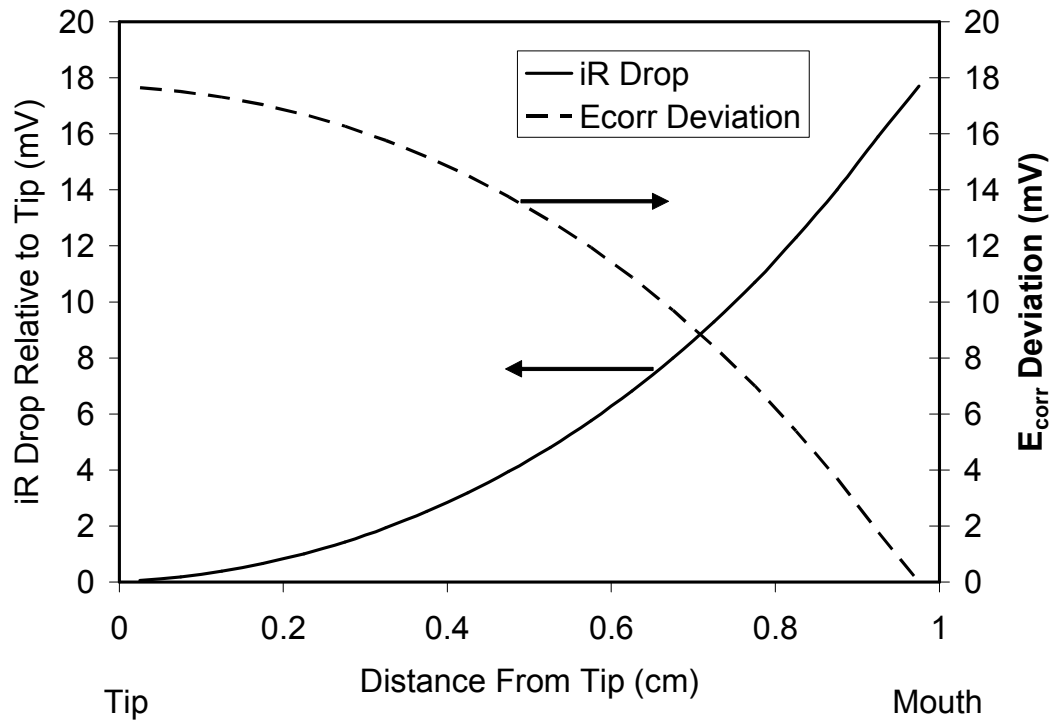


Figure 4.1.15. Spatial iR drop and E_{corr} deviation profile in a titanium crevice of $1 \mu\text{m}$ gap, 1 cm width, and 1 cm depth (0.5 M NaCl aqueous solution at 25°C)

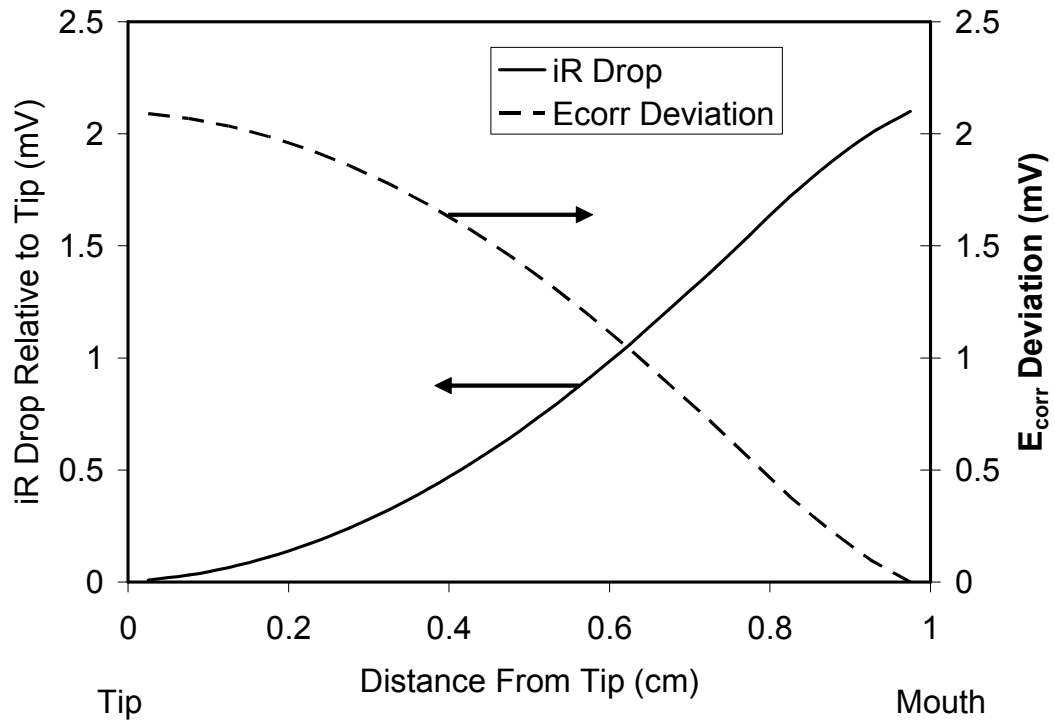


Figure 4.1.16. Spatial iR drop and E_{corr} deviation profile in a titanium crevice of $10\ \mu\text{m}$ gap, 1 cm width, and 1 cm depth (0.5 M NaCl aqueous solution at 25°C)

where $\delta = F \sum_j z_j C_j$, the electrolytic solution charge density. From equation (4.1.12), it can be concluded that for an electrically neutral system the potential gradient must be spatially independent and the iR drop profile must be linear. The non-linear shapes of the iR drop profiles for the 0.1, 1, and 10 μm gap titanium crevices, Figures 4.1.14 – 4.1.16, indicate a non-neutral charge distribution throughout the crevice solution for all crevice gap sizes.

However, comparison of these figures also shows that the iR drop profiles become increasingly linear as the crevice gap increases. Poisson's equation may be applied to determine the charge density profile from the iR drop field. Unidimensional integration assuming a constant source term, $-\delta/\varepsilon$, gives:

$$\Phi(x) = -\frac{\delta}{2\varepsilon}x^2 + k_1x + k_2 \quad (4.1.13)$$

Equation (4.1.13) is written for each computational control volume. From equation (4.1.13), it can be seen that charge density will result in localized parabolic contortion of the iR drop profile. By selecting a central point and two neighbouring points on the iR drop profile, δ , k_1 , and k_2 can be calculated via a quadratic fit for each control volume. The charge density profile $\delta(x)$, has been calculated based upon iR drop profiles for the 0.1, 1, and 10 μm gap crevices. Figure 4.1.17 illustrates the spatial charge density profile in a 0.1 μm crevice. As the crevice mouth is approached, the deviation from electroneutrality increases. This slight net charge density is due to electromigration through a spatially dependent potential gradient. The potential gradient contains two contributions, electrical potential and diffusion potential electromigration, which are the first and second terms respectively in equation (4.1.11).

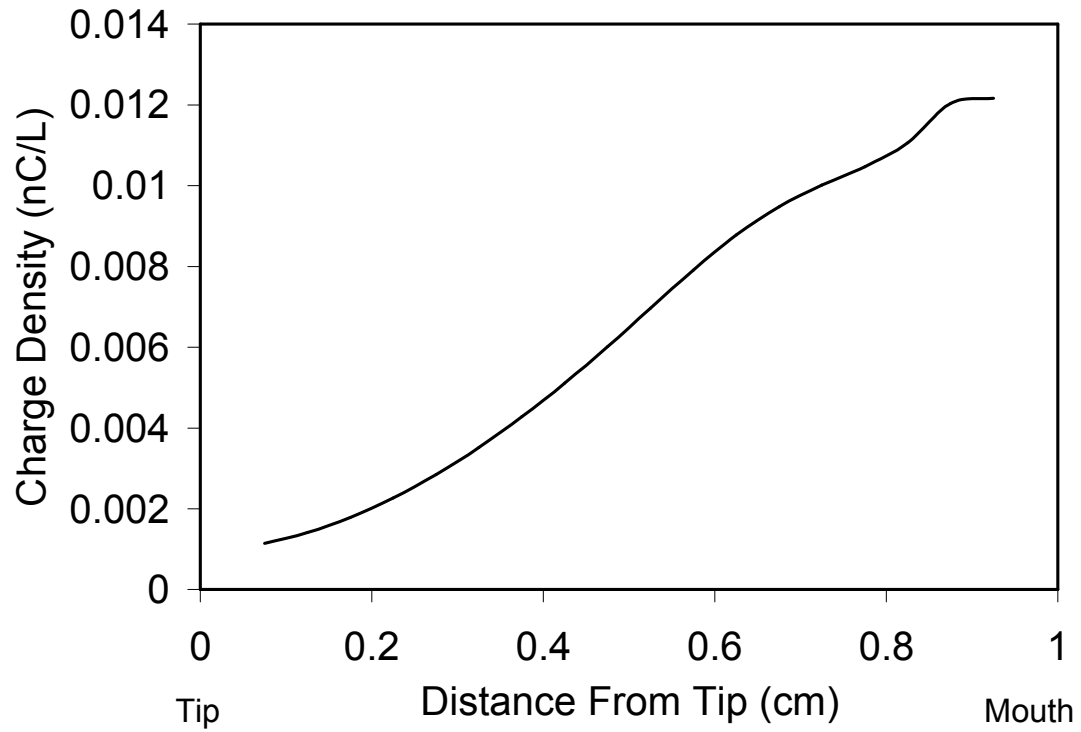


Figure 4.1.17. Spatial electroneutrality deviation profile in a titanium crevice of 0.1 μm gap, 1 cm width, and 1 cm depth (0.5 M NaCl aqueous solution at 25°C)

Because the slope of the potential gradient curve is proportional to the charge density, as the crevice mouth is approached, increased current density forces charge density to increase.

Figure 4.1.18 displays the spatial charge density profile in a 1 μm crevice. Near the crevice tip, chemical activity gradients are moderate; current density flowing through controls the iR drop. As the mouth is approached, chemical activity gradients become steep and the relative strength of electromigration via diffusion potential increases. Near the mouth of the 1 μm crevice, Figure 4.1.18 shows that electromigration via diffusion potential increases in strength relative to electromigration due to current density, evidenced by the sudden sign change in charge density. Figure 4.1.19, the spatial charge density profile in a 10 μm crevice, shows that the charge density undergoes a sign change near the crevice mouth. Where charge density becomes negative, electromigration via diffusion potential becomes significant relative to electromigration via current density. Taking the gradient of equation (4.1.11) and comparing with equation (4.1.12) will reinforce this statement:

$$-\nabla^2\Phi = \frac{\delta}{\varepsilon} = \nabla\left(\frac{i}{\kappa}\right) + \nabla\left(\frac{F}{\kappa} \sum_j z_j D_j \nabla C_j\right) \quad (4.1.14)$$

The gradient of the local potential gradient, $\nabla^2\Phi$, is proportional to the electroneutrality deviation δ . The gradient of $\nabla\Phi$ due to current density, $\nabla(i/\kappa)$, will always be positive.

This can be shown through substitution of equation (4.1.10):

$$\nabla\left(\frac{i}{\kappa}\right) = \frac{1}{\kappa} \nabla\left(\int \frac{i_p(1-\Psi)P}{A_{cs}} dx\right) + i \nabla\left(\frac{1}{\kappa}\right) = \frac{1}{\kappa} \frac{i_p(1-\Psi)P}{A_{cs}} + i \nabla\left(\frac{1}{\kappa}\right) \quad (4.1.15)$$

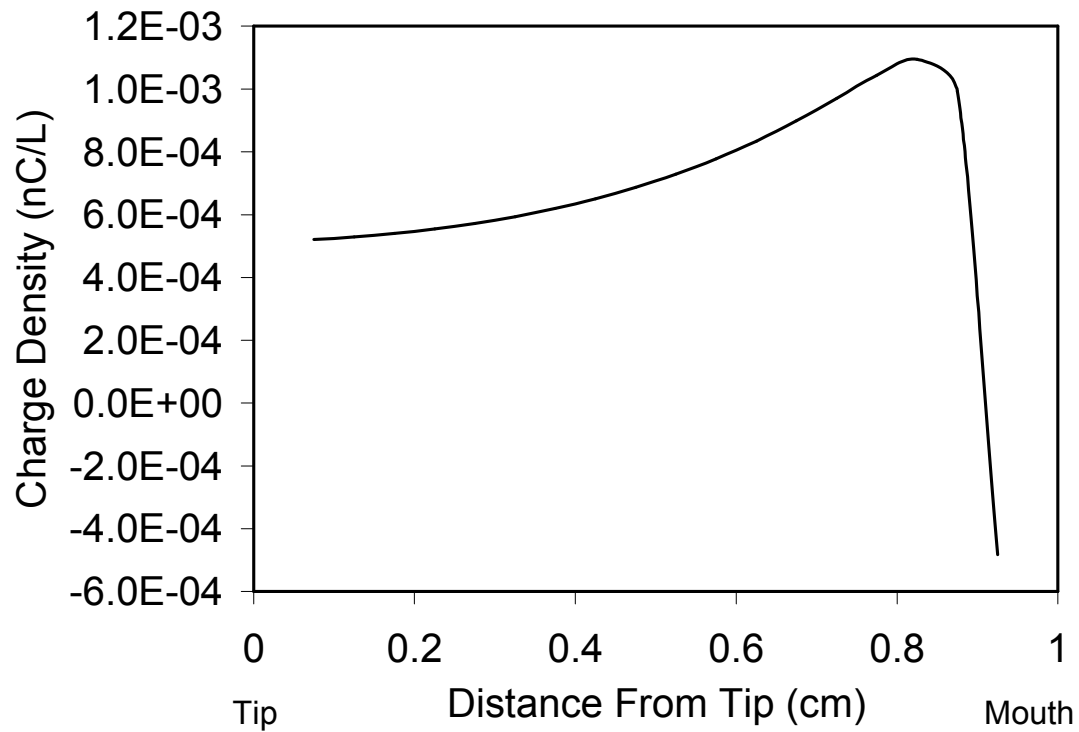


Figure 4.1.18. Spatial electroneutrality deviation profile in a titanium crevice of 1 μm gap, 1 cm width, and 1 cm depth (0.5 M NaCl aqueous solution at 25°C)

The first term of (4.1.15) must be positive because i_p cannot be negative. $\nabla(1/\kappa)$ will also be positive because the electrical resistance of the solution increases as the mouth is approached. The current density contribution to potential cannot possess a negative slope. Therefore, the diffusion potential contribution to the slope, $\nabla\left(F/\kappa \sum_j z_j D_j \nabla C_j\right)$, must become increasingly negative as the mouth is approached and be greater in magnitude than the current density contribution, $\nabla(i/\kappa)$, near the crevice mouth. Figures 4.1.18 and 4.1.19, the spatial charge density profiles for the 1 and 10 μm gap crevices respectively, demonstrate that the effect of electromigration via diffusion potential is greater in regions of strong diffusion and weak current density driven electromigration. As the crevice gap increases in size, the relative strength of electromigration decreases as the relative strength of diffusion increases. This is shown by the increasing influence of diffusion potential electromigration, manifested as a sign change in the charge density profile observed in the two larger crevices (Figures 4.1.18 and 4.1.19).

4.1.4 Conclusions

1. The present crevice corrosion model quantitatively matches experimental crevice solution composition observations of Alavi and Cottis [23] within experimental uncertainty.
2. Decreasing the crevice gap increases the electrical potential along the crevice, increases the electrical conductivity of the solution, and increases the corrosiveness of the crevice solution.

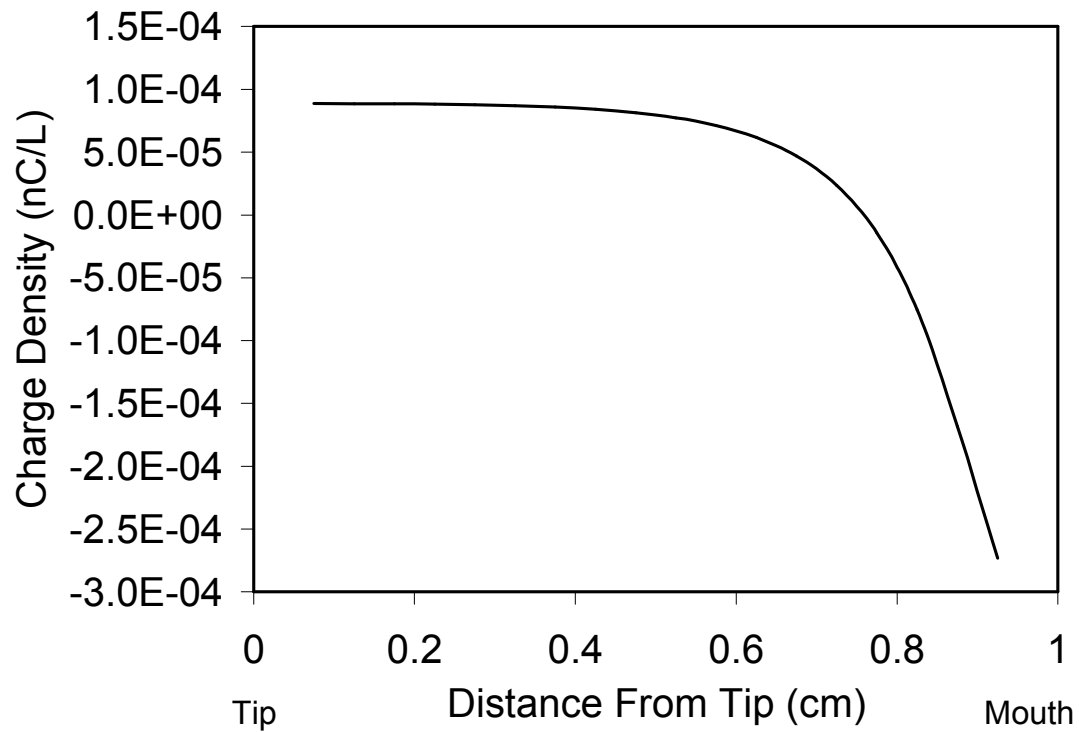


Figure 4.1.19. Spatial electroneutrality deviation profile in a titanium crevice of 10 μm gap, 1 cm width, and 1 cm depth (0.5 M NaCl aqueous solution at 25°C)

3. Increasing the crevice gap reduces the relative strength of electromigration, thereby increasing the relative strength of diffusion. This is shown by the spatial charge density profile – a negative charge density profile evidences the increasing influence of diffusion potential, and therefore diffusion, on the electrical potential gradient, the driving force for electromigration.
4. The predicted spatial iR drop profile for each crevice size shows distinct non-linearity. Because charge density causes localized parabolic contortion of the iR drop profile, the non-linearity is evidence of the influence of solution charge density on electromigration. Charge density throughout the crevice solution increases as gap size decreases. This is evidenced by the increasing linearity of the spatial iR drop profiles (Figures 4.1.14 – 4.1.16) as the crevice gap increases.
5. The influence of electromigration via diffusion potential is greatest in regions of strong diffusion and weak current density driven electromigration.

4.1.5 References

1. J. W. Oldfield, W. H. Sutton, *British Corrosion Journal* **13**, (1978): p. 13.
2. Bernhardsson, S., L. Eriksson, J. Ooppelstrup, I. Puigdomenech, T. Wallin, "Crevice Corrosion of Stainless Steels, Calculations of Concentrations and pH Changes" in "Proc. 8th International Congress on Metallic Corrosion" **1**, Mainz, Federal Republic of Germany, September 6-11, pp. 193 – 198 (1981).
3. Bernhardsson, S., L. Eriksson, J. Ooppelstrup, I. Puigdomenech, and T. Wallin, "A Model for the Initiation of Crevice Corrosion of Stainless Steels in a Chloride Environment" in "Proc. 9th Scandinavian Corrosion Congress", Copenhagen, Denmark, Sept 12-14 (1983), Addendum 1, p. 1.
4. J. W. Fu, S. Chan, *Corrosion* **40**, (1984): p. 540.
5. R. C. Alkire, , D. Siitari, *Journal of the Electrochemical Society* **129**, (1982): p. 488.
6. K. Hebert, R. Alkire, *Journal of the Electrochemical Society* **130**, (1983): p. 1007.
7. A. Turnbull, D. H. Ferris, *Corrosion Science* **26**, (1986): p. 601.
8. S. M. Sharland, *Corrosion Science* **28**, (1988): p. 621.

9. S. M. Sharland, *Corrosion Science* **33**, (1992): p. 183.
10. M.K. Watson, “Numerical Simulation of Crevice Corrosion”, Ph.D. Dissertation, University of Saskatchewan, Saskatoon SK (1989).
11. M. K. Watson, J. Postlethwaite, *Corrosion* **46**, (1990): p. 522.
12. M. K. Watson, J. Postlethwaite, *Corrosion Science* **32** (1991): p. 1253.
13. R. W. Evitts, J. Postlethwaite, M. K. Watson, “Numerical Simulation of Crevice Corrosion of Titanium”, *Corrosion* 92, held March 1992 (Houston, TX: NACE, 1992). pp. 275:1 – 275:18.
14. R. W. Evitts, M. M. A. Gad, M. K. Watson, J. Postlethwaite, “Crevice Corrosion of Nickel Alloys at Elevated Temperatures: Experimental and Modeling Studies”, *Corrosion* 93, held March 1993 (Houston, TX: NACE, 1992). pp. 601:1 – 601:10.
15. R. W. Evitts, J. Postlethwaite, M. K. Watson, “Numerical Simulation of the Initiation of Crevice Corrosion of Passive Alloys at Elevated Temperatures”, Proc. NACE International Canadian Regional Western Conference, (Houston, TX: NACE, 1995). pp. 367 – 377.

16. R. W. Evitts, M. K. Watson, J. Postlethwaite, "Numerical Simulation of Crevice Corrosion of Titanium: Effect of the Bold Surface", Proc. Corrosion 96, (Houston, TX: NACE, 1996). pp. 121:1 – 121:10.
17. R. W. Evitts, "Modeling of Crevice Corrosion", Ph.D. thesis, University of Saskatchewan, Saskatoon, Saskatchewan, Canada (1997).
18. J. Postlethwaite, R. W. Evitts, M. K. Watson, "Modeling the Initiation of Crevice Corrosion of Passive alloys at Elevated Temperatures", Proc. 5th International Symposium on Electrochemical Methods in Corrosion Research, Materials Science Forum, (Switzerland: Trans Tech Publications, 1994). pp. 121 – 132.
19. J. C. Walton, G. Cragolino, S. K. Kalandros, Corrosion Science **38**, (1996): p. 1.
20. J. W. Oldfield, G. L. Masters, K. R. Stokes, "Prediction of Initiation and Propagation of Crevice Corrosion on Aluminum Alloys in Sea Water by Mathematical Modeling" in "Proc. Corrosion/96", Denver, CO, March 24-29, 1996, (Houston, TX: NACE, 1996). pp. 512:1 – 512: 16.
21. K. L. Heppner, R. W. Evitts, and J. Postlethwaite, Canadian Journal of Chemical Engineering **80**, (2002): p. 849.

22. K. L. Heppner, R. W. Evitts, and J. Postlethwaite, *Canadian Journal of Chemical Engineering* **80**, (2002): p. 857.
23. A. Alavi, R. A. Cottis, *Corrosion Science* **27**, (1987): p. 443.
24. J. C. Griess Jr., *Corrosion* **24**, (1968): p. 96.
25. X. He, J. J. Noël, and D.W. Shoesmith, *Corrosion* **60**, (2003) pp. 378 – 386.
26. Pitzer, K.S., *Journal of Physical Chemistry* **77**, (1973) p. 268.
27. K. S. Pitzer, *Activity Coefficients in Electrolyte Solutions*, 2nd Ed. (Boca Raton, FL: CRC Press, 1991). pp. 88 – 90.
28. L. L. Shrier, R. A. Jarman, G. T. Burstein, *Corrosion*, 3rd Ed. (Oxford, UK: Butterworth-Heinemann Ltd, 1994). p. 2:20.
29. C. F. Baes and R. E. Mesmer, *The Hydrolysis of Cations*, (New York, NY: Wiley, 1976).
30. A. Liberti, V. Chiantella, F. Corigliano, *Journal of Inorganic and Nuclear Chemistry* **25**, (1963): p. 415.

31. G. Shi, "Study of Crevice Corrosion of Titanium", M.Sc. Thesis, University of Saskatchewan, Saskatoon, Saskatchewan, Canada (1990).

4.2 Effect of Solution Composition on Crevice Corrosion Initiation*

In the previous section, the effect of the crevice gap was illustrated using a sophisticated model of chemical equilibrium. However, it did not include the effects of non-ideal solution theory on mass transport. In this section, the comprehensive effect of non-ideal solution theory is accounted for in both chemical equilibrium and mass transport. The model is applied to show the effect of composition on the development of the crevice solution during the incubation period of crevice corrosion.

The focus of this work is the prediction of the effect of non-ideal solution behaviour on crevice corrosion using the ionic interaction model of Pitzer [1] coupled with an electrolyte mass transport model. This mathematical model was used to simulate the type 304 stainless steel crevice corrosion experiment of Alavi and Cottis [2]. The results are in excellent agreement with experimental observations. Then, the model was applied to simulate the crevice corrosion initiation period of a titanium crevice.

Passive metals are generally corrosion resistant due to the formation of a tenacious oxide surface film called the passive film. However, the geometric restrictions of a crevice and the passive current, which maintains the passive film, may cause the deoxygenation of the crevice which causes the formation of a differential aeration cell. In a differential aeration cell, the anodic and cathodic sites are physically separated, resulting in an electrical potential gradient. This potential gradient drives transport of cations out of the crevice and anions, such as the chloride ion, into the crevice. Chloride ions are known to disrupt the passive film.

* Reference: K.L. Heppner, R.W. Evitts, and J. Postlethwaite (2005) Effect of Ionic Interactions on the Initiation of Crevice Corrosion in Passive Metals. *Journal of the Electrochemical Society* **152**. pp. B89-B98. © The Electrochemical Society, Inc. 2005.

Metal dissolution inside the crevice produces cations which undergo hydrolysis producing metal hydroxides and hydrogen ions. In a differential aeration cell, oxygen reduction, which would normally occur in the crevice, is not available to produce hydroxide ions. Thus, metal dissolution and subsequent cation hydrolysis causes the pH to drop. In turn, the dropping pH causes the metal dissolution rate to increase. Thus, mass transport, chemical equilibrium, and electrode processes are autocatalytically inter-coupled; the end result of these processes is the formation of concentrated crevice solutions. The crevice solution may reach a critical pH and chloride ion activity whereby the protective passive film is destroyed. The time at which this occurs is called the incubation period.

Short and long range inter-ionic forces bear significant influence on transport and equilibrium in the concentrated crevice solution. However, previous crevice corrosion models have assumed the crevice solution to be infinitely dilute [3 – 6] or have relied on activity models such as the Davies Correction [7], or the B-dot Debye-Hückel equation [8] to calculate chemical equilibrium. Although useful for solutions of low ionic strength, the limits of applicability of these semi-empirical activity models are quickly surpassed in typical crevice solutions. This paper uses the ion interaction model of Pitzer [1], applicable for ionic strengths up to about six molar, to calculate crevice solution equilibrium and mass transport.

4.2.1 Mathematical model of crevice corrosion

4.2.1.1 Mass transport

In a deoxygenated crevice solution, several physical processes simultaneously occur:

1. Anodic dissolution at the metal-solution interface causes influx in metal cations into the crevice solution. According to mixed potential theory, this process occurs at the same rate as oxygen reduction at the bold surface in the absence of hydrogen evolution.
2. Chemical reaction of metal cations produces metal hydroxides, metal chlorides, and hydrogen ions.
3. A potential difference between anodic sites along the crevice interior and the bold surface cathode drives electromigration of anions in and cations out of the crevice. Electromigration and diffusion transport are strongest near the crevice mouth.

The flux of an ion through an electrolyte solution under the influence of an electrical field is [9]:

$$N_i = -z_i u_i F C_i \frac{\partial \Phi}{\partial x} - D_i \left(\frac{\partial C_i}{\partial x} + C_i \frac{\partial \ln \gamma_i}{\partial x} \right) \quad (4.2.1)$$

This equation is applicable to moderately dilute solutions at uniform temperature. Using this flux equation, a material balance combined with Poisson's equation for charge density yields:

$$\frac{\partial C_i}{\partial t} = -z_i u_i F \left(\frac{\partial C_i}{\partial x} \frac{i + i_{dp}}{\kappa} + C_i \frac{\delta}{\varepsilon} \right) + D_i \left(\frac{\partial^2 C_i}{\partial x^2} + \frac{\partial C_i}{\partial x} \frac{\partial \ln \gamma_i}{\partial x} + C_i \frac{\partial^2 \ln \gamma_i}{\partial x^2} \right) \quad (4.2.2a)$$

where:

$$i_{dp} = F \sum_j z_j D_j (\nabla C_j + C_j \nabla \ln \gamma_j) \quad (4.2.2b)$$

$$\kappa = F^2 \sum_j z_j^2 u_j C_j \quad (4.2.2c)$$

$$\delta = F \sum_j z_j C_j \quad (4.2.2d)$$

Here, C_i , z_i , u_i , D_i , and γ_i are the molar concentration, charge number, ionic mobility, diffusivity, and activity coefficient respectively of the i^{th} species. Faraday's constant and the permittivity are represented by F and ε . The solution conductivity is represented by κ . The two contributions to the electromigration driving force are i , the electromigration current density, and i_{dp} , the current density due to diffusion potential. Concentration boundary conditions are provided by the bulk solution concentration at the crevice mouth and by the dissolution current at the crevice tip. Because a reference current density is prescribed in the model, a boundary condition for potential is not required. Rather, the potential drop in the solution is calculated by Ohm's Law modified for concentration gradients [9].

4.2.1.2 Chemical equilibrium

Chemical equilibrium is attained when the Gibb's free energy of a chemical solution has reached a minimum. The chemical equilibrium criterion that must be satisfied is:

$$\prod_i a_i^{\nu_i} = K \quad (4.2.3)$$

where ν_i is the stoichiometric coefficient of the i^{th} species and the equilibrium constant is K . Equation (4.2.3) is solved for each reaction occurring in solution. The equilibrium relations are augmented with a set of mass balance relations and the resulting equation set is solved simultaneously using a Newton-Raphson non-linear equation solver.

4.2.1.3 Electrochemical reactions

Metal dissolution electrode reactions at the metal-solution interface supply a source term for chemical reaction and mass transport calculations. The dissolution rate, according to Faraday's Law, is proportional to the passive current. A function of temperature and acidity, calculation of the dissolution rate requires specification of a reference passive current specific to the metal studied; a reference passive current of the order of $0.1 \mu\text{A}/\text{cm}^2$ is typical [6, 10]. A Freundlich adsorption equation governs the effect of pH on the passive current [11]:

$$\log(i_p) = \log(k) - n \cdot pH \quad (4.2.4)$$

The value of k can be determined at reference conditions. Values of n are based upon the charge number of the dissolving metal ion [11].

Temperature effects on the passive current are accounted for through an Arrhenius expression [11]:

$$i_p = i_{p,T_0} \exp\left[-\frac{E_a}{RT}\right] \quad (4.2.5)$$

Through application of equations (4.2.4) and (4.2.5), passive current is adjusted for temperature and pH. For alloyed metals such as type 304 stainless steel (UNS S30400), dissolution of each metal is based upon its molar percentage in the alloy [12, 13]. However, other observations have shown that dissolution may be selective [14, 15]. This model assumes a non-selective dissolution process and the rate of dissolution is:

$$R_i = \frac{n_i z_i}{\sum_j n_j z_j} \left(\frac{i_p A_m}{z_i F} \right) \quad (4.2.6)$$

As well as providing the source term, the value of the passive current has a dominant effect on electromigration mass transport. To conserve charge, the primary electromigration current density i , presented in equation (4.2.1), is the integral of the passive current over the crevice interior metal surface area:

$$i(x) = \frac{\int_0^x i_p(x) dA_m(x)}{A_{cs}(x)} \quad (4.2.7)$$

In this study, oxygen reduction at the crevice bold surface is assumed not to limit the rate of metal dissolution during the incubation period. The diffusion limited oxygen reduction current is typically $50 - 100 \mu\text{A}/\text{cm}^2$ [11, 16]. Values of the limiting current that fall within this range have been obtained in cathodic polarization scans for several metals. Griess studied the crevice corrosion of titanium and obtained a limiting current of approximately $200\mu\text{A}/\text{cm}^2$ in 100°C one molar sodium chloride solution [10]. This result, when adjusted for temperature using the correlation of Wilke and Chang [17], predicts a limiting current of approximately $50\mu\text{A}/\text{cm}^2$ in 25°C NaCl solution. Sehgal et al. [18], in a study of the pitting corrosion of aluminum alloys (AA1100-O and AA2024-T3), found that the limiting current density for oxygen reduction in this situation was also approximately $50 \mu\text{A}/\text{cm}^2$. In the present work, a reference passive current of $0.1 \mu\text{A}/\text{cm}^2$ was prescribed. As a result, the calculated transient current densities were much smaller than the limiting current density and the crevice corrosion process was therefore not under mass transfer control. Thus, the assumption of non-limiting conditions in this work is valid providing that the cathodic surface area is at least 0.5% - 5% of the anodic surface area.

The time required for crevice deoxygenation to occur is calculated by the following equation:

$$t_{deoxygenation} = \frac{4FA_{cs}LC_{O_2}}{i_p A_m} \quad (4.2.8)$$

where L is the crevice depth and C_{O_2} is the dissolved oxygen concentration. The incubation period is calculated by summing the deoxygenation time and the time required to reach the critical pH.

4.2.2 Ionic interaction model

Pitzer's model is based upon a virial expansion of the excess Gibb's Free Energy of the solution:

$$\frac{G^E}{m_s RT} = f^\gamma(I) + \sum_i \sum_j m_i m_j \lambda_{ij}(I) + \sum_i \sum_j \sum_k m_i m_j m_k \mu_{ijk} + \dots \quad (4.2.9)$$

Only a function of ionic strength, the first term on the right hand side is the Debye-Hückel limiting law, $f^\gamma(I)$. m_i and m_s are the molality of the i^{th} solute and the solvent, usually water. The short-range potential effects are accounted for with the second and third virial coefficients, λ_{ij} and μ_{ijk} respectively. The second virial coefficient is a function of ionic strength, temperature, and pressure; neutral species have no effect on its value. Only binary and ternary short range interactions are considered; the probability of quaternary interactions is very low in the applicability range of the model. The calculation of ionic strength closes the system of equations.

Particular sums and differences of the second and third virial coefficients are experimentally observable, but the actual values of these virial coefficients not [19]. For this reason, equation (4.2.9) is arranged into experimentally observable sums and

differences of the virial coefficients, yielding the general form of the equations to determine the activity coefficients and the osmotic coefficient. Because a complete derivation of this activity model is given in Pitzer [19], it will not be included here. The general form of the osmotic coefficient, ϕ , is:

$$\begin{aligned}
\phi - 1 = & \frac{2}{\sum_i m_i} \left[\frac{-A_\phi I^{3/2}}{1 + b_\phi \sqrt{I}} + \sum_c \sum_a (m_c m_a (B_{ca}^\phi + ZC_{ca})) + \right. \\
& \sum_c \sum_{c'} \left(m_c m_{c'} (\Omega_{cc'}^\phi + \sum_a m_a \psi_{cc'a}) \right) + \\
& \sum_a \sum_{a'} \left(m_a m_{a'} (\Omega_{aa'}^\phi + \sum_c m_c \psi_{aa'c}) \right) + \\
& \left. \sum_n \sum_c (m_n m_c \lambda_{nc}) + \sum_n \sum_a (m_n m_a \lambda_{na}) + \right. \\
& \left. \sum_n \sum_{n'} (m_n m_{n'} \lambda_{nn'}) + \frac{1}{2} \sum_n m_n^2 \lambda_{nn} + \dots \right]
\end{aligned} \tag{4.2.10}$$

Similarly, the activity coefficient of each cation, γ_M , is:

$$\begin{aligned}
\ln(\gamma_M) = & z_M^2 F^\gamma + \sum_a m_a (2B_{Ma} + ZC_{Ma}) + \sum_c m_c (2\Omega_{Mc} + \sum_a m_a \psi_{Mca}) \\
& + \sum_a \sum_{a'} m_a m_{a'} \psi_{Maa'} + z_M \sum_c \sum_a m_c m_a C_{ca} + 2 \sum_n m_n \lambda_{nM} + \dots
\end{aligned} \tag{4.2.11}$$

The activity coefficient of each anion, γ_X , is:

$$\begin{aligned}
\ln(\gamma_X) = & z_X^2 F^\gamma + \sum_c m_c (2B_{cX} + ZC_{cX}) + \sum_a m_a (2\Omega_{Xa} + \sum_c m_c \psi_{cXa}) \\
& + \sum_c \sum_{c'} m_c m_{c'} \psi_{Xcc'} + |z_X| \left[\sum_c \sum_a m_c m_a C_{ca} + 2 \sum_n m_n \lambda_{nX} + \dots \right]
\end{aligned} \tag{4.2.12}$$

The activity coefficient of each neutral species, γ_N , is:

$$\ln(\gamma_N) = 2 \left(\sum_c m_c \lambda_{Nc} + \sum_a m_a \lambda_{Na} + \sum_n m_n \lambda_{Nn} \right) + \dots \tag{4.2.13}$$

Equations (4.2.10) – (4.2.13) are the working equations of the Pitzer activity model. Second and third virial coefficients have been recast to the parameters listed and defined in Table 4.2.1.

Parameter	Representation
B_{ij}^{ϕ}	Effect of cation-anion interactions on osmotic coefficient
Ω_{ij}^{ϕ}	Effect of interactions of ions of like charge on osmotic coefficient
C_{ca}	Effect of cation-anion interactions on osmotic coefficient and solute activity coefficient
ψ_{ijk}	Effect of anion-anion-cation or cation-cation-anion interactions on osmotic coefficient and solute activity coefficient
λ_{ij}	Effect of neutral-anion, neutral-cation, or neutral-neutral interactions on osmotic coefficient and solute activity coefficient
B_{ij}	Effect of cation-anion interactions on solute activity coefficient

Table 4.2.1. Parameters and their representation used in the activity model of Pitzer

Additional terms for ternary interactions involving neutral species are available but they have not been included here; a complete description of these terms was provided by Pitzer [19]. The quantity F^{γ} used in the preceding equations includes the Debye-Hückel limiting law and it is written as follows:

$$F^{\gamma} = f^{\gamma}(I) + \sum_c \sum_a m_c m_a B'_{ca} + \sum_c \sum_{c'} m_c m_{c'} \Omega'_{cc'} + \sum_a \sum_{a'} m_a m_{a'} \Omega'_{aa'} \quad (4.2.14)$$

The coefficients B_{ij}' and Ω_{ij}' account for effect of opposite and like charge interactions respectively. Accounting for long range interactions, the Debye-Hückel term, f^γ , is dependent upon ionic strength and temperature and is expressed as:

$$f^\gamma(I) = -A_\phi \left[\frac{\sqrt{I}}{1 + b_\phi \sqrt{I}} + \frac{2}{b_\phi} \ln(1 + b_\phi \sqrt{I}) \right] \quad (4.2.15)$$

The Debye-Hückel parameter, appearing in equation (4.2.15), is:

$$A_\phi = \frac{1}{3} \sqrt{\frac{2\pi N_0 \rho_s}{1000} \left(\frac{e^2}{\epsilon k T} \right)^{3/2}} \quad (4.2.16)$$

where ρ_s is the density of the solvent. The parameter, Z , in equations (4.2.10) – (4.2.12) is:

$$Z = \sum_i m_i |z_i| \quad (4.2.17)$$

The universal parameter, b_ϕ , is $1.2\sqrt{kg/mol}$ [19]. The B_{ij} parameters are functions of ionic strength. For the Pitzer model, the functional forms of these parameters incorporate empirical constants, $\beta_{ij}^{(0)}$ and $\beta_{ij}^{(1)}$, obtained from a best fit of data:

$$B_{ij}^\phi = \beta_{ij}^{(0)} + \beta_{ij}^{(1)} \exp(-\alpha\sqrt{I}) \quad (4.2.18)$$

$$B_{ij} = \beta_{ij}^{(0)} + \beta_{ij}^{(1)} g(\alpha\sqrt{I}) \quad (4.2.19)$$

$$B_{ij}' = \beta_{ij}^{(1)} \frac{g'(\alpha\sqrt{I})}{I} \quad (4.2.20)$$

where the functions g and g' , written as dependent upon the arbitrary independent variable x , are:

$$g(x) = 2 \left[\frac{1 - (1+x)\exp(-x)}{x^2} \right] \quad (4.2.21)$$

$$g'(x) = 2 \left[\frac{1 - (1 + x + \frac{1}{2}x^2)\exp(-x)}{x^2} \right] \quad (4.2.22)$$

The value of α is $2 \text{ (kg/mol)}^{1/2}$ for 1 – 1 and 1 – 2 electrolyte solutions [1]. Knowing C_{ij}^ϕ , a parameter obtained from tabular data found in Pitzer [19], the parameters C_{ij} are calculated by:

$$C_{ij} = \frac{C_{ij}^\phi}{2\sqrt{|z_i z_j|}} \quad (4.2.23)$$

To account for the effect of mixing of like charged ions, Ω_{ij} , Ω'_{ij} , and Ω_{ij}^ϕ are calculated [19]:

$$\Omega_{ij} = \theta_{ij} + {}^E \theta_{ij}(I) \quad (4.2.24)$$

$$\Omega'_{ij} = {}^E \theta'_{ij}(I) \quad (4.2.25)$$

$$\Omega_{ij}^\phi = \theta_{ij} + {}^E \theta_{ij}(I) + I^E \theta'_{ij}(I) \quad (4.2.26)$$

The long range interaction of ions of differing magnitude of like charge (i.e. a +2 charge ion interacting with a +3 charge ion) is highly dependent upon ionic strength. This situation is known as unsymmetrical mixing and the ${}^E \theta_{ij}(I)$ terms are not negligible in this case. This ionic strength dependence disappears when mixing is symmetric (i.e. interacting ions have the same charge) and only the θ_{ij} terms, taken as constant for any cation-cation or anion-anion pair, remain. This work incorporates the effect of unsymmetrical mixing into the predictions of the activity coefficient. Pitzer [19] details the calculation of the unsymmetrical mixing terms.

Six empirical parameters, $\beta_{ij}^{(0)}$, $\beta_{ij}^{(1)}$, C_{ij}^{ϕ} , θ_{ij} , ψ_{ijk} , and λ_{ij} , are required to solve Pitzer's Equations.

4.2.3 Results and discussion

The crevice corrosion of type 304 stainless steel (71% iron, 10% nickel, and 19% chromium) and pure titanium in aqueous 0.6 M NaCl solution was modelled. The Pitzer model parameters used to calculate the activity coefficient of each species in both crevice solutions are listed in Tables 4.2.2 – 4.2.4 [19 (and references therein)].

i	j	$\beta_{ij}^{(0)}$	$\beta_{ij}^{(1)}$	C_{ij}^{ϕ}
Na ⁺	Cl ⁻	0.0765	0.2664	0.00127
H ⁺	Cl ⁻	0.1775	0.2945	0.0008
Fe ²⁺	Cl ⁻	0.335925	1.53225	-0.00860725
Na ⁺	OH ⁻	0.0864	0.253	0.0044
Ni ²⁺	Cl ⁻	0.335925*	1.53225*	-0.00860725*
Cr ³⁺	Cl ⁻	0.73640	5.255	-0.04511

* assumed value

Table 4.2.2. Binary cation-anion interaction parameters for the type 304 stainless steel crevice solution

i	j	θ_{ij}
H ⁺	Na ⁺	0.036
OH ⁻	Cl ⁻	-0.05

Table 4.2.3. Binary anion-anion or cation-cation interaction parameters for the type 304 stainless steel crevice solution

<i>i</i>	<i>j</i>	<i>k</i>	ψ_{ijk}
Na ⁺	H ⁺	Cl ⁻	-0.004
Cl ⁻	OH ⁻	Na ⁺	-0.006

Table 4.2.4. Ternary anion-anion-cation or cation-cation-anion interaction parameters for the type 304 stainless steel crevice solution

For interactions where no parameter values were available, the default values listed in Table 4.2.5 were used.

Parameter	Default Value
$\beta_{ij}^{(0)}$	0.15
$\beta_{ij}^{(1)}$	0.25
C^ϕ	0.01
θ_{ij}	0.00
λ_{ij}	0.00
ψ_{ijk}	0.00

Table 4.2.5. Default values of Pitzer model parameters used when no experimentally determined values are available

These values were selected based upon mean parameter values for other ionic interactions. No values were available for neutral-ion interactions. However, because of the very low concentrations of neutral solutes in both crevice solutions, the absence of experimentally determined parameters for these interactions was inconsequential on the calculated results. It is proven mathematically in Appendix A that the sensitivity of the predicted activity coefficients of dissolved species is dependent upon the molality of the interacting ions. For both systems modelled in this work, most interactions which involve ions of higher ionic strength (i.e. chloride) are accounted for using experimentally determined parameters. Interactions with ions of low ionic strength (i.e. $\text{Cr}(\text{OH})_3$) have little influence on the activity coefficients of species in solution; the dearth of interaction data for these ions results in small error in the predicted activity coefficient.

4.2.3.1 Type 304 stainless steel crevice

Alavi and Cottis [2] used an engineered 304 stainless steel crevice with the following measurements: 90 μm across the gap, 2.5 cm in width and 8.0 cm deep. The crevice, formed between a plate of steel and an acrylic electrode holder, was immersed in a 0.6 mol/L sodium chloride solution at 25°C. Electrodes were placed along the crevice length to measure chloride ion activity and pH. The data that they collected is used to validate the pH profile predicted by the present crevice corrosion model.

The first 33 hours of the Alavi and Cottis experiment was simulated. The thirteen chemical reactions assumed to occur in the crevice solution are listed in Table 4.1.1 [12] [20]. The simulation required approximately 32 hours to run on a 3.06 GHz Pentium[®] 4 Processor with 1 GB of RAM, a simulated time to real time ratio of approximately 1.03 to 1. Because of the inter-coupling of individual activity profiles, accounting for ionic

interactions in a computer code increases the number of iterations required to solve the mass transport problem.

Figure 4.2.1 compares predicted transient pH in a type 304 stainless steel crevice solution with the experimental observations of Alavi and Cottis [2]. The model predicts the trends that Alavi and Cottis experimentally observed. Initially, aqueous sodium chloride solution ($\text{pH} = 7$) fills the steel crevice. Hydrogen ions are produced by hydrolysis of iron, chromium, and nickel ions released by metal dissolution within the crevice. The significant pH drop, prominent at the start of the simulation, increases the passive current, which increases the rate of metal dissolution. This shifts the chemical hydrolysis equilibrium which causes the pH to drop further, thus forming an autocatalytic coupling. An electrical potential gradient is established along the crevice length causing electromigration of anions into and cations out of the crevice. Although mass transport will eventually balance chemical equilibrium, continual crevice expansion as well as perturbations to transient and spatial activity profiles introduced by long and short range ionic and neutral interactions prevents establishment of a true steady state condition. The non-ideal behaviour of the crevice solution couples the transport of each neutral and ionic species in the crevice solution. Figure 4.2.1 shows that, after an initially rapid drop in pH, a very slight increase in pH results due to crevice expansion during the first ten hours. If this were an ideal solution, the pH would continue to increase due to crevice expansion; this trend is seen in the transient pH profiles predicted by ideal solution theory [21]. However, as the hydrogen ion activity depends upon the ionic strength of the crevice solution, and because the net rate of ionic species accumulation in the crevice due to electromigration is greater than the rate of volume increase, the effect of increasing

molality of surrounding ions eventually overpowers the crevice expansion effect and the pH experiences a secondary drop.

Figure 4.2.2 compares the predicted steady state spatial pH profile of the present crevice corrosion model with the model of Evitts [6], Sharland [7], and Walton et al. [8]. It is clearly seen that this model significantly improves on the predictions of the other models. A lower pH in the crevice is predicted by the current model, predominantly because inter-ionic forces that restrict the transport of the hydrogen ion out of the crevice are accounted for using a more sophisticated activity coefficient model. This results in a higher steady state hydrogen ion activity in the crevice solution. This prediction more closely corresponds with the experimental observations of Alavi and Cottis [2] than the other models.

Figure 4.2.3 displays the predicted transient activity coefficient profile for a few important species in the solution located 7.5 cm from the mouth of the crevice. At this location, the ionic strength of the solution is greatest. Although activity coefficients were calculated along the whole crevice length, only the activity coefficients 7.5 cm from the crevice mouth are presented here for brevity. The predicted transient activity profile of Na^+ 7.5 cm from the mouth of the steel crevice is also plotted on the secondary axis. The figure shows that activity coefficients for H^+ , Na^+ , and Cl^- (referred to as γ_{H^+} , γ_{Na^+} , and γ_{Cl^-} respectively from this point on) initially increase as the ionic strength of the crevice solution increases. Although Na^+ is driven from the crevice interior, γ_{Na^+} increases due to increased short range interactions with anions electromigrating into the crevice, locally produced cations, and neutral species. Cl^- is transported into the crevice at a faster rate than it is consumed by chemical reactions.

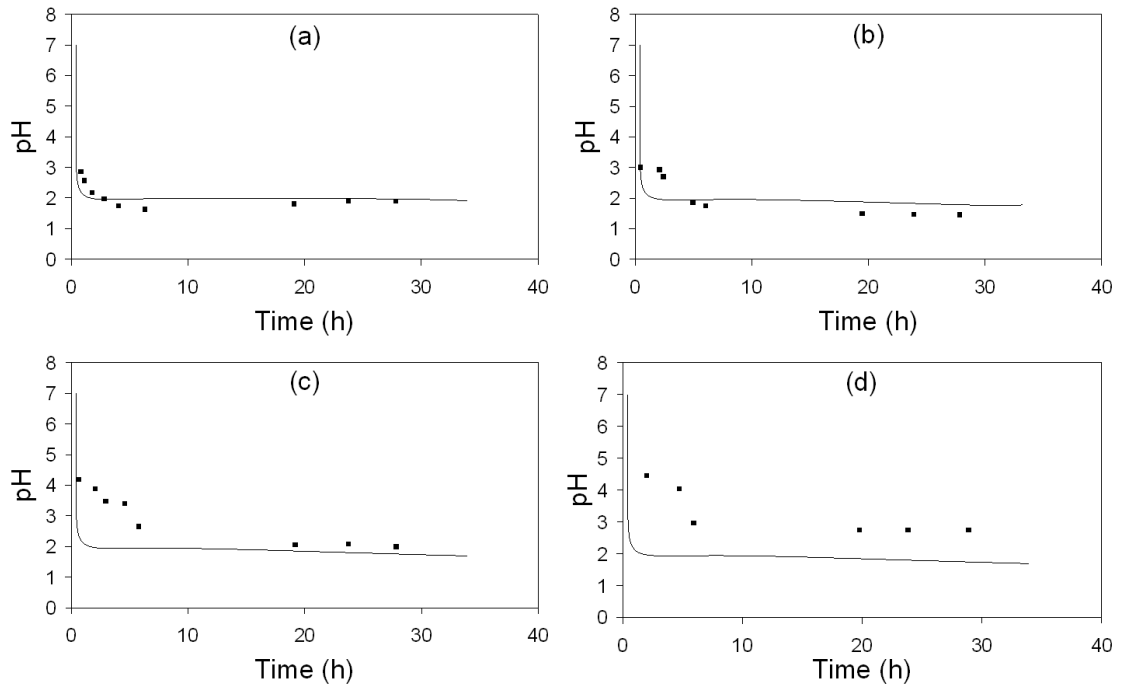


Figure 4.2.1. Comparison of Predicted Transient pH Profile to Experimentally Determined Profile in a Type 304 Stainless Steel Crevice (25°C, 0.6 Molar NaCl Bulk Solution, Dimensions 90 μm x 2.5 cm x 8.0 cm): a) 1 cm from mouth; b) 2 cm from mouth; c) 4 cm from mouth; d) 7.5 cm from mouth

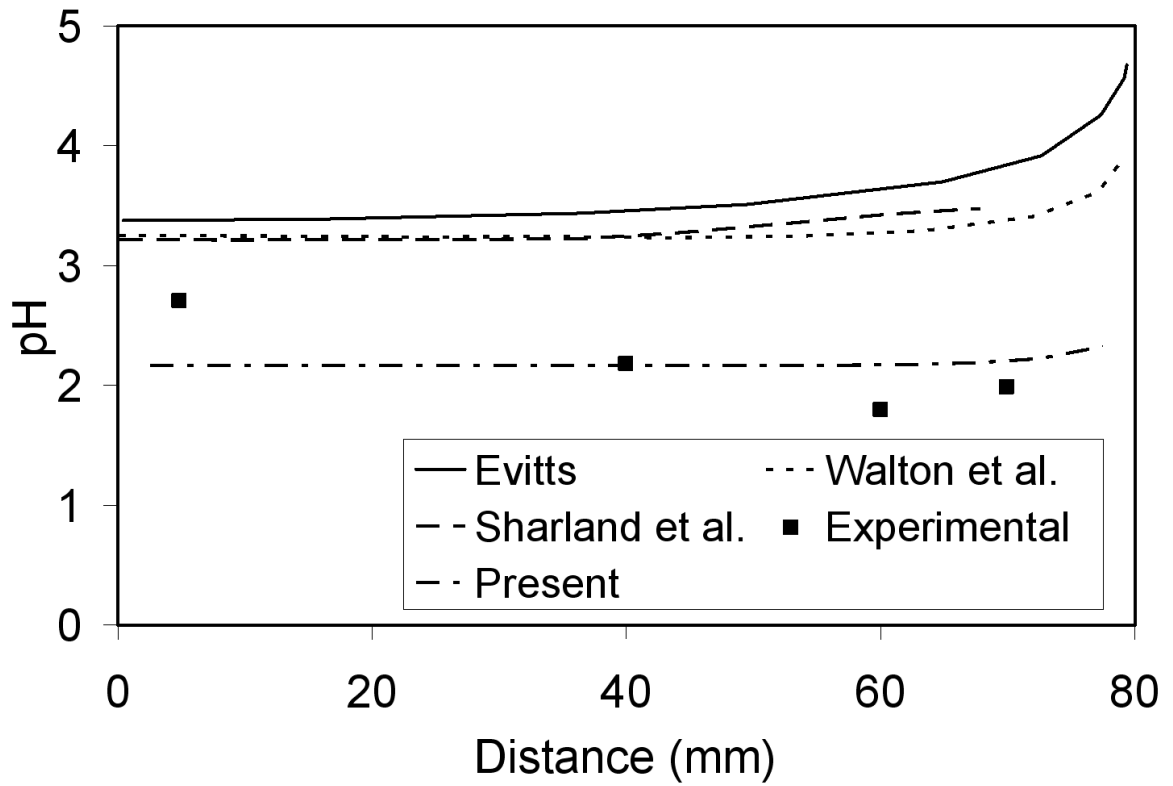


Figure 4.2.2. Comparison of Predicted pH Profile Against Predictions of Previously Published Models and the Experimental Observations of Alavi and Cottis in a Type 304 Stainless Steel Crevice (25°C, 0.6 Molar NaCl Bulk Solution, Dimensions 90 μm x 2.5 cm x 8.0 cm)

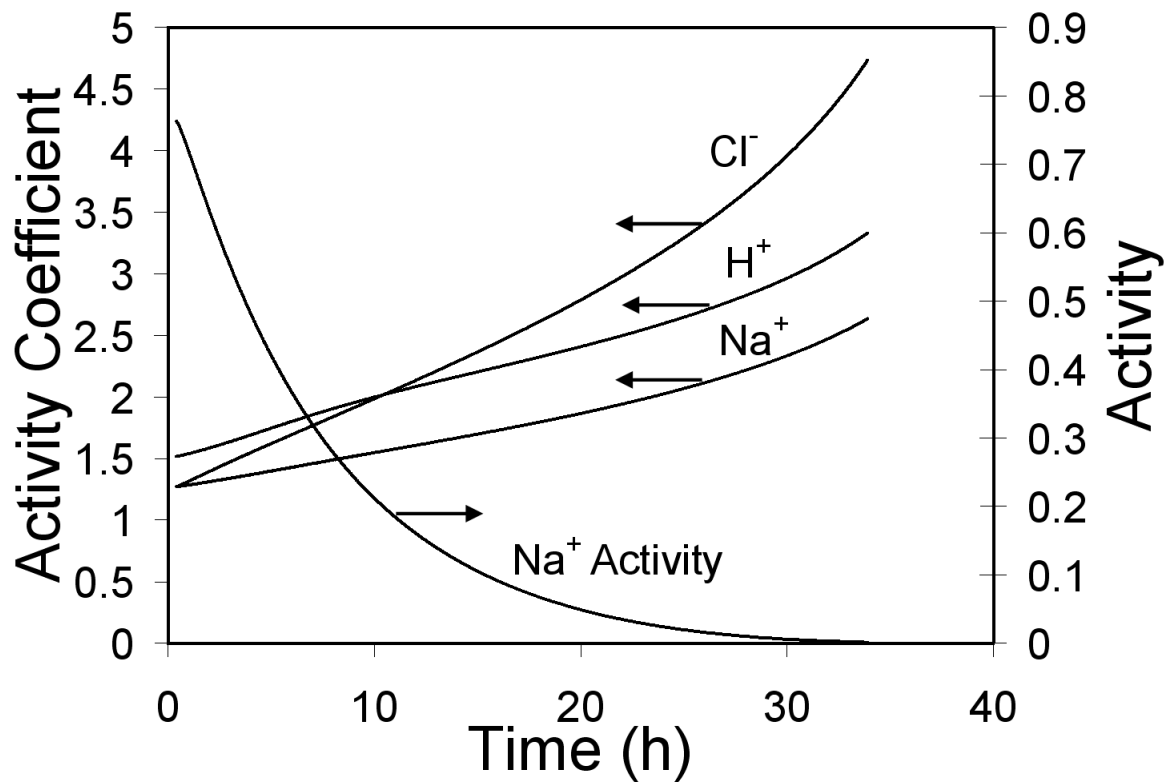


Figure 4.2.3. Predicted Transient Activity Coefficient Profile of Several Important Ions 7.5 cm From the Mouth of a Type 304 Stainless Steel Crevice (25°C, 0.6 Molar NaCl Bulk Solution, Dimensions 90 μm x 2.5 cm x 8.0 cm)

Increased short range ionic interaction combined with long range interactions increases γ_{Cl^-} . H^+ is essentially a point charge; its presence near other ions creates a large disturbance to the surrounding ionic cloud manifested as an initially large activity coefficient. At the time Na^+ is nearly depleted in the crevice solution 7.5 cm from the mouth, the rate of increase of γ_{Cl^-} increases. This suggests that the presence of Na^+ inhibits the non-ideal influence of Cl^- on the crevice solution. Even when Na^+ is nearly depleted in the crevice solution, γ_{Na^+} continues to rise due to increasing ionic strength. Short and long range interactions between H^+ and other ions in the crevice solution increases γ_{H^+} thereby dropping the pH. This in turn causes the passive current, which is proportional to the rate of metal dissolution, to exponentially increase. This secondary pH drop is due to ionic interactions. When inter-ionic forces are not incorporated into the model (the activity coefficient solver is turned off), the predicted pH slowly rises as the crevice gradually expands and no secondary pH drop is generated [21].

The transient passive current and ionic strength 7.5 cm from the crevice mouth is shown in Figure 4.2.4. The transient passive current profile nearly mirrors the shape of the transient pH curve while the transient ionic strength profile in the crevice solution is approximately linear. Mass transport and chemical equilibrium processes work to smooth out the non-linear increase in time of the rate of metal dissolution (proportional to the passive current). If cations were not being transported out of the region, the ionic strength would increase in a trend similar to the metal dissolution rate. However, as the dissolution rate increases, so does the rate of mass transport via electromigration. This plot shows a linear increase of the ionic strength with time. This implies that, even while the rates of transport and dissolution are changing, the ratio of the magnitude of the rates

of the two processes remains approximately constant. This results in a linear increase in ionic strength. This figure also shows that, because Pitzer's model is applicable only up to an ionic strength of about 6 mol/kg [19], the incubation period for this crevice can only be accurately simulated for about 40 hours.

Figure 4.2.5 shows transient activity profiles of Cl^- , Na^+ , and H^+ throughout the type 304 stainless steel crevice. Driven into the crevice by a potential gradient, the chloride ion activity approaches the limits of applicability of Pitzer's model [1].

4.2.3.2 Titanium crevice

The crevice corrosion incubation period of a titanium crevice measuring 1 cm deep and 1 cm wide with a 1 μm gap immersed in 0.5 M sodium chloride solution was simulated for 45 hours at 25°C to demonstrate the versatility of the model. The chemical reactions assumed to occur in the crevice solution are listed in Table 4.1.2 [22]. The ratio of simulated time to real time for this system was approximately 1.9 to 1 when run on a 3.06 GHz Pentium[®] 4 Processor with 1 GB of RAM.

Griess and He et al. reported that a significant portion of the cathodic charge is supplied by internal hydrogen ion reduction in a titanium crevice [10, 23]. In this model, hydrogen evolution is assumed to constitute 70% of the cathodic load. This is based upon the recent findings of He et al. [23] who reported that 60% to 75% of the cathodic charge is supported by internal hydrogen ion reduction. Hydrogen evolution affects both the solution pH and the current density flowing through the crevice solution. There is less current flowing through the solution because a portion of the anodic current is consumed inside the crevice.

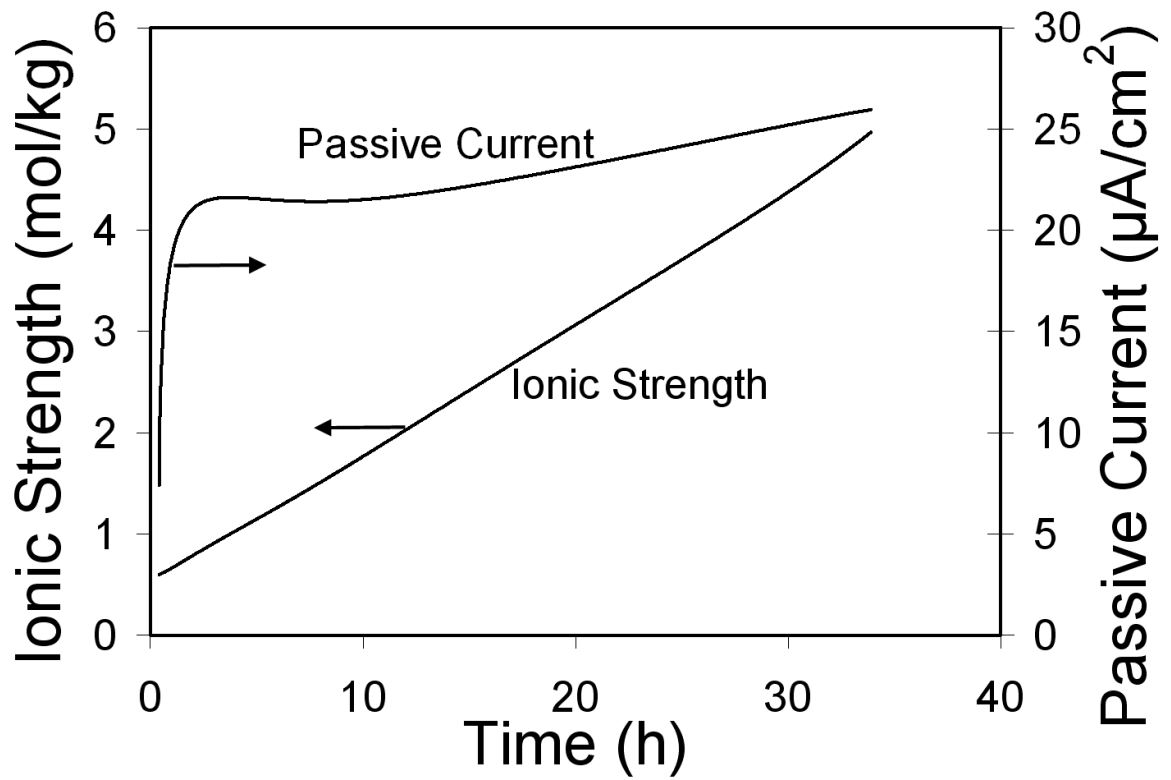


Figure 4.2.4. Predicted Transient Ionic Strength and Transient Passive Corrosion Current Profiles 7.5 cm From the Mouth of a Type 304 Stainless Steel Crevice (25°C, 0.6 Molar NaCl Bulk Solution, Dimensions 90 μm x 2.5 cm x 8.0 cm)

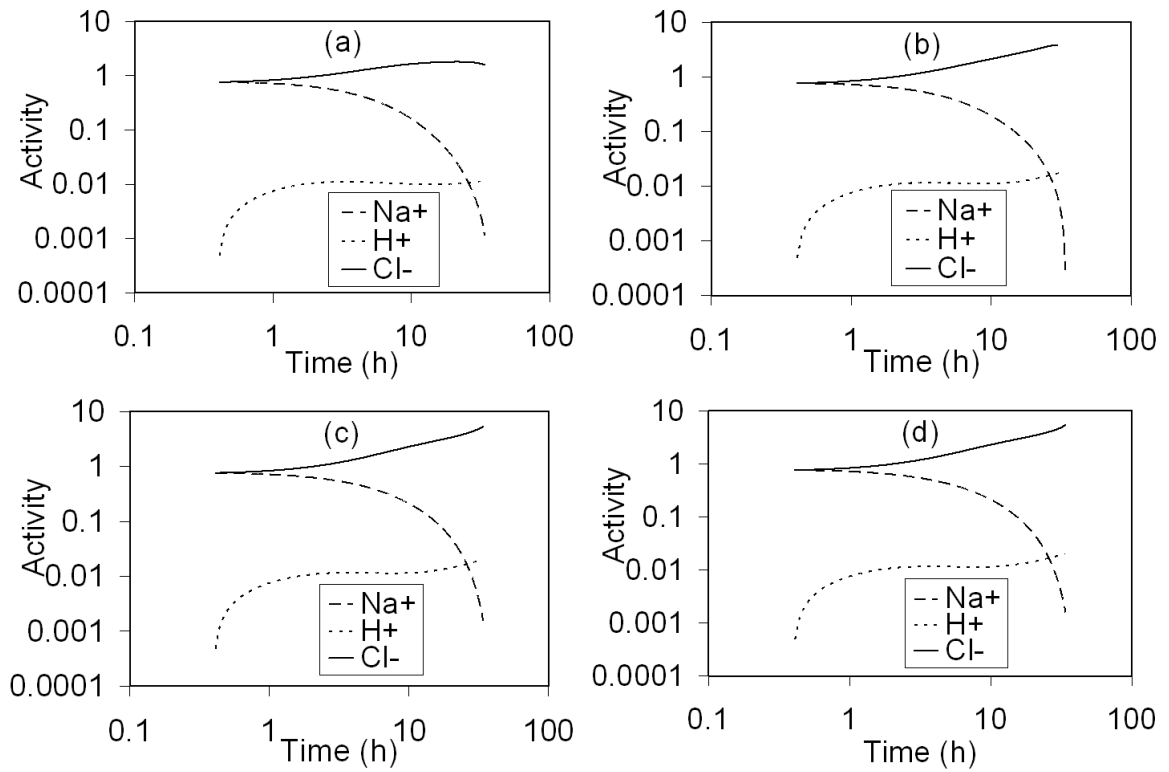


Figure 4.2.5. Predicted Activity of Several Important Ions in a Type 304 Stainless Steel Crevice (25°C, 0.6 Molar NaCl Bulk Solution, Dimensions 90 μm x 2.5 cm x 8.0 cm): a) 1 cm from Mouth; b) 2 cm from Mouth; c) 4 cm from Mouth; d) 7.5 cm from Mouth

Equation (4.2.7) is modified for this special case:

$$i(x) = \frac{\int_0^x i_p(x)(1 - \Psi) dA_m(x)}{A_{cs}(x)} \quad (4.2.27)$$

Here, Ψ represents the fraction of the anodic current supplied by hydrogen ion reduction. Furthermore, because the solution pH is increased by hydrogen ion reduction, this affects the magnitude of the passive current (see equation (4.2.4)).

Predicted transient activity coefficient profiles of Na^+ , Cl^- , and H^+ at the crevice tip are shown in Figure 4.2.6. It is apparent that interactions involving H^+ have significant influence on chemical conditions in the crevice solution because γ_{H^+} deviates significantly from unity. After deoxygenation, activity coefficients remain constant as the ionic strength increases. Hindered by interaction with other ions, H^+ is unable to migrate out of the crevice as fast as it is produced via hydrolysis. This increases the metal dissolution rate due to increased acidity levels. The influx of metallic cations into the crevice due to metal dissolution, and influx of anions due to electromigration both increase autocatalytically. A solution of high ionic strength results where the effects of short range inter-ionic forces are significant. Because H^+ has a very high surface charge density, γ_{H^+} is extremely sensitive to short range interactions and it therefore dramatically increases after approximately five hours of immersion. γ_{Na^+} increases more slowly while γ_{Cl^-} exhibits a slight inverse response.

Figures 4.2.7 and 4.2.8 show the transient pH and Cl^- activity at the tip, center, and mouth of the crevice. Hydrogen ions produced through metal ion hydrolysis are transported to the crevice mouth at a rate that slower than they are produced. The initial

rate of pH drop is high requiring small time steps to compute its trajectory. As the crevice mouth is approached, the electromigration current density builds in magnitude and, therefore, Cl^- migrates to the crevice tip with little opposition in the relatively dilute solution. Towards the crevice tip, the solution becomes increasingly concentrated; short range coulombic forces between ions become significant and offer increased resistance to mass transport. However, the iR drop decreases as the solution conductivity increases thereby lowering the resistance to mass transport. The pH reaches a minimum value at the crevice tip. Driven into the crevice by electromigration forces that are greater than smoothing diffusive forces, the chloride ion activity is also greatest at the crevice tip. Although the rate of increase of the chloride ion activity reduces due to slow crevice expansion, the pH undergoes a secondary drop. Therefore, the rate of increase of the hydrogen ion activity coefficient is greater than the rate of crevice expansion.

Using an infinitely dilute transport model, the transient pH and Cl^- concentration were simulated and compared with the results shown in Figures 4.2.7 and 4.2.8. The hydrogen ion concentration predicted using this model is higher than that predicted using infinitely dilute solution theory suggesting that the transport of H^+ is hindered by the presence of other cations repelling it and anions attracting it. However, the chloride ion concentration also higher using the non-ideal model suggesting that Cl^- is pulled into the crevice by electromigration and by attraction to cationic species in the crevice solution.

4.2.4 Conclusions

A mass transport model applicable to moderately dilute solutions has been solved simultaneously with chemical equilibrium and the ionic interaction model of Pitzer [1] to predict the incubation period of a type 304 stainless steel crevice and a titanium crevice.

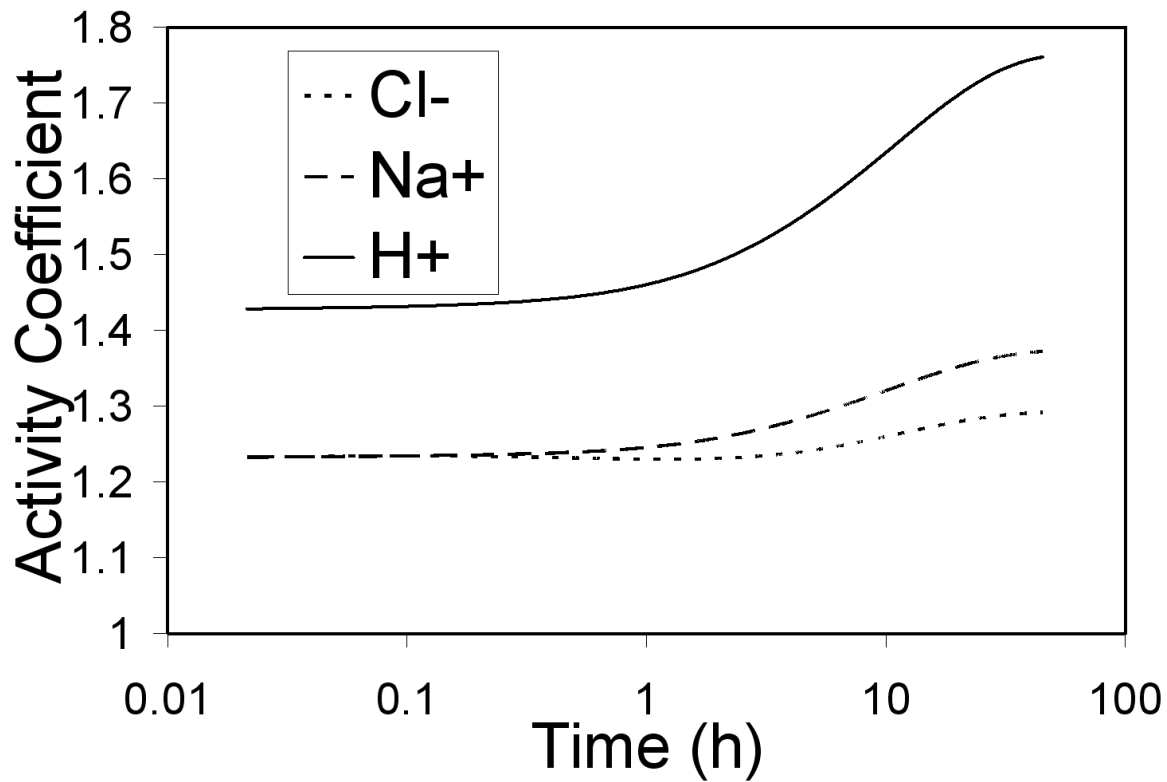


Figure 4.2.6. Predicted Activity Coefficients of Several Important Ions in a Titanium Crevice (25°C, 0.5 Molar NaCl Bulk Solution, Dimensions 1 μm x 1.0 cm x 1.0 cm)

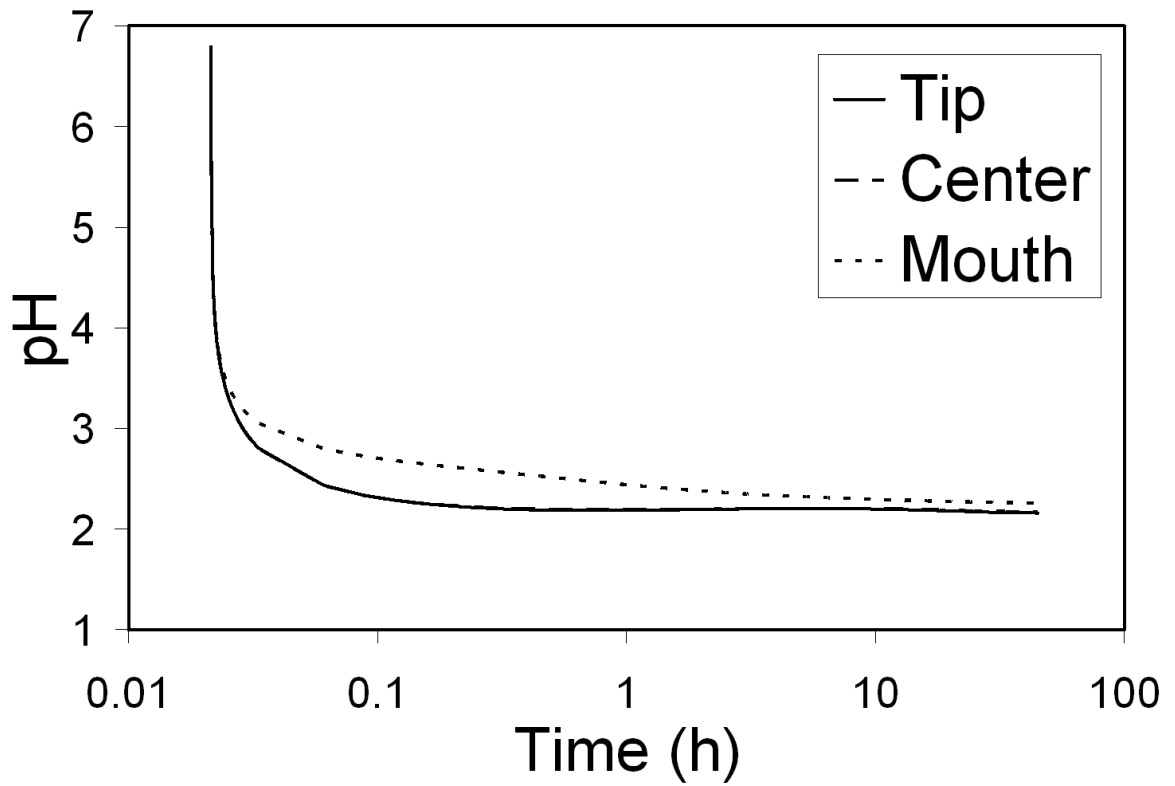


Figure 4.2.7. Predicted Transient pH Profile at the Tip, Center, and Mouth of a Titanium Crevice (25°C, 0.5 Molar NaCl Bulk Solution, Dimensions 1 μm x 1.0 cm x 1.0 cm)

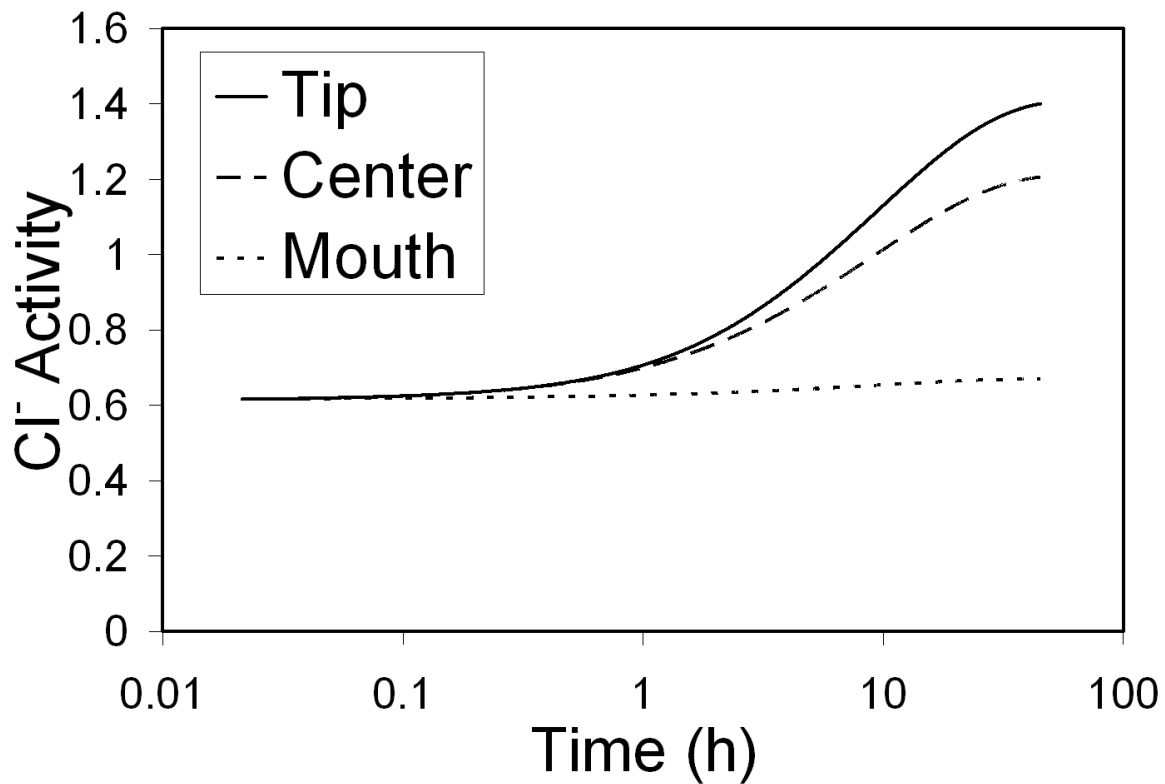


Figure 4.2.8. Predicted Transient Chloride Ion Activity Profile at the Tip, Center, and Mouth of a Titanium Crevice (25°C, 0.5 Molar NaCl Bulk Solution, Dimensions 1 μm x 1.0 cm x 1.0 cm)

The predictions of the model agree quite well with the experimental observations of Alavi and Cottis [2]. Based upon this work, the following conclusions can be made:

1. The model predicts that concentrated solutions form in an occluded crevice where convective transport is negligible. A potential difference between anode and cathode causes electromigration of anions and cations inside a differential aeration cell. The iR drop is the portion of the potential difference that drives electromigration; the electrical potential of the solution is transferred to ionic kinetic energy. Severe acidity develops because H^+ is generated by hydrolysis faster than it can be transported out.
2. Because the hydrogen ion concentration predicted using the moderately dilute model is higher than that predicted by ideal solution theory, inter-ionic short and long range forces hinder its rate of mass transport. However, the predicted chloride ion concentration is also higher using the moderately dilute solution model. Therefore, coulombic forces pull the chloride ion into the crevice thus increasing its rate of mass transport.
3. Binary and ternary interactions between anions, cations, and neutral species introduce continual perturbations to transient and spatial activity profiles in the crevice solution. As well as increasing the required iterations to solve the mass

transport equation, these interactions prevent attainment of a steady state condition in strong electrolytic solutions.

4. The effect of the sodium ion is to counteract the adverse influence of the chloride ion on crevice solution ideality. Model predictions show that upon depletion of Na^+ , γ_{Cl^-} increases more rapidly.

5. Ionic interactions are responsible for a secondary drop in pH. Immediately after deoxygenation, the pH drops rapidly due to chemical hydrolysis of metal ions. The pH would normally reach a minimum and begin to increase due to slow crevice expansion. However, competing with this is the increasing ionic strength of the solution causing the hydrogen ion activity to increase. The effect of increasing activity eventually supersedes the effect of the expanding crevice causing the secondary pH drop.

4.2.5 References

1. K. S. Pitzer, *J. Phys. Chem.*, 77, 268 (1973).
2. A. Alavi and R. A. Cottis, *Corrosion Science*, 27, 443 (1987).
3. M. K. Watson and J. Postlethwaite, *Corrosion*, 46, 522 (1990).
4. M. K. Watson and J. Postlethwaite, in *Proceedings of Corrosion/90*, National Association of Corrosion Engineers, pg. 156:1, Las Vegas, NV (1990).
5. M. K. Watson and J. Postlethwaite, *Corrosion Science*, 32, 1253 (1991).
6. R. W. Evitts, "Modeling of Crevice Corrosion", Ph.D. thesis, University of Saskatchewan, Saskatoon, Saskatchewan, Canada (1997).
7. S. M. Sharland, *Corrosion Science*, 33, 183 (1992).
8. J. C. Walton, G. Cragolino, and S. K. Kalandros, *Corrosion Science*, 38, 1 (1996).
9. J. Newman, "Electrochemical Systems", Prentice Hall, Toronto (1973).
10. J. C. Griess Jr., *Corrosion*, 24, 96 (1968).

11. L. L. Shrier, R. A. Jarman, G. T. Burstein, "Corrosion", 3rd Ed., pp. 1:101, 2:20, Butterworth-Heinemann Ltd, Oxford, UK (1994).
12. J. W. Oldfield and W. H. Sutton, *British Corrosion Journal*, 13, 13 (1978).
13. S. Bernhardsson, L. Eriksson, J. Ooppelstrup, I. Puigdomenech, and T. Wallin, in *Proceedings of 9th Scandinavian Corrosion Congress, Addendum 1*, p. 1, Copenhagen, Denmark, Sept 12 – 14 (1983).
14. S. E. Lott and R. Alkire, *Corrosion Science*, 28, 479 (1988).
15. G. Hultquist, M. Seo, T. Leitner, C. Leygraf, and N. Sato, *Corrosion Science*, 227, 479 (1987).
16. M. B. Vukmirovic, N. Vasiljevic, N. Dimitrov, and K. Sieradzki, *Journal of the Electrochemical Society*, 150, B10 (2003).
17. Wilke, C. R., Chang, Pin, *Am. Inst. Chem. Eng. J.*, 1, 264 (1955).
18. Sehgal, G. S. Frankel, B. Zoofan, and S. Rokhlin, *Journal of the Electrochemical Society*, 147, 140 (2000).

19. K. S. Pitzer, "Activity Coefficients in Electrolyte Solutions", 2nd Ed., pp. 77 – 91, 122 – 125, CRC Press, Boca Raton, FL (1991).
20. C. F. Baes and R. E. Mesmer, "The Hydrolysis of Cations", Wiley, New York (1976), pp. 212, 227, 243.
21. K.L. Heppner, R.W. Evitts, and J. Postlethwaite, Canadian Journal of Chemical Engineering, 80, 857 (2002).
22. A. Liberti, V. Chiantella, F. Corigliano, Journal of Inorganic and Nuclear Chemistry, 25, 415 (1963).
23. X. He, J. J. Noël, and D.W. Shoesmith, Corrosion, 60, 378 (2004).

4.3 Effect of Hydrogen Ion Reduction on Crevice Corrosion Initiation *

In the previous section, a sophisticated model was used to predict the crevice solution chemistry using Pitzer's Equations, and thus, showed the effect of the bulk solution composition on the incubation period of type 304 stainless steel and titanium. Of particular interest in the simulation of titanium crevice corrosion is the effect of crevice-internal hydrogen ion reduction. It is well known that hydrogen ion reduction plays a significant role in the titanium crevice corrosion process. Furthermore, because it is well known that titanium will not undergo active crevice corrosion in 0.5 M NaCl solution at 25°C, this section investigates the effect of crevice-internal hydrogen ion reduction in the same bulk solution at elevated temperatures.

In this research, the effect of the level of hydrogen ion reduction on a titanium crevice immersed in 0.5 M NaCl solution at 70°C was investigated. The fraction of the total dissolution current supplied by hydrogen ion reduction, Ψ , was varied from 0 to 0.8 in increments of 0.2 and the steady state pH, conductivity (κ), and iR drop (Φ) profiles in the crevice were calculated. The mass transport model of Watson and Postlethwaite [1] was employed and the crevice was assumed to be passivated.

As Ψ increased, the solution conductivity and the iR drop along the crevice were significantly reduced while the pH showed only a slight increase. A plot of total iR drop along the crevice length, pH at the crevice tip, and solution conductivity at the crevice against Ψ was constructed and the following relationships were obtained ($R^2 > 0.995$):

$$pH = 0.0091\Psi + 1.27 \quad (4.3.1)$$

* Reference: K.L. Heppner and R.W. Evitts (2005) "Modelling of the Effect of Hydrogen Ion Reduction on the Crevice Corrosion of Titanium" in *Environment-Induced Cracking. Chemistry, Mechanics, and Microstructure*. Eds. Shipilov S.A., Jones, R.H., Ulive, J.-M. and Rebak, R.B. Elsevier, Oxford, UK. In Press.

$$\Phi = -0.919\Psi + 97.0 \quad (4.3.2)$$

$$\kappa = -0.0044\Psi^2 - 0.399\Psi + 157 \quad (4.3.3)$$

Of the three solution properties studied, the pH showed the weakest dependence upon the hydrogen ion reduction fraction, varying linearly from 1.27 to 2.01 as Ψ varied from 0% to 80%. The iR drop along the crevice length showed the greatest sensitivity to the hydrogen ion reduction fraction.

4.3.1 Introduction

Crevice corrosion is a dangerous form of localized corrosion often initiated by environment induced cracking. Once a crack is initiated, localized attack is at least partially sustained by crevice corrosion or similar phenomena. Titanium is a metal which, under normal conditions, will resist corrosive attack quite well. However, it is susceptible to crevice corrosion. It is known that hydrogen evolution is a significant cathodic charge contributor in a titanium crevice system [2, 3]. The extent to which hydrogen evolution occurs in a titanium crevice is unique to this metal and can account for up to 80% of the total cathodic charge [2]. Heppner et al. [4] recently published a crevice corrosion model which accounted for the effect of internal hydrogen evolution on the crevice corrosion incubation period but did not investigate the effect of H^+ reduction in detail. The focus of the current study is to predict the overall effect of hydrogen ion reduction upon the crevice corrosion process. By varying the percentage of cathodic charge contributed by hydrogen evolution, the magnitude of the effect of hydrogen evolution upon mass transport through the crevice solution can be determined.

The rate of anodic metal dissolution is equal to the combined rate of external (to the crevice) oxygen reduction and internal hydrogen ion reduction in a differential

aeration cell. In the absence of internal crevice cathodic reactions, the entire current leaving the anodic crevice walls and entering solution as an ionic mass flux would induce electromigration transport through the crevice solution. However, hydrogen evolution near the anode consumes a portion of the current, thereby reducing electromigration transport rates in the solution. Reduced mass transport decreases the rate of chloride ion influx. However, reduced mass transport rates also hinder the transport of hydrogen ions out of the crevice. Yet, hydrogen evolution consumes hydrogen ions in solution and counteracts the effects of chemical hydrolysis of Ti^{4+} ions which produces H^+ . Overall, hydrogen ion reduction increases the crevice solution pH and therefore reduces the magnitude of the passive current in the crevice. The coupling between passive current and pH is autocatalytic and is a primary cause of the development of aggressive solutions in a crevice. Because hydrogen ion reduction directly affects the system pH, it has a large impact upon the entire crevice corrosion process. In this work, the effect of hydrogen evolution on mass transport in the crevice solution will be examined in detail.

4.3.2 The mathematical model

Watson and Postlethwaite developed a model of mass transport applicable for dilute solutions [1]. This model has been shown previously to adequately represent transport in a crevice solution [5, 6] and is therefore used in this study:

$$\frac{\partial C_i}{\partial t} = D_i \nabla^2 C_i - \frac{z_i D_i F}{RT} \left(\nabla C_i \cdot \frac{i + i_{dp}}{\kappa} + \frac{\delta}{\varepsilon} C_i \right) + G_i \quad (4.3.4)$$

where the charge density is defined as:

$$\delta = F \sum_j z_j C_j \quad (4.3.5)$$

and the diffusion potential current density is:

$$i_{dp} = F \sum_j z_j D_j \nabla C_j \quad (4.3.6)$$

The current density is determined from the passive current integrated along the crevice length:

$$i(x) = \frac{\int_{ip}^x i_p(x) dA_m(x)}{A_{cs}(x)} \quad (4.3.7)$$

The source term in equation (4.3.4), G_i , represents the influence of chemical reaction kinetics upon the concentration profile in space and time. In this study, reaction kinetics are assumed to occur much faster than mass transport processes. Therefore, chemical equilibrium is assumed at all times, an assumption which mathematically decouples mass transport and chemical reaction processes. With this assumption in place, the effect of chemical reaction is represented as a set of chemical equilibrium expressions for the hydrolysis of Titanium (IV) [7] (see Table 4.1.2). Equilibrium constants were adjusted for temperature using the method of Criss and Cobble [5, 8].

Electrode reactions which are assumed to occur inside the crevice are the dissolution of Titanium (IV) (anodic) and the reduction of hydrogen ions (cathodic):



At the bold surface surrounding the crevice mouth, oxygen reduction is assumed to occur:



In this model, only the crevice interior is modelled; the rate of mass transfer of oxygen to the bold surface is considered to be non-limiting. The time required to deoxygenate the crevice is calculated via the following equation:

$$t_{deoxy} = \frac{4FA_{cs}LC_{O_2}}{i_p A_m} \quad (4.3.11)$$

The incubation period is the sum of the deoxygenation time and the time for the crevice solution pH to drop below the critical pH. The rate of anodic and cathodic processes must be equal by mixed potential theory [9] and are proportional to the passive current. The passive current is adjusted for temperature using an Arrhenius type expression and pH using a Freundlich Isotherm [10]:

$$i_p = i_{p,T_0} \exp \left[- \left(\frac{E_a}{RT} \left(\frac{1}{T} - \frac{1}{T_0} \right) \right) \right] \quad (4.3.12)$$

$$\log(i_p) = \log(k) - n \cdot pH \quad (4.3.13)$$

The activation energy for Titanium (IV) is 12,700 J/mol [3]. Values of n are based upon the electrical charge of the dissolving metal ion and can be interpolated from values given by Shrier [10]. Use of both equations requires the specification of a reference passive current density, temperature, and pH. For titanium, a reference passive current of 0.1 $\mu\text{A}/\text{cm}^2$ is used at 25°C and a pH of 7. This value is interpolated from experimental data obtained by Griess [3].

4.3.3 Numerical solution of the model

The mass transport model, equation (4.3.4), was solved using a finite volume method. The electromigration term was discretized using an upwind formulation, i.e.:

$$\frac{dC}{dx} = \left(\frac{1+\alpha}{2} \right) \frac{C_{i+1} - C_i}{x_{i+1} - x_i} + \left(\frac{1-\alpha}{2} \right) \frac{C_i - C_{i-1}}{x_i - x_{i-1}} \quad (4.3.14)$$

where:

$$\alpha = \frac{z(i + i_{dp})}{|z(i + i_{dp})|} \quad (4.3.15)$$

Thus, the direction of the one-sided finite difference expression depends upon the direction of ionic electromigration. Use of an upwind formulation avoids the possibility of negative transport coefficients and therefore ensures that a more realistic solution of the transport equation will be obtained [11].

One boundary condition for the mass transport model was provided by the magnitude of the passive current at the crevice tip:

$$z_i u_i F C_i \frac{i + i_{dp}}{\kappa} - D_i \frac{dC_i}{dx} = \frac{i_p}{z_i F} \quad (4.3.16)$$

Equation (4.3.16) is a pseudo steady state mass balance at the metal-solution interface. The right hand side of equation (4.3.16) is the corrosion induced ionic flux. At the crevice mouth, the bulk concentration was assumed:

$$C_i = C_i^{bulk} \quad (4.3.17)$$

The finite volume grid over which the transport equation is solved, as well as the solution algorithm, have been shown previously (Figures 4.1.1 and 4.1.2).

4.3.4 Results and discussion

He et al. recently performed an experimental study upon a high purity titanium crevice immersed in an acid chloride solution at 70°C [2]. By comparing the weight loss measurement with the integrated current-time graph obtained during the course of the experiment, the relative influence of hydrogen evolution upon the anodic current was determined. He et al. determined that approximately 70% of the cathodic charge is carried by hydrogen ion reduction [2]. This measurement was the basis of selection of the value of Ψ , the fraction of cathodic charge carried by hydrogen evolution, for the present model. While the effect of hydrogen ion reduction upon metal dissolution is

experimentally measurable, its effects upon many properties within the crevice are not readily obtained. For this reason, the current study was undertaken.

At the start of the crevice corrosion process, the deoxygenation of the crevice solution causes the formation of a differential aeration cell. Once a differential aeration cell exists, a strong acid-chloride solution may develop in the crevice. The measurement of He et al. [2] gave an indication of the time-averaged influence of hydrogen ion reduction. However, at the beginning of the experiment when the solution pH was relatively high and oxygen was available, the portion of the cathodic charge carried by hydrogen ion reduction was likely quite low. As the crevice solution became more acidic and oxygen was depleted, the dependency of the anodic current upon hydrogen evolution, due to the concentration overpotential, would have increased substantially. Therefore, the portion of the anodic current supplied by hydrogen ion reduction likely varied between approximately 0% and 80%. This is the range of values of Ψ used in this study.

For each simulation in this work, a titanium crevice measuring 1 μm across the gap, 1 cm wide, and 1 cm deep was used. It was immersed in 0.5 M NaCl solution at 70°C. Figure 4.3.1 illustrates the effect of Ψ on the pH, iR drop, and conductivity of the crevice solution. From this figure, as the portion of the anodic current supported by hydrogen ion reduction was increased from 0 to 0.8, the iR drop in solution along the crevice length decreased. This is because the net current density or net charge flux flowing from the anodic crevice wall decreases as Ψ increases. The net current density at any point in the crevice is the difference between current supplied by metal dissolution and current consumed by hydrogen ion reduction, i.e.:

$$i_p^{net} = i_p (1 - \Psi) \quad (4.3.18)$$

The current density leaving the crevice wall adds to the current density flowing through solution, and thus, the magnitude of the current density in solution depends on the net anodic current. The addition of current released from the crevice wall to the current flowing through solution is analogous to tributaries adding to a river.

Further examination of Figure 4.3.1 reveals that as the iR drop decreases, the solution conductivity also decreases. This indicates that the magnitude of the current density flowing through solution is more sensitive to Ψ than conductivity is to Ψ . This can be clarified using Ohm's Law for a system of uniform composition:

$$\nabla\Phi = -\frac{i}{\kappa} \quad (4.3.19)$$

Because conductivity is in the denominator of equation (4.3.19), as it decreases it will tend to increase the potential gradient. Therefore, for the potential gradient to decrease, the current density must decrease to a greater extent than the conductivity.

Figure 4.3.1 also shows that as the rate of hydrogen ion reduction increases inside the crevice, the hydrogen ion concentration decreases and, thus, the pH increases. While hydrogen evolution consumes H^+ thereby increasing the pH, it also reduces the rate of electromigration which tends to increase the H^+ concentration in the crevice solution. Due to this competing effect, the pH is the property (of those studied in this work) which shows the least dependency upon the rate of hydrogen ion reduction. Furthermore, the iR drop is the solution property that is most sensitive to changes in Ψ .

In addition to its direct affect upon solution properties, the value of Ψ also affects the kinetic behaviour of the system. The conductivity is calculated from the concentration of each ionic species in solution and is therefore an indicator of the rate of change of the crevice solution composition with time. Conductivity is therefore used as

an indicator of the time to steady state onset. Examination of the conductivity profiles displayed in Figure 4.3.1 reveals that, as Ψ increases, so does the time required for the system to reach steady state.

As Ψ increases from 0 to 0.8, the time required for the system to reach a steady state condition increases from approximately 5 hours to approximately 18 hours.

Figure 4.3.2 shows the variation of pH and conductivity at the crevice tip, as well as iR drop along the crevice length as the value of Ψ is increased. Each solution property showed a distinct linear or parabolic variation with Ψ . The data points were fit to a best fit line and each correlation fit the data with excellent accuracy ($R^2 > 0.995$):

$$pH = 0.0091\Psi + 1.27 \quad (4.3.20)$$

$$\Phi = -0.919\Psi + 97.0 \quad (4.3.21)$$

$$\kappa = -0.0044\Psi^2 - 0.399\Psi + 157 \quad (4.3.22)$$

While the pH and the iR drop varied linearly with Ψ , conductivity showed a parabolic dependence. For pH to have linear dependence upon Ψ , the ratio of the rate of production of H^+ via chemical hydrolysis to the rate of transport of H^+ out of the crevice must remain constant for varying values of Ψ . However, for the conductivity to show concave-down parabolic dependence upon Ψ , the overall rate of transport of ions out of the crevice must outpace the rate of internal cationic production as Ψ increases. Thus, the dependency of these parameters upon Ψ gives insight into how the overall system adjusts to internal hydrogen ion reduction.

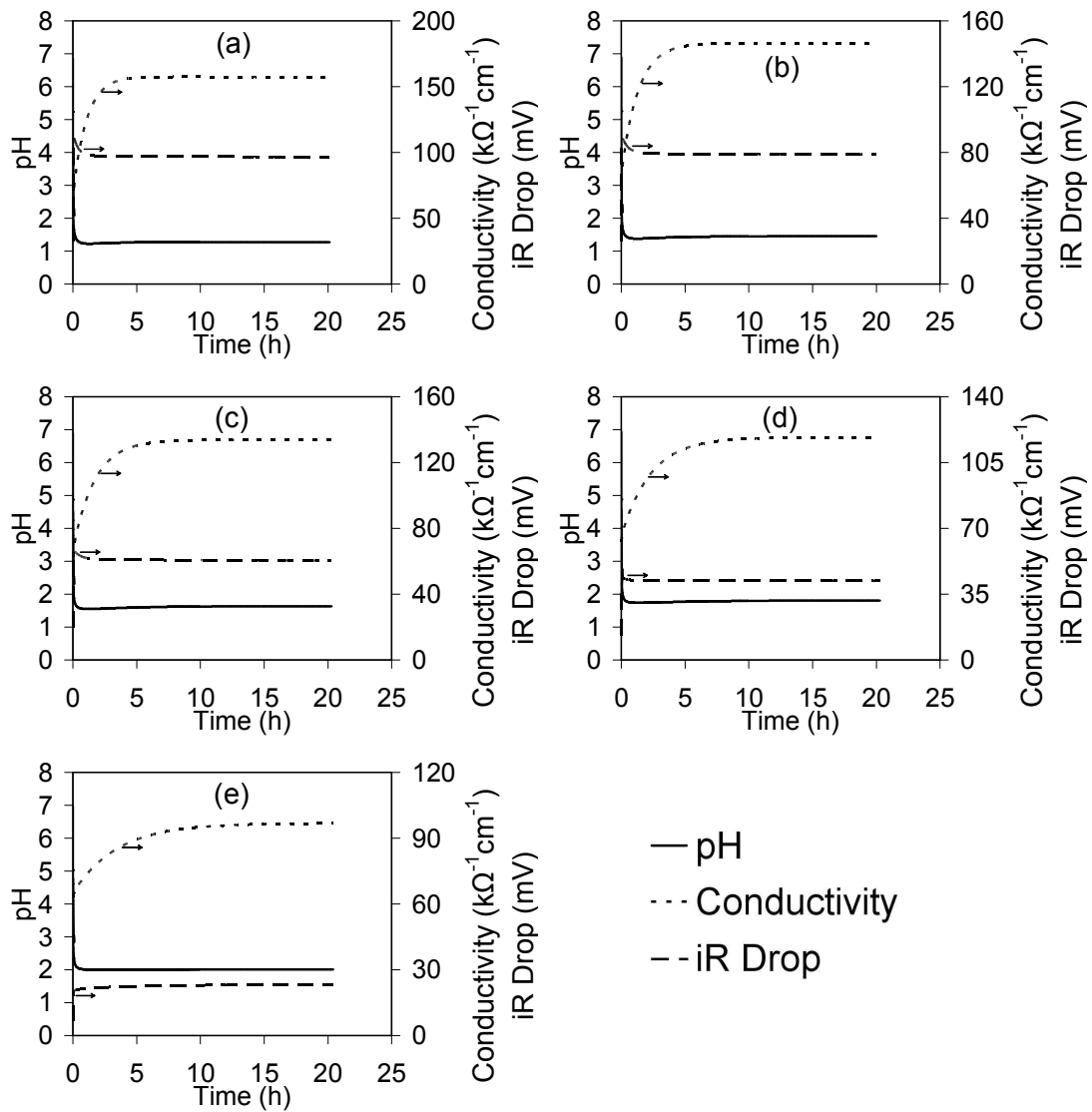


Figure 4.3.1. Predicted transient iR drop along the crevice length, pH at the tip, and conductivity at the tip in a titanium crevice measuring $1\ \mu\text{m}$ across the gap, $1\ \text{cm}$ deep, and $1\ \text{cm}$ wide and immersed in a $0.5\ \text{M}$ NaCl solution at 70°C : (a) 0% hydrogen evolution; (b) 20% hydrogen evolution; (c) 40% hydrogen evolution; (d) 60% hydrogen evolution; (e) 80% hydrogen evolution.

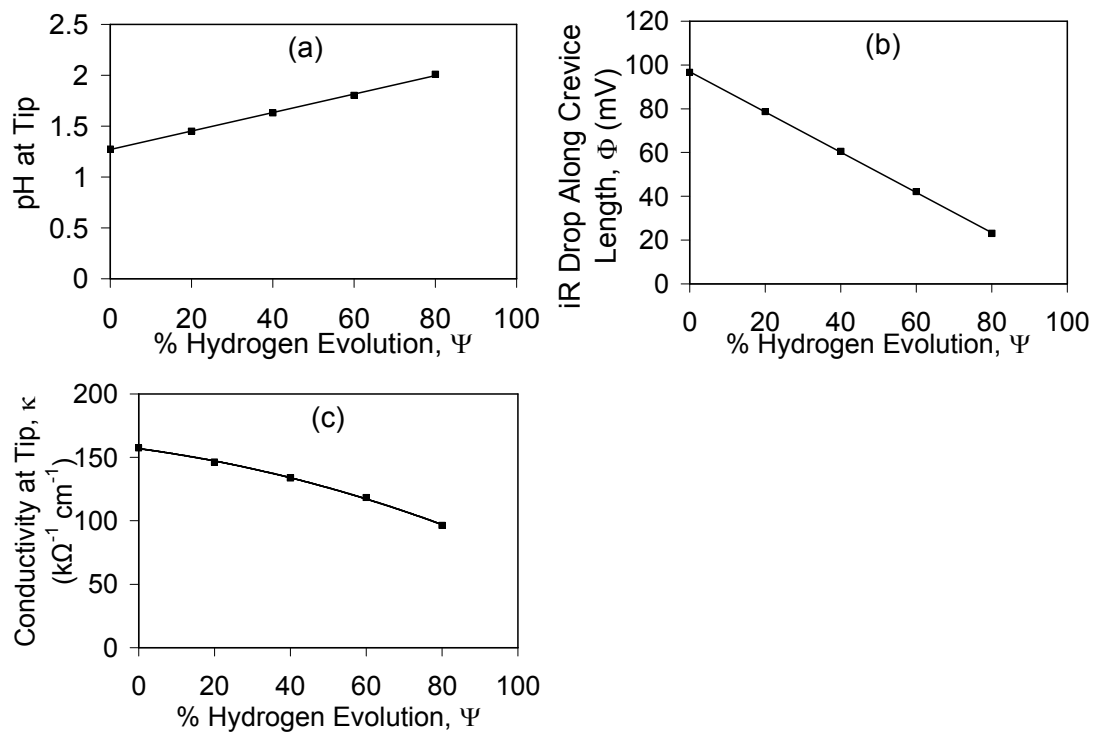


Figure 4.3.2. Variation of steady state solution properties with Ψ : (a) pH at the crevice tip; (b) iR drop along the crevice length; (c) conductivity at the crevice tip

4.3.5 Conclusions

Based upon the results of the preceding work, the following conclusions can be made:

1. Internal hydrogen ion reduction greatly impacts the crevice corrosion process in a titanium crevice. It has a marked effect upon the pH, conductivity, and iR drop in the crevice solution.
2. A linear dependence of pH upon Ψ is observed. This implies that, as Ψ is varied, the ratio of the rate of H^+ production due to chemical hydrolysis of Ti^{4+} to the rate of H^+ transport out of the crevice remains approximately constant.
3. A concave-down parabolic dependence of conductivity upon Ψ is also observed. This result suggests that the sum of ionic transport out of the crevice and H^+ reduction is more sensitive to changes in Ψ than the rate of anodic metal dissolution is to changes in Ψ . Because both mass transport out of the crevice and H^+ reduction decreases the conductivity while metal dissolution increases the conductivity, the conductivity decreases significantly with increasing Ψ .
4. Changing the value of Ψ causes the transient behaviour of the system to change. As the value of Ψ increases from 0 to 0.8, the time to steady state onset of the system changes from approximately 5 to approximately 18 hours.

5. As Ψ increases, both the iR drop and the conductivity in the crevice decrease. Therefore, the dependence of current density flowing through solution upon Ψ must be greater than the dependence of the conductivity upon Ψ .

6. Contrary to expectations, of the solution properties studied in this work, pH shows the least dependency upon the rate of hydrogen ion reduction. This is due to a competing effect. As Ψ increases, the rate of consumption of H^+ at crevice-internal cathodic sites increases while the rate of electromigration mass transport decreases. While H^+ consumption obviously increases the pH, decreased mass transport rates reduce the rate at which H^+ , which is produced via Ti^{4+} hydrolysis, electromigrates out of the crevice solution, thereby decreasing the pH. Overall, as Ψ increases, the crevice solution pH increases.

4.3.6 References

1. M. K. Watson, J. Postlethwaite, *Corrosion* **46** (1990) 522.
2. X. He, J. J. Noël, D.W. Shoesmith, *Corrosion* **60** (2004) 378.
3. J. C. Griess Jr., *Corrosion* **24** (1968) 96.
4. K.L. Heppner, R.W. Evitts, J. Postlethwaite, *Corrosion* **60** (2005) 718.
5. K.L. Heppner, R.W. Evitts, J. Postlethwaite, *Canadian Journal of Chemical Engineering* **80** (2002) 849.
6. K.L. Heppner, R.W. Evitts, J. Postlethwaite, *Canadian Journal of Chemical Engineering* **80** (2002) 857.
7. A. Liberti, V. Chiantella, F. Corigliano, *Journal of Inorganic and Nuclear Chemistry* **25** (1963) 415.
8. Criss, C. M. and J. W. Cobble, “The Thermodynamic Properties of High Temperature Aqueous Solutions. IV. Entropies of the Ions up to 200⁰ and the Correspondence Principle”, *Journal of the American Chemical Society* **86**, (1964) 5385 – 5390.
9. M. Stern, L. Geary, *J. Electrochem. Soc.* **104** (1957) 56.
10. L.L. Shrier, R. A. Jarman, G. T. Burstein (Eds.), *Corrosion* 3rd Ed., Butterworth-Heinemann Ltd, Oxford, UK, 1994, 2:20.
11. S.V. Patankar, *Numerical Heat Transfer and Fluid Flow*, Hemisphere, Washington, 1980.

4.4 Application of the Crevice Corrosion Initiation Model to Alloy Ranking*

The previous sections have shown the effect of the crevice gap, the solution composition and temperature, and the rate of crevice-internal hydrogen ion reduction. In this section, aspects of each of these studies are drawn upon to develop a comprehensive model of crevice corrosion initiation and apply it to predict the propensity of a passive alloy to crevice corrosion. It will be shown that the crevice corrosion initiation model herein presented – which accounts for non-ideal solution effects in both mass transport and chemical equilibrium, and includes the effect of crevice-internal hydrogen ion reduction – is capable of ranking alloys in accordance with their pitting resistance equivalence number (PREN) ranking.

In this work a mathematical model of crevice corrosion initiation is developed. The model utilizes a moderately dilute mass transport model that is augmented with Pitzer's ionic interaction equations, and it is therefore suitable for relatively concentrated electrolyte environments. It is applied to model the crevice corrosion initiation of Grade 2 titanium, along with four stainless steels, Types 304, 308, 314, and 405, in a typical Saskatchewan potash processing brine (3.62 M KCl, 3.39 M NaCl, 25°C, pH = 7). The simulation results are used to rank the alloys for their crevice corrosion resistance. The following ranking is obtained:

1. Grade 2 Titanium (UNS R50400)
2. Type 314 stainless steel (UNS S31400)
3. Type 308 stainless steel (UNS S30800)

* Reference: K.L. Heppner, K. and R.W. Evitts (2005) A Numerical Model to Rank Passive Alloys for Crevice Corrosion Susceptibility in Potash Brine. Canadian Metallurgical Quarterly. Submitted September 2005.

4. Type 304 stainless steel (UNS S30400)
5. Type 405 stainless steel (UNS 30500)

This model not only ranks titanium as the best material in terms of crevice corrosion resistance but it also places the stainless steels in order of decreasing PREN. Hence, the model may have important applications in the selection of candidate alloys for corrosive duty.

4.4.1 Introduction

Crevice corrosion is a localized acid-chloride attack. It occurs in occluded regions of the metal surface such as under deposits, at the meeting of metal surfaces, in imperfect welds, beneath gaskets and washers, and in corrosion and/or stress induced pits and cracks. This feature of crevice corrosion makes it particularly dangerous as it can go undetected until failure. This form of corrosion affects passive metals, which are generally corrosion resistant and form a thin tenacious oxide film of low electrical or ionic conductivity. This film is referred to as the passive film. Due to the low conductivity, only a small leakage current, which is called the passive current, can pass through the film. Thus, when the film is present, the metal dissolves at an extremely slow rate. However, in a sufficiently strong acid-chloride solution, which is often called a critical crevice solution, this protective film may be damaged. Due to differential aeration, such acid-chloride solutions may develop autocatalytically inside a crevice, which may then initiate active crevice corrosion.

Crevice corrosion is a common problem in the potash industry. Here, infrastructure and processing equipment is exposed to concentrated brines. Such environments are also ideal for the development of pitting corrosion, which is another

form of localized corrosion that is frequently associated with crevice corrosion. Once pits are formed, strong acid-chloride solutions may develop within them in the same manner as the solutions formed in crevices.

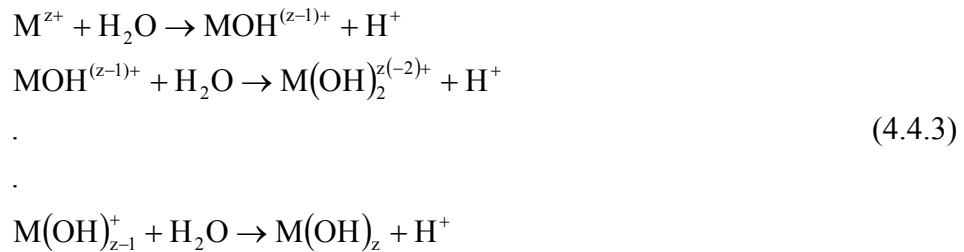
There have been a number of mathematical models proposed in the past to simulate crevice corrosion [1 – 15]. However, with the exception of a few, these models do not rigorously model the effect of ionic interactions in solution. Furthermore, these models are generally applied to one alloy or class of alloys (i.e., stainless steels). This work features a model of crevice corrosion initiation which incorporates the effect of ionic interactions upon mass transport and chemical equilibrium. Due to its generic coding structure, it can be applied to many passive metals immersed in many different electrolytes. In the current study, the transient composition of the solutions located within crevices formed from Grade 2 titanium and Types 304, 308, 314, and 405 stainless steel that are immersed in a potash brine (3.62 M KCl, 3.39 M NaCl, 25°C, pH = 7) are modelled. These alloys were chosen because they are comprised mainly of titanium, iron, chromium, and nickel – metals for which chemical equilibrium data is available in the literature.

4.4.2 Crevice corrosion mechanism

The mechanistic model used here follows Fontana and Greene [16]. Initially, the composition of the solution within the crevice is the same as that outside the crevice. A passive film initially covers the surface of the crevice walls and surrounding metal, which is called the bold surface. Microscopic corrosion cells initially cover the entire inside surface of the crevice. Throughout the crevice and on the bold surface, oxygen is consumed via reduction to support metal dissolution:



These two processes occur simultaneously and at equal rates (to satisfy charge conservation). The metal ions released due to equation (4.4.2) will react with water to form metal hydroxides with H^+ as the by-product:



Note that while both dissolution and oxygen reduction are occurring in the crevice, the production of H^+ is balanced by the production of OH^- and the pH remains neutral. However, due to geometric restrictions, oxygen may not diffuse into the crevice as quickly as it is consumed via reduction. Thus, crevice deoxygenation may occur. When this happens, there are two major consequences:

1. The cathodic process now occurs at the bold surface surrounding the crevice mouth. Thus, anode and cathode are separated inducing a potential gradient in the crevice solution. Due to the potential gradient, cations electromigrate out of the crevice while anions, such as chloride, electromigrate in.
2. Oxygen reduction now only occurs at the bold surface and not inside the crevice. However, H^+ is still produced in the crevice via chemical hydrolysis of dissolved metal ions. Thus, the pH of the solution inside the crevice will drop. This, in turn, reduces the electrical potential within the crevice and increases the rate of dissolution.

As the passive current increases and the crevice potential drops, the rate of dissolution and the rate of chloride ion influx will increase. Increased dissolution then exacerbates the crevice solution composition by lowering the pH further via hydrolysis. Due to this autocatalytic process, strong acid-chloride solutions form within the crevice. If a sufficiently strong acid-chloride solution is formed, the passive film will dissolve and crevice corrosion will ensue. With this mechanism now explained, a mathematical model will be developed to represent it.

4.4.3 Mathematical model

4.4.3.1 Mass transport

In a moderately dilute solution [17], a mass balance on a particular species in solution yields the following equation:

$$\begin{aligned} \frac{\partial C_i}{\partial t} = & -z_i u_i F \left(\frac{\partial C_i}{\partial x} \frac{i + i_{dp}}{\kappa} + C_i \frac{\delta}{\varepsilon} \right) \\ & + D_i \left(\frac{\partial^2 C_i}{\partial x^2} + \frac{\partial C_i}{\partial x} \frac{\partial \ln \gamma_i}{\partial x} + C_i \frac{\partial^2 \ln \gamma_i}{\partial x^2} \right) \end{aligned} \quad (4.4.4)$$

where the diffusion potential current density, the conductivity, and the charge density are, respectively:

$$i_{dp} = F \sum_j z_j D_j \left(\frac{\partial C_j}{\partial x} + C_j \frac{\partial \ln \gamma_j}{\partial x} \right) \quad (4.4.5)$$

$$\kappa = F^2 \sum_j z_j^2 u_j C_j \quad (4.4.6)$$

$$\delta = F \sum_j z_j C_j \quad (4.4.7)$$

The primary current in solution is determined by integrating the passive current along the crevice length:

$$i(x) = \frac{\int_{tip}^x i_p P(x)(1 - \Psi) dx}{A_{cs}(x)} \quad (4.4.8)$$

All symbols used in the above equations are defined in the nomenclature. This model accounts for the effect of charge density, primary and secondary electromigration, and solution non-ideality. Boundary conditions for this equation are provided by assuming that the bulk solution concentration at the crevice mouth is constant and the flux or dissolution rate at the crevice tip. Activity coefficients are calculated from Pitzer's Equations [18]. The application of these equations to the crevice corrosion model is detailed elsewhere [14]. This model has been previously validated by comparison with the experiments of Alavi and Cottis [14, 19]. The model is written in terms of current density rather than potential. Thus, potential boundary conditions are not required. Rather, a reference passive current and initial solution composition are prescribed as initial conditions for the model.

4.4.3.2 Electrode reactions

For an alloy, dissolution of each individual metal species is assumed to occur in proportion to its mole fraction in the alloy, i.e.:

$$R_i = \frac{M_i z_i}{\sum_j M_j z_j} \left(\frac{i_p A_m}{z_i F} \right) \quad (4.4.9)$$

This assumption has been used previously by other researchers [1, 2, 12]. However, some experimental studies have suggested that dissolution may be selective [20, 21]. The passive current is adjusted for pH using a Freundlich Isotherm [22]:

$$\log(i_p) = \log(k) - n \cdot pH \quad (4.4.10)$$

Here, k is a proportionality constant that can be determined at a reference condition while n is an experimentally determined parameter which is based upon the valence state of the dissolving metal. The value of n may be interpolated from data given by Shrier et al. [22].

4.4.3.3 Chemical equilibrium

To model chemical equilibrium, an equilibrium relation is written for each reaction occurring in solution, i.e.:

$$\prod_j a_j^{\nu_j} = K \quad (4.4.11)$$

This set of equations is augmented with mass balance equations, one for each species involved in the chemical reaction set:

$$C_i = C_i^{init} + \sum_j X_j \nu_{ij} \quad (4.4.12)$$

The entire set of equations is solved using the Newton-Raphson method to yield the equilibrated concentrations.

4.4.3.4 The numerical model

In its current form, equation (4.4.4) cannot be solved within a reasonable time frame. Due to the charge density term, this equation is incredibly stiff. To remedy this problem, the charge density term of this mass transport equation is solved separately from the electromigration and diffusion terms. Thus, the following two equations are solved sequentially:

$$\begin{aligned} \frac{\partial C_i}{\partial t} = & -z_i u_i F \left(\frac{\partial C_i}{\partial x} \frac{i + i_{dp}}{\kappa} \right) \\ & + D_i \left(\frac{\partial^2 C_i}{\partial x^2} + \frac{\partial C_i}{\partial x} \frac{\partial \ln \gamma_i}{\partial x} + C_i \frac{\partial^2 \ln \gamma_i}{\partial x^2} \right) \end{aligned} \quad (4.4.13)$$

$$\frac{dC_i}{dt} = -z_i u_i F \frac{\delta}{\varepsilon} C_i \quad (4.4.14)$$

First, equation (4.4.13) is solved using a finite volume method. Then, equation (4.4.14) is solved using the optimized time step derived in Chapter 3.

After discretization of (4.4.13) and subsequent rearrangement, the following finite volume equation results:

$$a_p C_{iP} = a_E C_{iE} + a_W C_{iW} + a_p^0 C_p^0 \quad (4.4.15)$$

where the mass transport coefficients are:

$$a_E = -z_i u_i F \frac{1 - \alpha}{2} \frac{i_P + i_{dp,P}}{\kappa_P} + \frac{D_i}{\Delta x} + \frac{D_i}{2} \left(\frac{\partial \ln \gamma_i}{\partial x} \right)_P \quad (4.4.16)$$

$$a_W = z_i u_i F \frac{1 + \alpha}{2} \frac{i_P + i_{dp,P}}{\kappa_P} + \frac{D_i}{\Delta x} - \frac{D_i}{2} \left(\frac{\partial \ln \gamma_i}{\partial x} \right)_P \quad (4.4.17)$$

$$a_p^0 = \frac{\Delta x}{\Delta t} \quad (4.4.18)$$

$$a_p = a_E + a_W + a_p^0 - D \left(\frac{\partial^2 \ln \gamma_i}{\partial x^2} \right)_P \Delta x \quad (4.4.19)$$

Here, E , W , and P are indices denoting the east, west, and point node respectively. The upwind parameter, α , increases the influence of the upwind node and is calculated based upon the ratio of the strength of electromigration to diffusion [23]. Thus, if the species is migrating from east to west, the value of a_E will be increased while the value of a_W will be decreased. Figure 4.4.1 (a) shows the computational grid over which the mass transport equation is solved. Figure 4.4.1 (b) shows a control volume that is labelled to illustrate the location of the point node (P), and its neighbours, the east (E) and west (W) node.

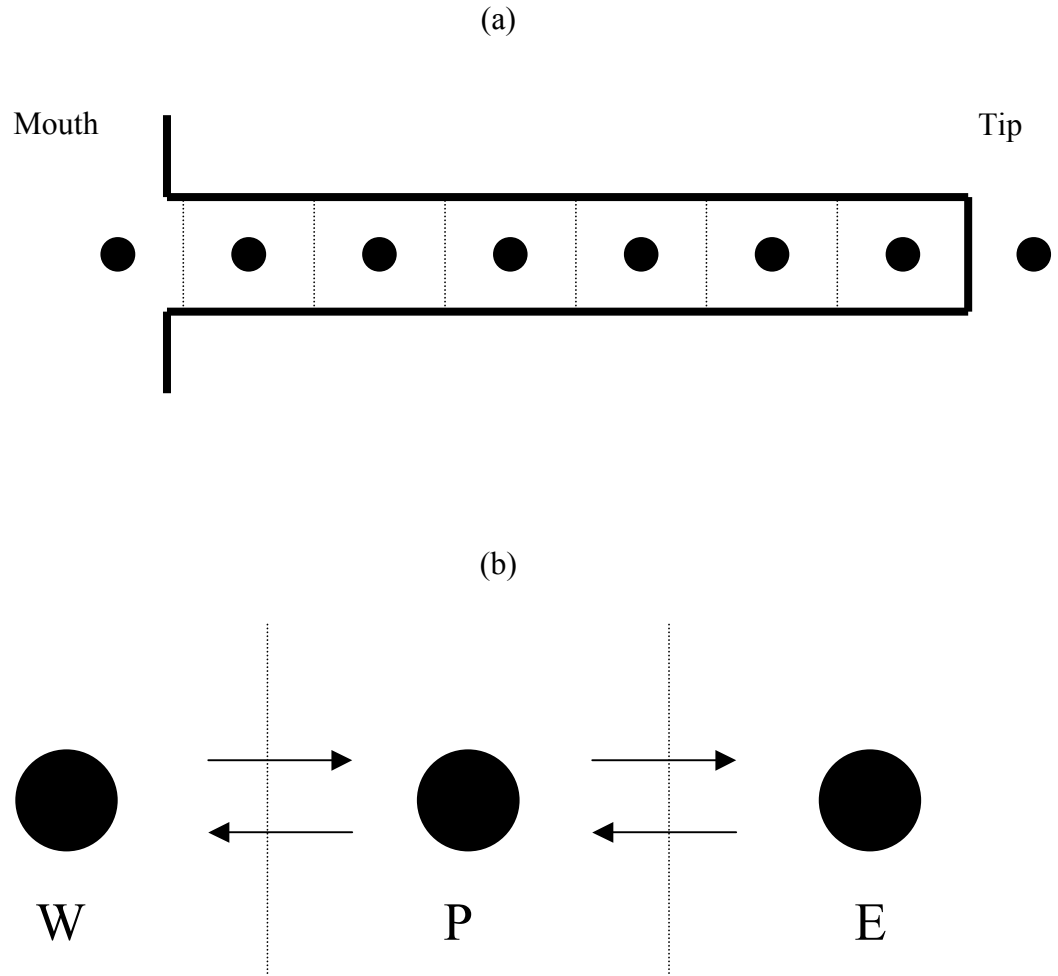


Figure 4.4.1. (a) Computational grid which is used to discretize the crevice solution; (b) Computational node which is labelled to illustrate the point (P), east (E), and west (W) indices.

Patankar states that the point coefficient must be equal to the sum of its neighbouring nodes and the transient coefficient [24], i.e.:

$$a_p = a_E + a_W + a_p^0 \quad (4.4.20)$$

This is one of four rules set out by Patankar that, if followed, ensure that the solution to the transport equation will be physically realistic by guaranteeing an overall balance of mass. However, in this formulation, the point coefficient (a_p) is the sum of not only its neighbour nodes (a_E and a_W) and the transient coefficient (a_p^0), but also an additional term that is proportional to the second order gradient of the activity coefficient. Thus, the non-ideal behaviour of the electrolyte solution may introduce numerical instability when solving the mass transport equation. However, the solution scheme is quite robust; numerical instability was not encountered in the current study when this mass transport model was applied to a concentrated brine system.

4.4.4 Simulation of crevice corrosion initiation

The crevice corrosion initiation of four stainless steels of varying iron, nickel, and chromium content were simulated in this study, namely Type 308, Type 314, Type 405, and Type 304 stainless steel. The crevice corrosion initiation of Grade 2 titanium was also simulated. Alloy compositions are listed in Table 4.4.1.

For each of the simulations, a crevice with the following dimensions was modelled: 90 μm gap, 2.5 cm width, and 8 cm depth. The electrolyte composition inputted into the simulation was that of Saskatchewan potash processing brine consisting of 3.62 M KCl and 3.39 M NaCl with a pH of 7 at 25°C. This composition was obtained by sampling the brine in a potash processing circuit in Saskatchewan.

Common name	UNS No.	% Chromium	% Nickel	% Titanium
Type 405 SS	S30400	13	-	-
Type 304 SS	S30400	19	9.25	-
Type 308 SS	S30800	20	11	-
Type 314 SS	S31400	24.5	20.5	-
Titanium, Gr 2	R50400	-	-	~100

Table 4.4.1. Assumed composition of alloys used in this study [16]. Iron comprises balance. Impurities are neglected.

To rank the alloys for their susceptibility to crevice corrosion, a common means of evaluation was adopted. In this study, alloys were ranked based upon the difference between the pH at the crevice tip and the critical pH approximately 3.5 hours after immersion. This time was chosen because, after 3.5 hours, the pH for each alloy was nearing a steady state condition, and thus did not vary significantly. Furthermore, because each simulation was very computationally expensive, a shorter simulation time was advantageous.

4.4.5 Results and discussion

4.4.5.1 Simulation of Grade 2 titanium crevice corrosion initiation

Grade 2 titanium alloy is known for its corrosion resistance due to the tenacity of its passive film. It is chosen only for extremely corrosive service due to its high cost. It is comprised of essentially pure titanium, but is doped with iron for increased ductility. It

was assumed that the sole anodic reaction occurring in this system was the dissolution of titanium (IV):



In addition to oxygen reduction, hydrogen ion reduction also supplies cathodic charge inside the Grade 2 titanium crevice:



It was assumed that crevice-internal hydrogen ion reduction supplies approximately 70% of the required cathodic current while the remaining 30% is supplied by crevice-external oxygen reduction [25]. The crevice-internal hydrogen ion reduction has a two-fold effect on the crevice corrosion process:

1. It consumes hydrogen ions in-situ and which increases the pH of the crevice solution.
2. It reduces the net current leaving electrode sites inside the crevice thus increasing the crevice potential and reducing the mass transport driving force. This lowers the rate of chloride ion influx.

If it were not for the detrimental effects of hydrogen embrittlement, internal proton reduction would extend the life of Grade 2 titanium alloy structures. To account for the effect of hydrogen ion reduction on mass transport, the primary current density equation is modified as follows:

$$i(x) = \frac{1}{A_{cs}(x)} \int_{i_p}^x i_p (1 - \Psi) P(x) dx \quad (4.4.23)$$

Here, Ψ is the fraction of the cathodic current that is supplied by crevice-internal hydrogen ion reduction. Chemical equilibrium is modelled using the mononuclear

hydrolysis reactions proposed by Liberti et al. [26]. These reactions have been listed in a previous section (see Table 4.1.2).

The transient pH profile in a Grade 2 titanium crevice is displayed in Figure 4.4.2. A rapid initial drop in pH is seen just after the crevice becomes deoxygenated. This is due to the autocatalytic coupling that exists between metal dissolution and chemical equilibrium processes. Metal ions enter the crevice solution at a rate which is proportional to the passive current. According to equation (4.4.10), the passive current is a function of pH. As metal is dissolved into the crevice solution, metal ions undergo hydrolysis reactions, which produce H^+ thereby lowering the solution pH. Due to increasing crevice solution acidity, the rate of metal dissolution increases. This autocatalytic coupling causes the initially rapid drop in pH seen in Figure 4.4.2. Eventually, the pH stabilizes and a more moderate decrease in pH is seen. The overall shape of the transient pH curve is due to four processes which occur simultaneously: metal dissolution, reduction of H^+ , transport of H^+ out of the tip region, and chemical reaction of metal ions to form H^+ . The first three processes act to increase the pH in the crevice solution. These processes are:

- Metal dissolution, which causes the crevice to expand slightly.
- Hydrogen ion reduction, which consumes H^+ thereby directly raising the pH.
- Current density emanating from the crevice wall, which causes H^+ electromigration out of the crevice towards the mouth.

However, chemical hydrolysis of Ti^{4+} , which causes a drop in pH, overpowers the previous three processes. As a result, the pH decreases throughout the crevice.

There is another phenomenon that occurs near the crevice mouth. Here, the pH also drops but this is due primarily to the effects of coupled electromigration and diffusion. Near the crevice mouth, the primary electromigration current is very strong while the anodic dissolution current is lower than at the crevice tip. The pH would therefore be expected to be much greater than at the crevice tip where dissolution is rapid and transport is slow. However, steep activity gradients also exist here, from which diffusion potential current results. This diffusion potential current opposes the primary current causing a localized stagnation of ionic species. Thus, anions, such as chloride ions, which are attempting to migrate further into the crevice and cations, such as hydrogen ions, which are attempting to leave the crevice, are trapped near the mouth. Due to the resultant high ionic strength near the mouth, the pH near the crevice mouth is quite low.

This simulation shows that Grade 2 titanium alloy is likely not susceptible to crevice corrosion in potash brine at 25°C. Its pH value after 3.5 hours is approximately 1.8 while its critical value is -1 [27].

4.4.5.2 Relationship between critical crevice pH and the PREN

The critical pH is the pH at which the passive film breaks down and is determined experimentally. However, the critical pH has been determined for only a few passive metals. Because the critical pH values of some of the alloys studied herein have not been experimentally determined, a relationship between the critical pH and the PREN was obtained.

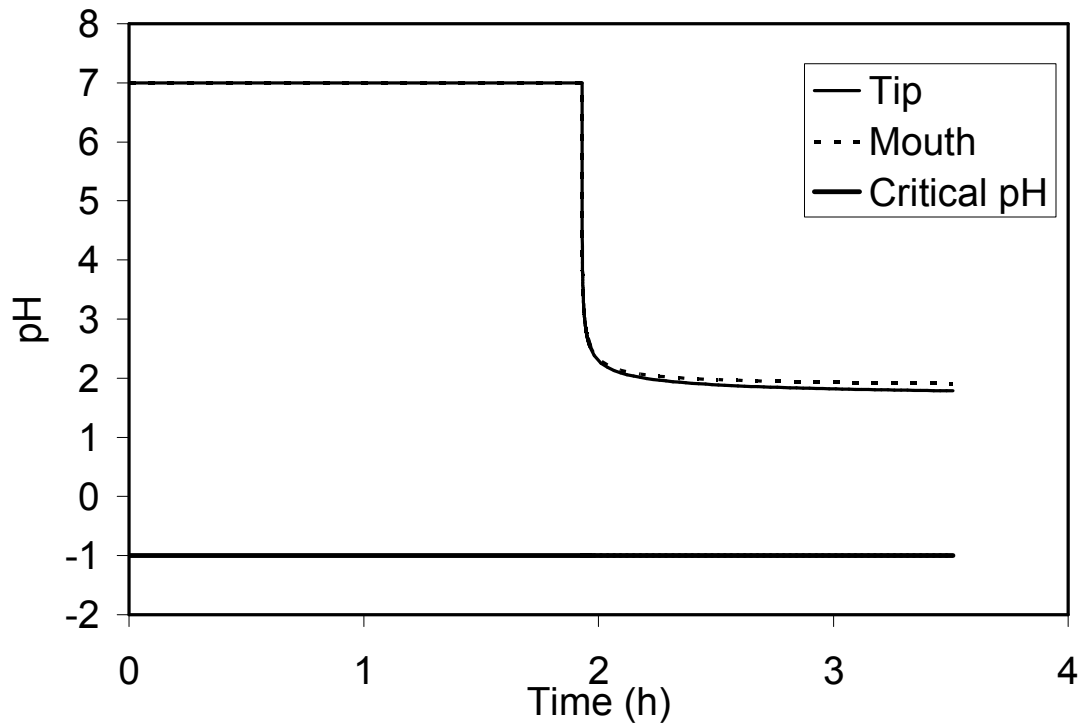


Figure 4.4.2. Transient pH profile in a Grade 2 titanium crevice measuring 90 μm across the gap, 2.5 cm wide, and 8 cm deep. Crevice is immersed in a Saskatchewan potash brine (3.39 M NaCl, 3.62 M KCl, 25°C, pH = 7).

This relationship was determined from four metals with known critical pH values [28]: Type 304 stainless steel (PREN = 19, Critical pH = 2), Type 316 stainless steel (PREN = 25.25, Critical pH = 1.7), Hastelloy C-276 (PREN = 68.3, Critical pH = -0.5), and Inconel 625 (PREN = 51.2, Critical pH = 0). In this work, the PREN was determined from the following equation:

$$PREN = \%Cr + 3.3(\%Mo) + 16(\%Ni) \quad (4.4.24)$$

This is the most commonly used form of the PREN. Alloy compositions, which were required to calculate PREN values, were taken from Treseder et al. [29]. Figure 4.4.3 shows that the PREN vs. critical pH data follows a linear trend. A least squares linear regression of the data yielded the following empirical relationship:

$$pH_{crit} = -0.053 \times PREN + 3.0 \quad (4.4.25)$$

This relationship was then used to estimate the unknown critical pH values of the alloys used in this study with literature values being used when available. The critical pH values for all five alloys simulated in this work are listed in Table 4.4.2.

Common Name	Critical pH	Reference
Type 304 stainless steel	2	20
Type 308 stainless steel	1.9	Estimated
Type 314 stainless steel	1.7	Estimated
Type 405 stainless steel	2.3	Estimated
Grade 2 Titanium	-1	15

Table 4.4.2. Critical crevice pH values used in this study.

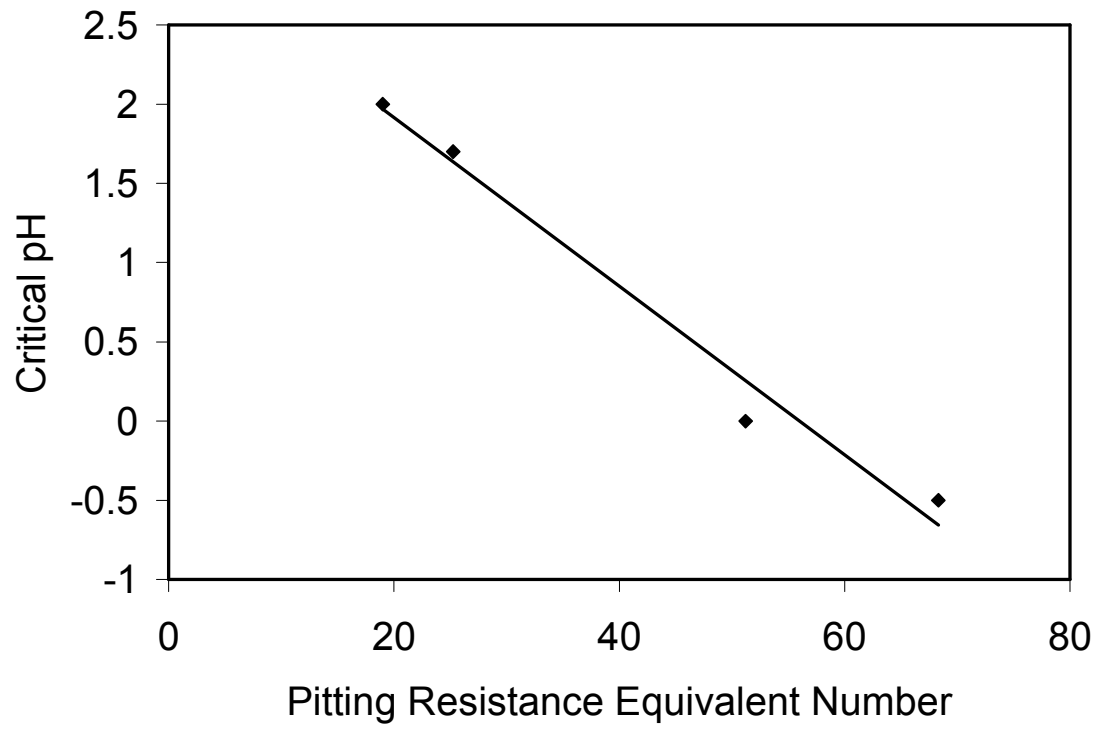


Figure 4.4.3. Relationship between the critical crevice pH (CCP) and the pitting resistance equivalent number (PREN).

4.4.5.3 Type 308 stainless steel

Type 308 stainless steel is comprised of chromium, nickel, and iron plus impurities. The anodic reactions assumed to occur are:



Fe^{2+} , Cr^{3+} , and Ni^{2+} then react with water and chloride to form metal hydroxides and metal chlorides. The reactions assumed to occur in solution have been listed previously (see Table 4.1.1) [1, 8, 30].

Figure 4.4.4 shows the transient pH profile inside a type 308 stainless steel crevice. For a stainless steel crevice, internal hydrogen ion reduction does not contribute significantly to the cathodic charge [19]. Upon deoxygenation, the pH drops off rapidly due to autocatalytically coupled dissolution and chemical hydrolysis. This is followed by a moderate pH decrease as the rates of chemical hydrolysis and H^{+} transport equalize. The mechanisms governing the dynamics of the crevice solution pH for type 308 stainless steel are similar to the mechanisms previously discussed during the presentation of the titanium simulation and, therefore, will not be discussed here. After 3.5 hours, the crevice pH at the tip is approximately 2.47 while its critical pH value is approximately 1.9.

4.4.5.4 Type 314 stainless steel

Type 314 stainless steel contains slightly more chromium than Type 308. Therefore, it is expected to be more resistant to localized corrosion than Type 308.

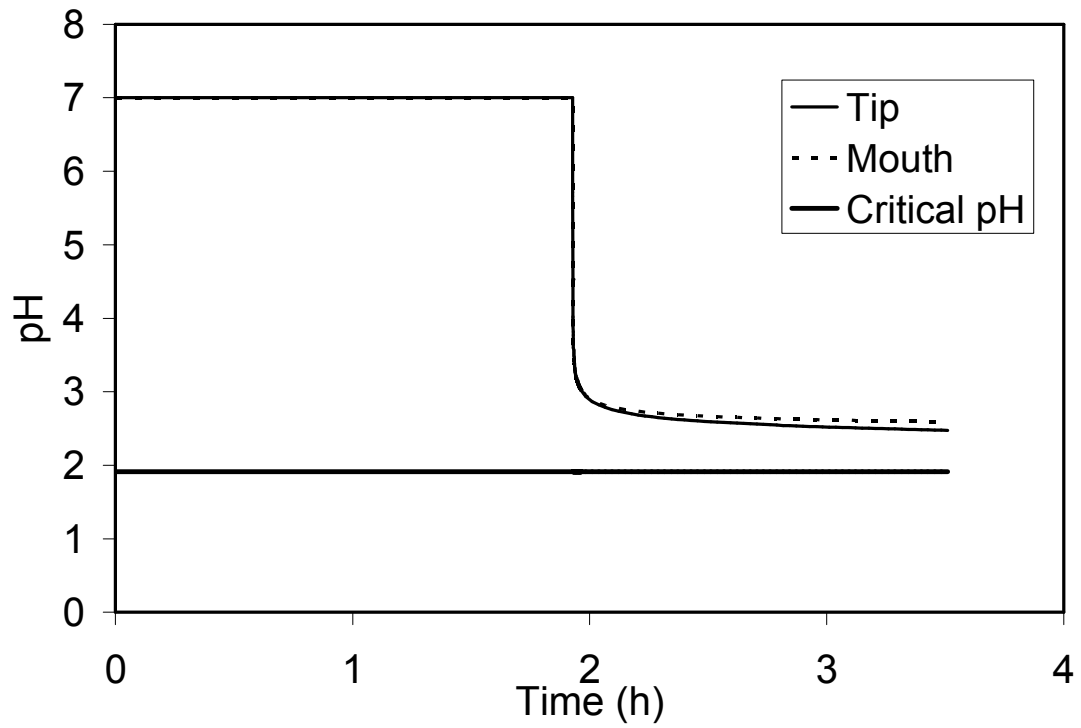


Figure 4.4.4. Transient pH profile in a type 308 SS crevice measuring 90 μm across the gap, 2.5 cm wide, and 8 cm deep. Crevice is immersed in a Saskatchewan potash brine (3.39 M NaCl, 3.62 M KCl, 25°C, pH = 7).

It is predominantly comprised of iron, nickel, and chromium and therefore the anodic reactions occurring inside the Type 314 crevice are the same as those of the type 308 crevice (equations (4.4.25) – (4.4.27)). The reactions occurring in solution are listed in Table 4.1.1 [1, 8, 30].

Figure 4.4.5 shows the transient pH profile in the type 314 stainless steel crevice. Because of the additional chromium and nickel in the alloy, the pH attained in the crevice solution is lower for type 314 than type 308. This is due to the value of the equilibrium constant for the Cr^{3+} hydrolysis reaction. By inspection of Table 4.1.1, it can be seen that the equilibrium constant for the reaction of Cr^{3+} to CrOH^{2+} is 4 to 5 orders of magnitude greater than any other hydrolysis reaction. Thus, the increase in concentration of Cr^{3+} , due to increased chromium content in the alloy, shifts equilibrium to the right, thus causing increased production of H^+ . However, increased chromium content also increases the passivity of the alloy. Based upon equation (4.4.24), the critical pH for type 314 stainless steel is estimated to be 1.7. After 3.5 hours, the pH at the crevice tip is approximately 2.37.

Thus, even though the pH in the type 314 stainless steel crevice solution is lower than in the type 308 crevice solution, type 314 is predicted to be more resistant to the onset of crevice corrosion, as the difference between crevice tip pH and critical pH has increased from 0.57, for type 308, to 0.72, for type 314.

4.4.5.5 Type 304 stainless steel

Type 304 stainless steel contains less chromium and nickel than both 308 and 314 stainless steel. According to its PREN, it should be less resistant to crevice corrosion than 308 and 314.

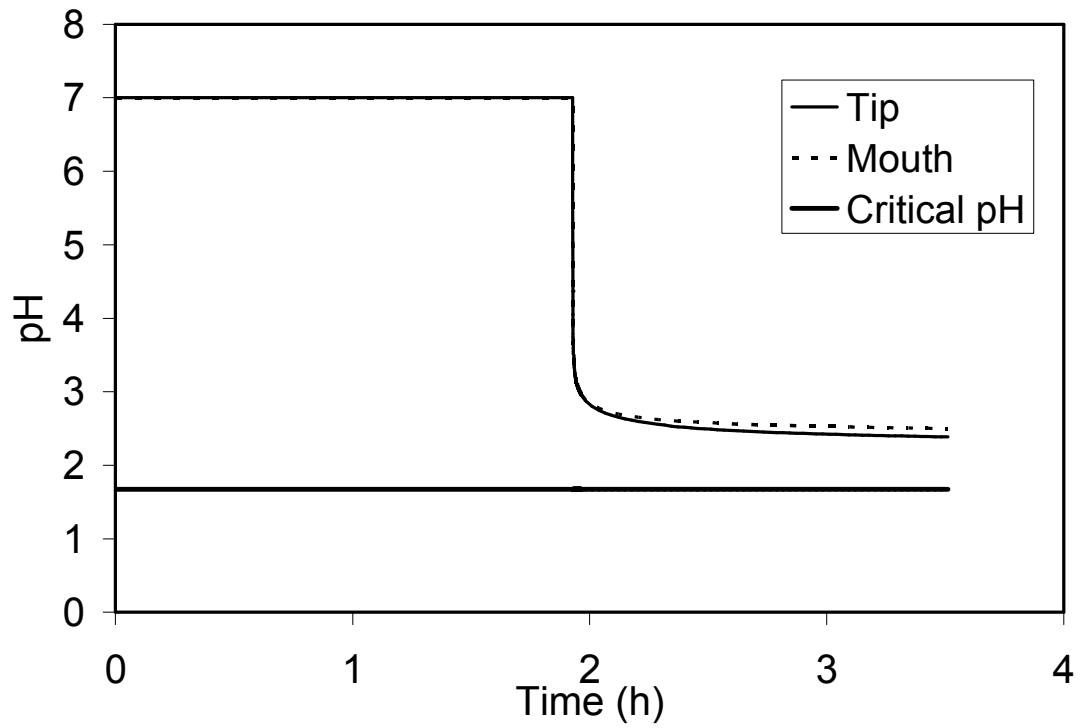


Figure 4.4.5. Transient pH profile in a type 314 SS crevice measuring 90 μm across the gap, 2.5 cm wide, and 8 cm deep. Crevice is immersed in a Saskatchewan potash brine (3.39 M NaCl, 3.62 M KCl, 25°C, pH = 7).

Type 304 stainless is, like Types 308 and 314, a chromium, nickel, and iron alloy, and thus, anodic reactions occurring in the crevice are the same as in Types 308 and 314 (equations (4.4.25) – (4.4.27)). Chemical reactions occurring in the Type 304 stainless steel crevice are listed in Table 4.1.1. Comparison of Figure 4.4.6 with Figures 4.4.4 and 4.4.5 shows that Type 304 stainless steel is less corrosion resistant than Type 308 or Type 314, which agrees with the PREN based prediction. The crevice tip pH after 3.5 hours is approximately 2.49 while its critical pH is 2 [28], a difference between crevice tip pH and critical pH of 0.49. After 3.5 hours, the difference between crevice tip pH and critical pH for both Type 308 and Type 314 is 0.57 and 0.72, respectively.

4.4.5.6 Type 405 stainless steel

Unlike the austenitic stainless steels simulated in this work, Type 405 is a ferritic stainless steel. It contains chromium, which is added for corrosion resistance, but contains no nickel, which is usually added for strength. All chromium and iron reactions shown in Table 4.1.1 are assumed to occur in the type 405 crevice solution; no nickel reactions occur due to the absence of nickel from the alloy. Anodic reactions assumed to occur in this crevice are shown in equations (4.4.25) and (4.4.27). Because the chromium content in this alloy is the lowest of all the stainless steels, it is expected to be the most susceptible to crevice corrosion. Figure 4.4.7 shows this to be the case. After 3.5 hours of exposure, the pH at the tip of the crevice is closely approaching the critical crevice pH. The difference between crevice tip pH and critical pH after 3.5 hours is 0.34.

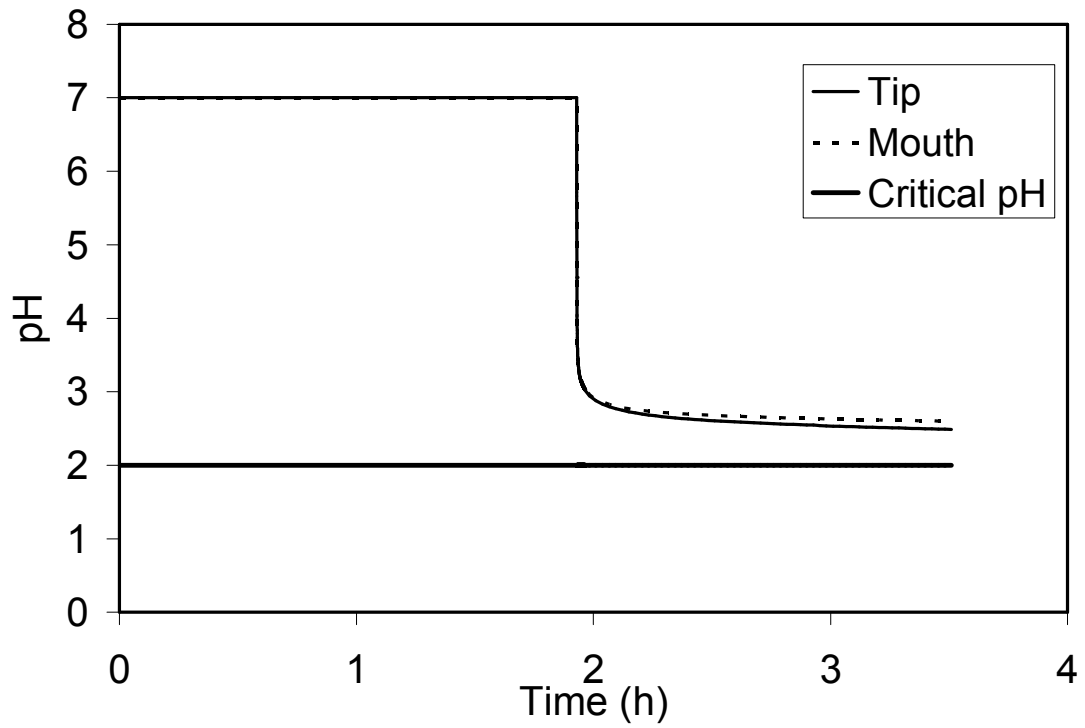


Figure 4.4.6. Transient pH profile in a type 304 SS crevice measuring 90 μm across the gap, 2.5 cm wide, and 8 cm deep. Crevice is immersed in a Saskatchewan potash brine (3.39 M NaCl, 3.62 M KCl, 25°C, pH = 7).

4.4.5.7 Ranking of the alloys

The crevice corrosion resistance of each alloy was measured based upon the difference between the pH at the crevice tip and the critical pH after 4.5 hours simulation time. Based upon this criterion, the ranking of the alloys, from most corrosion-resistant to most corrosion-susceptible, is as follows:

1. Grade 2 Titanium ($\text{pH} - \text{pH}_{\text{crit}} = 2.8$)
2. Type 314 stainless steel ($\text{pH} - \text{pH}_{\text{crit}} = 0.72$)
3. Type 308 stainless steel ($\text{pH} - \text{pH}_{\text{crit}} = 0.57$)
4. Type 304 stainless steel ($\text{pH} - \text{pH}_{\text{crit}} = 0.49$)
5. Type 405 stainless steel ($\text{pH} - \text{pH}_{\text{crit}} = 0.34$)

The order in which the stainless steels are ranked is identical to the order that would result from ranking according to their respective PRENs. Furthermore, the Grade 2 titanium was ranking higher than any of the stainless steels, a result which was also expected.

4.4.6 Conclusions

From the work presented in this paper, the following conclusions may be made:

1. A numerical model of crevice corrosion initiation has been developed which is capable of accurately ranking candidate alloys for highly corrosive service in potash brines. The simulation results produced by the model were used to rank the alloys in the following order (from most resistant to susceptible): Grade 2 titanium, Type 314 stainless steel, Type 308 stainless steel, Type 304 stainless steel, and Type 405 stainless steel. This is the expected ranking: titanium is a superior metal known for its corrosion resistance, and the stainless steels are ranked in order of descending PREN.

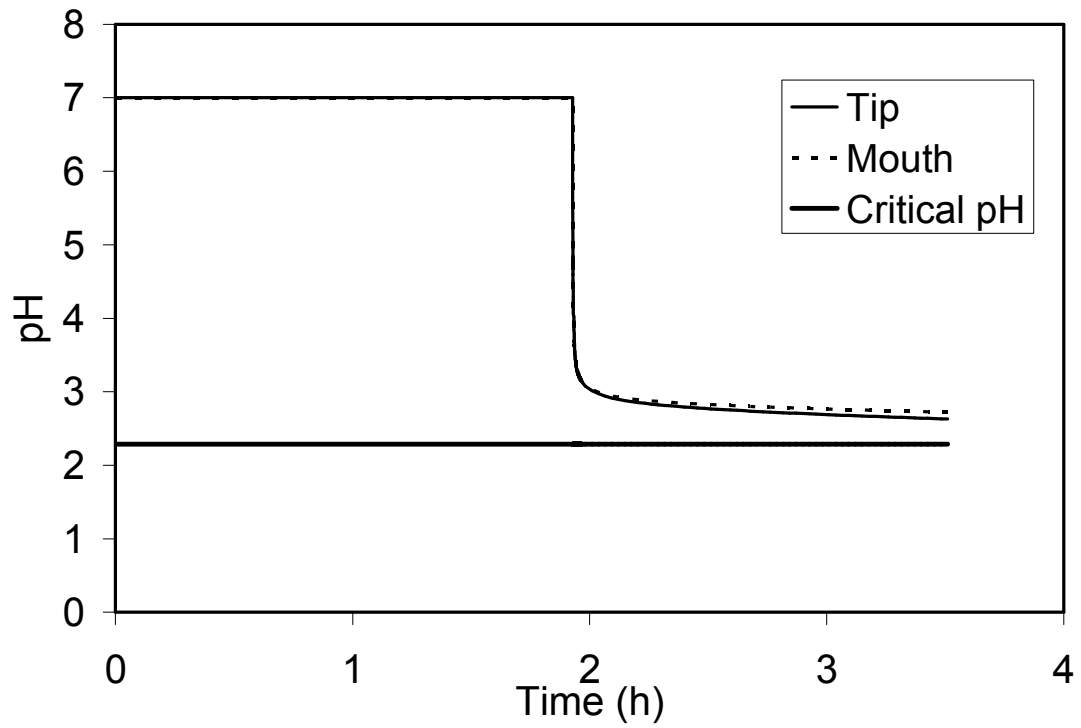


Figure 4.4.7. Transient pH profile in a type 405 SS crevice measuring 90 μm across the gap, 2.5 cm wide, and 8 cm deep. Crevice is immersed in a Saskatchewan potash brine (3.39 M NaCl, 3.62 M KCl, 25°C, pH = 7).

2. A plot of the critical pH versus the PREN shows a distinct linear trend. This trend was used to estimate the critical pH for Types 308, 314, and 405 stainless steel.
3. The addition of chromium to steel increases its passivity. This is shown in the model. As the chromium content increased, the difference between the crevice tip pH and the critical pH also increased, thus increasing the steel's resistance to the onset of crevice corrosion.
4. The code structure of this numerical model incorporates significant flexibility. Thus, many passive metals may be evaluated for their crevice corrosion resistance in many electrolytes with no modifications to the code. In this case, five differing alloys were ranked for their propensity to crevice corrosion in concentrated potash brine. This numerical model could therefore serve as a valuable tool for materials selection for highly corrosive service.

4.4.7 References

1. J. W. Oldfield, W. H. Sutton, *British Corrosion Journal* **13**, 1978, p. 13.
2. S. Bernhardsson, L. Eriksson, J. Ooppelstrup, I. Puigdomenech, and T. Wallin, in *Proceedings of 9th Scandinavian Corrosion Congress, Addendum 1*, p. 1, Copenhagen, Denmark, Sept 12 – 14, 1983.
3. R. C. Alkire, , D. Siitari, *Journal of the Electrochemical Society* **129**, 1982, p. 488.
4. K. Hebert, R. Alkire, *Journal of the Electrochemical Society* **130**, 1983, p. 1007.
5. Fu, J. W. and S. Chan, *Corrosion* **40**, 1984, pp. 540 – 544.
6. S. M. Sharland, *Corrosion Science* **28**, 1988, p. 621.
7. Oldfield, J. W., G. L. Masters, and K. R. Stokes, “Prediction of Initiation and Propagation of Crevice Corrosion on Aluminum Alloys in Sea Water by Mathematical Modelling” in “Proc. Corrosion/96”, Denver, CO, March 24-29, 1996, NACE International, Houston, TX (1996), pp. 512:1 – 512: 16.
8. J. C. Walton, G. Cragolino, S. K. Kalandros, *Corrosion Science* **38**, 1996, p. 1.
9. Watson, M. K. and J. Postlethwaite, *Corrosion* **46**, 1990, pp. 522 – 530.
10. M.K. Watson, and J. Postlethwaite, “Numerical Simulation of Crevice Corrosion” in “Proc. Corrosion/90”, Las Vegas, NV, April 23-27, 1990, NACE International, Houston, TX (1990b), pp. 156:1 – 156:19.
11. M.K. Watson and J. Postlethwaite, “Numerical Simulation of Crevice Corrosion: The Effect of the Crevice Gap Profile”, *Corrosion Science* **32**, 1991, pp. 1253 – 1262.
12. K.L. Heppner, R.W. Evitts, and J. Postlethwaite, *Canadian Journal of Chemical Engineering*, **80**, 2002, p. 849.

13. K.L. Heppner, R.W. Evitts, and J. Postlethwaite, *Canadian Journal of Chemical Engineering*, **80**, 2002, p. 857.
14. K. Heppner, R.W. Evitts, and J. Postlethwaite, *Journal of the Electrochemical Society* **152**, 2005, pp. B89-B98.
15. K.L. Heppner, R.W. Evitts, and J. Postlethwaite, *Corrosion*, **60**, 2004, pp. 718 – 728.
16. M.G. Fontana and N.D. Greene, *Corrosion Engineering*, 2nd Edition, McGraw-Hill, Toronto, 1978.
17. J. Newman, “*Electrochemical Systems*”, Prentice Hall, Toronto, 1973.
18. K.S. Pitzer, *Journal of Physical Chemistry* **77**, 1973, p. 268.
19. A. Alavi and R. A. Cottis, *Corrosion Science*, **27**, 1987, p. 443.
20. S. E. Lott and R. Alkire, *Corrosion Science*, **28**, 1988, p. 479.
21. G. Hultquist, M. Seo, T. Leitner, C. Leygraf, and N. Sato, *Corrosion Science*, **227**, 1987, p. 479.
22. Shrier, L. L., R. A. Jarman, and G. T. Burstein, “*Corrosion*”, Butterworth-Heinemann Ltd, Oxford, UK, 1994, 3rd Ed., pp. 2:20.
23. K.L. Heppner and R.W. Evitts, *International Journal of Numerical Methods for Heat and Fluid Flow*, 2005, In Press.
24. Patankar, S.V., “*Numerical Heat Transfer and Fluid Flow*”, Hemisphere, 1980.
25. X. He, J. J. Noël, and D.W. Shoesmith, *Corrosion*, **60**, 2004, p. 378.
26. A. Liberti, V. Chiantella, F. Corigliano, *Journal of Inorganic and Nuclear Chemistry* **25**, 1963, p. 415.

27. R. W. Evitts, "Modeling of Crevice Corrosion", Ph.D. thesis, University of Saskatchewan, Saskatoon, Saskatchewan, Canada (1997).
28. M.K. Watson, "Numerical Simulation of Crevice Corrosion", Ph.D. Dissertation, University of Saskatchewan, Saskatoon SK (1989).
29. Treseder, R.S. (Ed.), Baboian, R., and Munger C.G. (Co-Eds.), "NACE Corrosion Engineer's Reference Book", Second Edition, NACE International, Houston, TX, USA, 1991, pp. 168, 172, 187.
30. C. F. Baes and R. E. Mesmer, The Hydrolysis of Cations, New York, NY, Wiley, 1976.

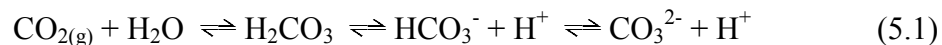
Chapter 5. Carbon Dioxide Corrosion

The mathematical models of electrolyte mass transport, which were developed in Chapters 3 and 4, are not only applicable to crevice corrosion. In this chapter, the models developed for crevice corrosion are applied to simulate carbon dioxide corrosion. This type of corrosion is accelerated by turbulent flow. The mathematical model developed for CO₂ corrosion will be developed and validated in this chapter.

5.1 Background on Carbon Dioxide Corrosion

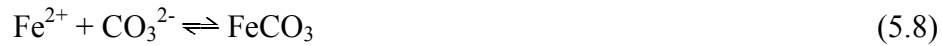
Carbon dioxide corrosion occurs when a carbonic acid solution, formed by the dissolution of CO₂ in water, comes into contact with steel. This type of corrosion is especially problematic for the oil and gas industry where mixtures of crude oil and water are transported. In this situation, a portion of the carbon dioxide in the crude will dissolve into water and form a corrosive flowing solution.

For the purpose of developing a mathematical model of CO₂ corrosion, consider steady, fully developed turbulent flow of water through a carbon steel pipe. If this water has contacted carbon dioxide gas, a small amount of the gas will dissolve by the reaction:



Carbon dioxide hydration provides HCO₃⁻, H⁺, and CO₃²⁻, three ions which participate significantly in the iron dissolution process. This hydration is slow and could be the rate-limiting step of the overall corrosion rate [1, 2]. The flow rate of solution through the

pipe determines the size of the mass transfer boundary layer, an important dimension for computation of mass transfer rates at the metal surface. Mass transfer is very important to the corrosion process, as it supplies the necessary reagents for the cathodic reactions. Very near the pipe wall, there exists a region of laminar flow known as the viscous sublayer. Velocity fluctuations induced by turbulent dissipation of momentum are damped by the solid boundary, and thus, turbulence-induced mixing of the solution does not occur to a significant extent. Mass transport occurs solely by diffusion in this region. Chemical reactions occurring in the solution are assumed to be the following:



Equation (5.2) is not assumed to be at equilibrium and the calculation of the production rate of H_2CO_3 will be discussed later in the section. Because they occur at a much faster rate, reactions (5.3) – (5.7) are assumed to be at equilibrium. Equilibrium constants for reactions (5.3) - (5.5) are available elsewhere [3, 4]. Equilibrium constants for Fe^{2+} hydrolysis, reactions (5.6) and (5.7), is listed in Table 4.1.1. An iron carbonate (FeCO_3) film will form if the product of the Fe^{2+} and CO_3^{2-} activities exceed the solubility product for this reaction, K_{sp, FeCO_3} . The solubility product for this reaction is available in Nesic et

al. [5]. Fe^{2+} required for hydrolysis and for film formation, equation (5.8), is supplied through anodic dissolution at the metal surface:



This is considered to be the only dissolution reaction occurring at the metal surface. Iron carbonate, formed in reaction (5.8), usually exceeds its solubility limit, and thus, it precipitates as a protective crystalline film on the pipe surface. This film is very protective at high temperature [6, 7]. This film acts as a diffusion barrier, thereby inhibiting the rate of transport of cathodic reagents to the surface. At cathodic sites on the pipe surface, these reactions occur:



Notice that with this form of corrosion, oxygen reduction may not contribute to the cathodic current. Of course, if a solution is aerated, oxygen reduction will provide another cathodic reaction. Hydrogen ions, H_2CO_3 , and water is reduced to supply the anodic current and satisfy the mixed potential theory. The mixed potential theory is an electron balance; any electron freed during oxidation must be consumed through reduction. Therefore, the absence of reagents will halt the corrosion process.

5.2 Literature on Carbon Dioxide Corrosion

Previous studies in CO_2 corrosion have included experimental and numerical investigations. A selection of experimental and theoretical studies will now be discussed.

5.2.1 Experimental work

5.2.1.1 De Waard and Milliams (1975)

De Waard and Milliams [8] conducted a study on X-52 carbon steel immersed in 0.1% sodium chloride solutions saturated with carbon dioxide. The corrosion rates determined were significantly different than that expected for completely dissociated acids at the same pH. It was concluded that carbonic acid in the solution was not completely dissociated. Furthermore, the remaining carbonic acid participated in the following cathodic reaction:



This work demonstrated that incompletely dissociated carbonic acid solutions were more corrosive than those with complete dissociation. It also showed that equation (5.13) is an important step of the CO₂ corrosion mechanism.

5.2.1.2 Schmitt and Rothmann (1977)

Using a rotating disk apparatus, experiments were conducted by Schmitt and Rothmann [2] to study the reduction of carbonic acid. Using a CO₂ in water solution, polarization experiments revealed that the cathodic limiting current is the sum of two parts: the H⁺ reduction limiting current, controlled by diffusion, and the H₂CO₃ reduction limiting current, controlled by the heterogeneous CO₂ hydration reaction:

$$i_{\text{lim}} = i_{\text{lim,diffusion}(\text{H}^+)} + i_{\text{lim,reaction}(\text{H}_2\text{CO}_3)} \quad (5.14)$$

5.2.1.3 Gray et al. (1989)

Gray et al. [9] confirmed the composition of the limiting cathodic current as reported by Schmitt and Rothmann. However, they challenged that the CO₂ hydration reaction was actually homogenous, rather than heterogeneous. Because similar cathodic limiting currents were observed on both platinum and iron (Schwenk, 1974; de Waard and Milliams, 1975a), they argue that the hydration reaction must not involve adsorption onto metals. Different metals would have different adsorptive properties and alter the limiting cathodic current. They suggested that between pH of six to ten, bicarbonate ion reduction could be the largest contributor to the cathodic current:



5.2.1.4 Nestic et al. (1995)

Through rotating cylinder experiments, increased flow rates were shown to increase the H₂CO₃ reduction limiting current at relatively high rotational speeds by Nestic et al [10]. A flow factor was introduced and a theoretical expression derived to superimpose diffusion and chemical reaction controlled limiting currents. They suggested that significant interaction occurs between mass transfer and chemical reaction at temperatures below 40 °C and flow velocities above 1 m/s when the thickness of the mass transfer boundary layer and chemical reaction boundary layer are of similar magnitude.

5.2.1.5 Schmitt and Rothmann (1978)

Schmitt and Rothmann [11] showed that anodic iron dissolution follows the pH-dependent reaction mechanism as proposed by Bockris et al. [12]:





5.2.2 Modelling work

5.2.2.1 DeWaard and Milliams (1975)

DeWaard and Milliams [13] presented a partially mechanistic model based upon experimental observations. A correlation between the corrosion rate and the CO₂ partial pressure, this model is really a worst-case scenario; no mass transfer limitations are imposed upon the reaction rate. Acidity increases are due solely to the rate of dissociation of carbonic acid. Therefore, pH is assumed to be only a function of CO₂ partial pressure. Since its introduction, correction factors have been developed to account for corrosion product films, pH, system pressure, etc.

5.2.2.2 Gray et al. (1989, 1990)

Gray et al. [9, 14] presented a mechanistic model that limited the rate of electrochemical reactions at the metal surface with a mass transport model. This model determined corrosion rates as they were affected by iron dissolution, diffusion controlled hydrogen ion reduction, chemical reaction controlled H₂CO₃ reduction, and charge transfer controlled H₂O reduction. Iron dissolution reactions were assumed to follow the Bockris mechanism [12]. Using mixed potential theory [15, 16], the corrosion current was calculated.

5.2.2.3 Nestic et al. (1995)

Nestic et al. [10] presented an electrochemical model as a follow-up to the study by Gray et al. The model closely resembled the work of Gray et al. However, the Bockris mechanism was found not to apply to their system above a pH of 4. Predictions generated

with this model were found to compare favourably with independent experimental results, the semi-empirical model of de Waard and Lotz [17], and the semi-empirical model of Dugstad et al. [18]. This study produced a correction factor to account for the effect of flow on H_2CO_3 reduction. The models of both Gray et al. and Nesic et al. used a simple treatment of transport in the boundary layer.

5.2.2.4 Turgoose et al. (1990)

Turgoose et al. [19] detailed a realistic approach to model the cathodic reactions involved in CO_2 corrosion. After the approach by Bard and Faulkner [20], the model accounts for the effect of electron transfer reactions, diffusion, convection, slow chemical hydration reactions, and rapid solution equilibrium. The results of this theoretical study showed that above a pH of 6, increases in the cathodic current resulted from solution chemical equilibrium rather than from reduction of bicarbonate ions as reported by Gray et al. [9, 14].

5.2.2.5 Wang (1997)

Wang [3] used a developing pipe flow CFD model to predict steady state CO_2 corrosion rates on bare mild steel.

5.2.2.6 Nordsveen et al., Nesic et al., Nesic and Lee (2003)

This recent work [4, 5, 21] used a reasonably detailed description of electrolyte mass transport in a fully developed turbulent flow. The main novelty was the inclusion of a film growth model for FeCO_3 . The transient CO_2 corrosion rate profile predicted using this model agreed well with experimental results using a rotating cylinder.

5.3 Numerical Model of Carbon Dioxide Corrosion

In this work, the Navier-Stokes equations are solved in one dimension to predict steady, fully developed turbulent flow field. The Van Driest turbulence model is applied to calculate the eddy viscosity. This turbulence model gives reasonable predictions of the wall shear stress (compared to the Moody diagram) for a fully developed, steady pipe flow, and is therefore used in this application. An infinitely dilute mass transport model is applied which assumes that the concentration profile is fully developed and unsteady. Thus, the mass transport model corresponds to equation (2.1.16) written for a one-dimensional grid. Boundary conditions are obtained from assuming symmetry at the flow centreline and from a pseudo steady state mass balance at the metal-solution interface, equation (2.1.18). The corrosion rate is determined using mixed potential theory and the Butler-Volmer equation:

$$\sum_j i_{o,j} \left(\exp \left[\frac{E - E_{rev,j}}{b_{a,j}} \right] - \exp \left[- \frac{E - E_{rev,j}}{b_{c,j}} \right] \right) = 0 \quad (5.19)$$

The kinetic parameters appearing in equation (5.19) are a function of temperature and solution composition at the metal-solution interface. The Tafel slopes for each electrode reaction are determined from the following equations:

$$b_a = \frac{RT}{\alpha_a F} \quad (5.20a)$$

$$b_c = \frac{RT}{\alpha_c F} \quad (5.20b)$$

In equation (5.20a) and (5.20b), the α values are transfer coefficients for the electrochemical reaction. The reversible potential for each reaction is determined using the Nernst equation:

$$E_{rev} = E_{rev}^0 - \frac{RT}{nF} \ln Q \quad (5.21)$$

Here, the reversible potential is calculated from a standard state potential and depends upon the temperature and species composition at the metal-solution interface change. For the electrochemical reactions involved in CO₂ corrosion, equations (5.9) – (5.12), the required equations to determine the exchange current density and Tafel slopes at a variety of temperatures and solution compositions are available elsewhere [3, 4].

The form of the Butler-Volmer equation used in this application, equation (5.19) does not directly include mass transfer limitations. However, limiting current conditions are accounted for using a sophisticated algorithm that will now be explained.

A novel method of estimating the limiting current has been developed. Rather than rely upon correlations to predict mass transfer coefficients, this method determines the limiting corrosion current based upon the concentration gradient. The numerical simulation proceeds using the corrosion rate (calculated assuming no mass transfer limitations) as a boundary condition until the concentration of a cathodic reagent becomes negative at the metal-solution interface. When this occurs, the boundary condition of that species is switched from the flux equation to a zero concentration condition and the concentration profile of each species in solution is recalculated. Chemical equilibrium and the charge density term of the mass transport equation cause the concentration of each species to be interdependent, and thus, changing the boundary condition of one

species in solution will affect the concentration profiles of every other species in solution. For the mass transport limited species, its diffusion current at the wall is then calculated:

$$i_{species} = -Fz_{species} D_{species} \left(\frac{\partial C_{species}}{\partial x} \right)_{wall} \quad (5.22)$$

This species diffusion current is then used in the calculation of the current consumed by the cathodic reaction in which it is a reagent. In this case, the rate of the cathodic reaction would be determined by the following expression:

$$i_{rxn} = \frac{i_{species}}{\nu_{species}} \quad (5.23)$$

where $\nu_{species}$ is the stoichiometric coefficient of the species in solution. Where more than one reagent in a particular reaction is predicted to be mass transport limited, the cathodic reaction current is calculated via (5.23) for each reagent. The lowest current is chosen as the reaction current and that species which minimized equation (5.23) is then the limiting reagent. Thus, when a reaction is under mass transfer control, its rate is no longer predicted using the Butler-Volmer equation, but rather, by the diffusion current of the limiting reagent (equations (5.22) and (5.23)). This is used in the application of mixed potential theory so that other reactions occurring in solution feel the effect of the mass transfer limited reaction. Thus, when the rate of consumption of a single species in solution switches from charge transfer control to mass transfer control, the effect of this change in control is felt throughout the system.

The rate of CO₂ dissolution is calculated by the following rate expression:

$$R_{H_2CO_3} = k_f C_{CO_2} - k_r C_{H_2CO_3} \quad (5.24)$$

The rate constants of the forward and reverse reaction are calculated using correlations and data provided by Kern [1] and Palmer and Eldik [22]. The rate at which H_2CO_3 is produced is dependent upon the partial pressure of CO_2 in the gas phase according to Henry's Law:

$$C_{CO_2} = k_{CO_2} P_{CO_2} \quad (5.25)$$

The Henry's Law constant is calculated using a correlation proposed by Roberts and Tremaine [23]. Thus, the CO_2 partial pressure has a direct influence on the corrosion rate, as one would expect.

Film formation kinetics are calculated based upon the $FeCO_3$ super-saturation, S :

$$S = \frac{[Fe^{2+}][CO_3^{2-}]}{K_{sp,FeCO_3}} \quad (5.26)$$

The value of S was used to determine the rate of film precipitation and dissolution [5]. In this model, film stripping due to mechanical wear was also accounted for [24]. Film formation causes damping of turbulent mixing near the wall and also decreases the effective molecular diffusivity of species via an increase in tortuosity. This was accounted for in the model by modifying the molecular diffusion coefficient in the following manner:

$$D_{eff} = D\varepsilon^2 \quad (5.27)$$

where ε is the porosity. This relationship comes from research into moisture transport in soils [25]. Also, the eddy viscosity was damped by presence of the film. The eddy viscosity was reduced by the porosity according to the following function:

$$\mu_{t,eff} = \max[\mu_t(1000\varepsilon - 999), 0] \quad (5.28)$$

Thus, the effective eddy viscosity varies linearly with porosity for $\varepsilon \in [0.999, 1]$ and is zero for $\varepsilon \in [0, 0.999]$. Equation (5.28) is used because of the discrete nature of the numerical model. Once the super-saturation of a particular control volume reaches a level such that precipitation will occur, the porosity of that control volume would immediately become lower than unity. If the eddy viscosity were immediately set to zero where the film was present, this would cause erratic changes in the corrosion rate profile. The linear function used to scale the eddy viscosity (equation 5.28) smoothes the transition from a turbulent flow condition to no flow condition within the film, thereby ensuring a smooth, physically realistic, transient corrosion current profile.

This model of CO₂ corrosion is implemented as a computer code. Figure 5.1 shows the predicted corrosion rate as a function of time compared with experimental observations of Nesic (2003) when the film growth model is included.

Figure 5.1 shows excellent agreement with the experimental studies of Nesic et al. (2003). In Figure 5.1, the rate of iron dissolution is balanced by the following cathodic reactions: H₂CO₃ reduction, H⁺ reduction, and water reduction. With the model validated, it was applied to predict the effect of the Reynolds number on the rate of CO₂ corrosion.

5.3.1 Effect of flow

Flow accelerates the rate of CO₂ corrosion in the following two ways:

1. Increased turbulence intensity enhances mixing of the solution, thereby shrinking the mass transfer boundary layer and increasing the rate of transport of cathodic reagents. This increases the limiting cathodic current which may increase the rate of corrosion if the process is mass transfer limited ($i_{corr} = i_{lim}$).

2. Stripping of the protective FeCO_3 film may occur. This will expose bare metal to the corrosive solution and increase the rate of CO_2 corrosion.

In Figure 5.2, the steady state corrosion rate is given as a function of increasing Reynolds number at 25°C . In this graph, the rate of mass transfer increases with the Reynolds number, as does the corrosion rate. Furthermore, at 25°C , the FeCO_3 film will not provide significant protection for the metal [5].

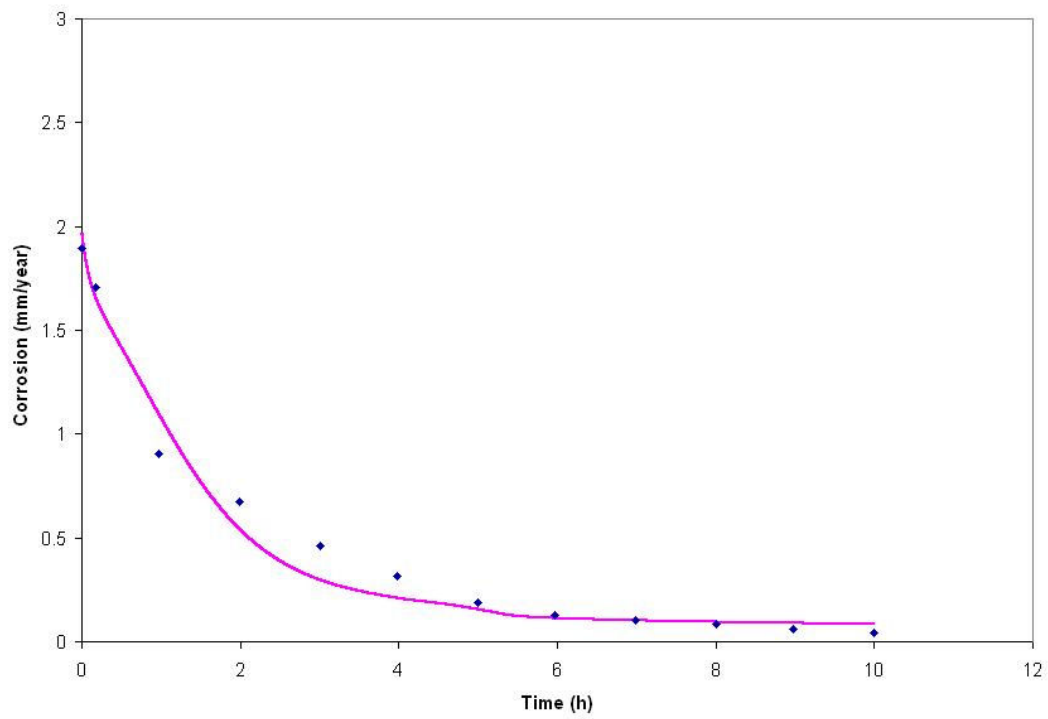


Figure 5.1. Corrosion rate in a mild steel pipe with carbonic acid solution flowing through it. ($T = 80\text{ }^{\circ}\text{C}$, $\text{pH} = 6.26$, $P_{\text{CO}_2} = 0.54\text{ bar}$, $[\text{Fe}^{2+}] = 250\text{ ppm}$, and $V_b = 1\text{ m/s}$).

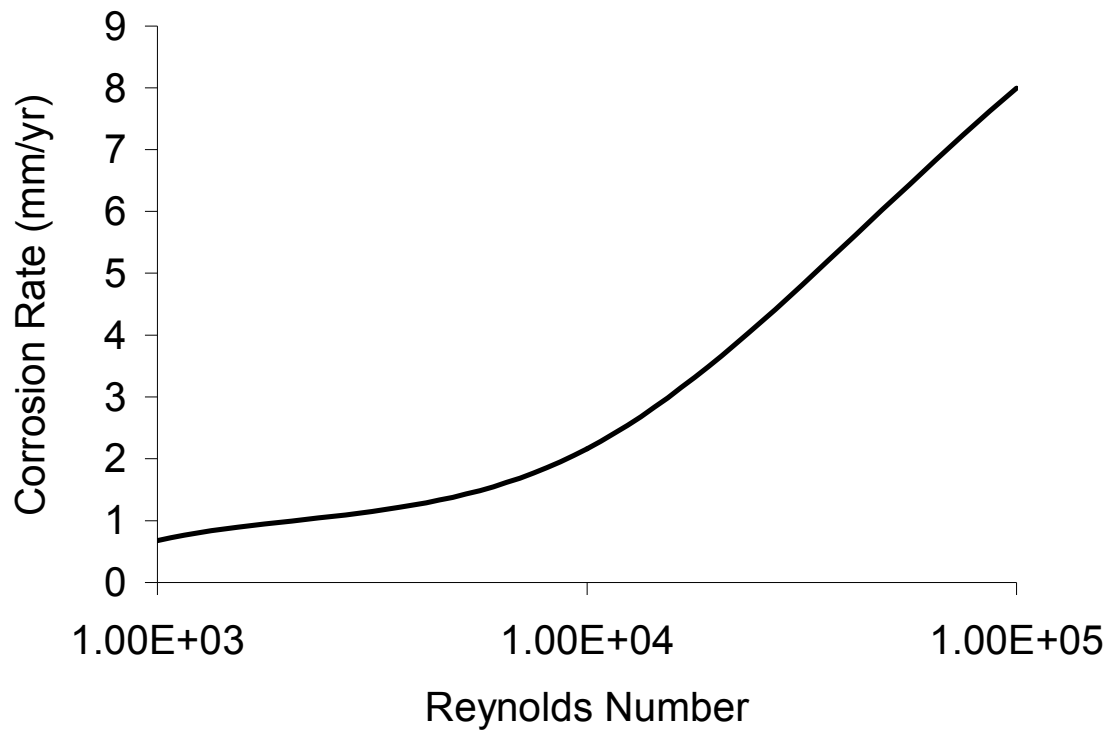


Figure 5.2. Effect of flowrate on steady state CO₂ corrosion rate of mild steel. (T = 25°C, pH = 6.26, $P_{CO_2} = 0.54 \text{ bar}$, $[Fe^{2+}] = 250 \text{ ppm}$)

5.4 References

1. D.M. Kern, (1960) *Journal of Chemical Education* **37**, pg. 9.
2. G. Schmitt and B. Rothmann (1977), *Werkstoffe und Korrosion* **28**, Vol. 28, 1977, pg. 816.
3. F. Wang, “Modelling of Aqueous Carbon Dioxide Corrosion in Turbulent Pipe Flow”, Ph. D. Thesis, University of Saskatchewan, 1999.
4. M. Nordsveen, S. Nestic, R. Nyborg, and A. Stangeland (2003), *Corrosion* **59**, pp. 443 – 456.
5. S. Nestic and K.-J. Lee (2003), *Corrosion* **59**, pp. 616 – 628.
6. K. Videm and A. Dugstad, “Film Covered Corrosion, Film Breakdown and Pitting Attack of Carbon Steels in Aqueous CO₂ Environments”, NACE International, *Corrosion* 88, 1988, Paper No. 186.
7. A. Dugstad, “The Importance of FeCO₃ Supersaturation on the CO₂ Corrosion of Carbon Steels”, *Corrosion* 92, NACE International, 1992, Paper No. 14.
8. C. De Waard and D.E. Milliams (1975), *Corrosion* **31**, p. 131.
9. L.G.S. Gray, B.G. Anderson, M.J. Danysh and P.R. Tremaine, “Mechanism of Carbon Steel Corrosion in Brines Containing Dissolved Carbon Dioxide at pH 4”, NACE International, *Corrosion* 89, 1989, Paper. No. 464.
10. S. Nestic, B.F.M. Pots, J. Postlethwaite, and N. Thevenot, *Journal of Corrosion Science and Engineering*, Vol. 1, <http://www.cp.umist.ac.uk/JCSE/>, 1995, Paper No. 3.
11. G. Schmitt, and B. Rothmann, *Werkstoffe und Korrosion*, Vol. 29, 1978, pg. 98.

12. J.O.M. Bockris, D. Drazic and A.R. Despic, *Electrochimica Acta*, Vol. 4, 1961, pg. 325.
13. C. De Waard, and D.E. Milliams (1975) "Prediction of Carbonic Acid Corrosion in Natural Gas Pipelines", First International Conference on the Internal and External Protection of Pipes, University of Durham, UK.
14. L.G.S. Gray, B.G. Anderson, M.J. Danysh and P.R. Tremaine, "Effect of pH and Temperature on the Mechanism of Carbon Steel Corrosion by Aqueous Carbon Dioxide", NACE International, *Corrosion* 90, 1990, Paper No. 40.
15. M. Stern and L. Geary, *J. Electrochem. Soc.*, Vol. 104, 1957, pg. 56.
16. J.O.M. Bockris and A.K.N. Reddy, "Modern Electrochemistry – An Introduction to an Interdisciplinary Area", Vol. 2, Plenum Press, New York, 1970.
17. C. De Waard, and U. Lotz, "Prediction of CO₂ Corrosion of Carbon Steel", NACE International, *Corrosion* 93, 1993, Paper No. 69.
18. A. Dugstad, L. Lunde and K. Videm, "Parametric Study of CO₂ Corrosion of Carbon Steel", NACE International, *Corrosion* 94, 1994, Paper No. 14.
19. S. Turgoose, R.A. Cottis and K. Lawson, "Modelling of Electrode Processes and Surface Chemistry in Carbon Dioxide Containing Solutions", ASTM Symposium on Computer Modelling for Corrosion, San Antonio TX, 1990.
20. A.J. Bard and L.R. Faulkner, "Electrochemical Methods, Fundamentals and Applications", John Wiley and Sons, 1980, Chapters 8 and 11.
21. S. Nestic, M. Nordsveen, R. Nyborg, and A. Stangeland (2003), *Corrosion* **59**, pp. 489 – 497.
22. D.A. Palmer and R.V. Eldik (1983), *Chem. Rev.* **83**, p. 651.

23. B.E. Roberts and P.R. Tremaine (1985), *Canadian Journal of Chemical Engineering* **63**, p. 294..
24. G. Kennell (2005), “A Mechanistic Model of Iron Carbonate Film Crystallization Due to Carbon Dioxide Corrosion of a Steel Pipe“, Unpublished report.
25. R.I. Papendick, and G.S. Campbell (1981). “Theory and measurement of water potential” in “Water Potential Relations in Soil Microbiology”. SSSA special publication No. 9. J.F. Parr, W.R. Gardner and L.F. Elliott, (eds.). Soil Science Society of America: Madison, Wis. U.S.A, pp. 1 – 22.

Chapter 6. Flow Influenced Crevice Corrosion

Previous work shown in this thesis has shown mathematical models for localized corrosion and flow influenced corrosion. In this chapter, the models developed for localized and flow influenced corrosion are applied to model the effect of flow on localized corrosion. Flow influenced localized corrosion is a difficult phenomenon to predict mathematically as it requires the solution of inter-coupled models of mass and momentum transfer in complex geometries. Furthermore, the influence of recirculation flow inside the crevice requires that a 2-D description of the crevice-internal environment be adopted.

The influence of flow may be beneficial or detrimental to a crevice undergoing localized attack. For a very small crevice, the external flowfield will be unable to penetrate into the crevice. Thus, while the internal crevice solution is stagnant, external flow will enhance mass transfer to the system cathode (the bold surface). This will allow for a smaller bold surface to sustain internal crevice dissolution processes. As a result, the rate of the electrode reactions may be governed by anodic charge transfer kinetics and, thus, not be hindered by mass transfer at the bold surface. In this case, external flow will accelerate crevice corrosion. However, if the crevice is large enough such that fluid penetrates into the crevice, convection into and out of the crevice will displace the acid-chloride solution in the crevice with less aggressive bulk solution. This will have two

effects. Firstly, enhanced mixing in the crevice solution will reduce the crevice solution conductivity, and thus, increase the resistance between the internal and external surfaces. This will result in decreased interaction between anode and cathode, and thus, lower the rate of electromigration mass transport. Secondly, cathodic reagents would be made available to anodic sites in the crevice due to flow penetration. As a result, these sites would begin to sustain all or part of their anodic process with localized reduction of cathodic reagent and, thus, wholly or partially return to a micro-celled state. The net effect of flow penetration is crevice washout, where the crevice is returned to a state of microscopic (uniform) corrosion. If the crevice is large enough, this will lower the rate of crevice corrosion and is thus beneficial. However, while penetrating flow may hinder crevice corrosion, the presence of a turbulent flowfield inside a crevice may cause accelerated uniform corrosion in and around the crevice. This is a form of corrosion known as mesa corrosion. This type of corrosion is not studied specifically in this work but it is a natural extension to the model.

In this work, a two-dimensional model of crevice corrosion was developed. Unlike the previous one-dimensional models shown in chapter 4, this crevice corrosion model does not assume that the metal is passivated. However, it is capable of modelling passive metals. The mass transfer limited form of the Butler-Volmer equation is used in this model. The Butler-Volmer equation is applicable to a passive metal in the following way: the slope of the anodic line for a passive metal is set to a very high number (such that the anodic line on the kinetic corrosion diagram is vertical). Because a very important aspect of crevice corrosion is the anode-cathode separation that occurs due to

differential aeration, this model implements an electrode coupling algorithm which will be discussed. The limiting current is calculated in the following manner:

1. The concentration boundary conditions of a particular species is set to zero at all solid boundaries
2. The two-dimensional mass transport equation is solved over a single time step using current solution conditions as the initial condition
3. The diffusion limited flux of the species currently being simulated is evaluated. This is the limiting species current.

These steps are repeated for each species in solution. The limiting current is updated at each time step for increased accuracy. The mathematical model will now be discussed.

6.1 Computational Fluid Dynamics Model

The velocity and pressure field must be such that both momentum and mass are conserved. Momentum conservation is described by the Reynolds-Averaged Navier-Stokes (RANS) equations:

$$\begin{aligned} \rho \frac{\partial v_x}{\partial t} + \frac{\partial}{\partial x} \left(\rho v_x^2 - (\mu + \mu_t) \frac{\partial v_x}{\partial x} \right) \\ + \frac{\partial}{\partial y} \left(\rho v_x v_y - (\mu + \mu_t) \frac{\partial v_x}{\partial y} \right) = - \frac{\partial p}{\partial x} \end{aligned} \quad (6.1)$$

$$\begin{aligned} \rho \frac{\partial v_y}{\partial t} + \frac{\partial}{\partial x} \left(\rho v_x v_y - (\mu + \mu_t) \frac{\partial v_y}{\partial x} \right) \\ + \frac{\partial}{\partial y} \left(\rho v_y^2 - (\mu + \mu_t) \frac{\partial v_y}{\partial y} \right) = - \frac{\partial p}{\partial y} \end{aligned} \quad (6.2)$$

Here, μ_t is the eddy viscosity, which is calculated using a suitable turbulence model.

The velocity field that satisfies equations (6.1) and (6.2) must also satisfy the mass

continuity equation. For an incompressible fluid, mass continuity states that the velocity field must be solenoidal, i.e.:

$$\nabla \cdot \mathbf{v} = 0 \quad (6.3)$$

There is a problem with the direct application of equation (6.3). Mass conservation is enforced in a flow by the pressure field. However, the pressure field does not appear in (6.3) and is a source term in (6.1) and (6.2). To resolve this problem, pressure correction schemes have been developed to calculate the pressure field and the continuity-satisfying velocity field in incompressible flows. The most commonly used types of pressure correction schemes fall in the SIMPLE (Semi-Implicit Method for Pressure Linked Equations) class of schemes. Descriptions of a number of SIMPLE schemes are available in Patankar [1] and Ferziger and Perić [2]. For the present CFD model, the SIMPLEC pressure correction scheme was chosen. This scheme offers the best convergence performance due to the fact that the pressure correction and momentum solvers require less underrelaxation.

In this model, the flow is modelled in the laminar sublayer due to the scale of the crevice. In this region, the Reynolds number of the flow is expected to be quite low. Thus, a turbulence model was not required for this application. Figure 6.1 illustrates the crevice system being modelled in this work.

6.1.1 Flow boundary conditions

The velocity boundary conditions at the flow inlet, flow outlet, and all solid boundaries are given below:

Inlet:

$$v_x = V_{bulk} \quad (6.4)$$

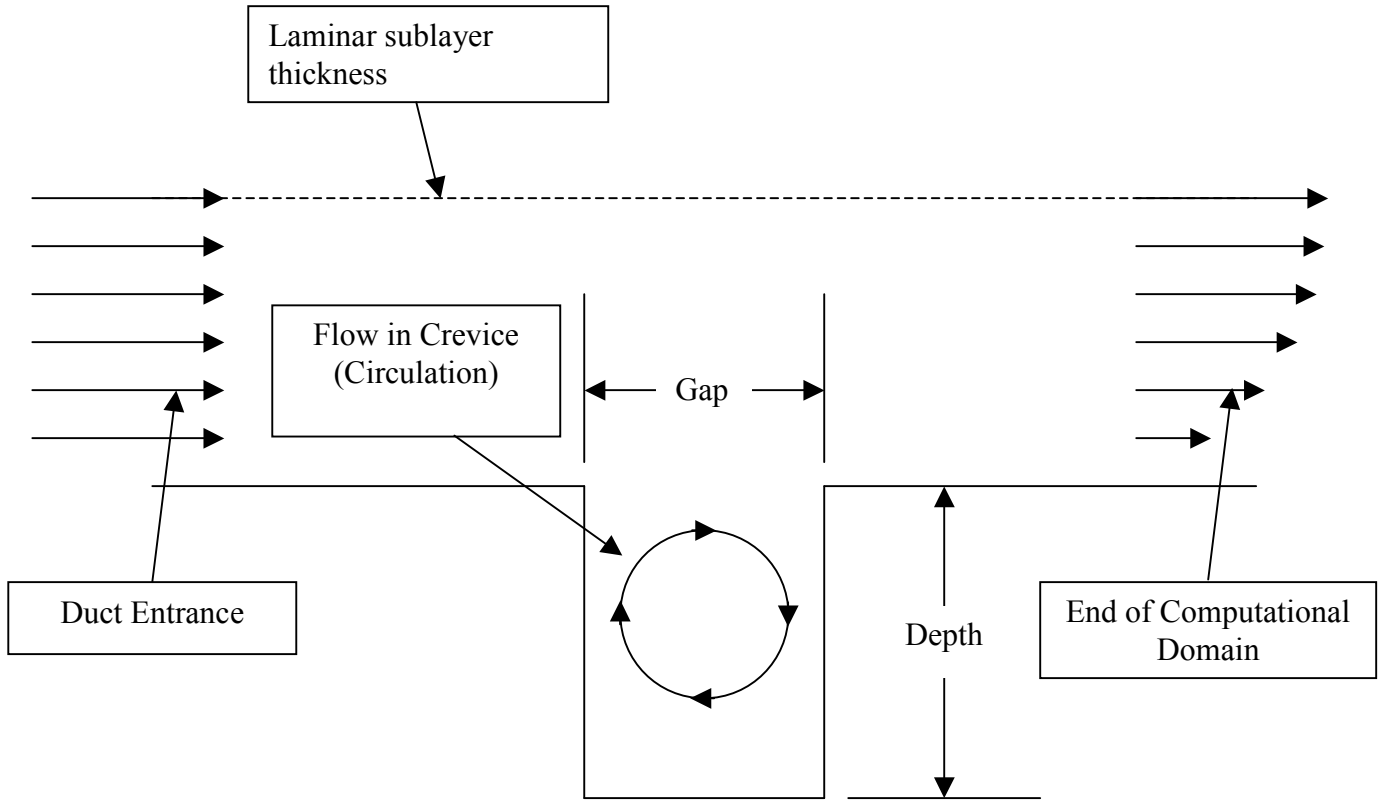


Figure 6.1. The coupled flow influenced and localized corrosion system. The size of the crevice on the duct wall is exaggerated for clarity.

$$v_y = 0 \quad (6.5)$$

Outlet:

$$\frac{\partial v_x}{\partial x} = \frac{\partial v_y}{\partial x} = 0 \quad (6.6)$$

Solid boundary:

$$v_x = v_y = 0 \quad (6.7)$$

A zero-gradient condition is used for the pressure correction variable at all boundaries [2].

6.1.1.1 Boundary conditions at laminar sublayer thickness

To determine the boundary condition for the edge of the laminar sublayer, consider the universal velocity profile (in the laminar sublayer region) [3]:

$$v_x = \frac{\rho u_\tau^2}{\mu} y \quad (6.8)$$

The shear stress at the edge of the laminar sublayer is therefore:

$$\mu \frac{\partial v_x}{\partial y} = \mu \frac{\partial}{\partial y} \left(\frac{\rho u_\tau^2}{\mu} y \right) \quad (6.9)$$

Performing the differentiation yields:

$$\mu \frac{\partial v_x}{\partial y} \Big|_{y=\lambda} = \rho u_\tau^2 \quad (6.10)$$

Or:

$$\frac{\partial v_x}{\partial y} \Big|_{y=\lambda} = \frac{5u_\tau}{\lambda} \quad (6.11)$$

Equation (6.11) is the boundary condition for the edge of the viscous sublayer. Here, λ is the thickness of the viscous sublayer, which is determined from the following equation:

$$y^+ = \frac{\lambda u_\tau}{\nu} = 5 \quad (\text{at the edge of the laminar sublayer}) \quad (6.12)$$

Thus:

$$\lambda = 5 \frac{\mu}{\rho u_\tau} \quad (6.13)$$

The friction velocity, u_τ , is defined as:

$$u_\tau = \sqrt{\frac{\tau_w}{\rho}} \quad (6.14)$$

Thus, when dealing with a flow with a known Reynolds number, the wall shear stress may be calculated. Thus, the friction velocity and the sublayer thickness may be computed. The bulk velocity in the sublayer is used as an entry boundary layer (plug flow is assumed coming in). This is shown above as V_b and its value can be calculated as follows:

$$V_b = \frac{1}{\lambda} \int_0^\lambda v_x(y) dy \quad (6.15)$$

In the laminar sublayer, the velocity profile is given in equation (6.8). Substituting equation (6.8) into (6.16) and performing the integration yields:

$$V_b = \frac{1}{\lambda} \int_0^\lambda \frac{\rho u_\tau^2}{\mu} y dy = \frac{1}{\lambda} \frac{\rho u_\tau^2}{\mu} \frac{\lambda^2}{2} = \frac{\rho u_\tau^2}{\mu} \frac{\lambda}{2} \quad (6.16)$$

This can be simplified by the substitution of (6.13) to yield:

$$V_b = 2.5 u_\tau \quad (6.17)$$

Equation (6.17) is substituted in the boundary condition for the flow inlet, equation (6.4).

6.1.2 Relationship between sublayer thickness and Reynolds number

It is more practical to represent the sublayer thickness as a more physically meaningful variable, namely the Reynolds number. In this section, the relationship between the sublayer thickness and the Reynolds Number will be explored. A method for calculating the Reynolds number from the sublayer thickness will be presented. Rearrangement of equation (6.13) yields the following relationship between the friction velocity and the sublayer thickness:

$$u_\tau = 5 \frac{\mu}{\rho \lambda} \quad (6.18)$$

From the friction velocity, the shear stress may be determined by rearranging equation (6.14):

$$\tau_w = u_\tau^2 \rho \quad (6.19)$$

The Reynolds number is related to the wall shear stress by the following equation [4]:

$$\text{Re} = \frac{D}{\mu} \sqrt{\frac{2\tau_w \rho}{f}} \quad (6.20)$$

However, the Reynolds number and the Fanning friction factor, f , are also related by Churchill's equations [4]:

$$f = 2 \left[\left(\frac{8}{\text{Re}} \right)^{12} + (A + B)^{-1.5} \right]^{\frac{1}{12}} \quad (6.21a)$$

where:

$$A = \left(-2.457 \ln \left[\left(\frac{7}{\text{Re}} \right)^{0.9} + 0.27 \left(\frac{k}{D} \right) \right] \right)^{16} \quad (6.21b)$$

$$B = \left(\frac{37530}{\text{Re}} \right)^{16} \quad (6.21c)$$

Equations (6.20) and (6.21) can be applied iteratively. Once the wall shear stress is known, the value of the Fanning friction factor can be guessed and the Reynolds number calculated by equation (6.20). With this value of the Reynolds number, a new estimate of the Fanning friction factor may be obtained using equation (6.21). This process is repeated until the Reynolds number stops changing, usually after a few iterations. For the calculation of the Fanning friction factor using Churchill's equations, equation (6.21), the pipe was assumed to be smooth, i.e. $k = 0$. Here, k is the sand grain roughness. The iterative procedure was implemented in a Microsoft Excel[®] spreadsheet.

6.2 Simulation of Crevice Washout

Using the boundary conditions shown above, the two-dimensional CFD model was used to calculate the flowfields shown in Figures 6.2 – 6.6. In each simulation, the Reynolds number was 5.4×10^5 , the crevice depth was $50 \mu\text{m}$, and the pipe diameter was 20 cm. To show the effect of the crevice gap on washout, the crevice gap was varied in size from $10 \mu\text{m}$ – $200 \mu\text{m}$.

From Figures 6.2 – 6.7, the effect of the crevice gap upon the crevice corrosion incubation period can be seen. Figures 6.2 – 6.6 show the velocity vector fields in each of the crevices. In each case, the crevice depth is $50 \mu\text{m}$. The crevice gaps analyzed are $10 \mu\text{m}$ (Figure 6.2), $20 \mu\text{m}$ (Figure 6.3), $50 \mu\text{m}$ (Figure 6.4), $100 \mu\text{m}$ (Figure 6.5), and $200 \mu\text{m}$ (Figure 6.6). Figure 6.7 shows the magnitude of the velocity in the crevice calculated at the crevice centerline as a function of depth inside the crevice. Using the results in these figures, the effect of flow on each crevice will now be explained.

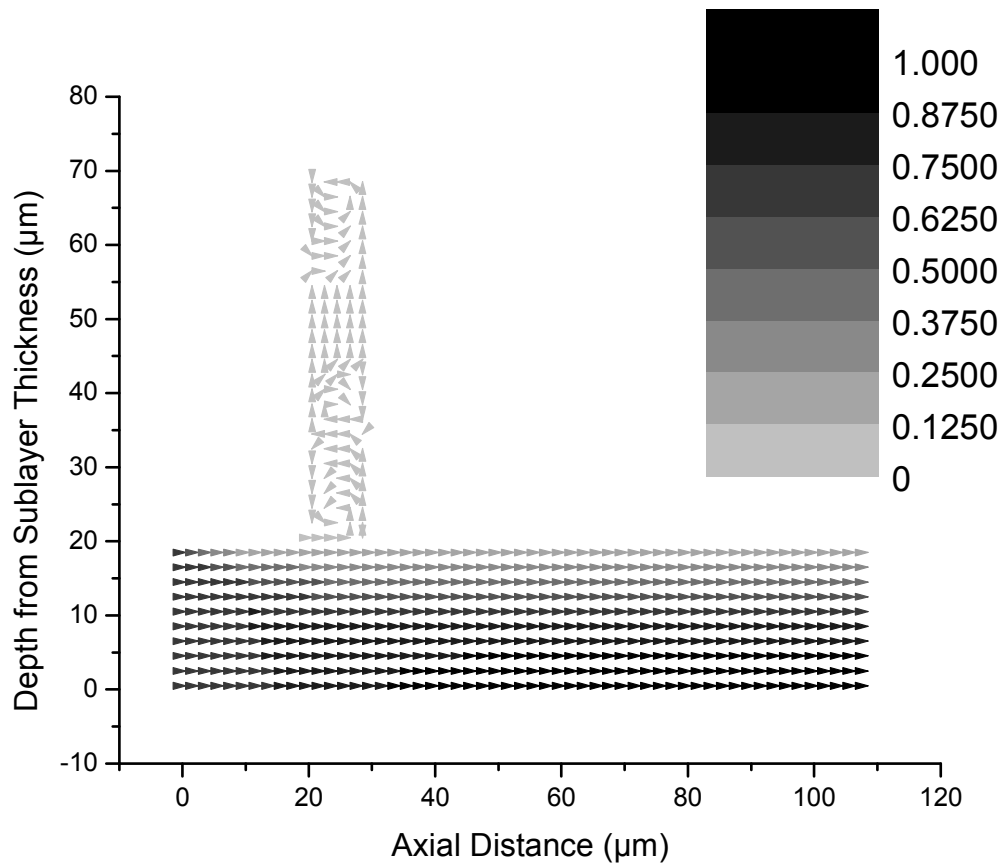


Figure 6.2. Predicted velocity field in the flow influenced crevice system. Crevice is 50 μm deep and 10 μm across the gap. Flow is modelled within 20 μm of the pipe wall. The bulk Reynolds number is 5.4×10^5 . The velocity is in units of m/s.

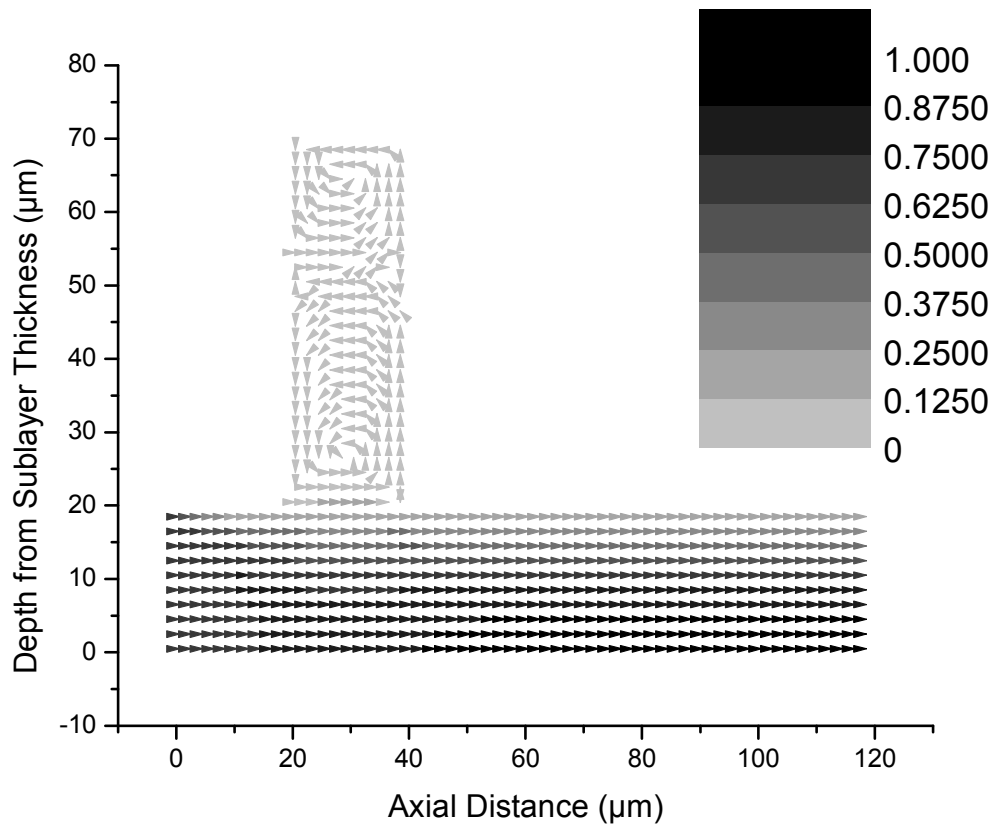


Figure 6.3. Predicted velocity field in the flow influenced crevice system. Crevice is 50 μm deep and 20 μm across the gap. Flow is modelled within 20 μm of the pipe wall. The bulk Reynolds number is 5.4×10^5 . The velocity is in units of m/s.

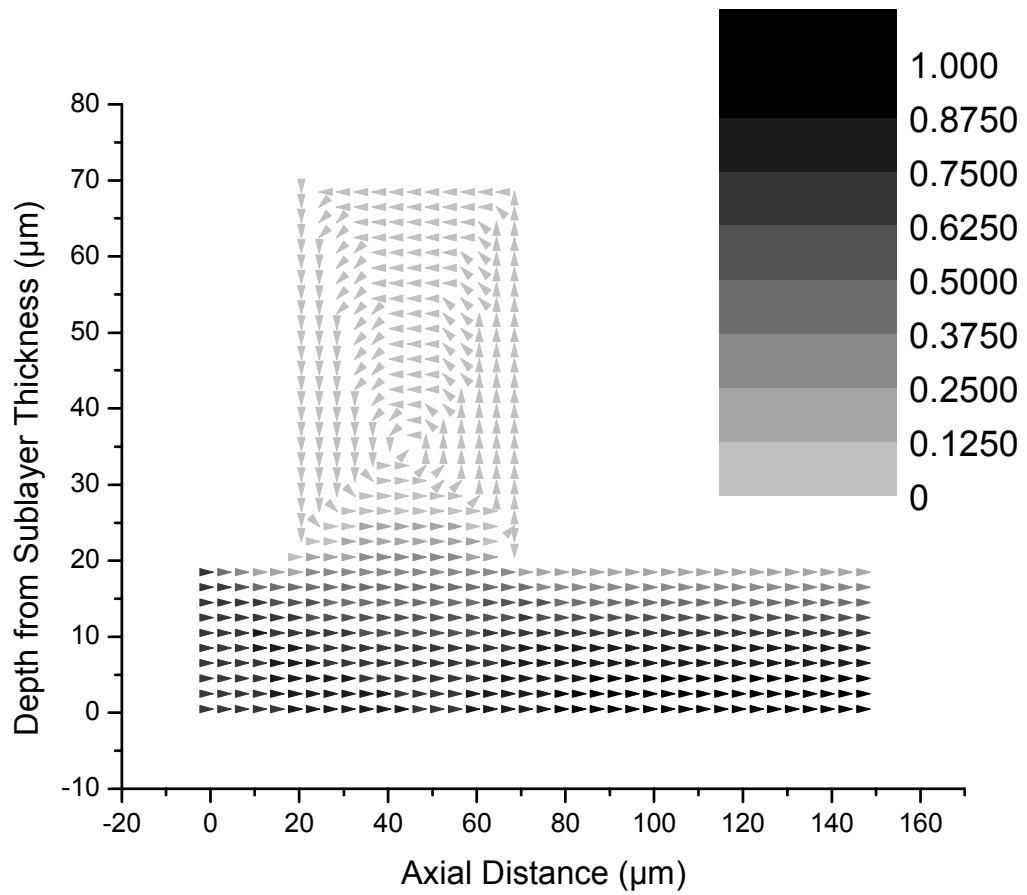


Figure 6.4. Predicted velocity field in the flow influenced crevice system. Crevice is 50 μm deep and 50 μm across the gap. Flow is modelled within 20 μm of the pipe wall. The bulk Reynolds number is 5.4×10^5 . The velocity is in units of m/s.

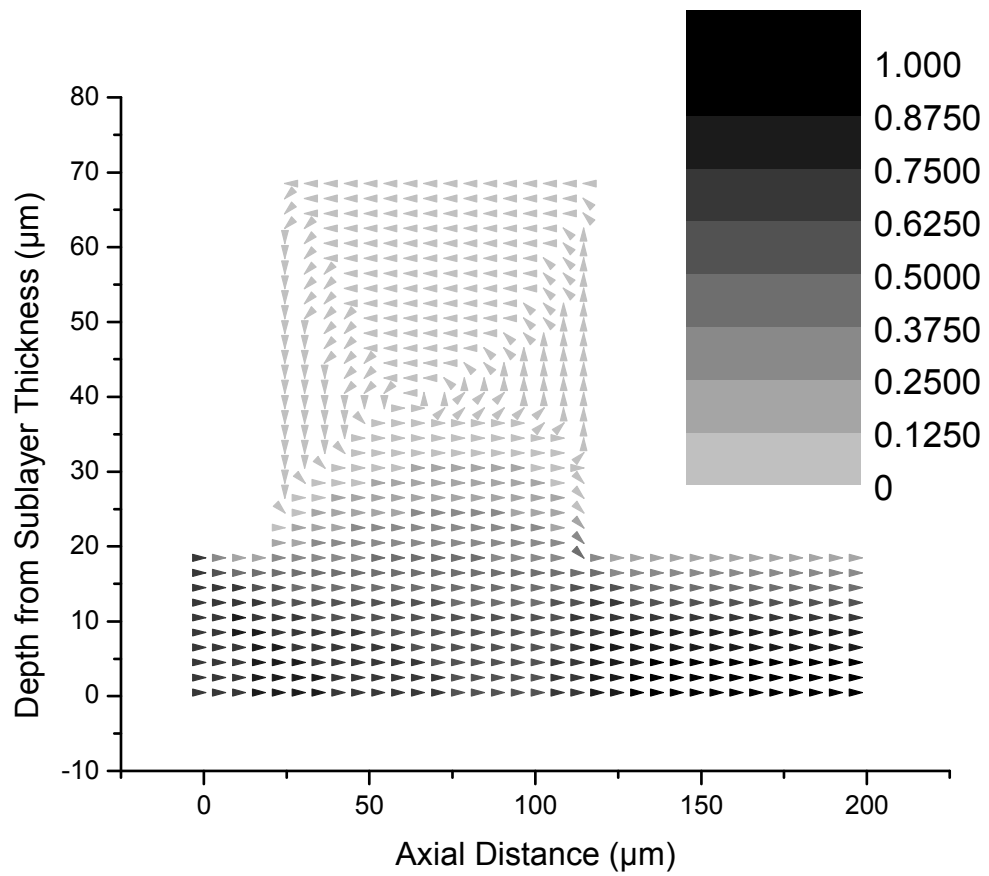


Figure 6.5. Predicted velocity field in the flow influenced crevice system. Crevice is 50 μm deep and 100 μm across the gap. Flow is modelled within 20 μm of the pipe wall. The bulk Reynolds number is 5.4×10^5 . The velocity is in units of m/s.

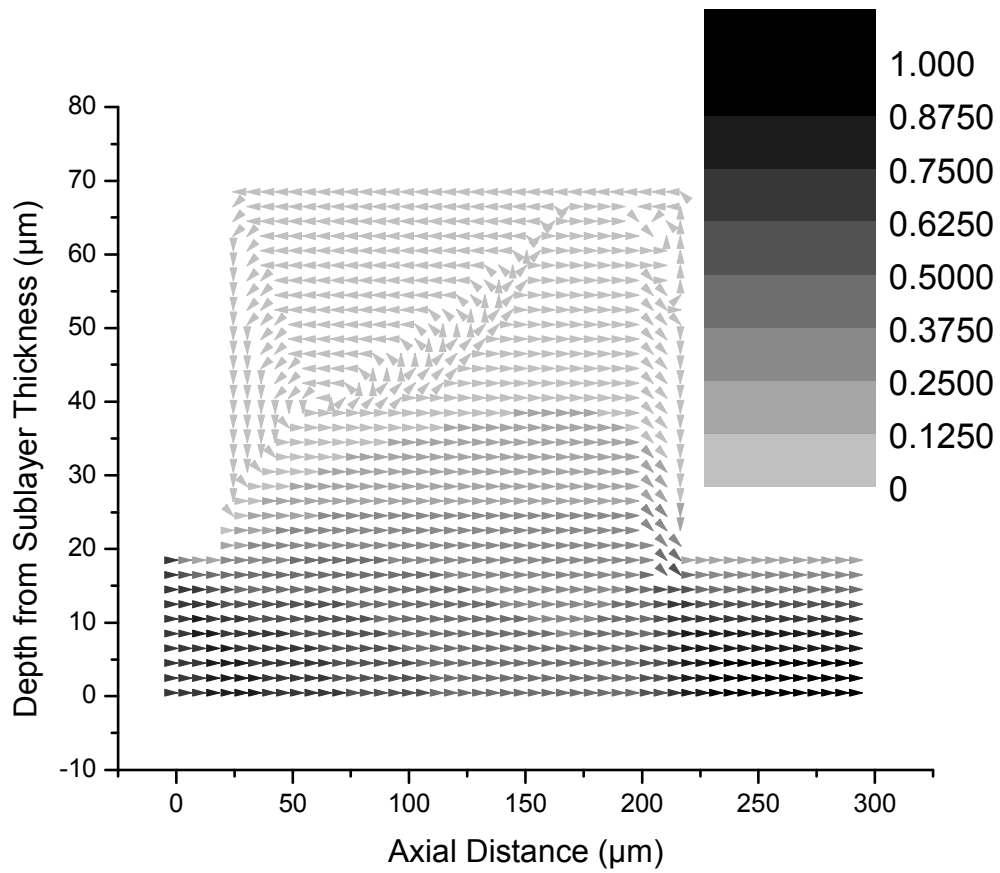


Figure 6.6. Predicted velocity field in the flow influenced crevice system. Crevice is 50 μm deep and 200 μm across the gap. Flow is modelled within 20 μm of the pipe wall. The bulk Reynolds number is 5.4×10^5 . The velocity is in units of m/s.

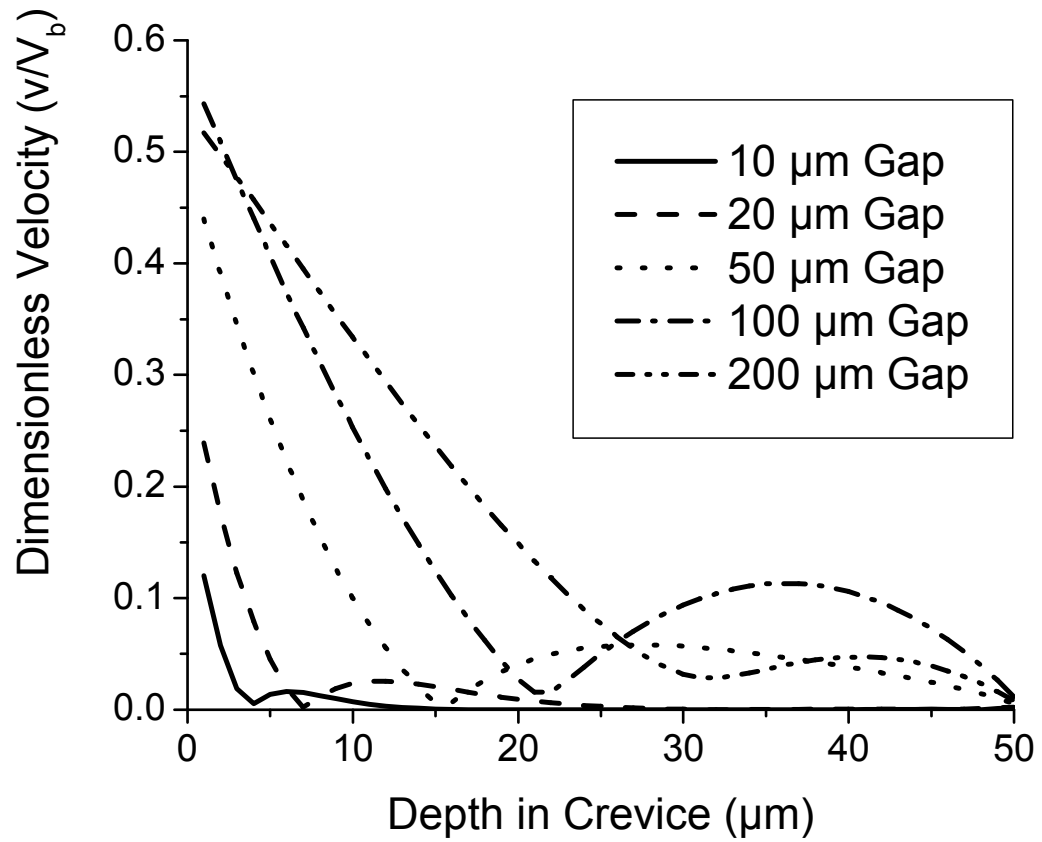


Figure 6.7. Velocity magnitude along crevice centreline for varying gap sizes. The magnitude of the velocity is determined from the vector velocity data presented in Figures 6.2 – 6.6.

In Figure 6.2 (10 μm gap), fluid from the bulk solution shears the crevice fluid causing a series of vortices inside the crevice. From Figure 6.7, it can be seen that the magnitude of the velocity in the 10 μm crevice is very small. Thus, there is only limited transport of momentum from the bulk solution to the crevice solution. Furthermore, from the flow regime in Figure 6.2, it can be seen that there is little or no penetration of the bulk fluid into the crevice, and thus, crevice washout is predicted to not occur. Because washout does not occur, acid-chloride solutions that form inside the crevice will not be replaced by more neutral bulk solution fluid. However, the transfer of momentum from the bulk solution to the crevice, which is manifested as vortices in the crevice fluid, will cause mixing of the crevice fluid. It was seen in previously presented studies on crevice corrosion initiation that, due to a lower rate of electromigration transport at the crevice tip, the most aggressive acid-chloride solutions will develop at the crevice tip. Mixing caused by vortices in the crevice will hinder the onset of crevice corrosion by more uniformly distributing H^+ and Cl^- species throughout the crevice solution. While the flowfield causes mixing of the crevice solution, which is beneficial, it also causes an increase in the cathodic limiting current at the bold surface, which is detrimental. Increasing the limiting current at the cathode may increase the bold surface potential, causing an increased driving force for crevice corrosion. In essence, increasing the cathodic limiting current will increase the throwing power of the bold surface and allow anodic reactions within the crevice to proceed at a faster rate. For the 10 μm crevice, the overall effect of crevice-external flow is detrimental to its crevice corrosion resistance.

In Figure 6.3 (20 μm gap), very slight fluid penetration begins to occur. However, the predominant effect of the external flowing fluid is to shear the crevice-internal fluid

and cause recirculation patterns in the crevice. While recirculation in the crevice is still very slow, the strength of the vortices has increased compared to the 10 μm crevice. Due to the aspect ratio of the crevice, the primary vortex nearest the crevice mouth does not extend over the crevice length. Rather, it causes a secondary vortex which spins in the opposite direction. This secondary vortex produces a third vortex at the crevice tip, which again rotates in the direction of the primary vortex. A similar recirculation pattern was observed in the 10 μm gap. Examination of the magnitude of the velocity in the centre of the 20 μm crevice shows that the velocity field does not significantly penetrate the crevice. This confirms that washout is not predicted for the 20 μm crevice.

In Figure 6.4 (50 μm gap), the gap is of sufficient size so that one large vortex exists in the crevice. This represents a significant change in flow pattern from the 20 μm crevice where a series of two vortices, each dissipating momentum transferred from the previous vortex, developed from a primary vortex at the crevice mouth. Furthermore, from Figure 6.7, it can be seen that the velocity field more significantly penetrates the crevice fluid. The fluid exchange occurs near the crevice mouth. However, due to mixing caused by recirculation flow in the crevice, this may cause crevice washout.

In Figure 6.5 (100 μm gap), one large vortex again develops inside the crevice. Both the strength of the vortex and the penetration of external fluid into the crevice have increased compared to the 50 μm gap. This is confirmed by examination of Figure 6.7. Penetration of the external fluid into the crevice is still quite shallow. However, as in the 50 μm crevice, mixing of the crevice solution due to recirculation could combine with the effect of fluid penetration to cause crevice washout.

In Figure 6.6 (200 μm gap), it is apparent that crevice washout will occur. Due to the direction of flow, the top right hand corner of the crevice is washed out while a vortex develops in the top left hand corner. Thus, crevice corrosion could still occur in the vortex region where fluid velocities are significantly lower. This phenomenon could result in irregular geometries in a crevice. However, it is likely that mixing caused by the vortex in the corner will also wash the corner out. Thus, total crevice washout is the likely outcome of this situation. However, due to increased mass transfer, the uniform corrosion rate inside the crevice will increase, but not to the extent caused by a differential aeration cell.

A theoretical model of mass transport and electrochemistry for a two-dimensional crevice has been developed. It is shown in Appendix B.

6.3 Conclusions

In this chapter, a computational fluid dynamics model has been developed and implemented to predict crevice washout. It has been shown that as the ratio of the crevice gap to depth increases, the penetration of the bulk fluid into the crevice increases, thereby increasing the extent of crevice washout. This is a beneficial effect as it reduces the propensity for aggressive solutions to develop in the crevice. However, it is also predicted that for small crevices, fluid penetration is minimal, thereby showing that flow outside of a small crevice is detrimental. In this case, while the benefits of crevice washout are not seen, the throwing power of the cathode is increased due to the increased limiting cathodic current density.

6.4 References

1. J.H. Ferziger and M. Perić, “Computational Methods for Fluid Dynamics”, 3rd Ed., Springer-Verlag, Berlin, Heidelberg, New York, 2002, pp.176 – 178.
2. S.V. Patankar (1980), “Numerical Heat Transfer and Fluid Flow”, Hemisphere Publishing Corp., New York.
3. R.W. Fox and A.T. McDonald, ”Introduction to Fluid Mechanics”, 3rd Edition, John Wiley and Sons, Inc., 1985, p. 354.
4. C.O. Bennett and J.E. Myers, “Momentum, Heat, and Mass Transfer”, 3rd Ed., McGraw Hill, Inc., USA, 1982.

Chapter 7. Summary and Conclusions

7.1 Summary

The goal of this work was to develop improved methods and algorithms for the prediction of localized and flow influenced corrosion. While there are significant differences in the mechanisms by which localized vs. flow influenced corrosion occur, both types of corrosion are profoundly influenced by mass transport. In localized corrosion, electromigration and diffusion mass transport between the exterior bold surface and the crevice interior limits the rate of corrosion and the depth of attack. If a turbulent flowfield is present outside of the crevice, convective mass transport will increase the cathodic limiting current at the bold surface, and depending upon the size of the crevice gap relative to the depth, may cause crevice washout. In flow influenced corrosion, the presence of turbulent flow enhances mass transport to the surface, thus increasing the limiting cathodic current. Thus, electrolyte mass transport is a common influence on each form of corrosion modelled in this work. Although the mass transport model is only applied to corrosion problems in this work, the transport model and the numerical algorithms presented for its solution are equally applicable to other electrochemical systems.

7.2 Conclusions

7.2.1 Modelling of electrolyte mass transport

Because mass transport plays such an important role in all forms of corrosion, a significant amount of work was also done to develop more sophisticated techniques to accurately and efficiently predict electrochemical mass transport. A key difficulty in mass transport modelling has been correctly accounting for the effect of charge density. Charge density effects occur at very different time scales from other forms of transport (convection, diffusion, and electromigration) and this feature makes solving the complete electrolyte mass transport equation impossible. Two new tools for the accurate calculation of electrolyte mass transport have been developed in this work – the hybrid differencing scheme for electrolyte mass transport and the algebraic charge density correction. From the work done in electrolyte mass transport modelling, the following conclusions can be made:

1. The hybrid differencing scheme uses a local pseudo-steady state description of electrolyte mass transport to calculate the Peclet number, a measure of the strength of electromigration to diffusion. The Peclet number, in turn, is used to calculate upwind parameters for use in transport coefficient calculation.
2. Use of the hybrid differencing scheme results in up to 87% more accurate calculation of the velocity of the Ag^+/K^+ moving boundary relative to the experimental observations of Fu and Chan.
3. The algebraic charge density correction scheme is derived from a linearization of the charge density term of the electrolyte mass transport equation. The fraction of

excess charge borne by an ionic species is proportional to the product of its charge number, ionic mobility, and concentration in solution.

4. Use of the algebraic charge density correction scheme improves upon the accuracy and numerical stability of previously proposed charge density calculation algorithms. For example, the application of the scheme to the Fu and Chan experiment resulted in a sixfold decrease in computation time compared to using the charge density correction scheme proposed by Evitts and Watson while enhancing the accuracy of the simulation.

7.2.2 Simulation of crevice corrosion initiation of passive metals

The crevice corrosion initiation model developed herein predicted that increased temperature, decreased crevice gap, decreased pitting resistance equivalent number (PREN) and increased electrolyte conductivity were detrimental to the crevice corrosion resistance of passive alloys. This crevice corrosion model improved upon previous crevice corrosion models by more accurately calculating non-ideal solution effects through the use of Pitzer's Equations (see Sections 4.1 and 4.2). The ability of this model to accurately rank stainless steels for their crevice corrosion resistance was demonstrated. The following conclusions can be made:

1. The size of the crevice gap has a dramatic influence on the crevice solution and the dominance of transport mechanisms in the crevice. For small gaps, electromigration is the dominant transport mechanism. Furthermore, activity gradients, which are steep due to strong electromigration, are smoothed by diffusion. The coupling of electromigration and diffusion induces charge density effects. For large gaps, the current density in solution is smaller, and therefore,

the strength of electromigration relative to diffusion is less. As a result, the charge density profile in a larger gap crevice is of smaller magnitude than that in a small gap crevice.

2. Ionic interactions affect the crevice corrosion process. Ionic interactions influence the rate of mass transport. For example, in a type 304 stainless steel crevice in 0.6 M NaCl at 25°C, the rate of H⁺ transport out of the crevice is hindered while the rate of Cl⁻ transport into the crevice is enhanced. In addition, ionic interactions may delay and/or prevent attainment of a steady state condition. When the ionic interaction model is included, a secondary pH drop is seen which is caused solely by ionic interaction.
3. The crevice corrosion initiation model augmented with Pitzer's equations is capable of modelling crevice corrosion initiation of stainless steels and titanium in potash brine. By calculating the predicted crevice pH, the following ranking from most resistant to susceptible was predicted: Grade 2 titanium, Type 314 stainless steel, Type 308 stainless steel, Type 304 stainless steel, and Type 405 stainless steel. This is the expected order – titanium is known to be highly resistant to corrosion and the steels are in order of their pitting resistance equivalent numbers (PRENs).
4. The crevice corrosion model developed in this work improves upon the accuracy of previous models. Figure 7.1 shows that the crevice pH distribution as predicted using the present model more closely represents experimentally determined pH values in a type 304 stainless steel crevice than previous models.

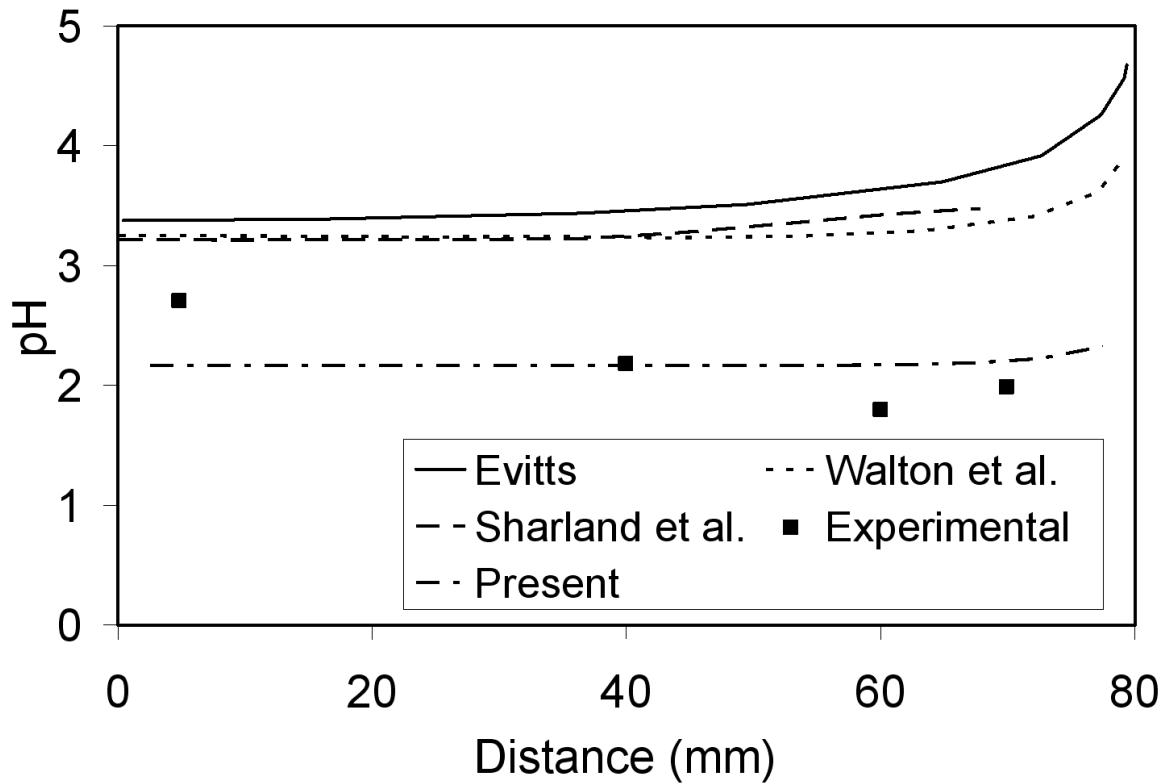


Figure 7.1. Comparison of Predicted pH Profile Against Predictions of Previously Published Models and the Experimental Observations of Alavi and Cottis in a Type 304 Stainless Steel Crevice (25°C, 0.6 Molar NaCl Bulk Solution, Dimensions 90 μm x 2.5 cm x 8.0 cm)

7.2.3 Simulation of flow influenced CO₂ corrosion

A CO₂ corrosion model was developed which accurately predicted experimental observations of others. This rigorous model accounted for FeCO₃ film growth. This model used a novel technique to calculate limiting current density. Rather than relying upon empirical correlations applicable to a specific situation, this technique calculated the limiting current by varying the boundary condition at the reactive wall from a corrosion induced flux (charge transfer control) to a zero concentration condition (mass transfer controlled). When a cathodic reaction is mass transfer controlled, the diffusion-limited current is used to calculate the contribution to the overall cathodic current, rather than the Butler-Volmer equation. It was shown that increased Reynolds number causes an increase in the corrosion rate, which is the expected result.

7.2.4 Simulation of flow influenced crevice corrosion

Using the flow influenced crevice corrosion model developed herein, it was found that turbulent flow outside a crevice with a small gap to depth ratio increases mass transfer rates to the bold surface, thereby increasing the cathodic limiting current. Momentum transferred from the bulk solution fluid to the crevice-internal fluid was manifested as a series of vortices in the crevice, which caused mixing of the crevice solution. Turbulent flow outside a crevice with a small gap was detrimental to the crevice corrosion resistance of the metal.

Turbulent flow outside a crevice with a large gap to depth ratio caused crevice washout. Thus, the acid-chloride solution that would normally have developed inside a

crevice was replenished with more neutral bulk fluid. Furthermore, because the bulk fluid was aerated, a differential aeration cell did not form. Thus, external flow aided in preventing crevice corrosion to occur for a crevice with a larger gap to depth ratio.

A rigorous description of mass transport was developed, which is shown in Appendix B. This model accounted for transport via convection, diffusion, electromigration, and convection diffusion potential electromigration. Convection diffusion potential is a small contribution to the electrical field formed when diffusion and convection induce slight charge separation. This electrical field drives a secondary current density which adds to the primary current density. Unlike the 1-D model used in Chapter 4, this model does not assume that anode-cathode couplings are established. Rather, a complex electrode coupling algorithm was developed which, based upon the net potential difference between electrodes, calculated the current density flowing between them. The net potential difference is the uncoupled electrode potential (i.e. the potential calculated via the Butler Volmer equation and mixed potential theory) less the ohmic potential drop required for current transfer between the electrodes. The electrode coupling algorithm is applied for each possible intercoupling.

This two-dimensional flow influenced crevice corrosion model is the first of its kind. While flow influenced crevice corrosion has been studied experimentally, it has not been modelled previously. The electrochemical model used in the flow influenced crevice corrosion model makes this code applicable to both crevice corrosion initiation and propagation.

7.3 Overall Conclusions

The objective of this research was to improve upon previous crevice corrosion models by using more sophisticated mass transport models and algorithms. In this work, these objectives have been met. A mass transport model has been developed which accurately accounts for charge density effects while ensuring computational efficiency. Furthermore, in the finite volume integration of the mass transport equation, a method has been developed that utilizes local physics to more accurately estimate the strength of interactions between neighbour nodes. This has resulted in a mass transport model that can more accurately predict mass transport in electrochemical systems.

When applying this improved mass transport model to crevice corrosion, improvements in the accuracy of the model compared to past models against experimental data were apparent. An additional improvement to the crevice corrosion initiation model came from the incorporation of Pitzer's equations to calculate non-ideal solution effects due to short and long range coulombic interactions between charged species. Figures shown in Chapter 4 demonstrated that the pH predictions of this model were markedly closer to independent experimental data than previously developed crevice corrosion models. Results from the model were used to calculate solution properties that are too small to measure, such as charge density in solution. It was shown that there is a distinct relationship between charge density and diffusion potential electromigration. Furthermore, charge density profiles were analyzed to give insight on the relative influence of diffusion potential electromigration and primary electromigration. It was found that the influence of diffusion potential electromigration relative to primary electromigration increases as the crevice gap increases. Finally, the flexibility of the

model was showcased by predicting the pH profile during the crevice corrosion incubation period for five different alloys. Using these simulation results, the five alloys (four stainless steels and Grade-2 titanium) were ranked for their crevice corrosion resistance in the expected order.

The same mass transport model was then incorporated into a flow influenced CO₂ corrosion model augmented with a FeCO₃ film growth model. Again, the model performed very well, matching independent experimental transient i_{corr} profiles in a fully developed turbulent pipe flow.

Finally, the mass transport model was applied to the two-dimensional simulation of crevice corrosion under the influence of a turbulent flow field. While the original form of the electromigration-diffusion equation was retained, a convection term was also added to the mass transport equation. A computational fluid dynamics solver was implemented to calculate the flow field inside and around a microscopic crevice. It was found that as the crevice gap to depth ratio increased, the influence of the turbulent flow field changed. For a very small crevice gap, the effect of turbulent flow was to increase the cathodic limiting current, thereby exacerbating the crevice corrosion problem by allowing for a greater rate of anodic dissolution inside the crevice. However, for a large crevice gap, the flow significantly penetrated into the crevice causing a washout of the crevice solution. Thus, the acid chloride solution that would normally develop in a flow-restricted crevice was not allowed to form and the presence of flow was beneficial. Details of the 2-D mass transport equation are shown in Appendix B.

Chapter 8. Recommendations

Using this work as a starting point, there are several directions that I recommend should be followed in future studies:

1. The flow influenced crevice corrosion model could be easily adapted for the prediction of mesa corrosion, and I strongly recommend this for a future study. Adaptation of the model would require a scale-up of the computational grid to model the entire pipe cross-section and the implementation of a turbulence model.
2. Pitzer's Equations were used in the simulation of the crevice corrosion initiation of stainless steel. Although this approach was justified by agreement with independently obtained experimental data, the utility of the model would be increased with more parameters for Pitzer's Equations. Thus, an experimental study to determine parameters for Pitzer's Equations specific to the stainless steel crevice solution at a variety of conditions would complement this work.
3. The carbon dioxide corrosion model is written for a fully developed, steady flow regime. The application of this model could be extended to flow in more complex geometry. This would make the model suitable for the numerical modelling of a variety of industrially relevant problems. The starting point for the development of this model could be the CFD model developed for flow influenced crevice corrosion.

4. The crevice corrosion initiation model could be extended to calculate transition of the crevice from a passive to active state. Currently, the model uses critical pH values to determine the incubation period of a particular metal crevice in an electrolyte solution. However, with knowledge of the complete kinetic corrosion diagram of a metal, the point at which the cathodic line intersected the nose of the anodic line could be determined, and thus, passive-active transition could be modelled (see Figure 4.1 for illustration of the crevice corrosion kinetic corrosion diagram).

Appendix A. Sensitivity of Predicted Activity Coefficients on Parameters for Pitzer's Equations

Reference:

A very similar version of this appendix appears in the following publication:
 K.L. Heppner, R.W. Evitts, and J. Postlethwaite (2005) Effect of Ionic Interactions on the Initiation of Crevice Corrosion in Passive Metals. *Journal of the Electrochemical Society* **152**. pp. B89-B98. © The Electrochemical Society, Inc. 2005.

A.1 Pitzer's Equations

The equations of the activity coefficient of cations, anions, and neutral species are:

$$\begin{aligned} \ln(\gamma_M) = & z_M^2 F^\gamma + \sum_a m_a (2B_{Ma} + ZC_{Ma}) \\ & + \sum_c m_c (2\Omega_{Mc} + \sum_a m_a \psi_{Mca}) + \sum_a \sum_{a'} m_a m_{a'} \psi_{Maa'} \\ & + z_M \sum_c \sum_a m_c m_a C_{ca} + 2 \sum_n m_n \lambda_{nM} + \dots \end{aligned} \quad (\text{A.1a})$$

$$\begin{aligned} \ln(\gamma_X) = & z_X^2 F^\gamma + \sum_c m_c (2B_{cX} + ZC_{cX}) + \sum_a m_a (2\Omega_{Xa} + \sum_c m_c \psi_{cXa}) \\ & + \sum_c \sum_{c'} m_c m_{c'} \psi_{Xcc'} + |z_X| \sum_c \sum_a m_c m_a C_{ca} + 2 \sum_n m_n \lambda_{nX} + \dots \end{aligned} \quad (\text{A.1b})$$

$$\ln(\gamma_N) = 2 \left(\sum_c m_c \lambda_{Nc} + \sum_a m_a \lambda_{Na} + \sum_n m_n \lambda_{Nn} \right) + \dots \quad (\text{A.2})$$

where:

$$F^\gamma = f^\gamma(I) + \sum_c \sum_a m_c m_a B'_{ca} + \sum_c \sum_{c'} m_c m_{c'} \Omega'_{cc'} + \sum_a \sum_{a'} m_a m_{a'} \Omega'_{aa'} \quad (\text{A.3})$$

$$B_{ij} = \beta_{ij}^{(0)} + \beta_{ij}^{(1)} g(\alpha\sqrt{I}) \quad (\text{A.4})$$

$$B'_{ij} = \beta_{ij}^{(1)} \frac{g'(\alpha\sqrt{I})}{I} \quad (\text{A.5})$$

$$C_{ij} = \frac{C_{ij}^\phi}{2\sqrt{|z_i z_j|}} \quad (\text{A.6})$$

$$\Omega_{ij} = \theta_{ij} + {}^E \theta_{ij}(I) \quad (\text{A.7})$$

$$\Omega'_{ij} = {}^E \theta'_{ij}(I) \quad (\text{A.8})$$

The sensitivity of the activity coefficient on the value of each of the six fundamental parameters $\beta_{ij}^{(0)}$, $\beta_{ij}^{(1)}$, C_{ij}^ϕ , θ_{ij} , λ_{ij} , and ψ_{ijk} will now be determined.

A.2 Parameter Sensitivity Analysis

1. Determine the variation of the activity coefficient with coefficients appearing directly in the equations: B , C , Ω , ψ , λ , and F^γ

B :

$$\frac{\partial \ln \gamma_M}{\partial B_{Ma}} = 2m_a \quad (\text{A.9})$$

C :

$$\frac{\partial \ln \gamma_M}{\partial C_{Ma}} = Zm_a + z_M m_M m_a \quad (\text{A.10})$$

$$\frac{\partial \ln \gamma_M}{\partial C_{ca}} = z_M m_c m_a; (c \neq M) \quad (\text{A.11})$$

Ω :

$$\frac{\partial \ln \gamma_M}{\partial \Omega_{Mc}} = 2m_c \quad (\text{A.12})$$

ψ :

$$\frac{\partial \ln \gamma_M}{\partial \psi_{Mca}} = m_c m_a \quad (\text{A.13})$$

$$\frac{\partial \ln \gamma_M}{\partial \psi_{Maa'}} = m_a m_{a'}; (a \neq a') \quad (\text{A.14})$$

λ :

$$\frac{\partial \ln \gamma_M}{\partial \lambda_{nM}} = 2m_n \quad (\text{A.15})$$

F^γ :

$$\frac{\partial \ln \gamma_M}{\partial F^\lambda} = z_M^2 \quad (\text{A.16})$$

2. *Coefficients B , C , and Ω are functions of base parameters. Transform derivative expressions to functions of base parameters using the chain rule.*

$\beta^{(0)}$ and $\beta^{(1)}$:

$$\frac{\partial \ln \gamma_M}{\partial \beta_{Ma}^{(0)}} = \frac{\partial \ln \gamma_M}{\partial B_{Ma}} \frac{\partial B_{Ma}}{\partial \beta_{Ma}^{(0)}} + \frac{\partial \ln \gamma_M}{\partial B'_{Ma}} \frac{\partial B'_{Ma}}{\partial \beta_{Ma}^{(0)}} \quad (\text{A.17})$$

$$\frac{\partial \ln \gamma_M}{\partial \beta_{Ma}^{(1)}} = \frac{\partial \ln \gamma_M}{\partial B_{Ma}} \frac{\partial B_{Ma}}{\partial \beta_{Ma}^{(1)}} + \frac{\partial \ln \gamma_M}{\partial B'_{Ma}} \frac{\partial B'_{Ma}}{\partial \beta_{Ma}^{(1)}} \quad (\text{A.18})$$

However, F^γ is a function of B'_{Ma} . Therefore, (A.17) and (A.18) become:

$$\frac{\partial \ln \gamma_M}{\partial \beta_{Ma}^{(0)}} = \frac{\partial \ln \gamma_M}{\partial B_{Ma}} \frac{\partial B_{Ma}}{\partial \beta_{Ma}^{(0)}} + \frac{\partial \ln \gamma_M}{\partial F^\gamma} \frac{\partial F^\gamma}{\partial B'_{Ma}} \frac{\partial B'_{Ma}}{\partial \beta_{Ma}^{(0)}} \quad (\text{A.19})$$

$$\frac{\partial \ln \gamma_M}{\partial \beta_{Ma}^{(1)}} = \frac{\partial \ln \gamma_M}{\partial B_{Ma}} \frac{\partial B_{Ma}}{\partial \beta_{Ma}^{(1)}} + \frac{\partial \ln \gamma_M}{\partial F^\gamma} \frac{\partial F^\gamma}{\partial B'_{Ma}} \frac{\partial B'_{Ma}}{\partial \beta_{Ma}^{(1)}} \quad (\text{A.20})$$

Substitution of equations (A.9) and (A.16) into both gives:

$$\frac{\partial \ln \gamma_M}{\partial \beta_{Ma}^{(0)}} = 2m_a \frac{\partial B_{Ma}}{\partial \beta_{Ma}^{(0)}} + z_M^2 \frac{\partial F^\gamma}{\partial B_{Ma}'} \frac{\partial B_{Ma}'}{\partial \beta_{Ma}^{(0)}} \quad (\text{A.21})$$

$$\frac{\partial \ln \gamma_M}{\partial \beta_{Ma}^{(1)}} = 2m_a \frac{\partial B_{Ma}}{\partial \beta_{Ma}^{(1)}} + z_M^2 \frac{\partial F^\gamma}{\partial B_{Ma}'} \frac{\partial B_{Ma}'}{\partial \beta_{Ma}^{(1)}} \quad (\text{A.22})$$

Now determine derivatives which appear in equations A.21 and A.22 from expressions

for B , B' , and F^γ (equations A.3 – A.5):

$$\frac{\partial B_{Ma}}{\partial \beta_{Ma}^{(0)}} = 1 \quad (\text{A.23})$$

$$\frac{\partial B_{Ma}}{\partial \beta_{Ma}^{(1)}} = g(\alpha\sqrt{I}) \quad (\text{A.24})$$

$$\frac{\partial F^\gamma}{\partial B_{Ma}'} = m_M m_a \quad (\text{A.25})$$

$$\frac{\partial B_{Ma}'}{\partial \beta_{Ma}^{(0)}} = 0 \quad (\text{A.26})$$

$$\frac{\partial B_{Ma}'}{\partial \beta_{Ma}^{(1)}} = \frac{g'(\alpha\sqrt{I})}{I} \quad (\text{A.27})$$

Substitute expressions (A.23) – (A.27) into expressions (A.21) and (A.22) to obtain final

result:

$$\frac{\partial \ln \gamma_M}{\partial \beta_{Ma}^{(0)}} = 2m_a \quad (\text{A.28})$$

$$\frac{\partial \ln \gamma_M}{\partial \beta_{Ma}^{(1)}} = 2m_a g(\alpha\sqrt{I}) + z_M^2 m_M m_a \frac{g'(\alpha\sqrt{I})}{I} \quad (\text{A.29})$$

C_{ij}^ϕ :

For M-a:

$$\frac{\partial \ln \gamma_M}{\partial C_{Ma}^\phi} = \frac{\partial \ln \gamma_M}{\partial C_{Ma}} \frac{\partial C_{Ma}}{\partial C_{Ma}^\phi} \quad (\text{A.30})$$

Substitution of equation (A.10) yields:

$$\frac{\partial \ln \gamma_M}{\partial C_{Ma}^\phi} = \frac{Zm_a + z_M m_M m_a}{2\sqrt{|z_M z_a|}} \quad (\text{A.31})$$

For c-a where c is not equal to M substitute equation (A.11) into (A.30) to obtain:

$$\frac{\partial \ln \gamma_M}{\partial C_{ca}^\phi} = \frac{z_M m_c m_a}{2\sqrt{|z_c z_a|}} \quad (\text{A.32})$$

θ_{Mc} :

$$\frac{\partial \ln \gamma_M}{\partial \theta_{Mc}} = \frac{\partial \ln \gamma_M}{\partial \Omega_{Mc}} = 2m_c \text{ because } \frac{\partial \Omega_{Mc}}{\partial \theta_{Mc}} = 1 \quad (\text{A.33})$$

λ_{Nj} :

$$\frac{\partial \ln \gamma_N}{\partial \lambda_{Nj}} = 2m_j \quad (\text{A.34})$$

A.3 Summary

For the cationic activity coefficient, the sensitivities are summarized in Table A.1:

Parameter	Sensitivity of $\ln \gamma_M$ to Parameter
$\beta_{Ma}^{(0)}$	$2m_a$
$\beta_{Ma}^{(1)}$	$2m_a g(\alpha\sqrt{I}) + z_M^2 m_M m_a \frac{g'(\alpha\sqrt{I})}{I}$
C_{Ma}^ϕ	$\frac{Zm_a + z_M m_M m_a}{2\sqrt{ z_M z_a }}$
$C_{ca}^\phi (c \neq M)$	$\frac{z_M m_c m_a}{2\sqrt{ z_c z_a }}$
θ_{Mc}	$2m_c$
Ψ_{Mij}	$m_i m_j$

Table A.1. Sensitivity of the cationic activity coefficient to the fundamental parameters of Pitzer's equations.

Similarly, for the anionic activity coefficient see Table A.2:

Parameter	Sensitivity of $\ln \gamma_X$ to Parameter
$\beta_{Xc}^{(0)}$	$2m_c$
$\beta_{Xc}^{(1)}$	$2m_c g(\alpha\sqrt{I}) + z_X^2 m_X m_c \frac{g'(\alpha\sqrt{I})}{I}$
C_{Xc}^ϕ	$\frac{Zm_c + z_X m_X m_c}{2\sqrt{ z_X z_c }}$
$C_{ca}^\phi (a \neq X)$	$\frac{ z_X m_c m_a}{2\sqrt{ z_c z_a }}$
θ_{Xa}	$2m_a$
Ψ_{Xij}	$m_i m_j$

Table A.2. Sensitivity of the anionic activity coefficient to the fundamental parameters of Pitzer's equations.

The sensitivity of the neutral species coefficient, $\ln \gamma_N$, upon λ_{Nj} is $2m_j$, where the j^{th} species is either anionic or cationic.

The functions, $g(x)$ and $g'(x)$, are bounded between 0 and 1 and are plotted in the Figure A.1.

From the results of this sensitivity study, the predicted anionic and cationic activity coefficients are weakly dependent upon the accuracy of ionic interaction parameters for interactions with ions of low molality. The sensitivity increases as the molality of the interacting ion increases. Because most interaction parameters fall within a typically small range, the error associated with assuming parameter values which fall within the typical range for that parameter type is small.

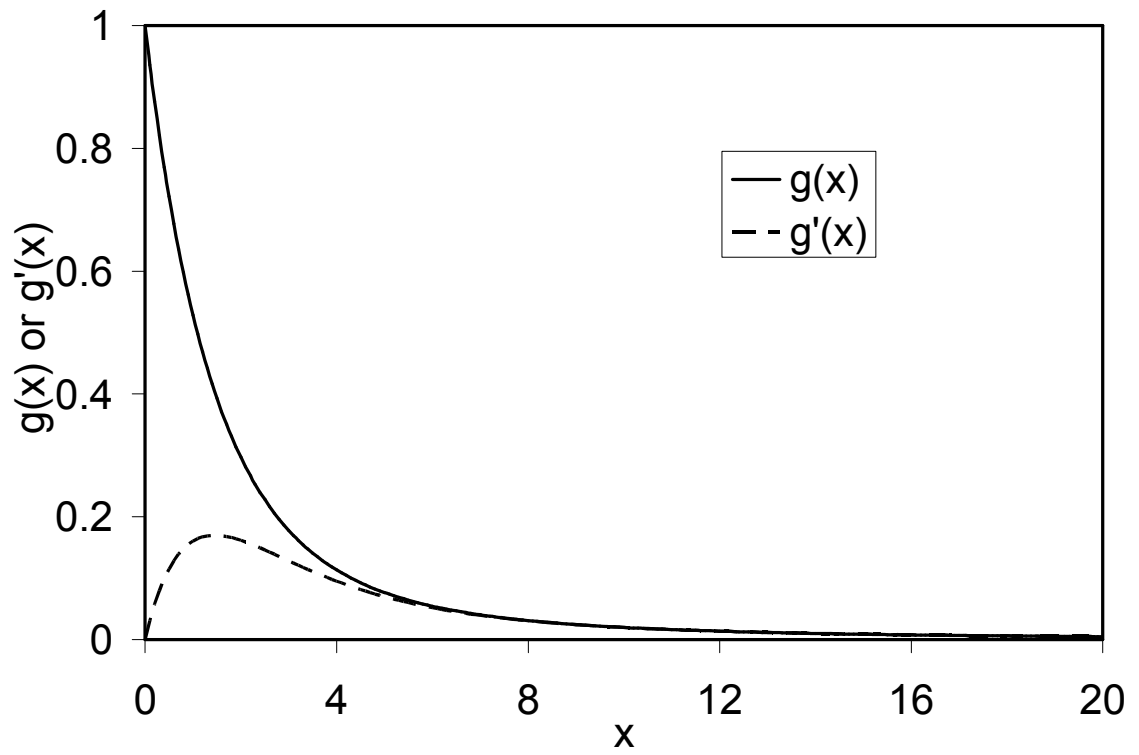


Figure A.1. Plot of $g(x)$ and $g'(x)$, functions utilized in Pitzer's equations.

Appendix B. Electrochemical Mass Transport Model in a Two-Dimensional Crevice

B.1 Mass Transport

In an electrolyte solution, chemical species transport is driven by both electrochemical potential differences and overall fluid momentum. Transport due to fluid momentum is due to a mechanical pressure difference. Thus, fluid travels towards regions of lower pressure and, in so doing, drags chemical species along with it. Similarly, chemical species are transported to regions of lower electrochemical potential. In both cases, transport occurs to bring the fluid to a lower energy state. The flux of a chemical species due to convection, electromigration, and diffusion in an infinitely dilute solution is [1]:

$$\mathbf{N}_i = -D_i \nabla C_i - z_i u_i C_i F \nabla \Phi + C_i \mathbf{v} \quad (\text{B.1})$$

In a moderately dilute solution, the mass flux is [1]:

$$\mathbf{N}_i = -z_i u_i F C_i \nabla \Phi - D_i (\nabla C_i + C_i \nabla \ln \gamma_i) + C_i \mathbf{v} \quad (\text{B.2})$$

The fundamental mass balance equation is:

$$\frac{\partial C_i}{\partial t} = -\nabla \cdot \mathbf{N}_i + R_i \quad (\text{B.3})$$

where R_i is a chemical reaction source term. Substitution of (B.1) into (B.3) gives the mass transport equation applicable for infinitely dilute solutions:

$$\frac{\partial C_i}{\partial t} = D_i \nabla^2 C_i + (z_i u_i F \nabla \Phi - \mathbf{v}) \nabla C_i + z_i u_i F \nabla^2 \Phi C_i + R_i \quad (\text{B.4})$$

Similarly, by substituting (B.2) into (B.3), the mass transport equation applicable to moderately dilute solutions is obtained:

$$\begin{aligned} \frac{\partial C_i}{\partial t} = & D_i \nabla^2 C_i + (z_i u_i F \nabla \Phi + D_i \nabla \ln \gamma_i - \mathbf{v}) \nabla C_i \\ & + (z_i u_i F \nabla^2 \Phi + D_i \nabla^2 \ln \gamma_i) C_i + R_i \end{aligned} \quad (\text{B.5})$$

In the development of equations (B.4) and (B.5), it was assumed that the fluid was incompressible, and thus, mass continuity demands that $\nabla \cdot \mathbf{v} = 0$.

Poisson's equation for charge density relates the second order gradient of the potential field to the charge density in solution. It describes how, when a charge density exists in solution, it is quickly eradicated through a parabolic contortion of the electrical field [2]. Mathematically, it is written as:

$$\nabla^2 \Phi = -\frac{\delta}{\varepsilon} \quad (\text{B.6})$$

where the charge density, δ , is:

$$\delta = F \sum_j z_j C_j \quad (\text{B.7})$$

and ε is the dielectric constant. Substitution of (B.6) into (B.4) and (B.5) yields:

Infinitely dilute solution:

$$\frac{\partial C_i}{\partial t} = D_i \nabla^2 C_i + (z_i u_i F \nabla \Phi - \mathbf{v}) \nabla C_i - z_i u_i F \frac{\delta}{\varepsilon} C_i + R_i \quad (\text{B.8})$$

Moderately dilute solution:

$$\begin{aligned} \frac{\partial C_i}{\partial t} = & D_i \nabla^2 C_i + (z_i u_i F \nabla \Phi + D_i \nabla \ln \gamma_i - \mathbf{v}) \nabla C_i \\ & + D_i C_i \nabla^2 \ln \gamma_i - z_i u_i F \frac{\delta}{\varepsilon} C_i + R_i \end{aligned} \quad (\text{B.9})$$

Equations (B.8) and (B.9) may be expressed in terms of potential or current density. In this work, the mass transport equations were usually solved in terms of current density rather than potential. Shrier [3] gives a method for calculating current density boundary conditions in a crevice during its incubation period. To determine the relationship between current density and potential, consider the definition of current density:

$$\mathbf{i} = F \sum_j z_j \mathbf{N}_j \quad (\text{B.10})$$

For a moderately dilute solution, this becomes:

$$\mathbf{i} = F \sum_j \left(-z_j^2 u_j F C_j \nabla \Phi - z_j D_j (\nabla C_j + C_j \nabla \ln \gamma_j) + z_j C_j \mathbf{v} \right) \quad (\text{B.11})$$

After some algebraic manipulation to isolate the potential gradient, the following equation is obtained:

$$\nabla \Phi = - \frac{\mathbf{i} + \mathbf{i}_{\text{cdp}}}{\kappa} \quad (\text{B.12})$$

Equation (B.12) is an expression of Ohm's Law for a solution with non-uniform concentration and a velocity field. Here, the conductivity is:

$$\kappa = F^2 \sum_j z_j^2 u_j C_j \quad (\text{B.13})$$

and the convection diffusion potential current is:

$$\mathbf{i}_{\text{cdp}} = F \sum_j z_j D_j (\nabla C_j + C_j \nabla \ln \gamma_j) - \mathbf{v} \delta \quad (\text{B.14})$$

Note that the convection diffusion potential for an infinitely dilute solution is obtained when $\nabla \ln \gamma_j = 0$, i.e.:

$$\mathbf{i}_{\text{cdp}} = F \sum_j z_j D_j \nabla C_j - \mathbf{v} \delta \quad (\text{B.15})$$

Unlike the previous convection-free models, here a current density forms to oppose the current produced by transporting a net charge via convection. The final form of the mass transport equations are:

Infinitely dilute solution:

$$\frac{\partial C_i}{\partial t} = D_i \nabla^2 C_i - \left(z_i u_i F \frac{\mathbf{i} + \mathbf{i}_{\text{cdp}}}{\kappa} + \mathbf{v} \right) \cdot \nabla C_i - z_i u_i F \frac{\delta}{\varepsilon} C_i + R_i \quad (\text{B.16})$$

Moderately dilute solution:

$$\begin{aligned} \frac{\partial C_i}{\partial t} = & D_i \nabla^2 C_i - \left(z_i u_i F \frac{\mathbf{i} + \mathbf{i}_{\text{cdp}}}{\kappa} + \mathbf{v} \right) \cdot \nabla C_i + D_i \nabla \ln \gamma_i \cdot \nabla C_i \\ & + D_i C_i \nabla^2 \ln \gamma_i - z_i u_i F \frac{\delta}{\varepsilon} C_i + R_i \end{aligned} \quad (\text{B.17})$$

Again, note that the infinitely dilute solution model is obtained from the moderately dilute solution model when $\nabla \ln \gamma_i = 0$. This implies that the infinitely dilute mass transport model may be applicable to moderately dilute solutions, providing that the spatial profile of the activity coefficient in solution is nearly uniform.

Activity coefficients required to solve equation (B.17) may be calculated using Pitzer's Equations (see equations 3.1.3 – 3.1.5) [4, 5].

The boundary condition for calculation of species concentration, equations (2.1.4) and (2.1.5), is based upon Faraday's Law and is:

$$-D \frac{\partial C_j}{\partial x} = \frac{1}{F} \sum_k \frac{i_k \nu_{jk}}{n_k} \quad (\text{B.18})$$

Here, i_k is the current density generated or consumed by the k^{th} electrode reaction, ν_{jk} is the stoichiometric coefficient of the j^{th} species in the k^{th} electrode reaction, and n_k is the charge transfer number of the k^{th} electrode reaction. The summation is taken over all

electrode reactions occurring in the system. Equation (B.18) is a pseudo steady state mass balance taken at the metal-solution interface and it balances the rate of corrosion to the rate to diffusion.

Applying a finite volume discretization technique to equation (B.17) results in the following set of equations (in two dimensions):

$$a_p C_{iP} = a_E C_{iE} + a_W C_{iW} + a_N C_{iN} + a_S C_{iS} + a_p^0 C_{iP}^0 + G_i \Delta x \Delta y \quad (\text{B.19})$$

Using the previously discussed hybrid differencing scheme (section 3.3) to express the interfacial concentrations, C_{ie} and C_{iw} , as nodal values, the discrete transport coefficients are:

$$a_E = \frac{D_i \Delta y}{\Delta x} \left[1 + \frac{P'_{xP}}{2} + \left| \frac{P'_{xP} \alpha_x}{2} \right| \right] + \left(\frac{v_x}{2} + \left| \frac{v_x \beta_x}{2} \right| \right) \Delta y \quad (\text{B.20})$$

$$a_W = \frac{D_i \Delta y}{\Delta x} \left[1 - \frac{P'_{xP}}{2} + \left| \frac{P'_{xP} \alpha_x}{2} \right| \right] - \left(\frac{v_x}{2} - \left| \frac{v_x \beta_x}{2} \right| \right) \Delta y \quad (\text{B.21})$$

$$a_N = \frac{D_i \Delta x}{\Delta y} \left[1 + \frac{P'_{yP}}{2} + \left| \frac{P'_{yP} \alpha_y}{2} \right| \right] + \left(\frac{v_y}{2} + \left| \frac{v_y \beta_y}{2} \right| \right) \Delta x \quad (\text{B.22})$$

$$a_S = \frac{D_i \Delta x}{\Delta y} \left[1 + \frac{P'_{yP}}{2} + \left| \frac{P'_{yP} \alpha_y}{2} \right| \right] - \left(\frac{v_y}{2} - \left| \frac{v_y \beta_y}{2} \right| \right) \Delta x \quad (\text{B.23})$$

$$a_p^0 = \frac{\Delta x \Delta y}{\Delta t} \quad (\text{B.24})$$

$$a_p = a_E + a_W + a_p^0 + z_i u_i F \frac{\delta_p}{\varepsilon} \Delta x \Delta y - D_i \left(\frac{\ln \gamma_{iE} + \ln \gamma_{iW} - 2 \ln \gamma_{iP}}{\Delta x} \Delta y + \frac{\ln \gamma_{iN} + \ln \gamma_{iS} - 2 \ln \gamma_{iP}}{\Delta y} \Delta x \right) \quad (\text{B.25})$$

Here, the stencil used to discretize the mass transport equation is illustrated in Figure B.1. In equations (B.20) – (B.23), the convective upwind parameter, β , is calculated based upon the local Reynolds number. The electromigration upwind parameter, α , is a function of the modified electromigration Peclet number, P' , and the calculation of both of these parameters were discussed in section 3.3.

B.2 Calculation of the Potential Field in Solution

In this two-dimensional model, the use of potential rather than current density in solution is more convenient. This is because current density is now a vector quantity while potential is a scalar, the gradient of which is proportional to the current density. The potential in solution is correctly described by Poisson's equation for charge density, equation (B.6). However, this equation is incredibly stiff. On the right hand side of this equation, the charge density is divided by the dielectric constant, ε , the value of which is of order of magnitude of 10^{-11} Farad / m. Thus, any variation in the charge density field causes high variability in the potential field. From the potential field, the current density field is calculated via Ohm's Law:

$$\mathbf{i} = -\kappa \nabla \Phi \tag{B.26}$$

Thus, charge density in solution will cause massive overcompensation of the current density field to eradicate the charge. Although in nature, this phenomenon would work to ensure that charge does not accumulate in solution, in a numerical algorithm, this causes numerical instability. This instability could only be avoided if extremely small time steps were used in the solution of the mass transport equation coupled with the Poisson equation solver. Such small time steps would allow for only short simulation times, as the computational efficiency would be extremely low.

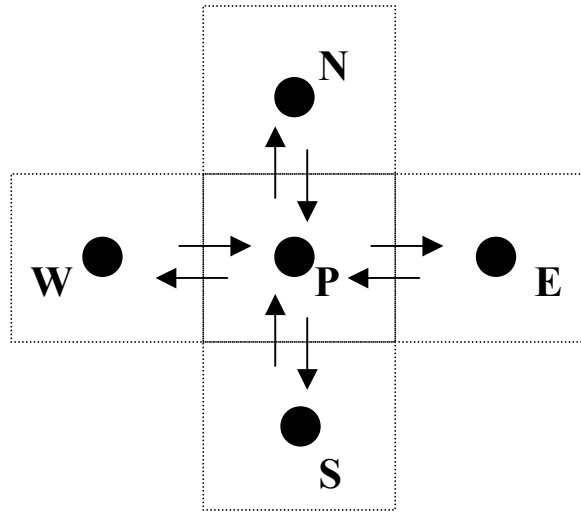


Figure B.1. Control volume stencil used in 2-D discretization. Dotted lines represent the control volume interfaces. Large black dots represent nodes where property values are calculated. Arrows represent flux through the control volume interface.

An alternate method has been derived to incorporate the effect of charge density upon the potential field in solution. This method is based upon the charge conservation equation and its derivation follows.

A statement of mass conservation yields the following expression:

$$\frac{\partial \delta}{\partial t} = -F \sum_j z_j \nabla \cdot \mathbf{N}_j \quad (\text{B.27})$$

Using the moderately dilute mass flux, equation (B.2), equation (B.27) becomes:

$$\begin{aligned} \frac{\partial \delta}{\partial t} &= \nabla \Phi F^2 \sum_j z_j^2 u_j \nabla C_j \\ &+ \nabla^2 \Phi F^2 \sum_j z_j^2 u_j C_j \\ &+ F \sum_j z_j D_j (\nabla^2 C_j + \nabla C_j \nabla \ln \gamma_j + C_j \nabla^2 \ln \gamma_j) \\ &- F \mathbf{v} \cdot \sum_j z_j \nabla C_j \end{aligned} \quad (\text{B.28})$$

This can be reduced to the following:

$$\frac{\partial \delta}{\partial t} = \nabla \kappa \cdot \nabla \Phi + \kappa \nabla^2 \Phi + \nabla \cdot \mathbf{i}_{\text{cdp}} - \mathbf{v} \cdot \nabla \delta \quad (\text{B.29})$$

This was obtained through the substitution of equations (B.13) and (B.14), the definition of conductivity and convection diffusion potential current density, respectively. It is desired to use equation (B.29) to determine the potential field. Thus, the conductivity, convection diffusion potential current density, and charge density fields must be known. The conductivity and convection diffusion current density field may be readily calculated from equations (B.13) and (B.14) with the known concentration and activity coefficient field. However, the charge density field should be prescribed. It is desired to obtain a potential field that will eradicate the charge density. To find this field, substitute the desired values for the rate of change and gradient of the charge density:

$$\frac{\partial \delta}{\partial t} = -\frac{\delta^0}{\Delta t} \quad (\text{B.30})$$

$$\nabla \delta = 0 \quad (\text{B.31})$$

Equation (B.31) sets the rate of change of the charge density such that δ^0 , the charge density accumulated over the previous time step, is eradicated, i.e.:

$$\delta = \delta^0 + \frac{\partial \delta}{\partial t} \Delta t = \delta^0 - \frac{\delta^0}{\Delta t} \Delta t = 0 \quad (\text{B.32})$$

A zero gradient of charge density will result from uniformly applying this equation throughout the solution domain, and hence, the gradient is set to zero (equation (B.31)).

Substitution of equations (B.30) and (B.31) into (B.29) yields the following:

$$\nabla \kappa \cdot \nabla \Phi + \kappa \nabla^2 \Phi = -\frac{\delta^0}{\Delta t} - \nabla \cdot \mathbf{i}_{\text{cdp}} \quad (\text{B.33})$$

Note that for a uniform concentration field, equation (B.33) becomes a Poisson equation:

$$\nabla^2 \Phi = -\frac{\delta^0}{\kappa \Delta t} \quad (\text{B.34})$$

This formulation is advantageous because the response of the potential field to charge density is averaged over an entire time step. This removes the stiffness that was inherent to equation (B.6). It is interesting to compare the right hand side of equations (B.6) and (B.34):

$$-\frac{\delta^0}{\kappa \Delta t} = -\frac{\delta^0}{\varepsilon} \quad (\text{B.35})$$

This gives insight into the time step required to use Poisson's equation for charge density.

Rearrangement of (B.35) yields:

$$\Delta t = \frac{\varepsilon}{\kappa} \approx 10^{-8} \text{ sec (in seawater)} \quad (\text{B.36})$$

Equation (B.36) shows that the time step required to solve the mass transport equation such that it is operating at the same time scale as Poisson's equation for charge density is extremely small. Use of the modified potential field calculation scheme therefore dramatically improves computational efficiency while still incorporating the effects of charge density in solution on the potential field.

The boundary condition for the potential field equation comes from conditions at the electrode. There are two types of boundary conditions that the electrode site may supply – a Neumann type boundary condition that is based upon Ohm's Law, and a Dirichlet type boundary condition that simply sets the solution potential to the metal potential, i.e.:

$$-\kappa \frac{\partial \Phi}{\partial x} = i \quad (\text{B.37})$$

$$\Phi = E \quad (\text{B.38})$$

Here, E is the potential of the metal at the metal-solution interface. Typically, equation (B.37) is applied to all but one electrode site to guarantee that current leaving the metal enters the solution. Equation (B.38) is then applied to one site to tether the potential field in solution to the corrosion potential. One Dirichlet condition is necessary because both the equation describing the potential field, equation (B.33), and the Neumann type boundary condition, equation (B.37), are only dependent upon the gradient of the potential. Hence, the potential must be specified at one point to avoid singularity of the potential field solution.

B.3 Electrode Reactions

Knowledge of the potential and current density emanating from the metal surface gives valuable boundary conditions for the calculation of mass transport, as seen in the

previous section. Thus, electrode processes are closely inter-coupled with mass transport. Because of this, accurately calculating conditions at the electrode is of primary importance.

The rate of an electrode reaction is predicted by the Butler Volmer equation modified for mass transfer limitation [6]:

$$i = \frac{\exp\left[\frac{E - E_{rev}}{b_a}\right] - \exp\left[-\frac{E - E_{rev}}{b_c}\right]}{\frac{1}{i_o} + \frac{1}{i_{a,lim}} \exp\left[\frac{E - E_{rev}}{b_a}\right] - \frac{1}{i_{c,lim}} \exp\left[-\frac{E - E_{rev}}{b_c}\right]} \quad (\text{B.39})$$

Equation (B.39) predicts the current density to be bounded between the anodic and cathodic limiting currents, $i_{a,lim}$ and $i_{c,lim}$, respectively. Equation (B.39) can be written for each electrode reaction occurring in the system. At mixed potential, the rate at which each reaction occurs may be determined:

$$\sum_j i_j = 0 \quad (\text{B.40})$$

Equation (B.40) defines mixed potential and is a statement of charge conservation. Substitution of (B.39) into (B.40) yields the equation from which the electrode potential is calculated:

$$\sum_j \left(\frac{\exp\left[\frac{E - E_{rev,j}}{b_{a,j}}\right] - \exp\left[-\frac{E - E_{rev,j}}{b_{c,j}}\right]}{\frac{1}{i_{o,j}} + \frac{1}{i_{a,lim,j}} \exp\left[\frac{E - E_{rev,j}}{b_{a,j}}\right] - \frac{1}{i_{c,lim,j}} \exp\left[-\frac{E - E_{rev,j}}{b_{c,j}}\right]} \right) = 0 \quad (\text{B.41})$$

An incremental search algorithm is applied to determine the electrode potential, E . Once known, the potential is used to calculate the rate of each individual reaction using equation (B.35). Thus, both the potential and current density may be obtained.

B.3.1 Coupling of anode-cathode pairs

If the potential difference between two electrode sites is greater than the iR drop between the two, the two will couple to form a separated anode and cathode. Such is the case when a differential aeration cell forms in a crevice; the crevice interior usually becomes anodic while the metal surface surrounding the crevice (the bold surface), becomes cathodic. This is a phenomenon that can be predicted mathematically. However, it is extremely complex to implement. In this work, a method has been proposed to numerically predict inter-couplings between anodes and cathodes. First, equations are written for each possible inter-coupling:

$$E_k - E_j = \Phi_k - \Phi_j + \frac{i_{ex,jk}}{\bar{\kappa}_{jk}} \Delta x_{jk} \quad (\text{B.42})$$

In equation (B.42), the space-averaged conductivity, $\bar{\kappa}_{jk}$, is determined by line integral averaging over the path between the j^{th} and k^{th} electrode:

$$\bar{\kappa}_{jk} = \frac{1}{\Delta x_{jk}} \int_{x_j}^{x_k} \kappa dS \quad (\text{B.43})$$

Here, S represents the shortest path between the two points. $i_{ex,jk}$ is the current density flowing between the j^{th} and k^{th} electrodes and Δx_{jk} is the distance between the two electrodes (along the path S). Whether a coupling is possible depends upon whether or not the metal potential difference, $E_k - E_j$, is greater than the iR drop, $\Phi_k - \Phi_j$. Equation (B.42), in essence, is an expression of Ohm's Law and calculates the maximum current that could flow between two coupled electrode sites.

Then, an expression is written for the metal potential:

$$E_j = E_j^0 + 2.303 \sum_k \text{if} \left[(E_k < E_j), b_a^{net} i_{ex,jk}, -b_c^{net} i_{ex,jk} \right] \quad (\text{B.44})$$

The “if statement” notation used in equation (B.44) means the following:

$$if[\text{Condition, What to do if condition is true, What to do if condition is false}]$$

Here, the net Tafel slopes, b_a^{net} and b_c^{net} , are calculated from all anodic and cathodic reactions occurring in the system:

$$b_a^{net} = \frac{1}{\ln \sum_j \exp\left(\frac{1}{b_a^j}\right)} \quad (\text{B.45})$$

Here, only the b_a^{net} calculation is shown as the b_c^{net} calculation is analogous. Equation (B.44) adjusts the metal potential for its inter-couplings with other electrode sites assuming Tafel behaviour. In equation (B.40), the old value of the potential, E_j^0 , is calculated using the Butler-Volmer equation modified for mass transfer limitations and mixed potential theory (equation (B.39)). Thus, couplings arise due to differential availability of cathodic reagents as well as concentration overpotential. The electrode potential will drop where mass transfer limits the rate of reaction. An electrode under mass transfer control will couple with another electrode or electrodes (at higher potential) to supply its cathodic charge demand.

Equation (B.42) is written for each $i_{ex,jk}$ while (B.40) is written for each E_j .

Thus, these two equations define a solvable, closed system. Note that equation (B.44) is linearized. Because equation (B.42) is also a linear equation, the complete system of equations is linear and, thus, solvable by a direct method (i.e. Gaussian elimination, LU decomposition, etc.). While a change in potential is proportional to a change in the logarithm of current, according to Tafel behaviour, the logarithms here have been replaced with linear functions. This is appropriate in this case because $i_{ex,jk}$ is very small,

and thus, a Taylor series expansion may be used to linearize it. The linearization technique will be explained in detail shortly. The complete algorithm for determining electrode couplings is:

1. Calculate all electrode potentials in the system using mixed potential theory (equation (B.41)).
2. Apply equations (B.42) and (B.44) to determine couplings between electrodes of differing potential.
3. Use the solution, the \mathbf{E} and \mathbf{i}_{ex} vectors, to update the electrode potential and current density.

This algorithm is applied in synchronization with an electrolyte mass transport solver.

It is noteworthy that, when the potential does not change significantly due to coupling, it can be assumed constant. This is likely the case for most applications, especially when this algorithm is applied successively at each time step. Assuming the potential to be constant decouples equations (B.42) and (B.44), thereby avoiding the solution of a very large set of linear equations. It is therefore advantageous from a computational standpoint to assume that the potential does not change during the coupling process. The derivation of this method follows.

As seen above, the extent of coupling between two electrodes can be modelled using a kinetic corrosion diagram. An excess current will flow between the two electrodes, manifested as transport of cationic species towards the cathode, anionic species towards the anode, and a transfer of electrons through the metal. The definition of ionic current used in this derivation is given as equation (B.10). The excess current that flows between anode and cathode will be proportional to the net driving force, that is, the

electrode potential difference less the solution resistance. In this model, the resistance of the metal is assumed negligible. Figure B.2 shows the coupling model in graphical terms.

A geometric analysis of Figure B.2 (c) may now be performed. The coupling current is that current which makes the difference between the two electrode potentials equal to the iR drop between them, i.e.:

$$E_{corr,1} - E_{corr,2} = \Phi_1 - \Phi_2 \quad (\text{B.46})$$

The coupled potential is related to the uncoupled potential by the net Tafel slope:

$$E_{corr,1} = E_{corr,1}^* - b_c (\ln i_{ex} - \ln i_{ref}) \quad (\text{B.47})$$

$$E_{corr,2} = E_{corr,2}^* + b_a (\ln i_{ex} - \ln i_{ref}) \quad (\text{B.48})$$

Substitution of (B.47) and (B.48) into (B.46) yields:

$$E_{corr,1}^* - b_c (\ln i_{ex} - \ln i_{ref}) - E_{corr,2}^* - b_a (\ln i_{ex} - \ln i_{ref}) = \Phi_1 - \Phi_2 \quad (\text{B.49})$$

Subsequent rearrangement yields the expression for the excess current:

$$\ln i_{ex} - \ln i_{ref} = \frac{E_{corr,1}^* - E_{corr,2}^* - (\Phi_1 - \Phi_2)}{b_a + b_c} \quad (\text{B.50})$$

Now apply a Taylor series expansion to $\ln i$ about the value $i = 1$:

$$\ln i = \ln(1) + (i-1) \left. \frac{d \ln i}{di} \right|_{i=1} + \dots = i-1 \quad (\text{B.51})$$

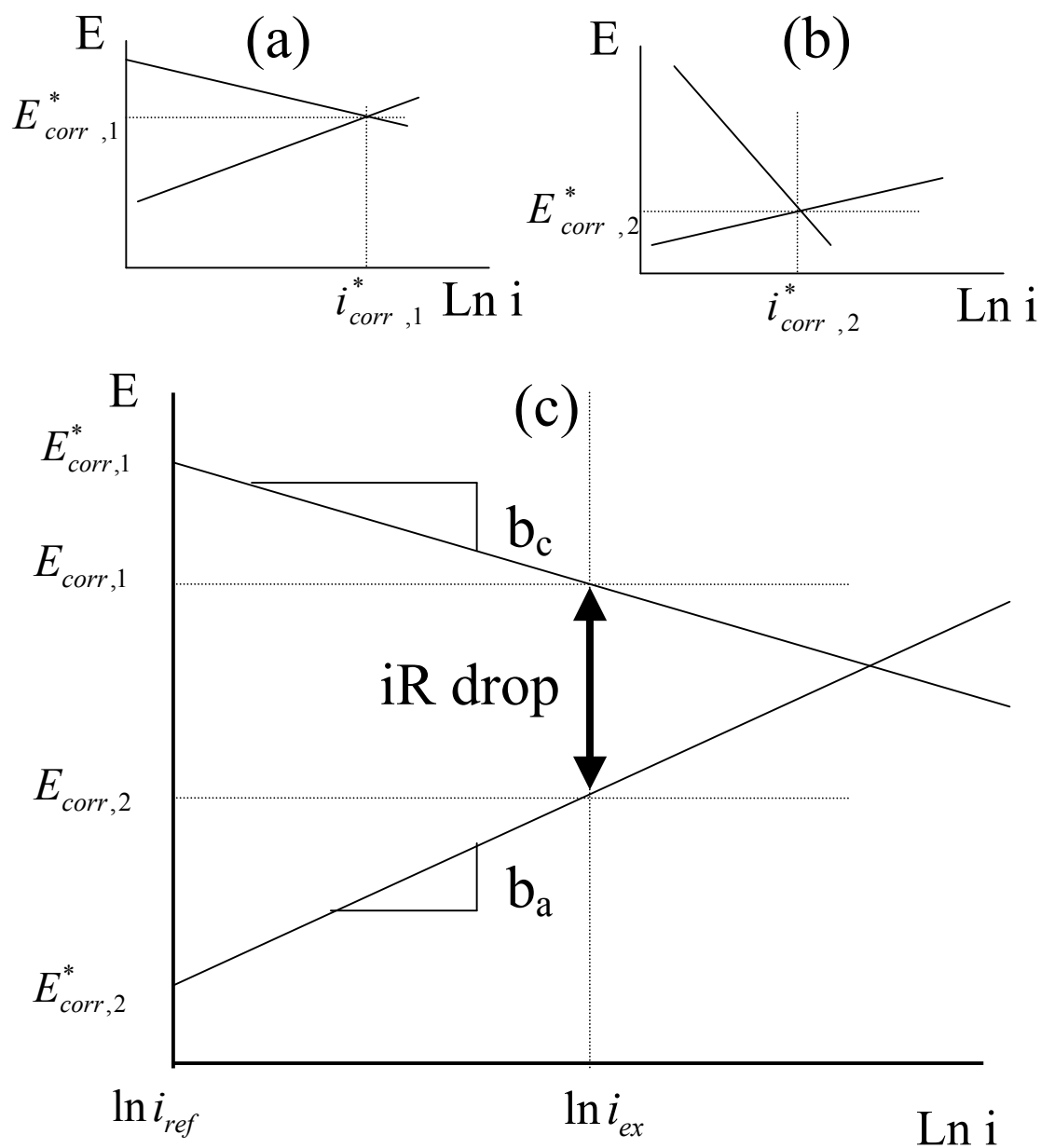


Figure B.2. Graphical representation of the electrode coupling algorithm: (a) Electrode which will become cathodic relative to the other; (b) Electrode which will become anodic relative to the other; (c) Coupling of the two electrodes to determine the excess current flowing between the two.

Substitution of (B.51) into (B.50) yields:

$$i_{ex} - i_{ref} = \frac{E_{corr,1}^* - E_{corr,2}^* - (\Phi_1 - \Phi_2)}{b_a + b_c} \quad (\text{B.52})$$

By definition, the current flowing between the two electrodes is $i_{ex} - i_{ref}$. Therefore, the choice of value of i_{ref} is arbitrary. Equation (B.52) can then be simplified to:

$$i_{ex} = \frac{E_{corr,1}^* - E_{corr,2}^* - (\Phi_1 - \Phi_2)}{b_a + b_c} \quad (\text{B.53})$$

This linearization technique is applied to avoid the computationally expensive calculation of logarithmic terms. Equation (B.53) is applicable for $i_{ex} < 0.01 \text{ A/m}^2$ (approximately 0.5% maximum error). Because the coupling current is typically much smaller than 0.01 A/m^2 , use of the linearized form of this equation is appropriate. Because this method is applied successively throughout the simulation, avoidance of the repeated calculation of a logarithmic term will be beneficial for computational efficiency. From equation (B.53), it can be seen that the excess current is a function of the net potential difference between the electrodes (the driving force less the resistance) and the sum of the net Tafel slopes.

The previous derivation assumed that the electrode coupling process exhibited Tafel behaviour. For a passive metal, the previous method breaks down because the numerical value of b_a would be infinite. In this case, the current between two electrodes may be directly calculated using a rearranged form of equation (B.42):

$$i_{ex,jk} = \left[E_k - E_j - (\Phi_k - \Phi_j) \right] \frac{\bar{\kappa}_{jk}}{\Delta x_{jk}} \quad (\text{B.54})$$

Equation (B.54) is simply an expression of Ohm's Law. The net driving potential is the difference between the two metal potentials less the iR drop in solution. If the current

predicted via (B.54) is greater than the passive current, i_p , then the coupling current is set to i_p and the coupling is controlled by electrode charge transfer kinetics. However, if it is less than i_p , the coupling is controlled by solution resistance. The calculation of a coupling current for a passive metal is slightly more computationally expensive than for a non-passivated metal because equation (B.54) requires line integration to determine the spatial average conductivity, $\bar{\kappa}_{jk}$.

B.4 Overall Algorithm

At the start of the simulation, the program will read pertinent physical and chemical data from text files. In this simulation program, the code structure assembles all chemical and electrode reactions at run time. The advantage of this is that any system may be modelled without code modifications. The functionalities of exchange current densities upon temperature and composition are also read from these text files. There are six data files that are required for the simulator, and these files are: AnodicReactions.dat, CathodicReactions.dat, ChemicalReactions.dat, Charge.dat, Diffusivity.dat, and BulkConcentration.dat. Once data is read in, various initiation tasks are performed. After this, simulation of the crevice corrosion problem proceeds. To simulate crevice corrosion initiation and propagation, the following algorithm is followed:

1. If the fluid is not stagnant, calculate the velocity profile throughout the system using CFD. It is assumed that the flow is at steady state.
2. Based upon the most recent estimate of the electrode kinetics and solution composition, calculate the potential field in solution.
3. Using the potential field calculation and the velocity profile, solve the mass transport equation.

4. Using the solution composition obtained from the mass transport solver, calculate the mixed potential of each electrode at the metal-solution interface.
5. Use differences in the mixed potential to calculate coupling currents between all possible anode-cathode pairs.
6. Output results, increment the time, and go back to step 2.

Preliminary simulations using the complete crevice corrosion model have shown that in occluded regions, the limiting current is lower, and as a result, the corrosion potential will drop in these regions. However, in regions that are more exposed, the limiting current will be higher, and in these regions, the corrosion potential will be higher. For example, at the point where the crevice and bold surface meet, and at the corner of the crevice at the tip, regions of high and low potential develop, respectively. This is because the meeting of the crevice and bold surface form a corner that juts out, while the corner of the crevice tip is an inward corner.

B.5 References

1. J. Newman, "Electrochemical Systems", Prentice Hall, Toronto (1973).
2. K. Heppner, and R.W. Evitts. (2004) Dynamics of Continuous, Discrete and Impulsive Systems, Series B **11**. pp. 29 – 46.
3. L. L. Shrier, R. A. Jarman, G. T. Burstein, *Corrosion*, 3rd Ed., pp. 1:101, 2:20, Butterworth-Heinemann Ltd, Oxford, UK (1994).
4. K. S. Pitzer, *J. Phys. Chem.*, **77**, 268 (1973).
5. K. S. Pitzer, *Activity Coefficients in Electrolyte Solutions*, 2nd Ed., pp. 77 – 91, 122 – 125, CRC Press, Boca Raton, FL (1991).
6. D.D. Macdonald, P.-C. Lu, M. Urquidi-Macdonald, and T.-K. Yeh, *Corrosion* **52**, pp. 768 – 784.

Appendix C. List of Publications

The following articles are a result of the work presented in this thesis.

1. Heppner, K. and Evitts, R.W. (2005) A New Method for Calculating Charge Density in Electrochemical Systems. *Corrosion Engineering, Science and Technology*. In Press.
2. Heppner, K. and Evitts, R.W. (2005) “Modelling of the Effect of Hydrogen Ion Reduction on the Crevice Corrosion of Titanium” in *Environment-Induced Cracking. Chemistry, Mechanics, and Microstructure*. Eds. Shipilov S.A., Jones, R.H., Ulive, J.-M. and Rebak, R.B. Elsevier, Oxford, UK, pp. 95 – 104.
3. Heppner, K. and Evitts, R.W. (2005) A Hybrid Differencing Scheme for Mass Transport in Electrochemical Systems. *International Journal of Numerical Methods for Heat and Fluid Flow* 15. pp. 842 – 862.
4. Heppner, K., Evitts, R.W., and Postlethwaite, J. (2005) Effect of Ionic Interactions on the Initiation of Crevice Corrosion in Passive Metals. *Journal of the Electrochemical Society* 152. pp. B89-B98.

5. Heppner, K., and Evitts, R.W. (2004) Computation of Mass Transport in Stagnant Electrolytic Systems. *Dynamics of Continuous, Discrete, and Impulsive Systems, Series B: Applications and Algorithms* 11. pp. 29 – 46.
6. Heppner, K., Evitts, R.W., and Postlethwaite, J. (2004) The Effect of the Crevice Gap on the Initiation of Crevice Corrosion in Passive Metals. *Corrosion* 80. pp. 718 – 728.
7. Heppner, K., Evitts, R.W., and Postlethwaite, J. (2002) Prediction of the Crevice Corrosion Incubation Period of Passive Metals at Elevated Temperatures: Part I – Mathematical Model. *Canadian Journal of Chemical Engineering* 80. pp. 849 – 856.
8. Heppner, K., Evitts, R.W., and Postlethwaite, J. (2002) Prediction of the Crevice Corrosion Incubation Period of Passive Metals at Elevated Temperatures: Part II – Model Verification and Simulation. *Canadian Journal of Chemical Engineering* 80. pp. 857 – 864.
9. Heppner, K. and Evitts, R.W. (2005) A Numerical Model to Rank Passive Alloys for Crevice Corrosion Susceptibility in Potash Brine. *Canadian Metallurgical Quarterly*. Submitted September 2005.

10. Heppner, K., Evitts, R.W. (2004) Modelling of Localized Corrosion in Typical Potash Processing Brines. Canadian Society for Civil Engineering Conference 2004. Saskatoon, SK, June 2004.
11. Heppner, K. and Evitts, R.W. (2004) A Novel Differencing Scheme for Electrolyte Mass Transfer Modelling. Submitted to the 2004 Graduate Student Paper Competition held at the 52nd Canadian Chemical Engineering Conference, CSChE, Calgary, AB, October 2004.
12. Heppner, K., Evitts, R.W., and Postlethwaite, J. (2003) Effect of Ionic Interactions on the Initiation of Crevice Corrosion in Passive Metals. 204th Meeting of the Electrochemical Society. Orlando, FL, USA, October 2003.
13. Heppner, K. and Evitts, R.W. (2003) Properties of the Electrolyte Solution Bounded By a Two-Dimensional Titanium Crevice. 204th Meeting of the Electrochemical Society. Orlando, FL, USA, October 2003.
14. Heppner, K., Evitts, R.W., and Postlethwaite, J. (2003) Determining the Crevice Corrosion Incubation Period of Passive Metals for Systems with Moderately High Electrolyte Concentrations – Application of Pitzer’s Ionic Interaction Model. CORROSION 2003. San Diego, CA, USA, March 2003.

15. Heppner, K., Evitts, R.W., and Postlethwaite, J. (2003) A Predictive Model for Flow Influenced Corrosion. NACE Northern Area Western Conference 2003. Calgary, AB, February 2003.